Quantum-Coupled Single-Electron Thermal to Electric Conversion Scheme

by

Dennis M. Wu

Submitted to the Department of Electrical Engineering and Computer Science
in partial fulfillment of the requirements for the degree of

Doctor of Philosophy in Electrical Engineering

at the

MASSACHUSETTS INSTITUTE OF TECHNOLOGY

[February 2007]
June 2007

Author ....
Department of Electrical Engineering and Computer Science
March 13, 2007

Certified by ....
Peter L. Hagelstein
Associate Professor
Thesis Supervisor

Accepted by ....
Arthur C. Smith
Chairman, Department Committee on Graduate Students

Quantum-Coupled Single-Electron Thermal to Electric Conversion Scheme

by

Dennis M. Wu

Submitted to the Department of Electrical Engineering and Computer Science
on March 13, 2007, in partial fulfillment of the
requirements for the degree of
Doctor of Philosophy in Electrical Engineering

Abstract

A new thermal to electric conversion scheme based on an excitation transfer and tunneling mechanism is studied theoretically. Coulomb coupling dominates when the hot side and the cold side are very close. Two important concepts went into the device scheme: (1) Coulomb coupling, to try to increase throughput power (which is not subject to blackbody limit), and (2) a quantum dot implementation, to restrict number of states, to try to increase efficiency. Modeling efforts from Bloch equations, brute force numerical simulations, and the secular equations partitioning method are discussed. A hot-side quantum dot design of the device is considered. Alternative implementation where the hot-side is a plain sheet of metal or aluminum oxide is analyzed. We found that the model power/area is higher than the blackbody limit, and the predicted conversion efficiency is very high.

Thesis Supervisor: Peter L. Hagelstein
Title: Associate Professor

Acknowledgments

First of all, I would like to express my gratitude to my supervisor Prof. Peter Hagelstein for always being patient, encouraging and enlightening.

I would like to express my gratitude to Mr. Robert DiMatteo for financial support and inspiring discussions.

I thank my thesis committee Prof. Mildred Dresselhaus and Prof. Clifton Fonstad for valuable comments and advices.

I admire Mr. PoNing Chen for his mathematical skills and insights.

I thank Dr. Andrew Meulenberg for helpful questions and comments.

Many thanks to my colleague Dr. Irfan Chaudhary for research advice and company.

I am thankful to the department and the institute for TAship support and various other resources.

Finally, I take this opportunity to express my gratitude to my love Agnes Feng, my parents, and my brother for their moral support during my time at MIT.

Contents

List of Figures

List of Tables

Chapter 1

Introduction

There has been a consistent increase in oil price in the past decade (see Figure 1-1 [1]), and the continued availability of oil at low cost over the next decades has been cast in doubt [2]. Since oil is our primary source of energy, this poses an energy security issue. There are a variety of renewable energy systems that could potentially replace oil energy, including hydropower, wind energy, bio-power, geothermal power, solar thermal power, and photovoltaics.

1.1 Thermophotovoltaics

We have been encouraged by a group at Draper Laboratory who works on a particular type of photovoltaics called the thermophotovoltaics (TPV) [3]. The basic idea of TPV is to produce electricity from heat through radiation. Please see Figure 1-2 [4]. There is a hot side emitter at a higher temperature that emits thermal radiation. The radiation travels through a gap and then impinges on a cold side photodiode at a lower temperature, which converts the radiation into electricity.

There are two important parameters associated with a TPV system, namely the power density per unit area and the conversion efficiency. A TPV system with higher power density can convert more power per unit area, and hence is more economical for fixed cost per unit area, leading to reduced costs. Also, if the conversion efficiency

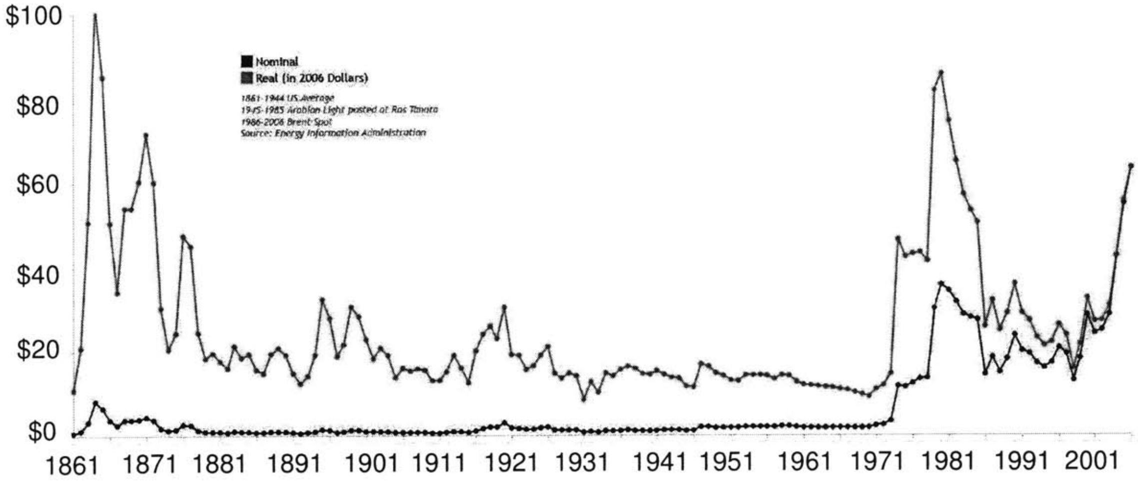

Figure 1-1: Oil prices from 1861-2006 in dollars of the day and 2006 dollars [1]

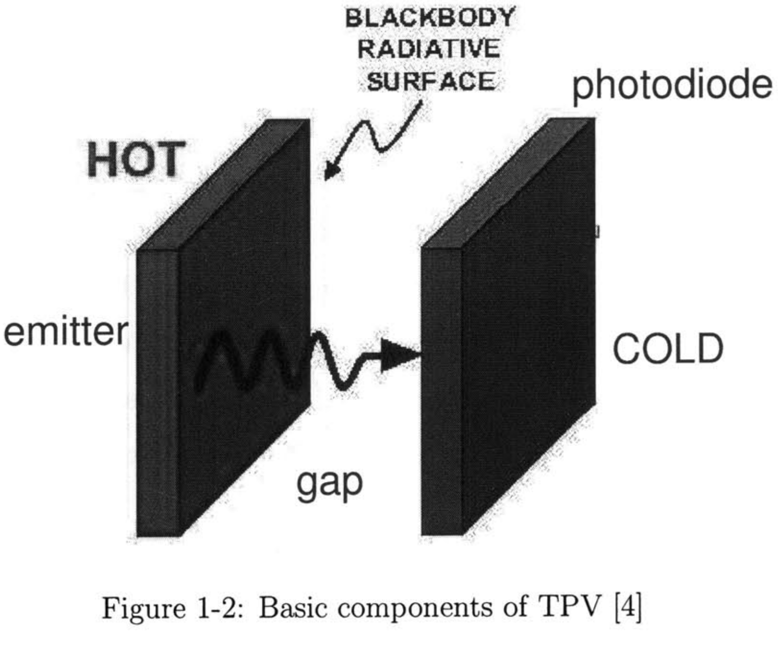

Figure 1-2: Basic components of TPV [4]

is higher, then less fuel is needed to generate power, leading to reduced expense and fewer pollutants.

The TPV system is limited in power per unit area by the blackbody radiation. In free space, the blackbody radiation total power per unit area is σT^4, where σ is the Stefan-Boltzmann constant and T is the absolute temperature. Inside a medium of refractive index n, the speed of light is lowered by a factor of n and the density of modes is increased by a factor of n^3, and therefore the radiation is increased by a factor of n^2 [5]. However, when the radiation exits the medium it suffers from internal reflections and the radiation is lowered by a factor of n^2. The amount of radiation coming out of the medium is still limited by the free space σT^4 and that is the maximum power the cold side photodiode can possibly convert.

In addition to the radiation limit, the TPV system has a spectral issue that impacts its conversion efficiency. On the one hand, photons with energy lower than the bandgap of the photodiode do not create electron-hole pairs and are responsible for heating the cell [3]. On the other hand, for high-energy photons, the difference between the photon energy and the bandgap is also lost to cold-side heating [3]. In order to improve the conversion efficiency we would like the photons to have energies just above the bandgap. Therefore, in a typical TPV scheme there is a spectral filter, placed in between the emitter and the diode, which ideally selects photons of the right energies and reflects back the rest of the radiation (Figure 1-3 [6]).

1.2 Micro-gap thermophotovoltaics (MTPV)

The group at Draper Laboratory has worked on a sub-type of TPV called micro-gap thermophotovoltaics (MTPV). In typical TPV where the distance (or gap) between the diode and the emitter is much larger than the wavelength of the light, the radiation heat transfer is limited by the blackbody radiation $\sigma \mathrm{T}^4$, as discussed above. However, in micro-gap thermophotovoltaics (MTPV), the gap is small (in the submicron regime) and the energy within the hot radiator can evanescently couple to the

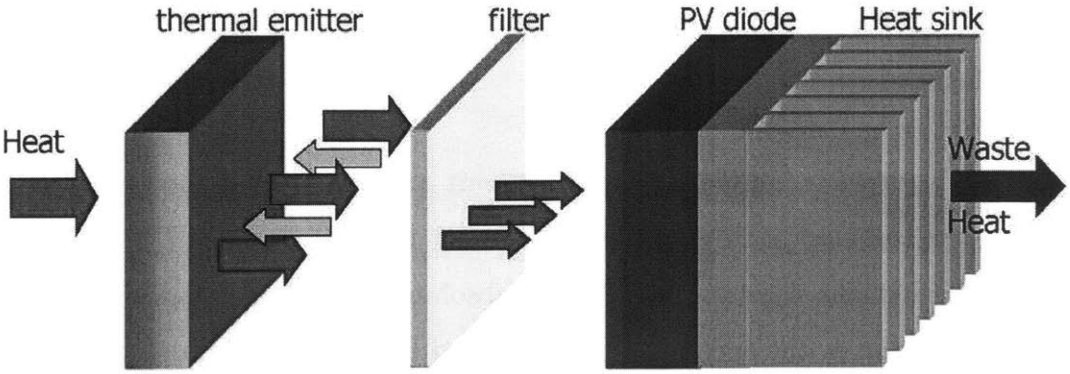

Figure 1-3: A typical TPV system [6]

TPV photodiode, as a result the thermal radiation inside the hot emitter can tunnel through the gap into the cold side photodiode, leading to a higher radiation limit of $n^2\sigma T^4$ for a hot side medium of refractive index n [4, 5]. To take into account the frequency-dependent nature of the refactive index, n^2 should be averaged over the blackbody spectrum:

$$\langle n^2 \rangle = \frac{\int_0^\infty \frac{8\pi h\nu^3}{c^3(e^{h\nu/k_BT}-1)} n^2(\nu) d\nu}{\int_0^\infty \frac{8\pi h\nu^3}{c^3(e^{h\nu/k_BT}-1)} d\nu}$$

Figure 1-4 [4] shows schematically how decreasing the gap between the hot emitter and the photovoltaic diode leads to an enhancement in power transfer.

1.3 Quantum-coupled single-electron conversion scheme

TPV and MTPV convert radiation coming from the hot side into electricity on the cold side. This is a photon exchange coupling; namely, an electron on the hot side emits a photon and an electron on the cold side accepts the photon. There exists another type of coupling: Coulomb coupling. Basically energy can be transferred from a hot-side electron to a cold-side electron through the Coulomb force between the two electrons. The magnitudes of the photon exchange coupling and the Coulomb

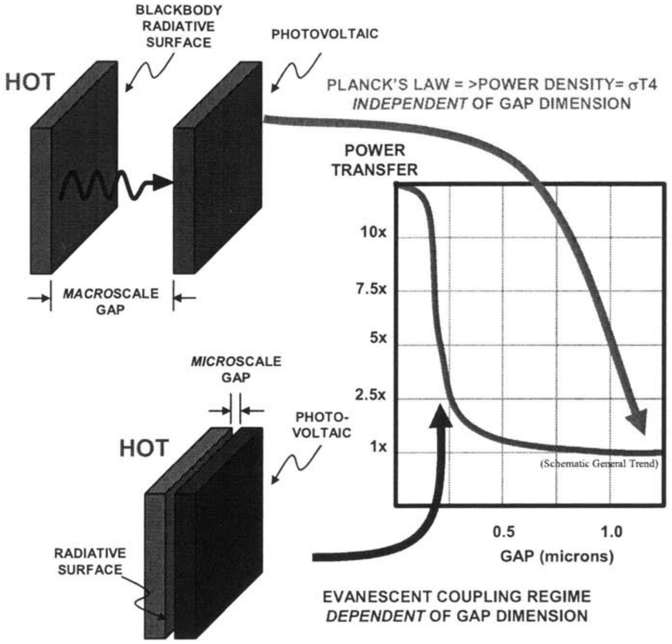

Figure 1-4: Decreasing the gap between the hot emitter and the photovoltaic diode leads to an enhancement in power transfer [4]

coupling have different distance dependences. The Coulomb coupling has a $1/R^3$ dependence on distance while the photon exchange coupling has a $1/R$ dependence. Shown in Figure 1-5 are the normalized matrix elements for these two types of coupling as a function of distance between two electrons in free space. The calculations are done using the expressions in [7]. We see from Figure 1-5 that the Coulomb coupling dominates over the photon exchange coupling at narrow distances roughly shorter than $\lambda/2\pi$. However, at larger distances the Coulomb coupling decays rapidly.

If we bring the photodiode close to the hot side emitter, would the Coulomb coupling lead to increased power throughput? In free space the Coulomb coupling is significant at short distances narrower than a couple hundred nanometers. In dielectrics Coulomb coupling is only significant at even shorter distances. Therefore, we would need a surface photodiode to take advantage of the Coulomb coupling. There is not such a photodiode at present of which we are aware. We are therefore motivated to propose a new single-electron thermal to electric conversion scheme

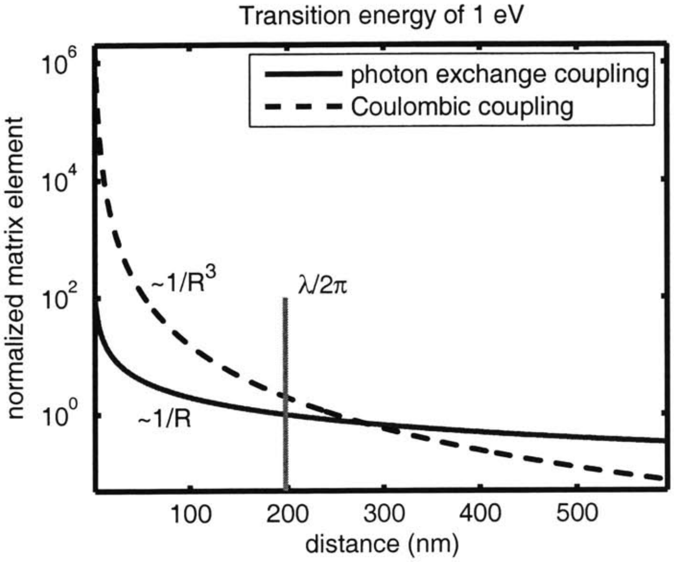

Figure 1-5: Distance dependence of the photon exchange coupling and the Coulombic coupling strengths.

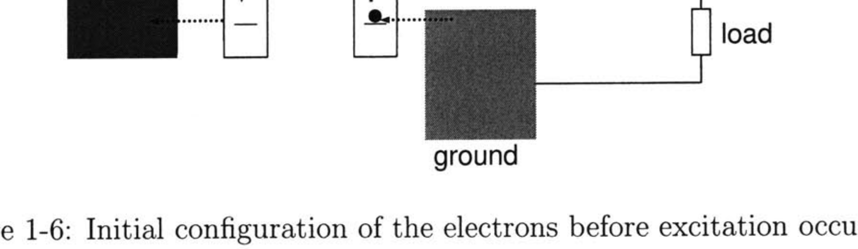

Figure 1-6: Initial configuration of the electrons before excitation occurs.

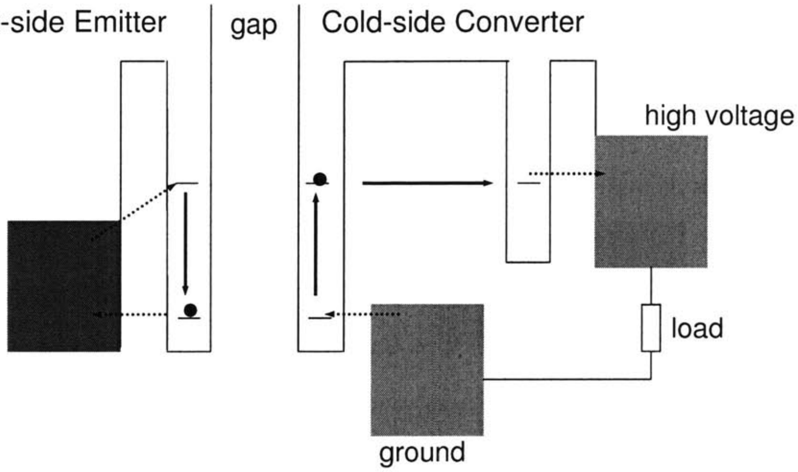

Figure 1-7: The cold-side electron receives energy transfer from the hot-side and becomes excited.

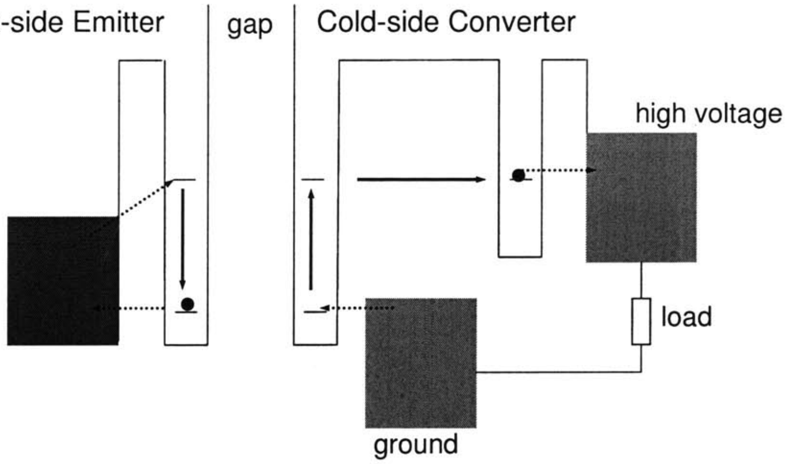

Figure 1-8: The cold-side electron tunnels through a barrier to the second cold-side potential well.

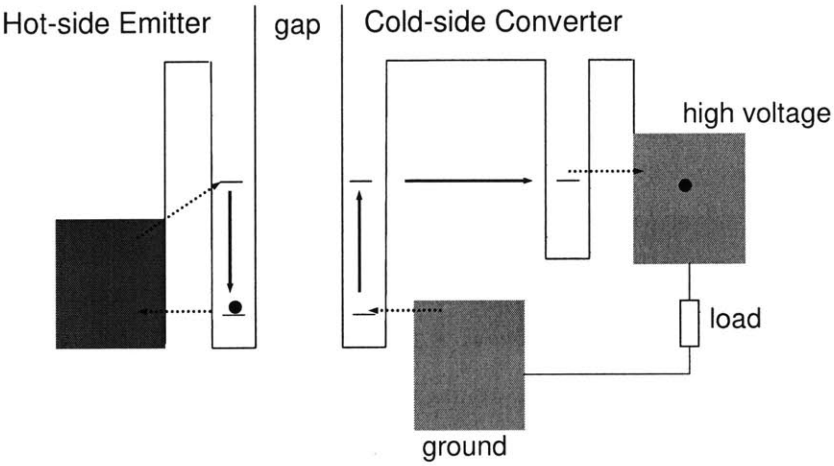

Figure 1-9: The cold-side electron tunnels into the high-voltage electron reservoir.

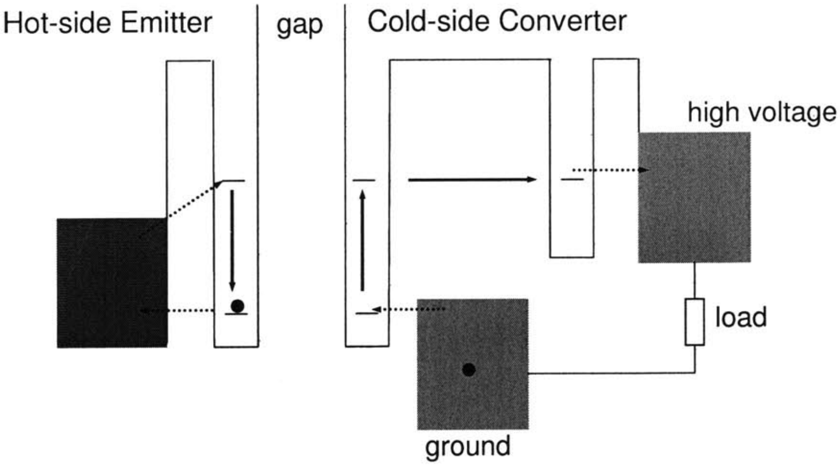

Figure 1-10: The cold-side electron does work on the load and then arrives at the ground reservoir.

which could accept energy and convert it to electrical work near the surface interface with a very narrow gap.

Please see Figures 1-6 to 1-10 for a schematic of this proposal and its operation. A hot-side emitter and a cold-side converter are separated by a vacuum gap. On the hot-side, there is a potential well holding two levels which communicate with an electron reservoir represented as a square. On the cold-side, there is a potential well holding two levels with energy spacing matched to that of the hot side potential well. There is another potential well on the cold-side holding only one level resonant with the excited state of the first cold-side well. The ground-state of the first cold-side well communicates with a ground electron reservoir while the level in the second cold-side well is coupled to an electron reservoir at a higher voltage. The two cold-side reservoirs are connected through a load. Note that the quantum well on the hot-side leads to two levels only to simplify the model; as such it stands in for more complicated versions of the scheme with more levels on the hot-side.

The hot-side reservoir is at a higher temperature, and it provides an excited electron into the hot-side potential well. The cold-side ground reservoir provides a ground-state electron into the first cold-side well. This is the initial configuration shown in Figure 1-6. The excitation of the hot-side electron is then transferred to the cold-side electron via Coulomb coupling, and we arrive at Figure 1-7. The excited electron on the cold-side then tunnels into the second cold-side well (Figure 1-8) and relaxes into the high-voltage reservoir (Figure 1-9). An electron from the high-voltage reservoir comes out to do work on the load, arriving at the ground reservoir (Figure 1-10). The cycle then restarts (Figure 1-6).

The conversion scheme that we propose here has several features. First, it is a single-electron conversion process in the sense that the cold-side current is produced one electron at a time. It is also a surface converter that is sitting right against the gap, taking advantage of the short-ranged Coulomb coupling. Since the conversion does not rely on the photon exchange coupling, there is no blackbody radiation limit to this scheme.

One possible way to implement this single-electron conversion scheme is to use quantum dots. Shown in Figure 1-11 are three quantum dots implementing the potential wells. The hot-side dot and the cold-side dot have matched level spacings and they face each other across the gap. The second cold-side dot (one-level dot) is positioned next to the first cold-side dot (two-level dot) to provide tunneling possibilities. Initially the ground bus provides an electron into the two-level dot. The electron then gets promoted to an excited state via Coulombic energy transfer. The excited electron subsequently tunnels into the one-level dot before relaxing into the high-voltage bus to do work on the load.

The wavefunction of the excited level of the two-level dot has a peak in the upper half of the dot. On the other hand, the ground state wavefunction of the two-level dot has a peak in the middle of the dot and is of lower value than the excited level in the upper half of the dot. The one-level dot 2 horizontally points to the upper half of the two-level dot and the one-level dot level couples to the excited state of the two-level dot preferentially due to the spatial configuration. In addition, the excited state of the two-level dot is more extended and it couples to the one-level dot more strongly due to its higher tunneling probability. The ground bus branch is horizontally positioned away from the center of the two-level dot. Due to this spatial orientation, the ground bus coupling to the excited level of the two-level dot is much smaller than the coupling between the ground bus and the ground state of the two-level dot.

Pumping one electron at a time produces only a small current, but if we have a lot of these device units repeated over the cold-side surface, the output can be significant. Figure 1-12 shows the array of device units on the cold-side surface. The periodicity of the device units is assumed somewhat arbitrarily to be 1000 Å × 1000 Å due to historical reasons. This choice has an impact on our calculated power density for the conversion scheme because the throughput is directly proportional to how dense the device units are packed. The shaded vertical rectangles are the two-level dots, namely

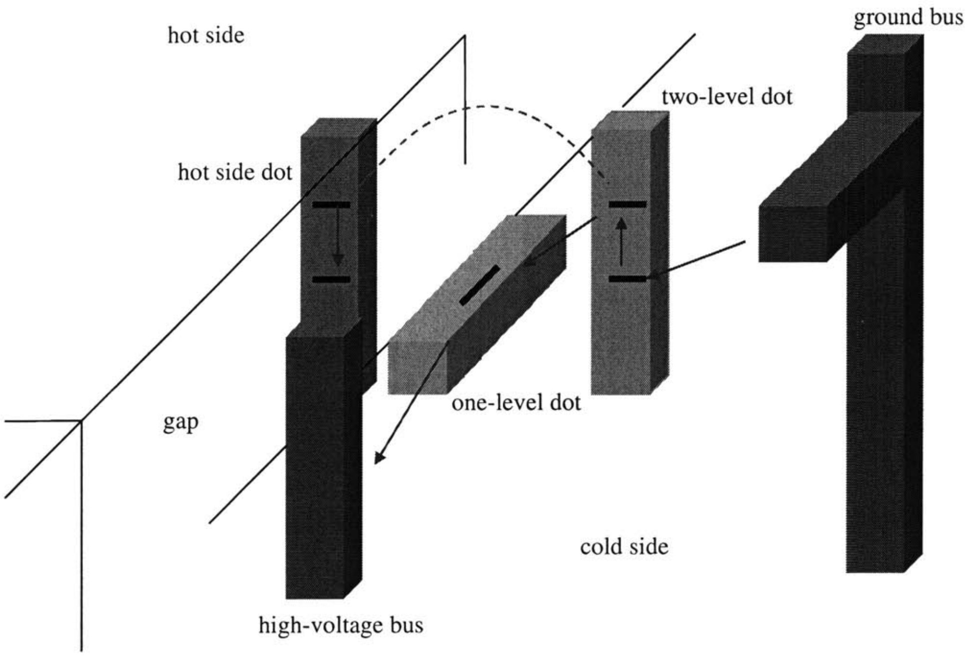

Figure 1-11: A quantum dot implementation of the single-electron conversion scheme.

the active area where the excitation transfer occurs. The active area represents the minimal area required for each device unit to function. With our assumed 1000 Å periodicity, the active area only takes up about 0.0065 of the cold-side surface.

1.4 Power per unit area

We compare the performances of TPV, MTPV, and quantum-coupled conversion scheme in Figure 1-13. The figures for TPV are taken from the experimental results of [8]. The numbers for MTPV are experimental results from [4] done at 0.12 μm gap. The values for the quantum-coupled conversion scheme are computed from our model of the aluminum oxide emitter design described in chapter 15. Figure 1-13 shows the total thermal power transferred from the emitter to the TPV diode or quantum converter, versus the hot-side temperature. Also shown are the blackbody limit σT^4 for TPV and the evanescent coupling limit $n^2 \sigma T^4$ for MTPV, where n^2 is the averaged refractive index of silicon for the case of [4]. We see that the TPV power is an order of magnitude or more below the blackbody limit, and the MTPV power

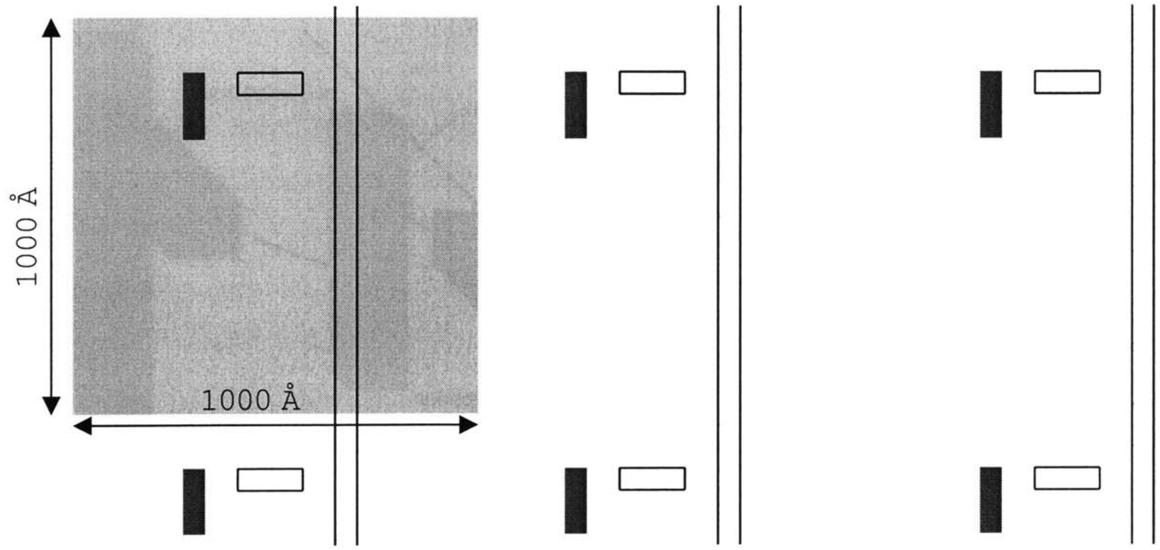

Figure 1-12: The cold-side surfac showing the area occupied by the quantum dots and the reservoir of the periodic device units .

is also an order of magnitude lower than the evanescent coupling limit. Also shown in the graph are the calculated data points for the quantum-coupled single-electron conversion scheme assuming a 1 nm gap and a 5 nm gap. We have presented the theoretical results in power per unit area with the assumed 1000 Å periodicity (the stars in the graph) and in power per unit active area (the squares in the graph). It is clear that the quantum-coupled conversion scheme can exceed both the free-space blackbody and the evanescent coupling limits on a per unit active area basis.

1.5 Efficiency

In addition to the power figure, we are also interested in the conversion efficiency. The maximum thermal to electric conversion efficiency is the Carnot limit, which is obtained when the entropy is conserved during the conversion process. For the TPV system, excitation transfer causes an electron-hole pair creation. Both the electron and the hole see many accessible states, and entropy is hence produced. (Note that there are other sources of entropy generation in TPV. This is one example associated with the photodiode.) For the single-electron conversion scheme, we start off with

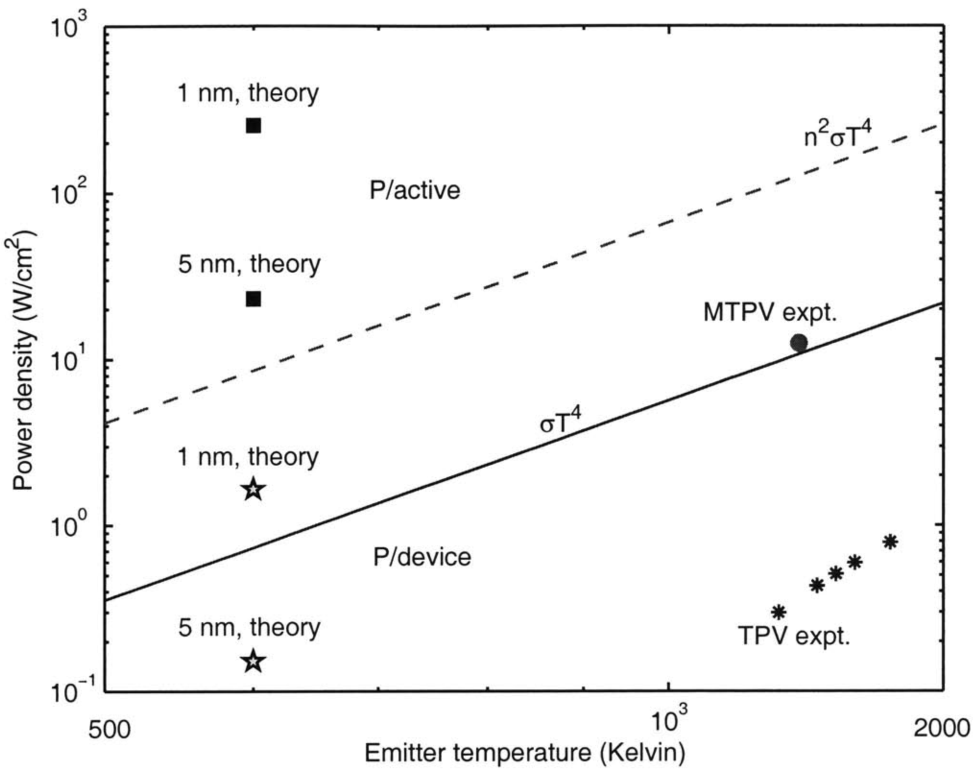

Figure 1-13: Thermal power for TPV, MTPV, and quantum-coupled conversion scheme. The values for TPV and MTPV are experimental results from [8] and [4] while those for the quantum-coupled case is from our calculations described in later chapters.

one state, a two-electron product state with the hot-side electron excited and the cold-side electron at ground. After the excitation transfer we end with one state, a two-electron product state with the hot-side electron at ground and the cold-side electron excited. Entropy is conserved in this excitation transfer process as we have restricted the number of states. Of course entropy can still be introduced via the finite lifetime of the excited level of the first cold-side potential well, and through thermalization into the reservoirs. Our calculations have attempted to capture these aspects of the problem as well.

Note that here we are exploring the idea of restricting the states to conserve entropy in the hope of improving the efficiency. The proposed quantum dot implementation

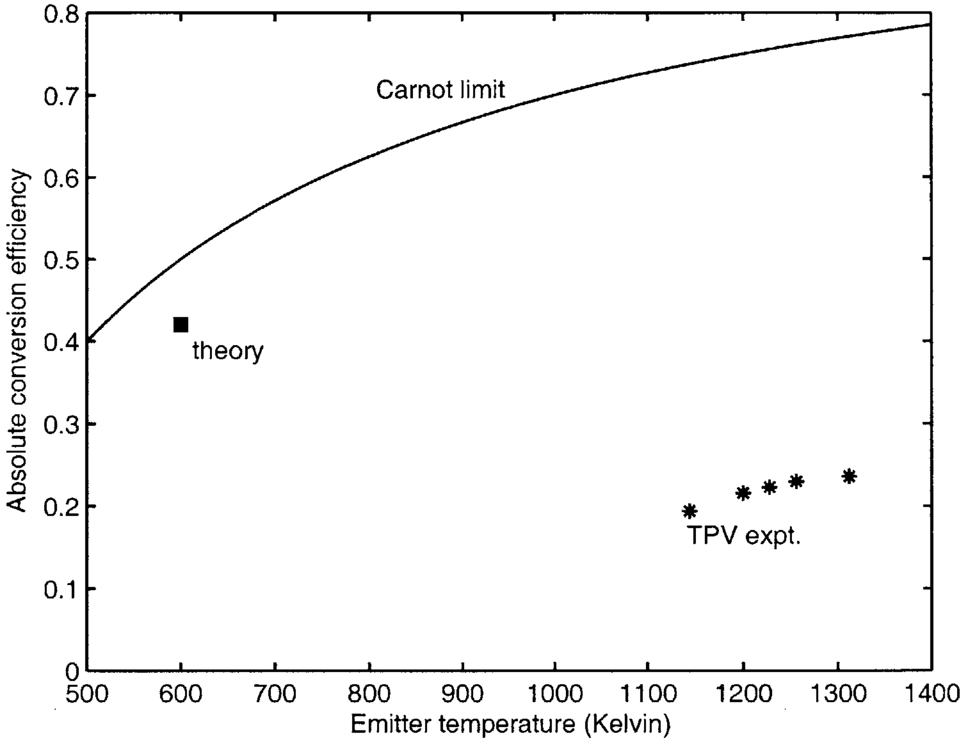

Figure 1-14: Efficiency for TPV and quantum-coupled conversion scheme. The values for TPV are experimental results from [8] while those for the quantum-coupled case is from our calculations described in later chapters. There is not an efficiency figure reported in [4] for MTPV.

may be out of reach of current technology but our goal here is to provide initial theoretical investigations.

Figure 1-14 shows the conversion efficiency for TPV [8] and the quantum-coupled scheme, along with the Carnot limit, the fundamental upper bound of thermal to electric conversion efficiency. The efficiency for MTPV is not reported in [4]. The 1 nm gap and 5 nm gap cases have the same efficiency and therefore only one data point is shown for the quantum-coupled scheme. We see that the potential conversion efficiency for the quantum-coupled scheme is high, approaching the Carnot limit, while the efficiencies for TPV are below 30% of the Carnot limit. Note that in our present calculation we have neglected Coulomb-coupled heat flow, which is expected to be the dominant loss mechanism. We have derived a formula for the evaluation of this loss in Appendix C and a calculation will be carried out in the future.

1.6 Overview of thesis

Figure 1-15 shows the road map of the thesis. General models for the quantum-coupled single-electron conversion scheme are first developed. These include the Bloch equations model, the brute-force numerical approach, and the secular equation partitioning method. To apply the general model to a specific design, we need to estimate the various parameters associated with each design. For this purpose, parameter estimation models are constructed for calculating the Coulomb coupling strengths, the electron wavefunctions and energies, and the relaxation times. Finally, we combine the above modeling efforts together to compute numerical performance figures for the different designs of the conversion scheme.

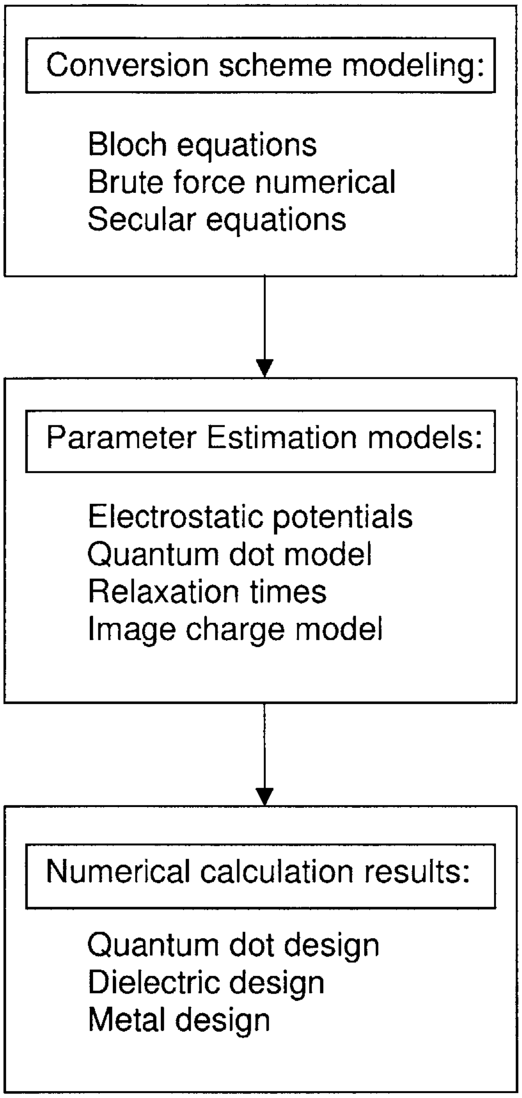

Figure 1-15: The various components of the thesis and their organizations.

Chapter 2

Bloch equations modeling

The first modeling attempts focus on a Bloch equation description of the quantum-coupled conversion scheme. Bloch equations are evolution equations for the expectations of quantum variables. They are analogs to the classical equations of motion and they allow easier interpretations and understandings of complex quantum systems. Nuclear magnetic resonance (NMR), masers, and lasers have all been developed with the aid of Bloch equations [9]. When applied to our quantum-coupled conversion scheme, the model results in some understandings about the behavior of the device but it runs into difficulties when trying to simulate the off-resonance characteristics. The reason is that it is hard to introduce losses into Bloch equations in such a way that they are consistent with thermodynamics. Below we give a detailed description of this initial model.

2.1 The conversion scheme

The scheme in its simplest implementation involves a two-level system on a hot-side that is coupled through a very thin gap to a two-level system in a cold converter.(See Figure 2-1). The upper state of the two-level system has the possibility of tunneling through a barrier to a level in a second quantum well that is coupled to an external circuit. The return path of the external circuit leads to population of the lower level

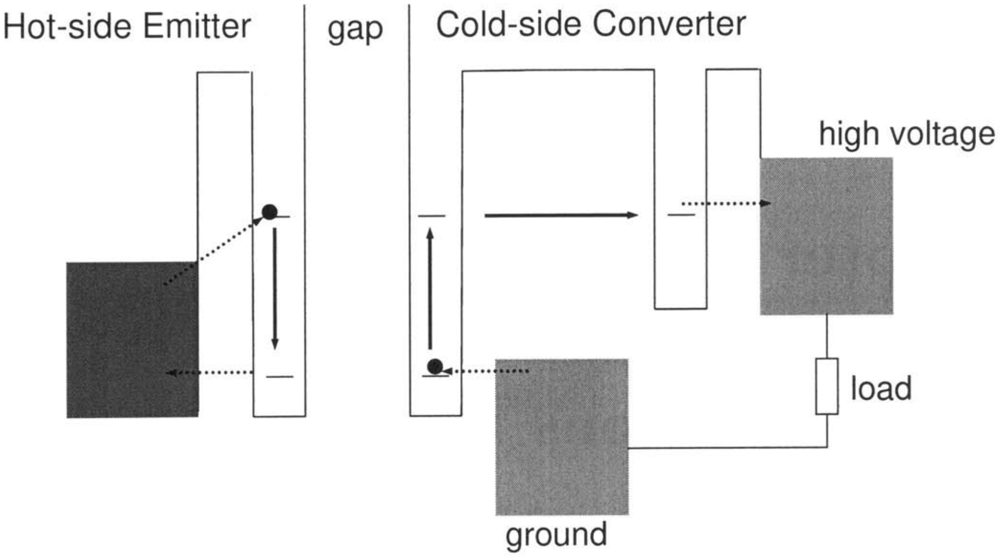

Figure 2-1: Schematic of quantum coupled thermal to electric conversion scheme. The hot-side is at an elevated temperature relative to the cold-side. There is a vacuum gap separating the hot and the cold-sides. A two-level system on the hot-side is matched to a two-level system on the cold-side. The upper state of the cold-side two-level system has the possibility of tunneling through a barrier to a level in a second quantum well that is coupled to an external circuit.

of the two-level system in the cold converter.

The structure of the scheme is as discussed in Chapter 1. On the hot-side, we see a two-level system that is coupled to a reservoir in thermal equilibrium at an elevated temperature. Both levels of the quantum well are assumed to communicate with the reservoir. On the cold-side, we see matched quantum well levels that are coupled with a reservoir in thermal equilibrium at room temperature. In addition, we see a second quantum well on the cold-side containing a single level on the other side of a barrier, which can be accessed by the cold-side two-level system through tunneling. This single level is coupled to a second cold-side reservoir, one which has an elevated Fermi level relative to the first cold-side reservoir. Both cold-side reservoirs are assumed to be at room temperature.

The basic idea is that Coulomb coupling with the hot-side two-level system results in promotion of carriers on the cold-side two-level system, and this leads to an enhanced voltage and current flow capable of doing electrical work.

The model is highly idealized in that it is the simplest version that implements the basic scheme, but we expect it to capture many important features of the scheme. Our approach initially is to specify the minimum possible implementation that has only enough pieces and parts to function as designed, such that the problem of modeling is thereby simplified. Our goal in what follows is to develop a theoretical model for this system.

2.2 A simplified quantum model

The scheme under discussion is interesting theoretically, in that it includes pieces that are fundamentally quantum mechanical (two-level systems, tunneling, and a quantum coupling effect), pieces that are statistical mechanics problems (the various reservoirs), and pieces that are classical (the current and voltage characteristic of the resistor and external circuit). To model this, we propose to begin with the quantum mechanical part of the problem. The underlying Hamiltonian must be specified, and the quantum problem must be analyzed. The analysis that we propose here involves the use of Ehrenfest's theorem in order to develop an equivalent "classical" model in terms of rate equations associated with the different states. The specification of this classical model can include coupling with the different reservoirs, where the statistical mechanics is implemented through the thermal relations between the different relaxation and source terms. In the end, the resulting model will produce a current and voltage relation for the emitter and converter as an electrical device, and we can then use circuit models to analyze the power delivered to the load. The efficiency of the device can be determined from the results of the analysis.

The underlying Hamiltonian of the two quantum well structures is of the general form

$$\hat{H} = \left[\hat{T}_1 + \hat{V}_1\right] + \left[\hat{T}_2 + \hat{V}_2\right] + \hat{U}_{12}$$

The simplest version of the problem comes about by assuming a one-dimensional spatial dependence in each of the two coupled quantum well structures. In this case, we would obtain a Hamiltonian of the general form

$$\hat{H} = \left[-\frac{\hbar^2}{2m_1}\frac{\partial^2}{\partial z_1^2} + V_1(z_1)\right] + \left[-\frac{\hbar^2}{2m_2}\frac{\partial^2}{\partial z_2^2} + V_2(z_2)\right] + U(z_1, z_2)$$

2.3 Single-particle basis states

We can simplify the problem further by restricting the associated Hilbert space. The idea is that most of the important physics involves only a few states. Hence it makes sense to recast the Hamiltonian in terms of the different states of interest. On the emitter side, we assume that the well and barrier is designed so that there are two single-particle states of interest – a ground state and an excited state of the quantum well. We will define these states as solutions of

$$\left[-\frac{\hbar^2}{2m_1}\frac{d^2}{dz_1^2} + V_1'(z_1)\right] u_1(z_1) = E_1^h \, u_1(z_1)$$

$$\left[-\frac{\hbar^2}{2m_1}\frac{d^2}{dz_1^2} + V_1'(z_1)\right] u_2(z_1) = E_2^h \, u_2(z_1)$$

where $V_1(z_1)$ is a modified version of the potential on the hot-side which has no allowed region to the left of the quantum well. The two quantum states of the hot-side quantum well are u_1 and u_2, with energy eigenvalues E_1^h and E_2^h. In addition, we use u_0 to denote the zero-particle state on the hot-side with energy eigenvalue E_0^h.

On the cold-side converter, we assume that the quantum well structure is designed so as to produce three relevant states. In general, these states will be a function of the difference between the Fermi level of the two reservoirs, and will involve contributions to the wavefunction in both wells. To simplify the underlying picture, we propose to work with cold-side single particle states that are simpler. We assume that the quantum well near the gap is designed so that two levels are produced that match the two levels on the emitter side of the gap, and that these states can be taken as solutions to

$$\left[-\frac{\hbar^2}{2m_2}\frac{d^2}{dz_2^2} + V_2'(z_2) \right] \phi_1(z_2) = E_1^c \, \phi_1(z_2)$$

$$\left[-\frac{\hbar^2}{2m_2}\frac{d^2}{dz_2^2} + V_2'(z_2) \right] \phi_2(z_2) = E_2^c \, \phi_2(z_2)$$

In this case, the potential $V_2'(z_2)$ is modified to eliminate any allowed region to the right of the quantum well. The two quantum states of the cold-side well are ϕ_1 and ϕ_2, with energies E_1^c and E_2^c.

We assume that the well on the right of the cold-side converter supports only a single bound state. We propose to model this state through

$$\left[-\frac{\hbar^2}{2m_2}\frac{d^2}{dz_2^2} + V_2''(z_2) \right] \phi_3(z_2) = E_3^c \, \phi_3(z_2)$$

where $V_2''(z_2)$ is a modified version of the cold-side potential that has no well next to the gap. The associated wavefunction is ϕ_3 with energy E_3^c. Similar to the hot-side, we use ϕ_0 to denote the zero-particle state on the cold-side with energy eigenvalue E_0^c.

2.4 A restricted Hamiltonian

We can construct a restricted Hamiltonian in terms of the single-particle basis states described above. The resulting restricted Hamiltonian is of the form

$$\begin{aligned}\hat{H} \;&=\; |u_1\rangle \, E_1^h \, \langle u_1| \;+\; |u_2\rangle \, E_2^h \, \langle u_2| \;+\; |\phi_1\rangle \, E_1^c \, \langle \phi_1| \;+\; |\phi_2\rangle \, E_2^c \, \langle \phi_2| \;+\; |\phi_3\rangle \, E_3^c \, \langle \phi_3| \\ &\quad+\; U\Big[|u_1\phi_2\rangle\langle u_2\phi_1| \;+\; |u_2\phi_1\rangle\langle u_1\phi_2|\Big] \;+\; V\Big[|\phi_2\rangle\langle\phi_3| \;+\; |\phi_3\rangle\langle\phi_2|\Big] \qquad (2.1)\end{aligned}$$

In this restricted Hamiltonian, we have used U for the matrix element

$$U \;=\; \langle \; u_1(z_1)\phi_2(z_2) \mid U(z_1, z_2) \mid u_2(z_1)\phi_1(z_2) \; \rangle$$

We have also used V for the matrix element

$$V \;=\; \langle \; \phi_2(z_2) \mid V_2(z_2) \mid \phi_3(z_2) \; \rangle$$

In this restricted model, we assume that the tunneling probability for transitions from the lower state of the cold-side quantum well near the gap to the quantum well on the right of the converter is much smaller than for the excited state.

2.5 Finite basis model

To analyze the restricted Hamiltonian, it is appropriate to make use of a finite basis expansion. We choose a basis expansion of the form

$$\Psi(z_1, z_2, t) \;=\; \sum_{j=0}^{2} \sum_{k=0}^{3} c_{jk}(t) \; |u_j(z_1)\phi_k(z_2)\rangle.$$

The evolution equations for the coefficients are

$$i\hbar\frac{d}{dt}c_{11}(t) = (E_1^h + E_1^c)\ c_{11}(t)$$

$$i\hbar\frac{d}{dt}c_{12}(t) = (E_1^h + E_2^c)\ c_{12}(t)\ +\ U\ c_{21}(t)\ +\ V\ c_{13}(t)$$

$$i\hbar\frac{d}{dt}c_{21}(t) = (E_2^h + E_1^c)\ c_{21}(t)\ +\ U\ c_{12}(t)$$

$$i\hbar\frac{d}{dt}c_{13}(t) = (E_1^h + E_3^c)\ c_{13}(t)\ +\ V\ c_{12}(t)$$

$$i\hbar\frac{d}{dt}c_{22}(t) = (E_2^h + E_2^c)\ c_{22}(t)\ +\ V\ c_{23}(t)$$

$$i\hbar\frac{d}{dt}c_{23}(t) = (E_2^h + E_3^c)\ c_{23}(t)\ +\ V\ c_{22}(t)$$

$$i\hbar\frac{d}{dt}c_{20}(t) = E_2^h\ c_{20}(t)$$

$$i\hbar\frac{d}{dt}c_{10}(t) = E_1^h\ c_{10}(t)$$

$$i\hbar\frac{d}{dt}c_{01}(t) = E_1^c\ c_{01}(t)$$

$$i\hbar\frac{d}{dt}c_{02}(t) = E_2^c\ c_{02}(t)\ +\ V\ c_{03}(t)$$

$$i\hbar\frac{d}{dt}c_{03}(t) = E_3^c\ c_{03}(t)\ +\ V\ c_{02}(t)$$

$$i\hbar\frac{d}{dt}c_{00}(t) = (E_0^c\ +\ E_0^h)\ c_{00}(t)$$

2.6 Evolution of the occupation probabilities

To include the statistical and classical physics of the overall model in with the quantum mechanical model, we require a description in terms of probabilities (that is, to obtain a Bloch equation equivalent or density matrix description). We begin with a computation of the evolution equations for the level occupation probabilities. We assume here that U and V are real.

$$\begin{aligned}
\frac{d}{dt}|c_{11}(t)|^2 &= 0 \\
\frac{d}{dt}|c_{12}(t)|^2 &= \frac{U}{\hbar}\left[\frac{c_{12}^*c_{21} - c_{12}c_{21}^*}{i}\right] + \frac{V}{\hbar}\left[\frac{c_{12}^*c_{13} - c_{12}c_{13}^*}{i}\right] \\
\frac{d}{dt}|c_{21}(t)|^2 &= \frac{U}{\hbar}\left[\frac{c_{21}^*c_{12} - c_{21}c_{12}^*}{i}\right] \\
\frac{d}{dt}|c_{13}(t)|^2 &= \frac{V}{\hbar}\left[\frac{c_{13}^*c_{12} - c_{13}c_{12}^*}{i}\right] \\
\frac{d}{dt}|c_{22}(t)|^2 &= \frac{V}{\hbar}\left[\frac{c_{22}^*c_{23} - c_{22}c_{23}^*}{i}\right] \\
\frac{d}{dt}|c_{23}(t)|^2 &= \frac{V}{\hbar}\left[\frac{c_{23}^*c_{22} - c_{23}c_{22}^*}{i}\right] \\
\frac{d}{dt}|c_{20}(t)|^2 &= 0 \\
\frac{d}{dt}|c_{10}(t)|^2 &= 0 \\
\frac{d}{dt}|c_{01}(t)|^2 &= 0
\end{aligned}$$

$$\begin{aligned}
\frac{d}{dt}|c_{02}(t)|^2 &= \frac{V}{\hbar}\left[\frac{c_{02}^*c_{03} - c_{02}c_{03}^*}{i}\right] \\
\frac{d}{dt}|c_{03}(t)|^2 &= \frac{V}{\hbar}\left[\frac{c_{03}^*c_{02} - c_{03}c_{02}^*}{i}\right] \\
\frac{d}{dt}|c_{00}(t)|^2 &= 0
\end{aligned}$$

Antisymmetric combinations of the coefficients arise in the coupled evolutions equations for this problem. The associated evolution equations are readily computed. We obtain

$$\begin{aligned}
\frac{d}{dt}\left[\frac{c_{12}^*c_{21} - c_{12}c_{21}^*}{i}\right] &= \frac{E_1^h + E_2^c - E_2^h - E_1^c}{\hbar}\left[c_{12}^*c_{21} + c_{12}c_{21}^*\right] \\
&\quad + \frac{2U}{\hbar}\left[|c_{21}|^2 - |c_{12}|^2\right] + \frac{V}{\hbar}\left[c_{21}^*c_{13} + c_{21}c_{13}^*\right]
\end{aligned}$$

$$\begin{aligned}
\frac{d}{dt}\left[\frac{c_{12}^*c_{13} - c_{12}c_{13}^*}{i}\right] &= -\frac{E_3^c - E_2^c}{\hbar}\left[c_{12}^*c_{13} + c_{12}c_{13}^*\right] \\
&\quad + \frac{2V}{\hbar}\left[|c_{13}|^2 - |c_{12}|^2\right] + \frac{U}{\hbar}\left[c_{21}^*c_{13} + c_{21}c_{13}^*\right]
\end{aligned}$$

$$\begin{aligned}
\frac{d}{dt}\left[\frac{c_{13}^*c_{21} - c_{13}c_{21}^*}{i}\right] &= \frac{E_1^h + E_3^c - E_2^h - E_1^c}{\hbar}\left[c_{13}^*c_{21} + c_{13}c_{21}^*\right] \\
&\quad - \frac{U}{\hbar}\left[c_{13}^*c_{12} + c_{13}c_{12}^*\right] + \frac{V}{\hbar}\left[c_{12}^*c_{21} + c_{12}c_{21}^*\right]
\end{aligned}$$

$$\frac{d}{dt}\left[\frac{c_{22}^{*}c_{23} - c_{22}c_{23}^{*}}{i}\right] = -\left(\frac{E_3^c - E_2^c}{\hbar}\right)\left[c_{22}^{*}c_{23} + c_{22}c_{23}^{*}\right] + \frac{2V}{\hbar}\left[|c_{23}|^2 - |c_{22}|^2\right]$$

$$\frac{d}{dt}\left[\frac{c_{03}^{*}c_{02} - c_{03}c_{02}^{*}}{i}\right] = \frac{E_3^c - E_2^c}{\hbar}\left[c_{03}^{*}c_{02} + c_{03}c_{02}^{*}\right] + \frac{2V}{\hbar}\left[|c_{02}|^2 - |c_{03}|^2\right]$$

There are also symmetric combinations of coefficients that arise in the problem which are also readily computed. We obtain

$$\frac{d}{dt}\left[c_{12}^{*}c_{21} + c_{12}c_{21}^{*}\right] = \frac{E_2^h + E_1^c - E_1^h - E_2^c}{\hbar}\left[\frac{c_{12}^{*}c_{21} - c_{12}c_{21}^{*}}{i}\right] + \frac{V}{\hbar}\left[\frac{c_{21}^{*}c_{13} - c_{21}c_{13}^{*}}{i}\right]$$

$$\frac{d}{dt}\left[c_{12}^{*}c_{13} + c_{12}c_{13}^{*}\right] = \frac{E_3^c - E_2^c}{\hbar}\left[\frac{c_{12}^{*}c_{13} - c_{12}c_{13}^{*}}{i}\right] + \frac{U}{\hbar}\left[\frac{c_{13}^{*}c_{21} - c_{13}c_{21}^{*}}{i}\right]$$

$$\begin{aligned}\frac{d}{dt}\left[c_{13}^{*}c_{21} + c_{13}c_{21}^{*}\right] &= \frac{E_1^h + E_3^c - E_2^h - E_1^c}{\hbar}\left[\frac{c_{21}^{*}c_{13} - c_{21}c_{13}^{*}}{i}\right] \\ &\quad + \frac{U}{\hbar}\left[\frac{c_{13}^{*}c_{12} - c_{13}c_{12}^{*}}{i}\right] + \frac{V}{\hbar}\left[\frac{c_{21}^{*}c_{12} - c_{21}c_{12}^{*}}{i}\right]\end{aligned}$$

$$\frac{d}{dt}\left[c_{22}^{*}c_{23} + c_{22}c_{23}^{*}\right] = \frac{E_3^c - E_2^c}{\hbar}\left[\frac{c_{22}^{*}c_{23} - c_{22}c_{23}^{*}}{i}\right]$$

$$\frac{d}{dt}\left[c_{03}^*c_{02}+c_{03}c_{02}^*\right] = -\left(\frac{E_3^c-E_2^c}{\hbar}\right)\left[\frac{c_{03}^*c_{02}-c_{03}c_{02}^*}{i}\right]$$

2.7 Generalized Bloch equations

The form of the evolution equations is similar to that of the Bloch equations that arise in the analysis of the two-level system. We would like to write the evolution equations that we have obtained in a similar form. To do so, we introduce a new notation for the different combinations of the coefficients. In the case of the level probabilities, we write

$$N_{jk}(t) = |c_{jk}(t)|^2$$

For the symmetric combinations, we write

$$Q_A(t) = c_{12}^*c_{21}+c_{12}c_{21}^*$$

$$Q_B(t) = c_{12}^*c_{13}+c_{12}c_{13}^*$$

$$Q_C(t) = c_{13}^*c_{21}+c_{13}c_{21}^*$$

$$Q_D(t) = c_{22}^*c_{23}+c_{22}c_{23}^*$$

$$Q_E(t) = c_{02}^*c_{03}+c_{02}c_{03}^*$$

For the antisymmetric combinations, we write

$$P_A(t) = \frac{c_{12}^* c_{21} - c_{12} c_{21}^*}{i}$$

$$P_B(t) = \frac{c_{12}^* c_{13} - c_{12} c_{13}^*}{i}$$

$$P_C(t) = \frac{c_{13}^* c_{21} - c_{13} c_{21}^*}{i}$$

$$P_D(t) = \frac{c_{22}^* c_{23} - c_{22} c_{23}^*}{i}$$

$$P_E(t) = \frac{c_{02}^* c_{03} - c_{02} c_{03}^*}{i}$$

In terms of these variables, the evolution equations become

$$\frac{d}{dt} N_{11}(t) = 0$$

$$\frac{d}{dt} N_{12}(t) = \frac{U}{\hbar} P_A(t) + \frac{V}{\hbar} P_B(t)$$

$$\frac{d}{dt} N_{21}(t) = -\frac{U}{\hbar} P_A(t)$$

$$\frac{d}{dt} N_{13}(t) = -\frac{V}{\hbar} P_B(t)$$

$$\frac{d}{dt} N_{22}(t) = \frac{V}{\hbar} P_D(t)$$

$$\frac{d}{dt} N_{23}(t) = -\frac{V}{\hbar} P_D(t)$$

$$\frac{d}{dt} N_{20}(t) = 0$$

$$\frac{d}{dt}N_{10}(t) = 0$$

$$\frac{d}{dt}N_{01}(t) = 0$$

$$\frac{d}{dt}N_{02}(t) = \frac{V}{\hbar}P_E(t)$$

$$\frac{d}{dt}N_{03}(t) = -\frac{V}{\hbar}P_E(t)$$

$$\frac{d}{dt}N_{00}(t) = 0$$

The evolution equations for the symmetric combinations becomes

$$\frac{d}{dt}Q_A(t) = (\Omega_{21} - \omega_{21})\ P_A(t) - \frac{V}{\hbar}P_C(t)$$

$$\frac{d}{dt}Q_B(t) = \omega_{32}\ P_B(t) + \frac{U}{\hbar}P_C(t)$$

$$\frac{d}{dt}Q_C(t) = (\Omega_{21} - \omega_{31})\ P_C(t) - \frac{V}{\hbar}P_A(t) - \frac{U}{\hbar}P_B(t)$$

$$\frac{d}{dt}Q_D(t) = \omega_{32}\ P_D(t)$$

$$\frac{d}{dt}Q_E(t) = \omega_{32}\ P_E(t)$$

The evolution equations for the antisymmetric combinations become

$$\frac{d}{dt}P_A(t) = -\left(\Omega_{21}-\omega_{21}\right)Q_A(t) + \frac{2U}{\hbar}\Big[N_{21}(t)-N_{12}(t)\Big] + \frac{V}{\hbar}Q_C(t)$$

$$\frac{d}{dt}P_B(t) = -\omega_{32}\,Q_B(t) + \frac{2V}{\hbar}\Big[N_{13}(t)-N_{12}(t)\Big] + \frac{U}{\hbar}Q_C(t)$$

$$\frac{d}{dt}P_C(t) = -\left(\Omega_{21}-\omega_{31}\right)Q_C(t) + \frac{V}{\hbar}Q_A(t) - \frac{U}{\hbar}Q_B(t)$$

$$\frac{d}{dt}P_D(t) = -\omega_{32}\,Q_D(t) + \frac{2V}{\hbar}\Big[N_{23}(t)-N_{22}(t)\Big]$$

$$\frac{d}{dt}P_E(t) = -\omega_{32}\,Q_E(t) + \frac{2V}{\hbar}\Big[N_{03}(t)-N_{02}(t)\Big]$$

In writing these equations, we have used the notation

$$\hbar\Omega_{jk} = E_j^h - E_k^h$$

$$\hbar\omega_{jk} = E_j^c - E_k^c$$

2.8 Discussion

We have developed a set of evolution equations for the populations and polarizations (symmetric and antisymmetric combinations) of the two-electron product states for the simplified quantum model incorporating the Coulomb and the tunneling couplings. What is still missing in our model is the losses, or the relaxations between the quantum well states and the reservoirs. This will be the goal of the next chapter.

Chapter 3

Reservoir and relaxation

It is well-known that when a state is coupled to a continuum of states (reservoir), it decays (relaxes) exponentially into the reservoir with a rate given by the Golden Rule [10]. Including a large number of states into a model can be overwhelming. In the case of NMR and lasers what is often done is to include such a loss mechanism by adding a phenomenological term n/T into the Bloch equations, where n is, say, the population of a level and T is the relaxation time associated with that level. We now attempt to follow the same approach to incorporate such incoherent relaxations into the model. Please see Figure 3-1. For the sake of simplicity, we model the reservoir as quantum levels $u_0(z_1)$, $\phi_a(z_2)$, and $\phi_b(z_2)$. $u_0(z_1)$ aligns with $u_1(z_1)$ and $\phi_a(z_2)$ aligns with $\phi_1(z_2)$. When there is no voltage difference between the two reservoirs on the cold-side, $\phi_b(z_2)$ aligns with $\phi_a(z_2)$. When a voltage drop occurs between the two reservoirs, $\phi_b(z_2)$ deviates from its original energy level and no longer aligns with $\phi_a(z_2)$ and $\phi_1(z_2)$. We assume there are relaxations between $u_0(z_1)$ and $u_1(z_1)$, $u_0(z_1)$ and $u_2(z_1)$, $\phi_1(z_2)$ and $\phi_a(z_2)$, $\phi_3(z_2)$ and $\phi_b(z_2)$. For now we assume $\phi_2(z_2)$ does not relax into the reservoir. The relaxations can be described in the following set of equations.

$$\frac{d}{dt}n_j + \frac{n_j}{T_j} = \sum_k A_{jk}n_k$$

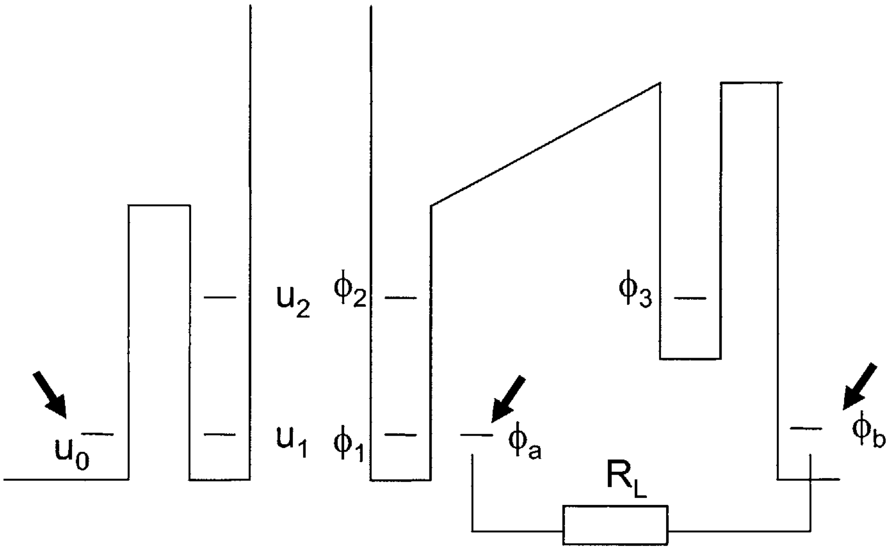

Figure 3-1: Single-level Reservoir. The reservoirs are represented by single levels, pointed to by thick arrows in the figure. This is an over-simplification but it facilitates the construction of our Bloch equation models. In a later subsection we will correct the equilibrium values to better reflect the properties of reservoirs.

where we define

$$\frac{1}{T_j} = -A_{jj}$$

The quantity T_j is the relaxation time constant associated with a quantum level j which indicates how long it takes for an electron occupying state j to relax into other states. Since the $u_2(z_2)$ state does not relax into a reservoir, the relaxation time T_2^c is infinity.

Due to the conservation of particles, the summation over j of all the relaxation equations should be zero.

$$\frac{d}{dt}\sum_j n_j = 0 = \sum_{j,k} A_{jk} n_k$$

Collecting all the n_k terms gives the following:

$$n_k \cdot \sum_j A_{jk} = 0$$

Because there is no particular restriction on n_k, the coefficient in front of n_k should be zero.

$$\sum_j A_{jk} = A_{kk} + \sum_{j \neq k} A_{jk} = 0$$

An additional set of equations can be obtained through detailed balance:

$$\frac{A_{ij}}{A_{ji}} = \frac{g_i}{g_j} \exp\left[-\frac{(E_i - E_j - (\mu_i - \mu_j))}{kT}\right],$$

where the μ is the Fermi level of the material in which the quantum level resides, and g_i and g_j are the degeneracies of the two levels. In our model we simply assume the degeneracies are all equal to 1.

Our problem at hand is a two-electron one, with our Bloch equations expressed in terms of two-electron occupation probabilities and polarizations. To generalize the one-electron relaxation equations into two-electron ones, we first define two-electron occupation probabilities and products of two single-electron occupation probabilities, and then use the chain-rule to derive the relaxation equations.

$$N_{ij} = n_i n_j \tag{3.1}$$

$$\frac{d}{dt} N_{ij} = \sum_k A^c_{jk} n^h_i n^c_k + \sum_k A^h_{ik} n^h_k n^h_j$$

$$\frac{d}{dt} N_{ij} = \sum_k A^c_{jk} N_{ik} + \sum_k A^h_{ik} N_{kj}$$

$$\frac{d}{dt}N_{ij} \; - \; A^c_{jj}N_{ij} \; - \; A^h_{ii}N_{ij} = \sum_{k\neq j} A^c_{jk}N_{ik} \; + \; \sum_{k\neq j} A^h_{ik}N_{kj}$$

invoking the definitions of relaxation times,

$$-A^c_{jj} \; = \; \frac{1}{T^c_{jj}}$$

$$-A^h_{ii} \; = \; \frac{1}{T^h_{ii}}$$

$$\frac{d}{dt}N_{ij} \; + \; N_{ij}\left[\frac{1}{T^c_{jj}} \; + \; \frac{1}{T^h_{ii}}\right] = \sum_{k\neq j} A^c_{jk}N_{ik} \; + \; \sum_{k\neq j} A^h_{ik}N_{kj}.$$

Given the above general equations, we can write out the specific Bloch equations. First of all, we need to express the A_{ij} coefficients into relaxation time constants. On the hot-side:

$$A^h_{01} \; + \; A^h_{11} \; = \; 0 \Longrightarrow A^h_{01} \; = \; - \; A^h_{11} \; = \; \frac{1}{T^h_1}$$

$$A^h_{10} \; = \; A^h_{01} \; e^{\frac{-(E^h_1 - E^h_0)}{k \; T_h}} \; = \; A^h_{01} \; = \; \frac{1}{T^h_1}$$

$$A^h_{10} \; + \; A^h_{20} \; + \; A^h_{00} \; = \; 0 \Longrightarrow A^h_{20} \; = \; -A^h_{10} \; - \; A^h_{00} \; = \; \frac{1}{T^h_0} \; - \; \frac{1}{T^h_1}$$

$$A^h_{02} \; + \; A^h_{22} \; = \; 0 \Longrightarrow A^h_{02} \; = \; - \; A^h_{22} \; = \; \frac{1}{T^h_2}.$$

A constraint on the relaxation times is identified through detailed balance:

$$\frac{A^h_{20}}{A^h_{02}} \; = \; \frac{\frac{1}{T_0} \; - \; \frac{1}{T_1}}{\frac{1}{T_2}} \; = \; e^{\frac{-(E^h_2 - E^h_0)}{k \; T_h}}$$

On the cold-side:

$$A^c_{a1} \; + \; A^c_{11} \; = \; 0 \; \Longrightarrow \; A^c_{a1} \; = \; - \; A^c_{11} \; = \; \frac{1}{T^c_1}$$

$$A^c_{1a} \; = \; A^h_{a1} \; e^{\frac{-(E^c_1 - E^c_a)}{k \; T_c}} \; = \; A^c_{a1} \; = \; \frac{1}{T^c_1}$$

$$A^c_{1a} \; + \; A^c_{ba} \; + \; A^c_{aa} \; = \; 0 \; \Longrightarrow \; A^c_{ba} \; = \; - \, A^c_{1a} \; - \; A^c_{aa} \; = \; \frac{1}{T^c_1} \; - \; \frac{1}{T^c_a}$$

$$A^c_{b3} \; + \; A^c_{33} \; = \; 0 \; \Longrightarrow \; A^c_{b3} \; = \; - \, A^c_{33} \; = \; \frac{1}{T^c_3}$$

$$A^c_{3b} \; = \; A^c_{b3} \; e^{\frac{-(E^c_3 - E^c_b)}{k \; T_c}} \; = \; A^c_{b3} \; = \; \frac{e^{\frac{-(E^c_3 - E^c_b)}{k \; T_c}}}{T^c_3}$$

$$A^c_{ab} \; + \; A^c_{3b} \; + \; A^c_{bb} \; = \; 0 \; \Longrightarrow \; A^c_{ab} \; = \; - \, A^c_{3b} \; - \; A^c_{bb} \; = \; - \; \frac{e^{\frac{-(E^c_3 - E^c_b)}{k \; T_c}}}{T^c_3} \; + \; \frac{1}{T^c_b}$$

A restriction on the relaxation times can be similarly obtained:

$$\frac{A^h_{ba}}{A^h_{ab}} \; = \; \frac{\frac{1}{T^c_a} \; - \; \frac{1}{T^c_1}}{\frac{1}{T^c_b} \; - \; \frac{e^{\frac{-(E^c_3 - E^c_b)}{k \; T_c}}}{T^c_3}} \; = \; e^{-\frac{(E^c_b - E^c_a - q(\mu_b - \mu_a))}{k \; T_c}}$$

Given the above relations, we are ready to write out all the Bloch equations. Polarizations terms are incorporated to account for the effects of quantum coupling.

$$\frac{d}{dt} N_{01} \; + \; N_{01} \left[\frac{1}{T^c_1} \; + \; \frac{1}{T^h_1} \; + \; \frac{e^{-\frac{(E^h_2 - E^h_0)}{k \; T_h}}}{T^h_2} \right] \; = \; \frac{N_{0a}}{T^c_1} \; + \; \frac{N_{11}}{T^h_1} \; + \; \frac{N_{21}}{T^h_2} \qquad (3.2)$$

$$\frac{d}{dt}N_{02} + N_{02}\left[\frac{1}{T_1^h} + \frac{e^{-\frac{(E_2^h - E_0^h)}{k\ T_h}}}{T_2^h}\right] = \frac{N_{12}}{T_1^h} + \frac{N_{22}}{T_2^h} + \frac{V}{\hbar}P_E \tag{3.3}$$

$$\frac{d}{dt}N_{03} + N_{03}\left[\frac{1}{T_3^c} + \frac{1}{T_1^h} + \frac{e^{-\frac{(E_2^h - E_0^h)}{k\ T_h}}}{T_2^h}\right] = \frac{N_{13}}{T_1^h} + \frac{N_{23}}{T_2^h} + N_{0b}\frac{e^{-\frac{(E_3^c - E_b^c)}{k\ T_c}}}{T_3^c} - \frac{V}{\hbar}P_E \tag{3.4}$$

$$\frac{d}{dt}N_{11} + N_{11}\left[\frac{1}{T_1^c} + \frac{1}{T_1^h}\right] = \frac{N_{1a}}{T_1^c} + \frac{N_{01}}{T_1^h} \tag{3.5}$$

$$\frac{d}{dt}N_{12} + N_{12}\frac{1}{T_1^h} = \frac{N_{02}}{T_1^h} + \frac{U}{\hbar}P_A + \frac{V}{\hbar}P_B \tag{3.6}$$

$$\frac{d}{dt}N_{13} + N_{13}\left[\frac{1}{T_1^h} + \frac{1}{T_3^c}\right] = \frac{N_{03}}{T_1^h} + N_{1b}\frac{e^{\frac{-(E_3^c - E_b^c)}{k\ T_c}}}{T_3^c} - \frac{V}{\hbar}P_B \tag{3.7}$$

$$\frac{d}{dt}N_{21} + N_{21}\left[\frac{1}{T_2^c} + \frac{1}{T_2^h}\right] = \frac{N_{2a}}{T_1^c} + N_{01}\frac{e^{-\frac{(E_2^h - E_0^h)}{k\ T_h}}}{T_2^h} - \frac{U}{\hbar}P_A \tag{3.8}$$

$$\frac{d}{dt}N_{22} + N_{22}\left[\frac{1}{T_2^c} + \frac{1}{T_2^h}\right] = N_{02}\frac{e^{-\frac{(E_2^h - E_0^h)}{k\ T_h}}}{T_2^h} + \frac{V}{\hbar}P_D \tag{3.9}$$

$$\frac{d}{dt}N_{23} + N_{23}\left[\frac{1}{T_3^c} + \frac{1}{T_2^h}\right] = N_{2b}\frac{e^{-\frac{(E_3^c - E_b^c)}{k\ T_c}}}{T_3^c} + N_{03}\frac{e^{-\frac{(E_2^h - E_0^h)}{k\ T_h}}}{T_2^h} - \frac{V}{\hbar}P_D \tag{3.10}$$

$$\frac{d}{dt}N_{0b} + N_{0b}\left[\frac{1}{T_b^c} + \frac{1}{T_1^h} + \frac{e^{-\frac{(E_2^h - E_0^h)}{k\ T_h}}}{T_2^h}\right]$$

$$= \frac{N_{03}}{T_3^c} + \frac{N_{1b}}{T_1^h} + \frac{N_{2b}}{T_2^h} + N_{0a}\, e^{-\frac{(E_b^c - E_a^c - (\mu_b^c - \mu_a^c))}{k\ T_c}}\left[\frac{1}{T_b^c} - \frac{e^{\frac{-(E_3^c - E_b^c)}{k\ T_c}}}{T_3^c}\right] \tag{3.11}$$

$$\frac{d}{dt}N_{0a} + N_{0a}\left[\frac{1}{T_a^c} + \frac{1}{T_1^h} + \frac{e^{-\frac{(E_2^h - E_0^h)}{k\ T_h}}}{T_2^h}\right] = \frac{N_{01}}{T_1^c} + \frac{N_{1a}}{T_1^h} + \frac{N_{2a}}{T_2^h} + N_{0b}\,e^{\frac{(E_b^c - E_a^c\ -\ (\mu_b^c - \mu_a^c))}{k\ T_c}}\left[\frac{1}{T_a^c} - \frac{1}{T_1^c}\right. \tag{3.12}$$

$$\frac{d}{dt}N_{1b} + N_{1b}\left[\frac{1}{T_b^c} + \frac{1}{T_1^h}\right] = \frac{N_{13}}{T_3^c} + \frac{N_{0b}}{T_1^h} + N_{1a}\,e^{-\frac{(E_b^c - E_a^c\ -\ (\mu_b^c - \mu_a^c))}{k\ T_c}}\left[\frac{1}{T_b^c} - \frac{e^{\frac{-(E_3^c - E_b^c)}{k\ T_c}}}{T_3^c}\right] \tag{3.13}$$

$$\frac{d}{dt}N_{1a} + N_{1a}\left[\frac{1}{T_a^c} + \frac{1}{T_1^h}\right] = \frac{N_{11}}{T_1^c} + \frac{N_{0a}}{T_1^h} + N_{1b}\,e^{\frac{(E_b^c - E_a^c\ -\ (\mu_b^c - \mu_a^c))}{k\ T_c}}\left[\frac{1}{T_a^c} - \frac{1}{T_1^c}\right] \tag{3.14}$$

$$\frac{d}{dt}N_{2a} + N_{2a}\left[\frac{1}{T_a^c} + \frac{1}{T_2^h}\right] = \frac{N_{21}}{T_1^c} + \frac{N_{0a}e^{-\frac{(E_2^h - E_0^h)}{k\ T_h}}}{T_2^h} + N_{2b}\,e^{\frac{(E_3^c - E_1^c\ -\ (\mu_3^c - \mu_1^c))}{k\ T_c}}\left[\frac{1}{T_a^c} - \frac{1}{T_1^c}\right] \tag{3.15}$$

$$\frac{d}{dt}N_{2b} + N_{2b}\left[\frac{1}{T_b^c} + \frac{1}{T_2^h}\right] = \frac{N_{23}}{T_3^c} + \frac{N_{0b}\ e^{-\frac{(E_2^h - E_0^h)}{k\ T_h}}}{T_2^h} + N_{2a}\,e^{-\frac{(E_b^c - E_a^c\ -\ (\mu_b^c - \mu_a^c))}{k\ T_c}}\left[\frac{1}{T_b^c} - \frac{e^{\frac{-(E_3^c - E_b^c)}{k\ T_c}}}{T_3^c}\right] \tag{3.16}$$

In order to facilitate discussion, we define the following equivalent relaxation times, keeping in mind that we are assuming a lossless level 2 and its lifetime is infinite, $T_2^c = \infty$:

$$\frac{1}{T_{01}} \equiv \frac{1}{T_1^c} + \frac{1}{T_1^h} + \frac{e^{-\frac{(E_2^h - E_0^h)}{k\ T_h}}}{T_2^h} \tag{3.17}$$

$$\frac{1}{T_{02}} \equiv \frac{1}{T_1^h} + \frac{e^{-\frac{(E_2^h - E_0^h)}{k\ T_h}}}{T_2^h} \tag{3.18}$$

$$\frac{1}{T_{03}} \equiv \frac{1}{T_3^c} + \frac{1}{T_1^h} + \frac{e^{-\frac{(E_2^h - E_0^h)}{k\ T_h}}}{T_2^h} \tag{3.19}$$

$$\frac{1}{T_{11}} \equiv \frac{1}{T_1^c} + \frac{1}{T_1^h} \tag{3.20}$$

$$\frac{1}{T_{12}} \equiv \frac{1}{T_1^h} \tag{3.21}$$

$$\frac{1}{T_{13}} \equiv \frac{1}{T_3^c} + \frac{1}{T_1^h} \tag{3.22}$$

$$\frac{1}{T_{21}} \equiv \frac{1}{T_1^c} + \frac{1}{T_2^h} \tag{3.23}$$

$$\frac{1}{T_{22}} \equiv \frac{1}{T_2^h} \tag{3.24}$$

$$\frac{1}{T_{23}} \equiv \frac{1}{T_3^c} + \frac{1}{T_2^h} \tag{3.25}$$

$$\frac{1}{T_{0b}} \equiv \frac{1}{T_b^c} + \frac{1}{T_1^h} + \frac{e^{-\frac{(E_2^h - E_0^h)}{k\ T_h}}}{T_2^h} \tag{3.26}$$

$$\frac{1}{T_{0a}} \equiv \frac{1}{T_a^c} + \frac{1}{T_1^h} + \frac{e^{-\frac{(E_2^h - E_0^h)}{k\ T_h}}}{T_2^h} \tag{3.27}$$

$$\frac{1}{T_{1b}} \equiv \frac{1}{T_b^c} + \frac{1}{T_1^h} \tag{3.28}$$

$$\frac{1}{T_{1a}} \equiv \frac{1}{T_a^c} + \frac{1}{T_1^h} \tag{3.29}$$

$$\frac{1}{T_{2a}} \equiv \frac{1}{T_a^c} + \frac{1}{T_2^h} \tag{3.30}$$

$$\frac{1}{T_{2b}} \equiv \frac{1}{T_b^c} + \frac{1}{T_2^h} \tag{3.31}$$

We similarly introduce relaxation terms into the evolution equations for the polarizations:

$$\frac{d}{dt}Q_A(t) + \frac{Q_A(t)}{T_A} = (\Omega_{21} - \omega_{21})\, P_A(t) - \frac{V}{\hbar}P_C(t) \tag{3.32}$$

$$\frac{d}{dt}P_A(t) + \frac{P_A(t)}{T_A} = -(\Omega_{21} - \omega_{21})\, Q_A(t) + \frac{2U}{\hbar}\Big[N_{21}(t) - N_{12}(t)\Big] + \frac{V}{\hbar}Q_C(t) \tag{3.33}$$

$$\frac{d}{dt}Q_B(t) + \frac{Q_B(t)}{T_B} = \omega_{32}\, P_B(t) + \frac{U}{\hbar}P_C(t) \tag{3.34}$$

$$\frac{d}{dt}P_B(t) + \frac{P_B(t)}{T_B} = -\omega_{32}\, Q_B(t) + \frac{2V}{\hbar}\Big[N_{13}(t) - N_{12}(t)\Big] + \frac{U}{\hbar}Q_C(t) \tag{3.35}$$

$$\frac{d}{dt}Q_C(t) + \frac{Q_C(t)}{T_C} = (\Omega_{21} - \omega_{31})\, P_C(t) - \frac{V}{\hbar}P_A(t) - \frac{U}{\hbar}P_B(t) \tag{3.36}$$

$$\frac{d}{dt}P_C(t) + \frac{P_C(t)}{T_C} = -(\Omega_{21} - \omega_{31})\, Q_C(t) + \frac{V}{\hbar}Q_A(t) - \frac{U}{\hbar}Q_B(t) \tag{3.37}$$

$$\frac{d}{dt}Q_D(t) + \frac{Q_D(t)}{T_D} = \omega_{32}\, P_D(t) \tag{3.38}$$

$$\frac{d}{dt}P_D(t) + \frac{P_D(t)}{T_D} = -\omega_{32}\, Q_D(t) + \frac{2V}{\hbar}\Big[N_{23}(t) - N_{22}(t)\Big] \tag{3.39}$$

$$\frac{d}{dt}Q_E(t) + \frac{Q_E(t)}{T_E} = \omega_{32}\, P_E(t) \tag{3.40}$$

$$\frac{d}{dt}P_E(t) + \frac{P_E(t)}{T_E} = -\omega_{32}\, Q_E(t) + \frac{2V}{\hbar}\Big[N_{02}(t) - N_{03}(t)\Big] \tag{3.41}$$

3.1 Equilibrium values

We have specified above a set of coupled Bloch equations. The source constant terms to the Bloch equations are the occupation probabilities of the two-electron reservoir states N_{0a} and N_{0b} which are products of the single-electron thermal equilibrium values according to Eq.(3.1). Below we calculate the single-electron equilibrium probabilities. Let us look at the hot-side relaxation equations:

$$\frac{d}{dt}n_0^h + \frac{n_0^h}{T_0^h} = \frac{n_1^h}{T_1^h} + \frac{n_2^h}{T_2^h} \tag{3.42}$$

$$\frac{d}{dt}n_1^h + \frac{n_1^h}{T_1^h} = \frac{n_0^h}{T_1^h} \tag{3.43}$$

$$\frac{d}{dt}n_2^h + \frac{n_2^h}{T_2^h} = n_0^h\left[\frac{1}{T_0^h} - \frac{1}{T_1^h}\right] \tag{3.44}$$

We solve for the equilibrium values by demanding the derivatives to be zero, which leads to

$$n_1^h \ = \ n_0^h \tag{3.45}$$

$$n_2^h \ = \ n_0^h \ = \ \frac{\frac{1}{T_0^h} \ - \ \frac{1}{T_1^h}}{\frac{1}{T_2^h}} \ = \ e^{-\frac{E_2^h - E_0^h}{k \ T_h}} \tag{3.46}$$

Since we assume the existence of one single electron residing on the hot-side, we have

$$n_0^h \ + \ n_1^h \ + \ n_2^h \ = \ 1 \tag{3.47}$$

which results in

$$n_0^{h,0} \ = \ n_1^{h,0} \ = \ \frac{1}{2 \ + \ e^{-\frac{E_2^h \ - \ E_0^h}{k \ T_h}}} \tag{3.48}$$

$$n_2^{h,0} \ = \ \frac{e^{-\frac{E_2^h \ - \ E_0^h}{k \ T_h}}}{2 \ + \ e^{-\frac{E_2^h \ - \ E_0^h}{k \ T_h}}} \tag{3.49}$$

where the 0 in the superscript indicates equilibrium value. Similarly for the cold-side we have relaxation equations:

$$\frac{d}{dt} n_1^c \ + \ \frac{n_1^c}{T_1^c} \ = \ \frac{n_a^c}{T_1^c} \tag{3.50}$$

$$\frac{d}{dt} n_a^c \ + \ \frac{n_a^c}{T_a^c} \ = \ \frac{n_1^c}{T_1^c} \ + \ n_b^c \left[\frac{-e^{\frac{-(E_3^c - E_b^c)}{k \ T_c}}}{T_3^c} \ + \ \frac{1}{T_b^c} \right] \tag{3.51}$$

$$\frac{d}{dt} n_b^c \ + \ \frac{n_b^c}{T_b^c} \ = \ \frac{n_3^c}{T_3^c} \ + \ n_a^c \left[\frac{-1}{T_1^c} \ + \ \frac{1}{T_a^c} \right] \tag{3.52}$$

$$\frac{d}{dt} n_3^c + \frac{n_3^c}{T_3^c} = n_b^c \frac{e^{\frac{-(E_3^c - E_b^c)}{k\ T_c}}}{T_3^c} \tag{3.53}$$

as well as conservation of probability and constraint on relaxation times

$$n_1^c + n_a^c + n_3^c + n_b^c = 1 \tag{3.54}$$

$$\frac{\frac{1}{T_a^c} - \frac{1}{T_1^c}}{\frac{1}{T_b^c} - \frac{e^{\frac{-(E_3^c - E_b^c)}{k\ T_c}}}{T_3^c}} = e^{-\frac{(E_b^c - E_a^c - (\mu_b^c - \mu_a^c))}{k\ T_c}} \tag{3.55}$$

Solving these equations with the derivatives being zero gives the equilibrium values

$$n_1^{c,0} = n_a^{c,0} = \frac{1}{2 + e^{-\frac{E_b^c - E_a^c - (\mu_b - \mu_a)}{k\ T_c}} + e^{-\frac{(E_3^c - E_a^c - (\mu_b^c - \mu_a^c))}{k\ T_c}}} \tag{3.56}$$

$$n_b^{c,0} = \frac{e^{-\frac{E_b^c - E_a^c - (\mu_b^c - \mu_a^c)}{k\ T_c}}}{2 + e^{-\frac{(E_b^c - E_a^c - (\mu_b - \mu_a))}{k\ T_c}} + e^{-\frac{E_3^c - E_a^c - (\mu_b^c - \mu_a^c)}{k\ T_c}}} \tag{3.57}$$

$$n_3^{c,0} = \frac{e^{-\frac{E_3^c - E_a^c - (\mu_b^c - \mu_a^c)}{k\ T_c}}}{2 + e^{-\frac{E_b^c - E_a^c - (\mu_b^c - \mu_a^c)}{k\ T_c}} + e^{-\frac{E_3^c - E_a^c - (\mu_b^c - \mu_a^c)}{k\ T_c}}} \tag{3.58}$$

3.2 Coherence times

We have previously established the two-electron occupation relaxation times from the one-electron ones. In this section we derive the relationship between the polarization relaxation times (coherence times) and the occupation relaxation times, following the same approach as in Problem 24.5 on pp.496 of [10]. Suppose we have a simple situation where a coupling V exists between two states, state 0 and state 1. These two states communicate with a reservoir and we assume that the effects of relaxation into the reservoir can be represented as a loss in probability amplitude with lifetimes

τ_0 and τ_1 for the two corresponding states. We then write down an empirical model

$$i\hbar\left[\frac{d}{dt}c_0(t) + \frac{c_0(t)}{\tau_o}\right] = E_0\, c_0(t) + V\, c_1(t) \tag{3.59}$$

$$i\hbar\left[\frac{d}{dt}c_1(t) + \frac{c_1(t)}{\tau_1}\right] = E_1\, c_1(t) + V\, c_0(t). \tag{3.60}$$

With the definition of occupation probabilities and polarizations,

$$N_0(t) = |c_0(t)|^2 \tag{3.61}$$

$$N_1(t) = |c_1(t)|^2 \tag{3.62}$$

$$Q = c_0^* c_1 + c_1^*\, c_0 \tag{3.63}$$

$$P = \frac{c_0^* c_1 - c_1^* c_0}{i} \tag{3.64}$$

we write down the Bloch equations

$$\frac{d}{dt}N_0 + \frac{N_0}{\tau_0/2} = \frac{V}{\hbar}\, P \tag{3.65}$$

$$\frac{d}{dt}N_1 + \frac{N_1}{\tau_1/2} = -\frac{V}{\hbar}\, P \tag{3.66}$$

$$\frac{d}{dt}P + P\left(\frac{1}{\tau_0} + \frac{1}{\tau_1}\right) = -\left(\frac{E_1 - E_0}{\hbar}\right) Q + 2\frac{V}{\hbar}(N_1 - N_0) \tag{3.67}$$

$$\frac{d}{dt}Q + Q\left(\frac{1}{\tau_1} + \frac{1}{\tau_0}\right) = \frac{E_1 - E_0}{\hbar}P. \tag{3.68}$$

If we denote T_0 as the state 0 relaxation time, T_1 as the state 1 relaxation time, and T as the coherence time, we can deduce from the above equations

$$T_0 = \frac{\tau_0}{2} \tag{3.69}$$

$$T_1 = \frac{\tau_1}{2} \tag{3.70}$$

$$\frac{1}{T} = \frac{1}{2}\left(\frac{1}{T_0} + \frac{1}{T_1}\right) \tag{3.71}$$

The above equations suggest the following relationships between the coherence times and occupation relaxation times for our model

$$\frac{1}{T_A} = \frac{1}{2}\left(\frac{1}{T_{12}} + \frac{1}{T_{21}}\right) \tag{3.72}$$

$$\frac{1}{T_B} = \frac{1}{2}\left(\frac{1}{T_{12}} + \frac{1}{T_{13}}\right) \tag{3.73}$$

$$\frac{1}{T_C} = \frac{1}{2}\left(\frac{1}{T_{13}} + \frac{1}{T_{21}}\right) \tag{3.74}$$

$$\frac{1}{T_D} = \frac{1}{2}\left(\frac{1}{T_{22}} + \frac{1}{T_{23}}\right) \tag{3.75}$$

$$\frac{1}{T_E} = \frac{1}{2}\left(\frac{1}{T_{02}} + \frac{1}{T_{03}}\right) \tag{3.76}$$

3.3 The steady-state limit

As is typical in this kind of problem, the polarization terms will be nearly static, while the level population terms will be slowly varying. Of interest to us is the limit in which the level populations are time independent. In this limit, we can obtain the various quantities by solving the following matrix equation, treating N_{0a} as an input source to our system of equations. We define

$$\Delta\Omega = \Omega_{21} - \omega_{31} \tag{3.77}$$

$$\Delta\omega = \Omega_{21} - \omega_{21} \tag{3.78}$$

We make some definitions of matrices: M_1 is a 24×12 matrix with the following nonzero elements:

$$M_1(1,1) = \frac{1}{T_E} , \quad M_1(1,2) = -\omega_{32} , \quad M_1(2,1) = \omega_{32} , \quad M_1(2,2) = \frac{1}{T_E}$$

$$M_1(2,4) = 2\frac{V}{\hbar} , \quad M_1(2,5) = -2\frac{V}{\hbar} , \quad M_1(3,3) = \frac{1}{T_{01}} , \quad M_1(3,12) = -\frac{1}{T_1^h}$$

$$M_1(4,2) = -\frac{V}{\hbar} , \quad M_1(4,4) = \frac{1}{T_{02}} , \quad M_1(5,2) = \frac{V}{\hbar} , \quad M_1(5,5) = \frac{1}{T_{03}}$$

$$M_1(6,6) = \frac{1}{T_A} , \quad M_1(6,7) = -\Delta w , \quad M_1(6,11) = \frac{V}{\hbar} , \quad M_1(7,6) = \Delta w$$

$$M_1(7,7) = \frac{1}{T_A} , \quad M_1(7,10) = -\frac{V}{\hbar} , \quad M_1(8,8) = \frac{1}{T_B} , \quad M_1(8,9) = -\omega_{32}$$

$$M_1(8,11) = -\frac{U}{\hbar} , \quad M_1(8,7) = \frac{V}{\hbar} , \quad M_1(8,9) = \frac{U}{\hbar} , \quad M_1(8,10) = \frac{1}{T_C}$$

$$M_1(8,11) = -\Delta\Omega , \quad M_1(9,8) = \omega_{32} , \quad M_1(9,9) = \frac{1}{T_B} , \quad M_1(9,10) = \frac{-U}{\hbar}$$

$$M_1(10,7) = \frac{V}{\hbar} , \quad M_1(10,9) = \frac{U}{\hbar} , \quad M_1(10,10) = \frac{1}{T_C} , \quad M_1(10,11) = -\Delta\Omega$$

$$M_1(11,6) = -\frac{V}{\hbar} \ , \quad M_1(11,8) = \frac{U}{\hbar} \ , \quad M_1(11,10) = \Delta\Omega \ , \quad M_1(11,11) = \frac{1}{T_C}$$

$$M_1(12,3) = -\frac{1}{T_1^h} \ , \quad M_1(12,12) = -\frac{1}{T_{11}} \ , \quad M_1(13,4) = -\frac{1}{T_1^h} \ , \quad M_1(13,7) = -\frac{U}{\hbar}$$

$$M_1(13,9) = -\frac{V}{\hbar} \ , \quad M_1(14,5) = -\frac{1}{T_1^h} \ , \quad M_1(14,9) = -\frac{V}{\hbar} \ , \quad M_1(15,9) = -\frac{V}{\hbar}$$

$$M_1(17,3) = \frac{e^{-\frac{(E_2^h - E_0^h)}{k \ T_h}}}{-T_2^h} \ , \quad M_1(17,7) = \frac{U}{\hbar} \ , \quad M_1(18,4) = \frac{e^{-\frac{(E_2^h - E_0^h)}{k \ T_h}}}{-T_2^h} \ , \quad M_1(19,5) = \frac{-e^{-\frac{(E_2^h - E_0^h)}{k \ T_h}}}{T_2^h}$$

$$M_1(20,5) = -1/T_3^c \ , \quad M_1(21,12) = -1/T_1^c$$

M_2 is a 24×12 matrix with the following nonzero elements:

$$M_2(3,5) = \frac{-1}{T_2^h} \ , \quad M_2(4,1) = \frac{-1}{T_h} \ , \quad M_2(4,6) = \frac{-1}{T_2^h} \ , \quad M_2(5,2) = \frac{-1}{T_1^h}$$

$$M_2(5,7) = \frac{-1}{T_2^h} \ , \quad M_2(5,8) = \frac{e^{\frac{-(E_3^c - E_b^c)}{k \ T_c}}}{-T_3^c} \ , \quad M_2(7,1) = 2\frac{U}{\hbar} \ , \quad M_2(7,2) = -2\frac{U}{\hbar}$$

$$M_2(9,1) = 2\frac{V}{\hbar} \ , \quad M_2(9,2) = -2\frac{V}{\hbar} \ , \quad M_2(13,1) = \frac{1}{T_1^h} \ , \quad M_2(14,2) = \frac{1}{T_{13}}$$

$$M_2(14,10) = \frac{e^{\frac{-(E_3^c - E_b^c)}{k \ T_c}}}{-T_3^c} \ , \quad M_2(15,3) = \frac{1}{T_D} \ , \quad M_2(16,3) = -\omega_{32} \ , \quad M_2(16,4) = \frac{1}{T_D}$$

$$M_2(16,6) = 2\frac{V}{\hbar} \ , \quad M_2(16,7) = -2\frac{V}{\hbar} \ , \quad M_2(17,5) = \frac{1}{T_{21}} \ , \quad M_2(17,11) = -\frac{1}{T_1^c}$$

$$M_2(18,5) = -\frac{V}{\hbar} \ , \quad M_2(18,7) = \frac{1}{T_{22}} \ , \quad M_2(19,5) = \frac{V}{\hbar} \ , \quad M_2(19,8) = \frac{1}{T_{23}}$$

$$M_2(19,12) = \frac{e^{\frac{-(E_3^c - E_b^c)}{k \ T_c}}}{-T_3^c} \ , \quad M_2(20,8) = \frac{1}{T_{0b}} \ , \quad M_2(20,10) = -\frac{1}{T_2^h} \ , \quad M_2(20,12) = -\frac{1}{T_2^h}$$

$$M_2(21,9) = \frac{1}{T_{1a}} \ , \quad M_2(21,10) = -A_{ab}^c \ , \quad M_2(22,2) = -\frac{1}{T_3^c} \ , \quad M_2(22,9) = -A_{ba}^c$$

$$M_2(22,10) = \frac{1}{T_{1a}} \ , \quad M_2(23,5) = -\frac{1}{T_1^c} \ , \quad M_2(23,11) = \frac{1}{T_{2a}} \ , \quad M_2(23,12) = -A_{ab}^c$$

$$M_2(24,7) = -\frac{1}{T_3^c}\ , \quad M_2(24,8) = \frac{e^{-\frac{(E_2^h - E_0^h)}{k\ T_h}}}{-T_2^h}\ , \quad M_2(24,11) = -A_{ba}^c\ , \quad M_2(24,12) = \frac{1}{T_{2b}}$$

Matrix M is composed of matrices M_1 and M_2:

$$M \ \equiv \ (M_1\ M_2) \tag{3.79}$$

X is a 24×1 column vector, with the following elements: $X(1) = Q_E$, $X(2) = P_E$, $X(3) = N_{01}$, $X(4) = N_{02}$, $X(5) = N_{03}$, $X(6) = Q_A$, $X(7) = P_A$, $X(8) = Q_B$, $X(9) = P_B$, $X(10) = Q_C$, $X(11) = P_C$, $X(12) = N_{11}$, $X(13) = N_{12}$, $X(14) = N_{13}$, $X(15) = Q_D$, $X(16) = P_D$, $X(17) = N_{21}$, $X(18) = N_{22}$, $X(19) = N_{23}$, $X(20) = N_{0b}$,$X(21) = N_{1a}$, $X(22) = N_{1b}$, $X(23) = N_{2a}$, and $X(24) = N_{2b}$.

Y is a 24×1 column vector, with three non-zero elements: $Y(3) = \frac{N_{0a}}{T_1^c}$, $Y(21) = \frac{N_{0a}}{T_1^h}$, and $Y(23) = N_{0a}A_{ba}^c$.

Solving the matrix equation $M \cdot X = Y$ would give us the values of the quantities involved in this model. However, the equation is too complicated to be solved analytically and therefore must be solved numerically.

3.4 Discussion

We have introduced losses into our Bloch equation model of the quantum-coupled thermal to electric conversion device. We have also included the thermodynamics aspect by deriving the equilibrium values associated with the states. Taking the steady-state limit, we arrive at a set of equations from which all the quantities essential to the device performance can be solved. In the next chapter we dwell on the device characteristics and see what the model tells us about the behavior of the device.

Chapter 4

Device characteristics

Given the Bloch equation model developed in the previous two chapters, we are now in a position to compute the key device performance figures. First of all, we are interested in finding the current that would flow on the cold-side. The current is the electron charge multiplied by the rate at which an electron at $|\phi_3\rangle$ relaxes into the reservoir. Since the hot-side electron could be at level $|u_0\rangle$, $|u_1\rangle$, or $|u_2\rangle$, the current is a sum of three terms:

$$\text{current} \;=\; q\left[\frac{N_{03}-N_{0b}}{T_3^c}+\frac{N_{13}-N_{1b}}{T_3^c}+\frac{N_{23}-N_{2b}}{T_3^c}\right] \tag{4.1}$$

In subsequent discussions we denote the current as I. We can express the current in terms of the polarization terms by substituting Equations (3.4), (3.7), and (3.10) into Equation (4.1), noting that time derivatives are zero in the steady state limit:

$$\left[\frac{N_{03}-N_{0b}}{T_3^c}\right]+\left[\frac{N_{13}-N_{1b}}{T_3^c}\right]+\left[\frac{N_{23}-N_{2b}}{T_3^c}\right] \;=\; \left[-\frac{N_{03}}{T_1^h}-N_{03}\frac{e^{-\frac{(E_2^h-E_0^h)}{kT_h}}}{T_2^h}+\frac{N_{13}}{T_1^h}+\frac{N_{23}}{T_2^h}-\frac{V}{\hbar}P_E\right] \;+$$

$$\left[-\frac{N_{13}}{T_1^h}+\frac{N_{03}}{T_1^h}-\frac{V}{\hbar}P_B\right]+\left[-\frac{N_{23}}{\hbar}+N_{03}\frac{e^{-\frac{(E_2^h-E_0^h)}{k\;T_h}}}{T_2^h}-\frac{V}{\hbar}P_D\right] \;+$$

$$= -\frac{V}{\hbar}P_E - \frac{V}{\hbar}P_B - \frac{V}{\hbar}P_D \tag{4.2}$$

We can further re-express above expression. From Equation (3.3) we have:

$$\frac{N_{12}}{T_1^h} - \frac{N_{02}}{T_1^h} = N_{02}\frac{e^{-\frac{(E_2^h - E_0^h)}{k\ T_h}}}{T_2^h} - \frac{N_{22}}{T_2^h} - \frac{V}{\hbar}P_E \tag{4.3}$$

From Equation (3.6) we have:

$$\frac{U}{\hbar}P_A + \frac{V}{\hbar}P_B = \frac{N_{12}}{T_1^h} - \frac{N_{02}}{T_1^h} \tag{4.4}$$

From Equation (3.9) we have:

$$N_{02}\frac{e^{-\frac{(E_2^h - E_1^h)}{k\ T_h}}}{T_2^h} - \frac{N_{22}}{T_2^h} = -\frac{V}{\hbar}P_D \tag{4.5}$$

Summing up the above three equations we obtain:

$$\frac{U}{\hbar}P_A = -\frac{V}{\hbar}P_E - \frac{V}{\hbar}P_B - \frac{V}{\hbar}P_D = \frac{I}{q} \tag{4.6}$$

The calculation of current is hence reduced to the calculation of P_A.

4.1 Power and efficiency

The thermal power transferred from the hot-side to the cold-side is equal to the energy difference between $|u_2\rangle$ and $|u_1\rangle$ multiplied by the rate at which $|u_2(z_1)\phi_1(z_2)\rangle$ transitions to $|u_1(z_1)\phi_2(z_2)\rangle$. We can see from Eq. (3.8) that this rate is $\frac{U}{\hbar}P_A$. The left-hand side of Eq. (3.8) is the increase rate of N_{21} plus the relaxation rates from N_{21} to other states. The right-hand side of Eq.(3.8) is the relaxation rates from N_{2a} and

N_{01} into N_{21}, minus the rate of transfer from N_{21} to N_{12}. Therefore we identify the last term in Eq. (3.8) $\frac{U}{\hbar}P_A$ as the transfer rate from $|u_2(z_1)\phi_1(z_2)\rangle$ to $|u_1(z_1)\phi_2(z_2)\rangle$. Hence, the power transferred is:

$$P_T \;=\; \text{power transferred} \;=\; (E_2^h \;-\; E_1^h)\,\frac{U}{\hbar}P_A \;=\; \Omega_{21}\,\frac{U}{\hbar}\,P_A \tag{4.7}$$

The power delivered to the load is equal to the current multiplied by the voltage drop, which is in turn equal to the difference in Fermi levels divided by electron charge:

$$P_D \;=\; \text{power delivered} \;=\; \text{current} \;\times\; \text{voltage drop} \;=\; q\frac{U}{\hbar}P_A \;\cdot\; \frac{\mu_b^c \;-\; \mu_a^c}{q} \tag{4.8}$$

The efficiency of the device would be the ratio of power delivered over power transferred:

$$\text{efficiency} \;=\; \frac{\mu_b^c \;-\; \mu_a^c}{E_2^h \;-\; E_1^h} \tag{4.9}$$

Hereafter we may denote the power transferred as P_T and the power delivered as P_D. Also, we denote $q\;\Delta V = \mu_b^c - \mu_a^c$ and $\Delta E = E_2^h - E_1^h$.

4.2 Calculation of P_A

Even though we could solve for P_A (and therefore current and power) numerically as mentioned before, we would like to have some more analytical understanding. There is much algebra but the main goal is to arrive at Eq. (A.53), showing that $P_A \propto \left(n_2^{h,0}n_1^{c,0} - n_1^{h,0}n_3^{c,0}\right)$. The detailed calculations are done in Appendix A.

4.3 Case of on-resonance

The most important situation in a physical device corresponds to the most trivial mathematical limit of the equations under discussion. We would expect the largest throughput under conditions where there is a resonance between the hot-side quantum well and the cold-side quantum well, and in addition where there is a resonance between the excited state of the quantum well on the left side of the converter and the single state on the right side of the converter. In the case that the different two-level models are in resonance, we have

$$\Delta\omega \;=\; \Omega_{21} - \omega_{21} \;=\; 0 \tag{4.10}$$

In the event that there is a resonance between the two converter levels, we have

$$\omega_{32} \;=\; 0 \tag{4.11}$$

This is consistent with

$$\Delta\Omega \;=\; \Omega_{21} - \omega_{31} \;=\; 0 \tag{4.12}$$

In this section, we assume the case of on-resonance and denote $E_2^h - E_1^h = E_2^c - E_1^c = \Delta E$.

From previous discussions we know current $= q\frac{U}{\hbar}P_A$, which is proportional to

$$n_2^{h,0} n_1^{c,0} \;-\; n_1^{h,0} n_3^{c,0} \;=\; \frac{e^{-\frac{\Delta E}{k\ T_h}} \;-\; e^{-\frac{E_3^c - E_a^c}{k\ T_c}} e^{\frac{q\ \Delta V}{k\ T_c}}}{\left[2 \;+\; e^{-\frac{E_2^h \;-\; E_0^h}{k\ T_h}}\right]\left[2 \;+\; e^{-\frac{E_b^c \;-\; E_a^c \;-\; (\mu_b^c \;-\; \mu_a^c)}{k\ T_c}} + e^{-\frac{E_3^c - E_a^c \;-\; (\mu_b^c \;-\; \mu_a^c)}{k\ T_c}}\right]} \tag{4.13}$$

Since $E_3^c - E_a^c = \Delta E$, the numerator in the above equation can be re-written as

$$e^{-\frac{\Delta E}{k\ T_h}} \;-\; e^{-\frac{\Delta E}{k\ T_c}} e^{\frac{q\ \Delta V}{k\ T_c}} \;=\; e^{-\frac{\Delta E}{k\ T_h}}\left[1 \;-\; e^{\Delta E\left(\frac{1}{k\ T_h} \;-\; \frac{1}{k\ T_c}\right) \;+\; \frac{q\Delta V}{k\ T_c}}\right] \tag{4.14}$$

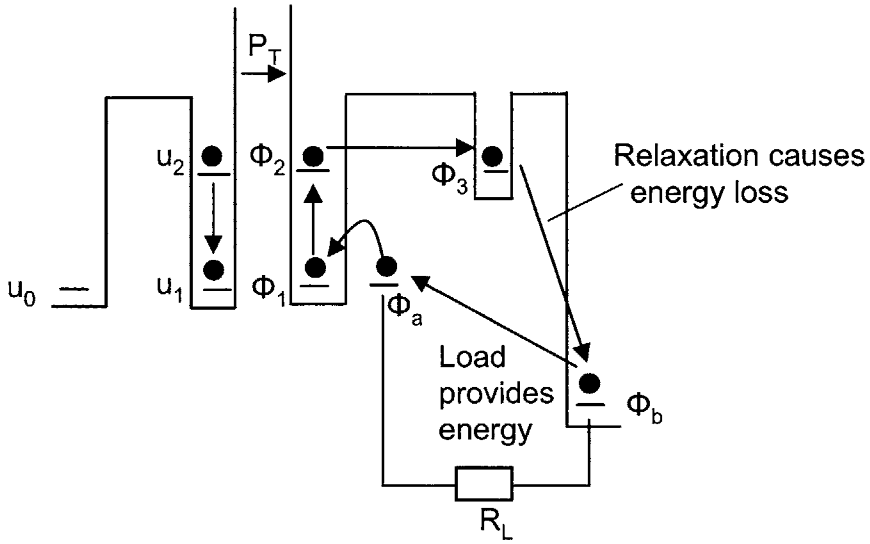

Figure 4-1: Negative-voltage case. In this regime, the load is providing power to heat up the cold-side, which is also receiving heat from the hot-side. We want to avoid operating in this range of voltage.

The sign of current is dependent on the exponent

$$\frac{\Delta E}{k}\left(\frac{1}{T_h} - \frac{1}{T_c}\right) + \frac{q\Delta V}{k\,T_c}$$

and hence we identify four regimes of operation, depending on the efficiency $\frac{q\,\Delta V}{\Delta E}$:

(1) $\frac{q\,\Delta V}{\Delta E} < 0$:

In this case, both I and P_T are positive, and P_D is negative. The hot-side and the load are both providing power to heat the cold-side. Energy is lost when an electron relaxes from ϕ_3 to ϕ_b. The efficiency is negative in this case. Please see Fig 4-1.

(2) $\frac{T_h - T_c}{T_h} < \frac{q\,\Delta V}{\Delta E} < 1$:

I, P_T, are negative, which means the cold-side is giving energy to the hot-side. P_D is negative, which means the load is providing the cold-side with energy. Efficiency smaller than 1 gives $|P_T| > |P_D|$, which says the cold-side gives the hot-side more

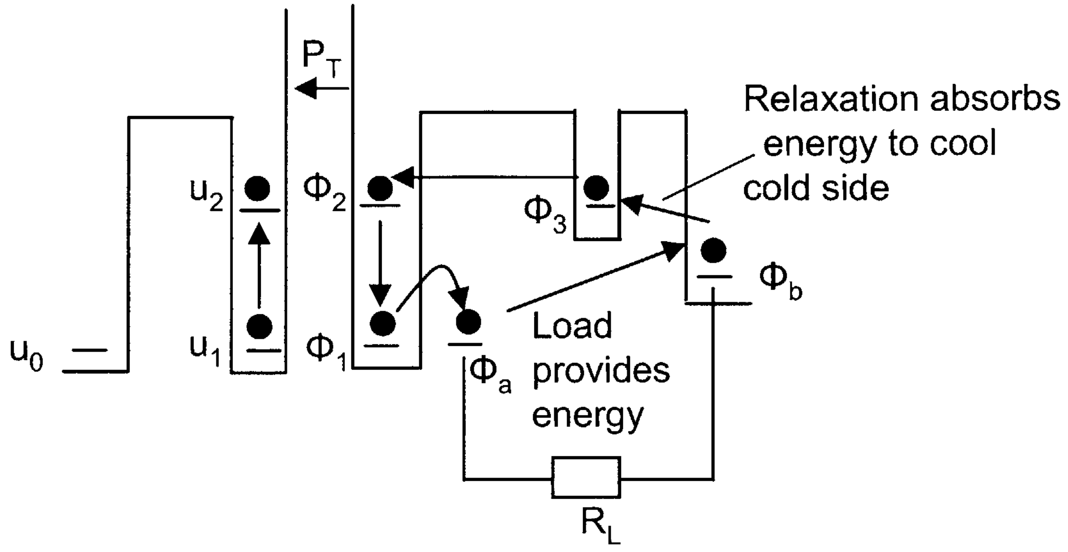

Figure 4-2: "Efficiency" greater than Carnot but smaller than 1. In this regime, the device functions like a refrigerator where the load is a power source providing energy into the system to cool the cold-side down and to heat up the hot-side.

power than it receives from the load; hence the cold-side is being cooled and the energy is lost when an electron jumps from ϕ_b to ϕ_3. Please see Fig 4-2. The device in this case acts as a refrigerator, which is a very interesting limit that we have not explored.

(3) $1 < \frac{q\,\Delta V}{\Delta E}$:

I, P_T,and P_D are again all negative. Efficiency greater than 1 gives $|P_D| > |P_T|$, which says the cold-side gives the hot-side less power than it receives from the load; hence the cold-side is being heated and it gains this energy when an electron relaxes from ϕ_b to ϕ_3. Please see Fig 4-3.

(4) $0 \leq \frac{q\,\Delta V}{\Delta E} \leq \frac{T_h - T_c}{T_h}$:

This is the normal mode of operation for the device. The current and the power transferred are both positive and the efficiency is within the Carnot limit. Energy loss occurs when an electron relaxes from ϕ_3 to ϕ_b. The efficiency increases linearly

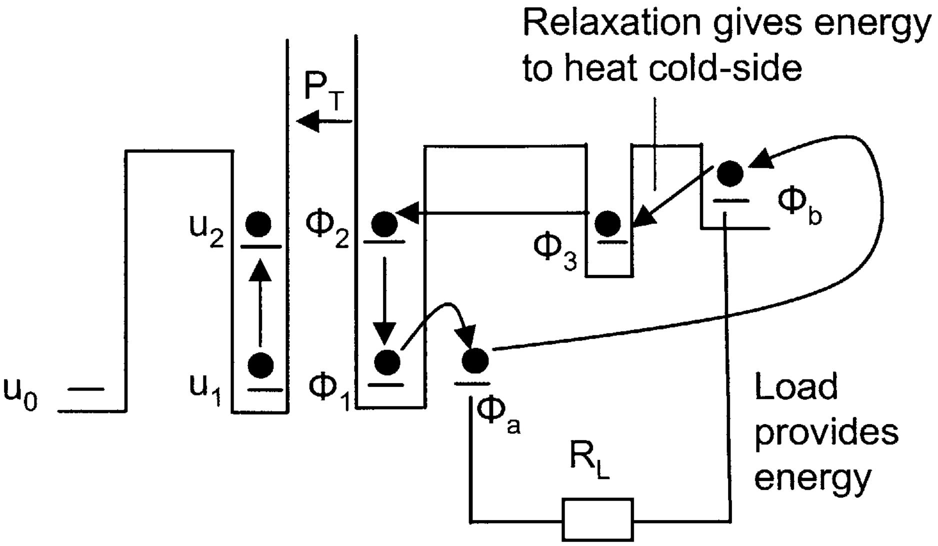

Figure 4-3: "Efficiency" greater than 1. In this regime, the cold-side load is actually a battery providing power to the cold-side. A fraction of this power is transferred to the hot-side. In short, a battery is heating both the cold-side and the hot-side in this case.

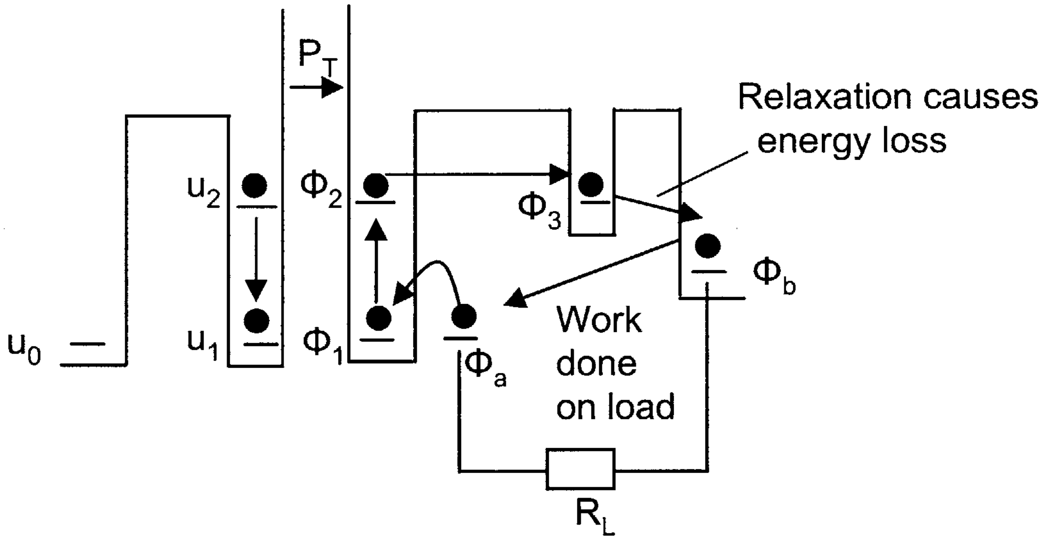

Figure 4-4: "Efficiency" between 0 and Carnot limit – normal operation mode. In this regime, the device functions as a thermal to electric converter consuming heat from the hot-side and producing electricity on the cold-side. The efficiency increases linearly with the voltage but the current decreases with increasing voltage, and the efficiency reaches the Carnot limit at zero current.

with voltage as is evident from Eq. (4.9). When $\frac{q\,\Delta V}{\Delta E} = \frac{T_h - T_c}{T_h}$, the current is zero and the efficiency reaches the Carnot limit. Please see Fig 4-4.

4.4 Equilibrium values revisited

In the above model we have used quantum levels to represent the reservoirs, and the equilibrium values obtained are thus different from the more realistic case where the reservoirs are not simplified to quantum levels. In this section we consider the equlibrium values in the latter setting.

We ignore spin in our analysis and hence the degeneracy of each quantum level is 1. Also, we ignore the possibility of multiple-electron occupation on either hot or the cold-side. The partition function on the hot-side is:

$$Z_h = 1 + e^{-\left(\frac{E_1^h - \mu^h}{k\,T_h}\right)} + e^{-\left(\frac{E_2^h - \mu^h}{k\,T_h}\right)} \tag{4.15}$$

We denote $n_0^{h,0}$, $n_1^{h,0}$, and $n_2^{h,0}$ as the equilibrium values for the no-electron occupation probability, one-electron occupation probability on $|\phi_1(z_1)\rangle$, and one-electron occupation probability on $|\phi_1(z_1)\rangle$. These values are:

$$n_0^{h,0} = \frac{1}{Z_h} \tag{4.16}$$

$$n_1^{h,0} = \frac{e^{-\left(\frac{E_1^h - \mu^h}{k\,T_h}\right)}}{Z_h} \tag{4.17}$$

$$n_2^{h,0} = \frac{e^{-\left(\frac{E_2^h - \mu^h}{k\,T_h}\right)}}{Z_h} \tag{4.18}$$

Similarly, the cold-side partition function and equilibrium occupation probabilities are as follows. Note that there is no equilibrium value for the occupation probability of $\phi_2(z_2)$ as the quantum level does not relax to the reservoir.

$$Z_c = 1 + e^{-\left(\frac{E_1^c - \mu_1^c}{k\ T_c}\right)} + e^{-\left(\frac{E_3^c - \mu_3^c}{k\ T_C}\right)} \tag{4.19}$$

$$n_a^{c,0} = \frac{1}{Z_c} \tag{4.20}$$

$$n_1^{c,0} = \frac{e^{-\left(\frac{E_1^c - \mu_1^c}{k\ T_c}\right)}}{Z_c} \tag{4.21}$$

$$n_3^{c,0} = \frac{e^{-\left(\frac{E_3^c - \mu_3^c}{k\ T_c}\right)}}{Z_c} \tag{4.22}$$

This change in equilibrium values would only affect the absolute magnitude of the current, but the three regimes of operation for the device would still hold true, as the ratio of $n_2^{h,0}$ to $n_1^{h,0}$, and the ratio of $n_3^{c,0}$ to $n_1^{c,0}$, remain unchanged.

4.5 Numerical results

We present an example calculation of the device characteristics in the normal operation mode using the above model. In this calculation the hot-side is assumed to be at 600 K and the cold-side is at 300 K. The single-electron relaxation times are assumed to be $\tau = 1/(2\pi)$ ps. The Coulomb and tunneling matrix elements are: $U = 2V = 2\hbar/\tau$. Each device, or pixel, is assumed to occupy an area of 1000 Å × 1000 Å = 10^{-10} cm^2. The level spacing is: $\Delta E = 0.1$ eV. Fermi levels μ^h and μ_1^c are at energy level 0 eV, same as E_1^h and E_1^c. Fermi level μ_3^c is dependent on the voltage. Note here we are under the on-resonance assumption and different voltage points actually correspond to different devices on-resonant at the particular voltages.

Figure 4-5 shows the current versus voltage characteristics. The short-circuit current is 15.5 nA/pixel. With an assumed pixel area of 10^{-10} cm^2, the short-circuit

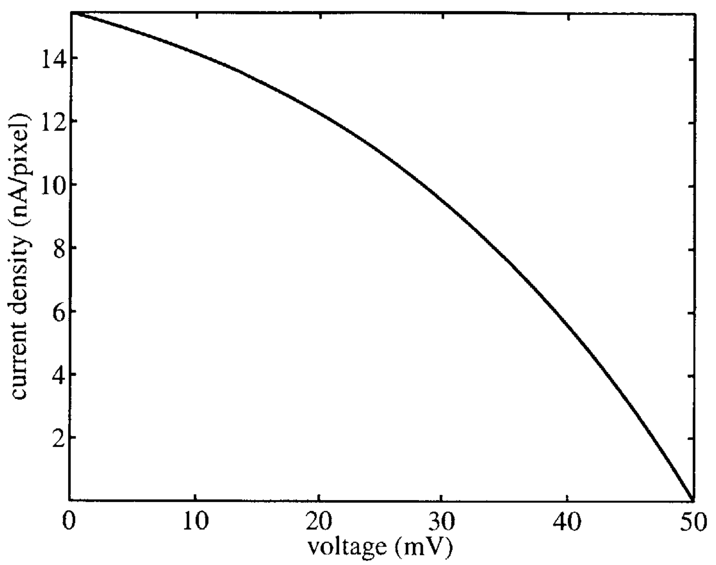

Figure 4-5: Current versus voltage characteristic for the on-resonance case, which refers to a set of devices, each of which has level 3 matched to level 2 at the particular voltage.

current density is 155 A/cm^2. The open-circuit voltage is as expected from the analytical argument $\Delta E/q$ × Carnot limit $=$ 50 mV. Figure 4-6 shows power delivered to the load per pixel versus voltage. The peak power is 0.29 nW/pixel or 2.9 W/cm^2 at the voltage of 30 mV, with corresponding efficiency of 30%, as can be seen from the efficiency versus voltage plot of Figure 4-7. The efficiency plot is a straight line consistent with above analytical derivations. According to Eq. (4.6) and Eq. (4.7), the thermal power transferred is simply the current multiplied by $\Delta E/q$ and is not plotted here.

4.6 Discussion

The Bloch equation modeling yields some understanding of the device behavior and the results indicate that this new thermal to electric conversion scheme could potentially have high efficiency and high power throughput. However, an issue arises when we try to model the device in the off-resonance case. For a single device, if we increase the voltage by ΔV then the Fermi level of reservoir b increases by ΔV.

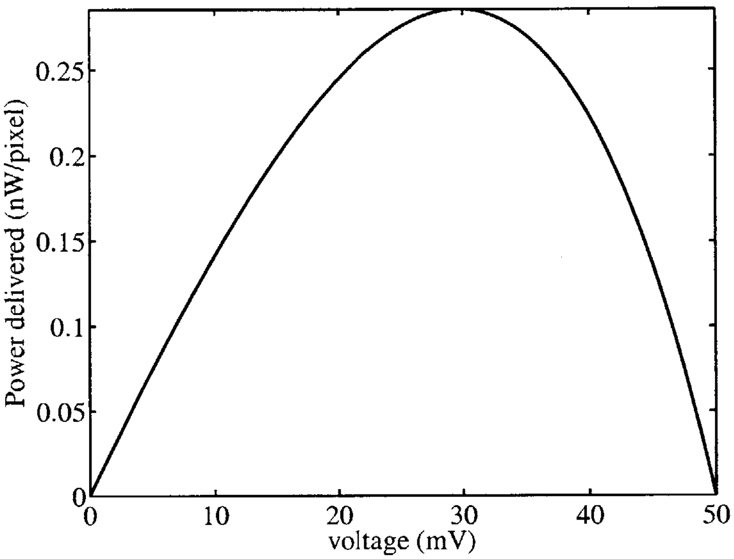

Figure 4-6: load power as a function of voltage for the on-resonance case. The on-resonance case refers to a set of devices, each of which has level 3 matched to level 2 at the particular voltage.

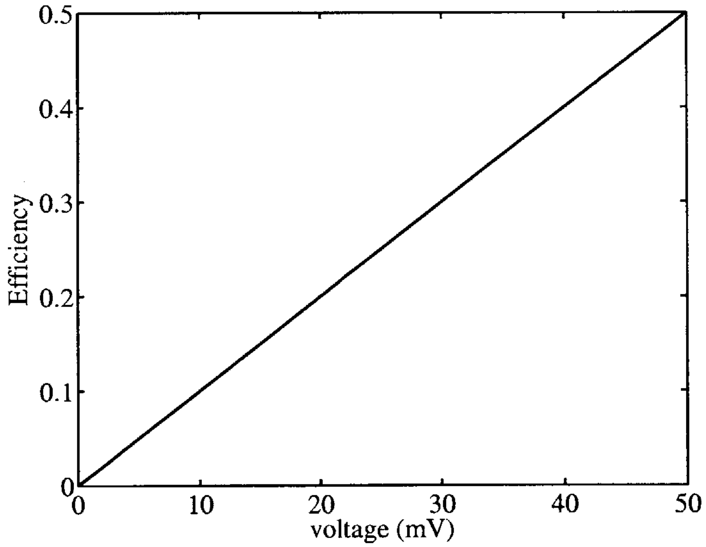

Figure 4-7: Efficiency as a function of voltage. Each point on the curve corresponds to a different device with level 3 matched to level 2 at that particular operating voltage. The efficiency approaches the Carnot limit 0.5 as the voltage approaches 50 mV

Since level 3 relaxes to reservoir b, level 3 energy also increases by ΔV. As a result, the value of $n_3^{c,0}$ does not change with ΔV and therefore the current and thermal power transferred would not change with ΔV. This is erroneous as the load power increases with ΔV and for sufficiently large ΔV the load power would exceed the thermal power, breaking the law of conservation of energy.

The above contradiction indicates that the Bloch equations amended with phenomenological relaxation terms are inconsistent with thermodynamics and thus a different model needs to be developed to more sensibly simulate the device characteristics. However, even though the model breaks for the off-resonance case, the on-resonance case results from Bloch equation modeling still give us decent intuition about the device and these results are not far off from those obtained with the more sophisticated model described in Chapter 7.

Chapter 5

Brute force numerical approach and the secular equations partitioning method

As pointed out at the end of the last chapter, the issue with the Bloch equation approach is that relaxation to the reservoirs can not be modeled correctly with the added phenomenological terms in Bloch equations. To solve this problem, one method is to approximate the reservoirs as many discrete levels spread over an energy spectrum, each coupled to the quantum well levels with a matrix element. We can then solve the system dynamics with Schrodinger's equation numerically. This approach has been demonstrated in section 24.3 of [10]. In principle, denser levels and a wider energy spectrum lead to a better approximation of the reservoir, but experience shows that the energy spacing between two adjacent levels only needs to be on the order of the coupling matrix element and the number of levels only needs to be a couple hundreds for the technique to give sensible results. In this chapter we solve some example problems with this brute-force numerical approach. We also cross-check the validity of the results by the use of the secular equations partitioning method, which will be further explained in the next chapter.

5.1 Basic demonstration

To show how the brute-force numerical approach works, we first consider a simple problem depicted in Figure 5-1. Since this exercise is for demonstration purposes, for simplicity $\hbar$ is taken to be 1 and the units of quantities are of less concern at the moment. On the left-hand side there is a reservoir called continuum α that consists of 600 levels with energies evenly distributed between -300 and 300. On the right-hand side there is an exactly the same reservoir called continuum β. In between these two reservoirs is a single discrete level Ψ_1 that is coupled to each of the levels in the two reservoirs with matrix element $W = 1$. The energy of Ψ_1 is zero: $E_1 = 0$.

Suppose the wavefunction starts out at state Ψ_1. Due to the couplings to the reservoir level, over time the wavefunction will spread out to other states and the occupation probability of Ψ_1 will decay. Then the wavefunction will oscillate back onto state Ψ_1, and therefore we would have an oscillatory behavior of the level Ψ_1 occupation probability. If the two reservoirs are true continua, the wavefunction will simply decay away and never oscillate back, with a decay rate given by the Golden Rule. Our numerical model has finite levels and is not a true continuum but the initial decay behavior predicted by the numerics will be close to that of a true continuum, as long as we use enough levels to represent the reservoirs. Figure 5-2 shows the occupation probability of Ψ_1 as a function of time. The asterisks are the numerical data points computed from the above mentioned model while the green line is the exponential fitting. The decay rate obtained from the fitting is $\Gamma = 12.4$ while the one obtained from the Golden Rule is:

$$\Gamma = \frac{2\pi}{\hbar}|W|^2\rho(E = E_1) = 2\pi \times 2 \times \frac{600}{600} \approx 12.57$$

The two numbers obtained above are close to each other, which gives us some confidence in the feasibility of the numerical approach.

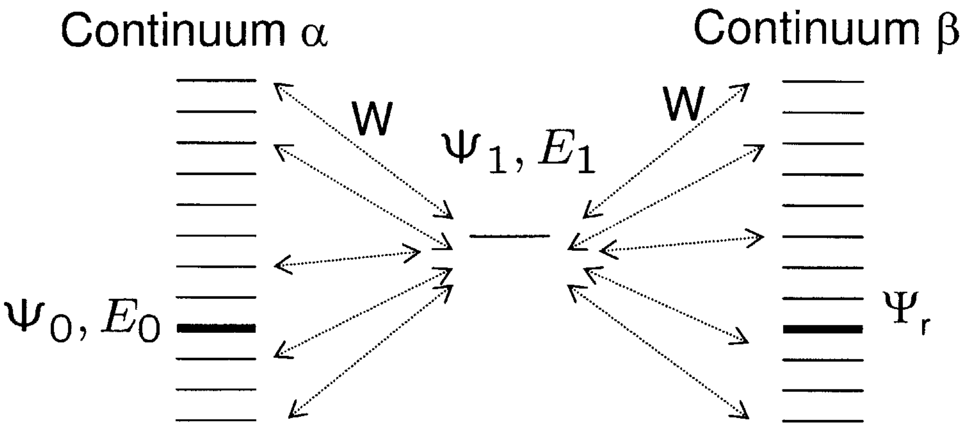

Figure 5-1: Schmatics of the basic demonstration problem. There is one discrete level Ψ_1 coupled to two reservoirs, continuum α and continuum β. Each of the reservoir is modeled as 600 even distributed levels over the energy range -300 to 300. The coupling matrix element between Ψ_1 and each of the reservoir level is 1. ψ_0 is a level in continuum α while Ψ_r is a continuum β level that is resonant with Ψ_0.

5.2 Transition probability

In the following calculations we have used more states, 1201 levels with energies evenly distributed between -300 and 300 to better model each reservoir. In this case, the Golden Rule decay rate of state Ψ_1 is $\Gamma = 25.13$.

Suppose the wavefunction initially starts off at a level Ψ_0 in continuum α, we compute the occupation probability at the resonant level Ψ_r in continuum β as a function of time. Figure 5-3 shows the transition probability versus time for $E_0 = 0$. The probability increases exponentially in the beginning, but it reaches maximum value 1 and starts decreasing at time = 12.5 due to the reflection back to state Ψ_1. The initial increase rate of the Ψ_r occupation probability can be thought of as the transition rate from Ψ_0 to Ψ_r. A summation of transition rates over all the reservoir levels would give us the electron flux from reservoir α to reservoir β. This is basically how the numerical approach could be used to calculate device figures such as current and power.

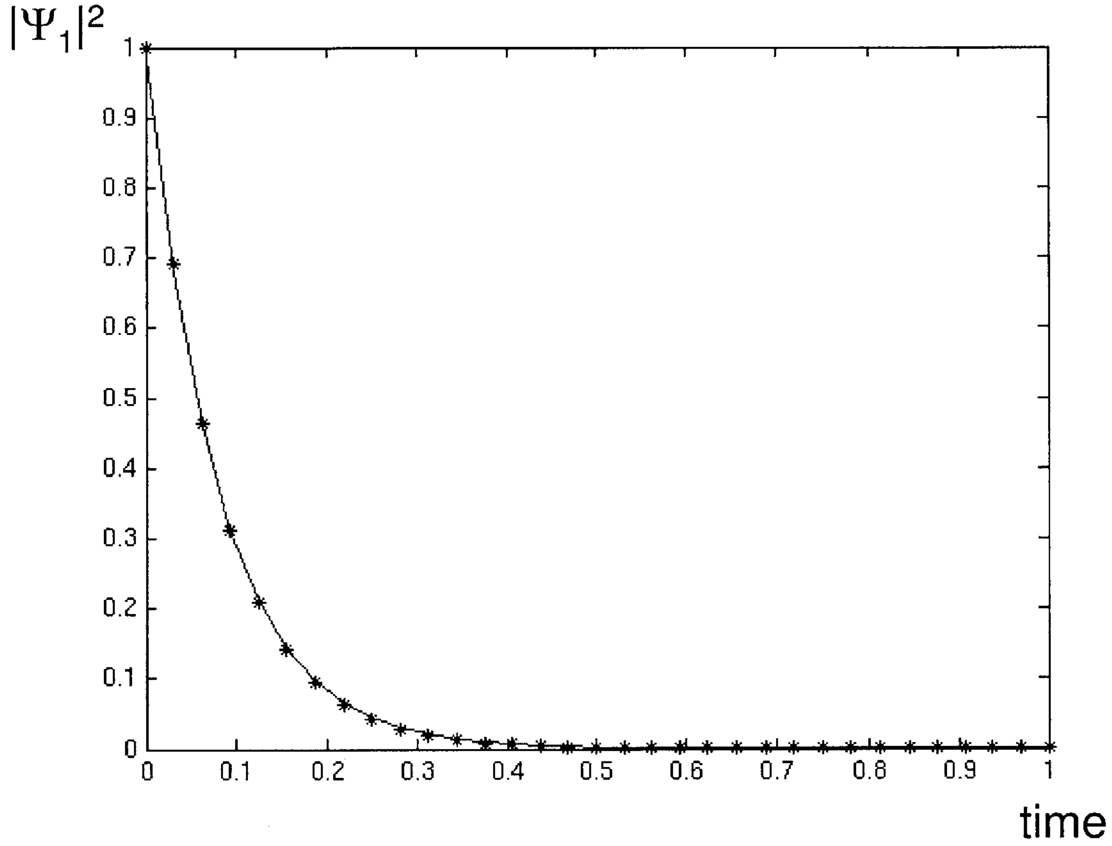

Figure 5-2: Decay of the occupation probability of state Ψ_1 over time. The asterisks are the data points from the numerical model with the green line is the exponential fitting.

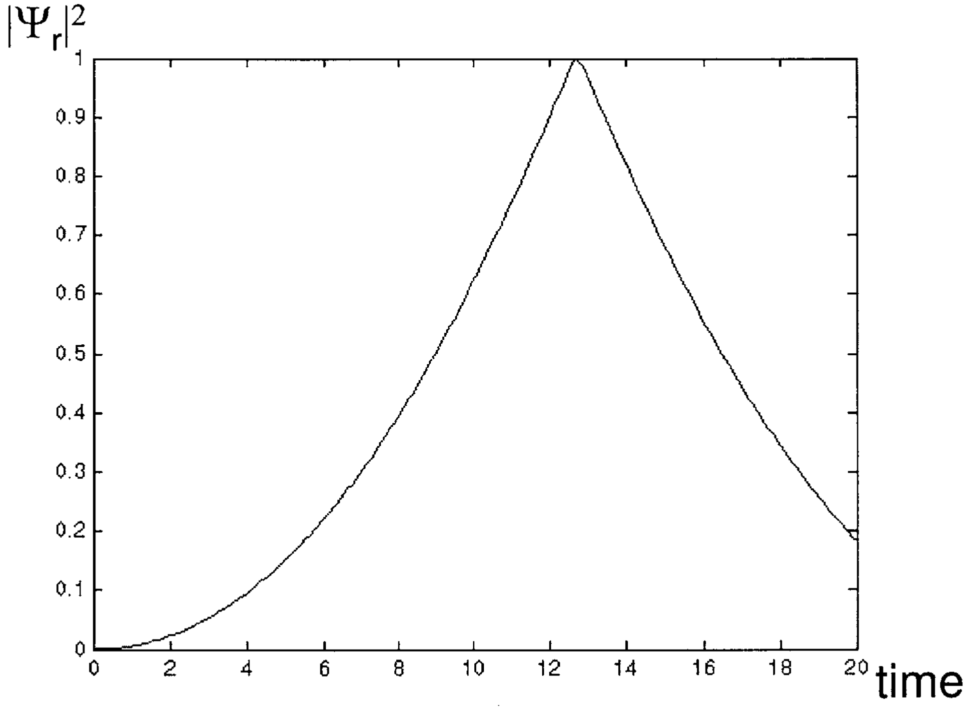

Figure 5-3: Transition probability from state Ψ_0 in continuum α to a resonant state Ψ_r in continuum β with the resonant energy $E_0 = E_1 = 0$. The probability increases exponentially with time in the beginning and then at time = 12.5 it reaches maximum 1 and starts decreasing.

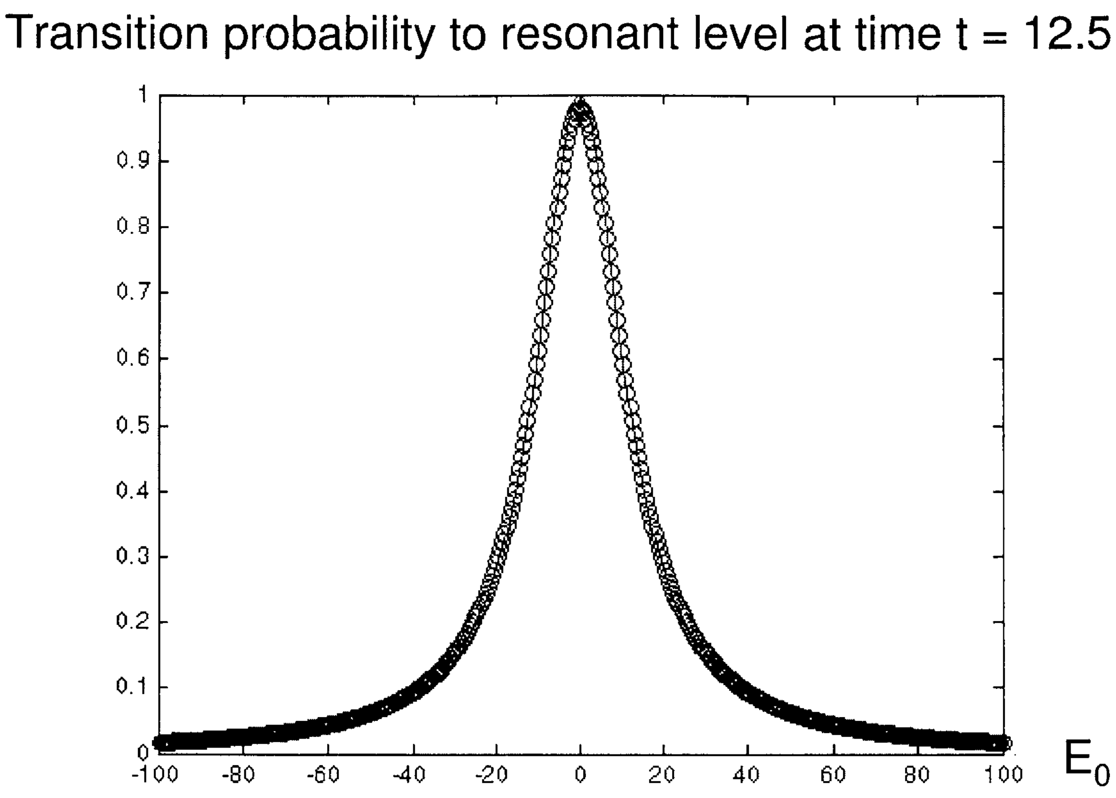

Figure 5-4: Transition lineshape for the basic demonstration problem. The cirlces are the data points obtained from the numerical model, while the green line is the lineshape obtained from the secular equations partitioning method augmented with loss.

If we choose a different Ψ_0 with a different energy, the transition probability would be different because of the presence of level Ψ_1. The transition probability is higher if E_0 is closer to E_1.

Figure 5-4 shows the lineshape of the transition probability versus E_0 at time $t = 12.5$. The circles are the data points obtained from the numerical model, while the green line is the lineshape obtained from the secular equations partitioning method, which will be described in the next section. The linewidth is as predicted from the BW theory to be $\Gamma/2 = 12.57$. The results of the numerical approach and the BW theory match fairly well, which is an indication of the validity of both approaches.

5.3 Secular equations partitioning method

A secular equations partitioning method by Löwdin [11, 12] could be used to analyze the type of problems we are considering. Secular equations are basically the set of algebraic equations or Hamiltonian matrix obtained from finite-basis expansion. We partition the basis states into ones (subset A) which we concentrate our interest on and ones (subset B) which are of less concern to us. We can solve for states in subset B in terms of states in subset A and then substitute back into the full Hamiltonian matrix to obtain the effective Hamiltonian for subset A. We can then focus on subset A with the effective Hamiltonian matrix which already takes into account the influence of subset B. The original secular equations partitioning method is for loss free problems. However, in our problem loss Γ is present. We extend the secular partitioning method to include loss by incorporating an imaginary part $-i\hbar\Gamma/2$ into the energy of the level. Applied to our example, we have the following secular equation:

$$E\Psi_1 = E_1\Psi_1 + W\Psi_0 - i\hbar\frac{\Gamma}{2}\Psi_1$$

Rearranging terms gives:

$$\Psi_1 = \frac{W\Psi_0}{E - E_1 + i\hbar\frac{\Gamma}{2}}$$

State Ψ_1 eventually relaxes into Ψ_r and therefore:

$$\Psi_r = -i\hbar\frac{\Gamma}{2}\Psi_1 = \frac{-i\hbar\frac{\Gamma}{2}W\Psi_0}{E - E_1 + i\hbar\frac{\Gamma}{2}}$$

We have now substituted out Ψ_1 from our equations. Since we start off at Ψ_0, we take $\Psi_0 = 1$ and obtain the lineshape (remembering that we have taken $\hbar$ and W to be 1):

$$|\Psi_r|^2 = \frac{\hbar^2\frac{\Gamma^2}{4}|W^2|\cdot|\Psi_0|^2}{(E-E_1)+\hbar^2\frac{\Gamma^2}{4}} = \frac{(\Gamma/2)^2}{(E-E_1)+(\Gamma/2)^2}$$

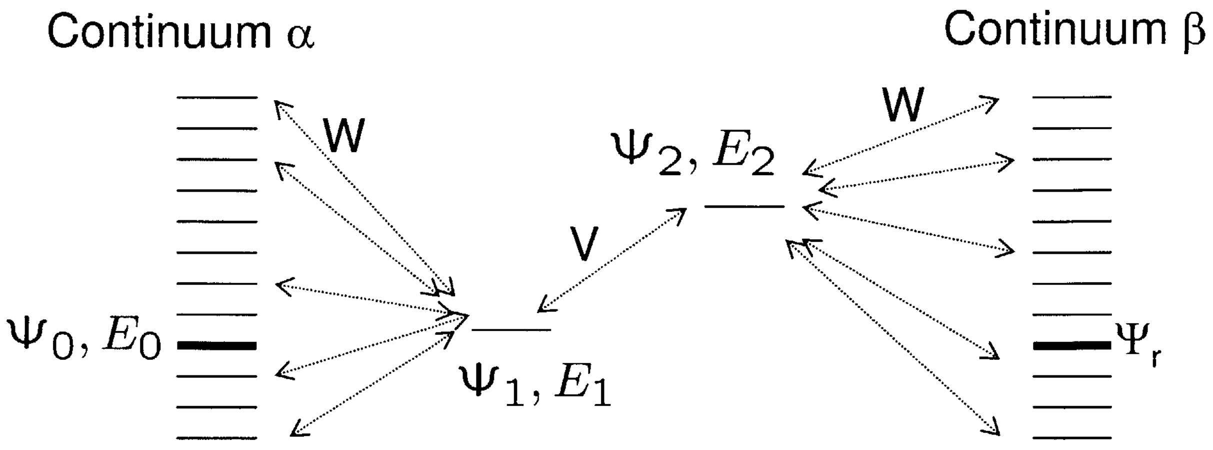

Figure 5-5: Two continuua coupled through two discrete levels. There are two discrete levels Ψ_1 and Ψ_2 in between the two continua. Ψ_1 and Ψ_2 are coupled with matrix element V. Ψ_1 is coupled to each of the continuum α level with matrix element W while Ψ_2 is coupled to each of the continuum β levels with matrix element W. Ψ_r is a level in continuum β that is resonant with level Ψ_0 in continuum α.

5.4 Two discrete levels case

To show the generalizability of this numerical approach, we consider a more complicated problem in this section. Please see Figure 5-5. In this case, there are two discrete levels, Ψ_1 and Ψ_2, in between the two continua. Ψ_1 and Ψ_2 are coupled with matrix element V. Ψ_1 is coupled to each of the continuum α level with matrix element W while Ψ_2 is coupled to each of the continuum β levels with matrix element W. Again, each continuum consists of 1201 levels with energies evenly distributed between -300 and 300. $\hbar$ is assumed to be 1 for the sake of convenience. The following values for the parameters are used: $W = 1$, $E_1 = 10$, $E_2 = -10$, $V = 20$. The wavefunction starts out at state Ψ_0, and then evolves according to Schrodinger's equation. The decay rate of Ψ_1 and Ψ_2 is calculated from the Golden Rule:

$$\Gamma = \frac{2\pi}{\hbar}|W|^2\rho(E = E_1) = 2\pi \times 2 \times \frac{1200}{600} \approx 12.57$$

We look at the transition probability $|\Psi_r|^2$ over time, plotted in Figure 5-6 for the case of $E_0 = 10$. The transition probability first increases exponentially, but at time

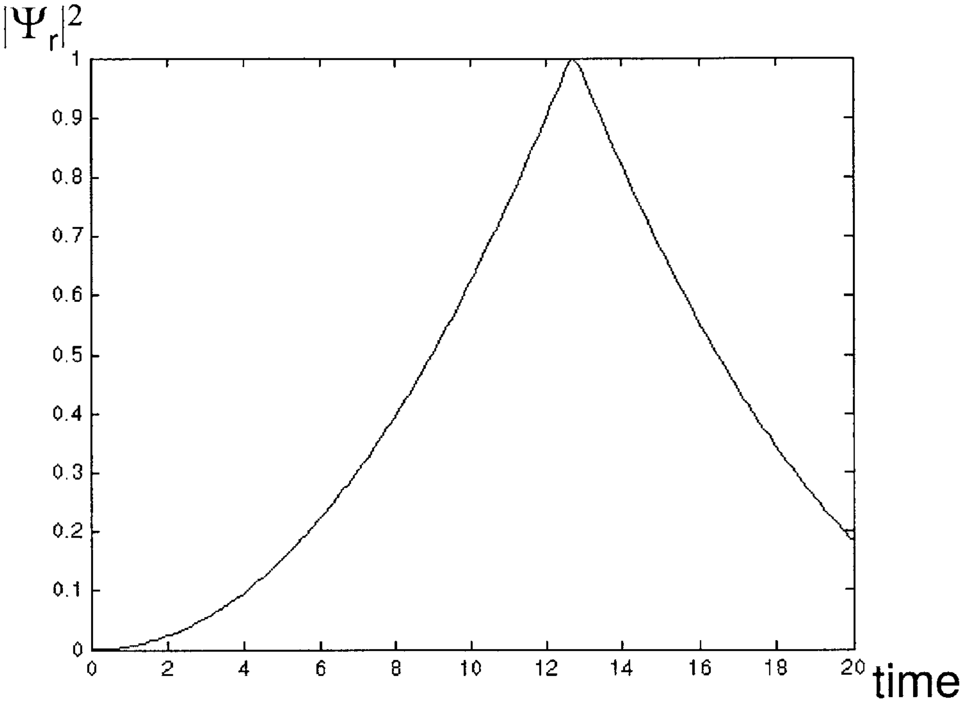

Figure 5-6: Transition Probability from state Ψ_0 in continuum α to a resonant state Ψ_r in continuum β with the resonant energy $E_0 = 10$. The probability increases exponentially with time in the beginning and then at time = 12.5 the simulation becomes invalid due to reflections back from the reservoir levels.

12.5 there is a discontinuity in slope. We attribute this discontinuity to our use of finite levels to represent continua and the simulation is only valid before this point. The lineshape can be computed using the secular equations partitioning method. The algebraic secular equations are:

$$E \cdot \Psi_1 = E_1 \, \Psi_1 + W\Psi_0 + V\Psi_2 - i\hbar\frac{\Gamma}{2}\Psi_1$$

$$E \cdot \Psi_2 = E_2 \cdot \Psi_2 + V \cdot \Psi_1 - i\hbar\frac{\Gamma}{2}\Psi_2$$

which give

$$\Psi_2 = \frac{VW\Psi_0}{\left(E - E_1 + i\hbar\frac{\Gamma}{2}\right)\left(E - E_2 + i\hbar\frac{\Gamma}{2}\right) - V^2}$$

which in turn gives the lineshape

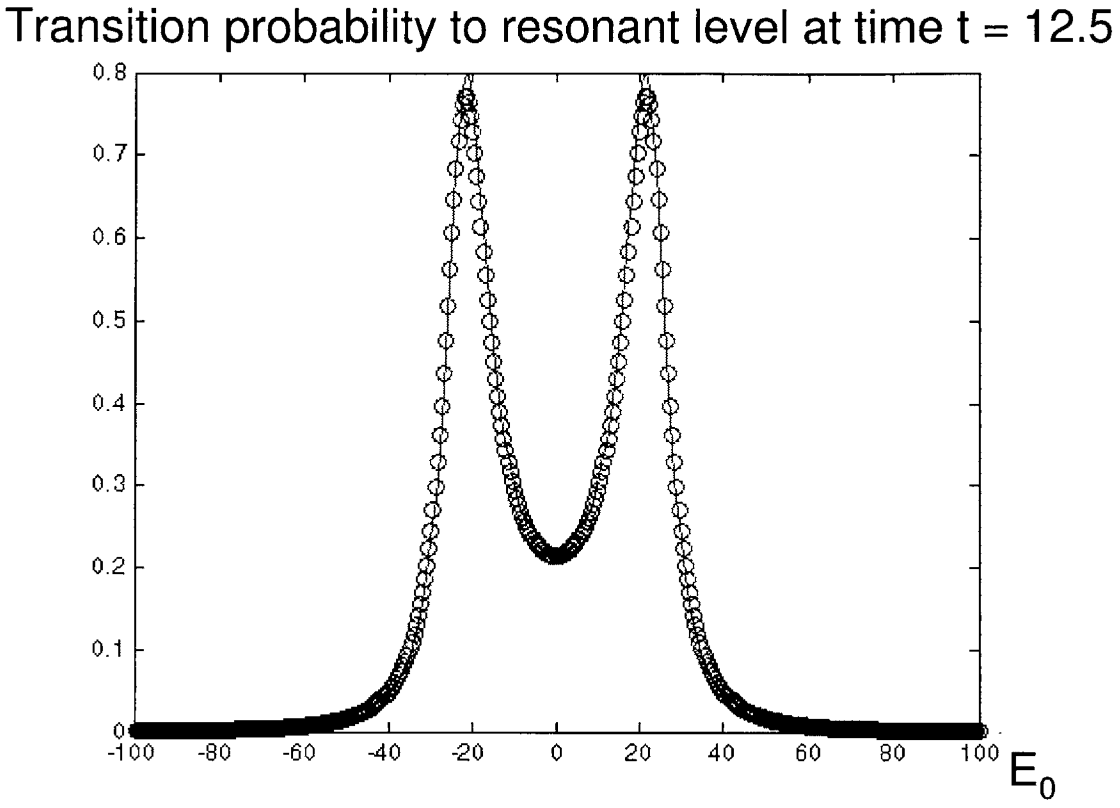

Figure 5-7: Transition lineshape for the two discrete levels problem. The cirlces are the data points obtained from the numerical model, while the green line is the lineshape obtained from the infinite-order Brillouin-Wigner theory.

$$|\Psi_r|^2 = |-i\hbar\frac{\Gamma}{2}\Psi_2|^2 = \frac{\frac{|\hbar\Gamma V W|^2}{4}}{\left[(E-E_+)+\frac{\Gamma^2\hbar^2}{4}\right]\left[(E-E_-)+\frac{\Gamma^2\hbar^2}{4}\right]}$$

where

$$E_\pm = \frac{E_1+E_2}{2} \pm \frac{1}{2}\sqrt{(E_1-E_2)^2+4V^2}$$

Figure 5-7 shows the transition probability lineshape. The circles are the data points generated by the numerical model, while the green line is secular equations partitioning method lineshape. The results obtained from these two methods again match, which indicates that both methods can be extended to solve more general and complicated problems.

5.5 Discussion

We have seen how the brute force numerical approach works and how it could be generalized to compute transition rates between discrete levels and continua (reservoirs). However, our device has one reservoir on the hot-side and two reservoirs on the cold-side. Due to the presence of Coulomb coupling, two-electron states need to be used and two-electron reservoirs, namely products of two one-electron reservoirs, need to be modeled. To accurately represent these reservoirs would require the use of a lot of levels and the simulation time would be long. Therefore it is foreseeable that using the brute-force numerical approach would lead to slow progress. In addition, the numerical model simply gives us some numbers and we would have little understanding of the results. We would much prefer some more advanced approach that would allow analytic checks and more intuition. We have seen that the secular equations partitioning method augmented with loss yields results matching those of the numerical approach. Given its validity and analytic capabilities, we use the secular equations partitioning method in the following chapter to solve our device problem.

Chapter 6

Secular equations partitioning method modeling

In this chapter we present the device modeling results from the augmented secular equations partitioning method. As described in the last chapter, we can partition the full secular equations to give us an effective Hamiltonian matrix focusing on the subset of states which are of interest to us. There are a lot of states involved in our model and we wish to reduce the system to those states crucial to computing the device performance. We follow an approach similar to that described by Löwdin [11, 12]. The original method did not include loss and we have extended the approach to include loss properly. Please note that the notations used in this chapter might be different from those used previously. Before jumping into the analysis of the device, let us review the basic model. Please see Figure 6-1. One sees that there are five discrete energy levels in the problem: levels a and b on the hot side; and levels 1, 2, and 3 on the cold-side. In addition, one sees five different sets of continuum states associated with the five different reservoirs: reservoirs R_a and R_b on the hot side, with associated continuum states denoted by r_a and r_b; and reservoirs R_1, R_2, and R_3 on the cold-side, with associated states denoted by r_1, r_2 and r_3.

To model the device, we require a set of two-electron state definitions. It will be convenient to adopt a bra and ket notation for the two-electron states such as $|r_a, 2\rangle$.

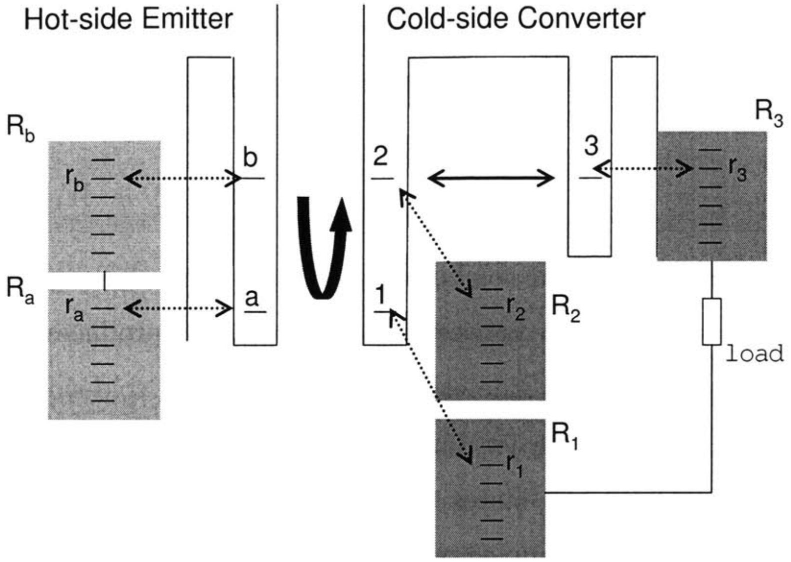

Figure 6-1: Model of the device. On the hot-side, the optical transition is modeled as two discrete levels, each of which is coupled to a reservoir and the two reservoirs are connected and have the same Fermi level. There are two levels in the first cold-side well and one level in the second cold-side well. Coulomb coupling between the hot-side levels and the first cold-side well levels exists across a vacuum gap. The excited level of the first cold-side well is coupled to the level in the second cold-side well through tunneling.

The 24 possible combinations of two-electron states are listed in Table 6.1.

Table 6.1: List of possible two-electron states.

HOT-SIDE	COLD-SIDE	POSSIBLE STATES
discrete	discrete	$\|a,1\rangle$, $\|b,1\rangle$, $\|a,2\rangle$, $\|b,2\rangle$, $\|a,3\rangle$, and $\|b,3\rangle$
discrete	continuum	$\|a,r_1\rangle$, $\|b,r_1\rangle$, $\|a,r_2\rangle$, $\|b,r_2\rangle$, $\|a,r_3\rangle$, and $\|b,r_3\rangle$
continuum	discrete	$\|r_a,1\rangle$, $\|r_b,1\rangle$, $\|r_a,2\rangle$, $\|r_b,2\rangle$, $\|r_a,3\rangle$, and $\|r_b,3\rangle$
continuum	continuum	$\|r_a,r_1\rangle$, $\|r_b,r_1\rangle$, $\|r_a,r_2\rangle$, $\|r_b,r_2\rangle$, $\|r_a,r_3\rangle$, and $\|r_b,r_3\rangle$

6.1 Model Hamiltonian

To analyze the device dynamics, we require a model Hamiltonian that is relevant to the two-electron states. The simplest such Hamiltonian is one in which states are coupled with interaction terms that are relevant to the problem. For example, consider the coupled-channel equation for a two-electron state $|b,1\rangle$ which contains an excited electron on the hot-side, and a ground state electron on the cold-side:

$$E|b,1\rangle \;=\; (E_b + E_1)|b,1\rangle \;+\; U|a,2\rangle \;+\; W_b|r_b,1\rangle \;+\; W_1|b,r_1\rangle \tag{6.1}$$

The diagonal term is simply the combination of the two one-electron energies E_b and E_1. The Coulomb interaction between the two electrons produces a dipole-dipole coupling which lowers the hot-side electron and raises the cold-side electron. The associated interaction strength for this coupling is U. There are in addition loss terms that couple the discrete states to continuum states; these are parameterized by W_b and W_1. All of the coupled-channel equations together combine to form a very large eigenvalue problem, since there are two-electron basis states involving one-electron continuum states on both the hot-side and the cold-side. The couplings that we have included in the model under discussion are illustrated in Figure 6-2. Though not directly relevant to our current discussion, the three-level system consisting of the states $|b,1\rangle$, $|a,2\rangle$, and $|a,3\rangle$ has some interesting bandwidth behaviour and it is further discussed in Appendix B.

6.2 Transition rate

To extract a transition rate from such a model is not difficult in principle. We compute the transition rate for an effective transition from an initial continuum state (with electrons in the R_b and R_1 reservoirs) to a final continuum state (with electrons in the R_a and R_3 reservoirs). We begin by selecting initial one-electron reservoir states r_b and r_1 to make $|r_b, r_1\rangle$, with a total energy $E = \epsilon_b + \epsilon_1$, where ϵ_b is the energy of reservoir state r_b and ϵ_1 is the energy of reservoir state r_1. The final state is taken to be $|r_a, r_3\rangle$, with the same total energy $E = \epsilon_a + \epsilon_3$, where ϵ_a is the energy for reservoir state r_a, and ϵ_3 is the energy for the reservoir state r_3. The transition rate between these two states is

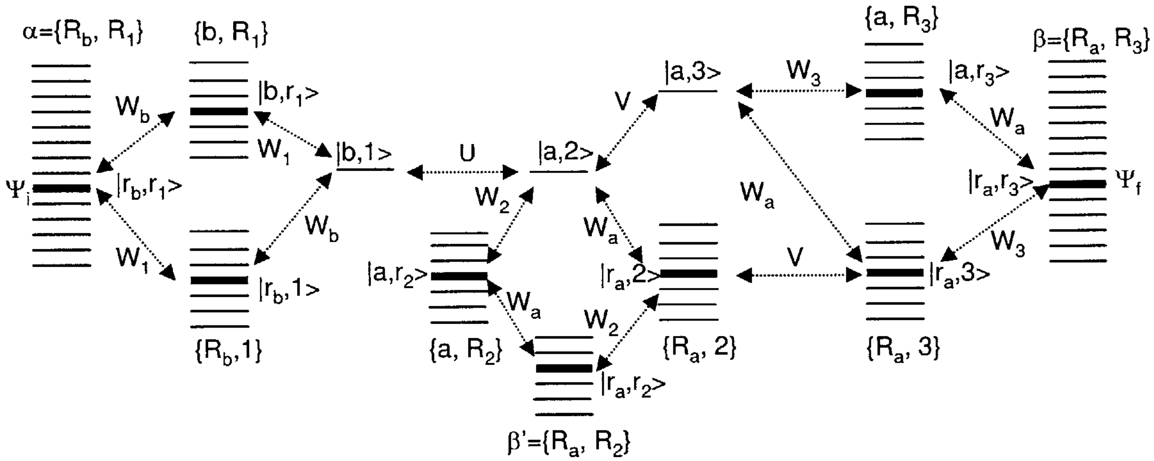

Figure 6-2: Level diagram showing the couplings among the two-electron states. Each state consists of a hot-side electron state and a cold-side electron state. Initially the hot-side electron occupies a reservoir level r_b while the cold-side electron occupies the reservoir level r_1, and the two-electron state is denoted Ψ_i in continuum α on the left-hand side of the figure. After the excitation conversion process the hot-side electron ends up in a reservoir level r_a and the cold-side electron is promoted to reservoir level r_3, and the two-electron state is denoted Ψ_f in continuum β on the right-hand side of the figure.

$$\gamma(E) = \frac{2\pi}{\hbar}|\langle r_a, r_3|U_{eff}(E)|r_b, r_1\rangle|^2\rho(E) \tag{6.2}$$

The effective interaction U_{eff} is obtained by eliminating algebraically all other basis states in the eigenvalue equation (which is possible since the energy is fixed). This procedure is discussed in the next chapter.

6.3 Summation over initial states

The current which flows from the reservoirs R_b and R_1 can be calculated by summing the transition rate over all initial states. In summing over these states, we need to weigh the states by their occupation probability (assuming thermal equilibrium within the reservoirs). Similarly, we also need to weigh the final states by the (thermodynamic) probability that they are not occupied. Taking these issues into account, we write for the current

$$\begin{aligned} I = & -e\int d\epsilon_b \int d\epsilon_1 \int d\epsilon_a \int d\epsilon_3\ \rho_b(\epsilon_b)\rho_1(\epsilon_1)\rho_a(\epsilon_a)\rho_3(\epsilon_3) \\ & \frac{2\pi}{\hbar}|\langle r_a, r_3|U_{eff}(\epsilon_1+\epsilon_b)|r_b, r_1\rangle|^2\ \delta(\epsilon_b+\epsilon_1-\epsilon_a-\epsilon_3) \\ & \Big\{p_b(\epsilon_b)p_1(\epsilon_1)[1-p_a(\epsilon_a)][1-p_3(\epsilon_3)] - p_a(\epsilon_a)p_3(\epsilon_3)[1-p_b(\epsilon_b)][1-p_1(\epsilon_1)]\Big\} \end{aligned} \tag{6.3}$$

One sees in this equation contributions both in the forward direction (starting from $|r_b, r_1\rangle$), and in the return direction (starting from $|r_a, r_3\rangle$). The integrations are taken over the one-electron continuum states associated with the initial and final two-electron states. The associated one-electron density of states functions are $\rho_b(\epsilon_b)$, $\rho_1(\epsilon_1)$, $\rho_a(\epsilon_a)$, and $\rho_3(\epsilon_3)$. The one-electron occupation probabilities are $p_b(\epsilon_b)$, $p_1(\epsilon_1)$, $p_a(\epsilon_a)$, and $p_3(\epsilon_3)$. These are given by

$$p_a(\epsilon_a) = \frac{1}{1+e^{(\epsilon_a-\mu_a)/kT_h}} \qquad p_b(\epsilon_b) = \frac{1}{1+e^{(\epsilon_b-\mu_b)/kT_h}} \tag{6.4}$$

$$p_1(\epsilon_1) = \frac{1}{1+e^{(\epsilon_1-\mu_1)/kT_c}} \qquad p_3(\epsilon_3) = \frac{1}{1+e^{(\epsilon_3-\mu_3)/kT_c}}$$

In these formula, the different μ_j are the Fermi levels associated with the reservoir R_j.

6.4 Power and efficiency

The basic operation of the converter is straightforward: an electron in the ground state on the cold-side is promoted by excitation transfer due to Coulombic quantum coupling from the hot-side; it tunnels to level 3 and then eventually goes into reservoir R_3 which is at an elevated voltage; an electron goes from this reservoir into the circuit where work is done on the load; and finally an electron from the circuit rejoins reservoir 1 which is at ground. To characterize the device, we need to determine both the power delivered from the hot-side and the power delivered to the load, from which we can calculate the efficiency.

6.4.1 Power delivered from the hot-side

The calculation of the thermal power P_{th} delivered from the hot-side involves multiplying individual transition rates within the integral that makes up the current by the electron energy difference on the hot-side. We obtain

$$\begin{aligned} P_{th} = & \int d\epsilon_b \int d\epsilon_1 \int d\epsilon_a \int d\epsilon_3 \ \rho_b(\epsilon_b)\rho_1(\epsilon_1)\rho_a(\epsilon_a)\rho_3(\epsilon_3) \\ & \frac{2\pi}{\hbar}|\langle r_a, r_3|U_{eff}(\epsilon_1+\epsilon_b)|r_b, r_1\rangle|^2 \ \delta(\epsilon_b+\epsilon_1-\epsilon_a-\epsilon_3) \ (\epsilon_b-\epsilon_a) \\ & \Big\{p_b(\epsilon_b)p_1(\epsilon_1)[1-p_a(\epsilon_a)][1-p_3(\epsilon_3)] - p_a(\epsilon_a)p_3(\epsilon_3)[1-p_b(\epsilon_b)][1-p_1(\epsilon_1)]\Big\} \end{aligned} \tag{6.5}$$

6.4.2 Power delivered to the load

The power delivered to the load can be calculated directly from the product of the current and the voltage drop on the load. The voltage drop on the load is

$$V_L = -\frac{\mu_3 - \mu_1}{e} \tag{6.6}$$

Consequently, we obtain for the load power P_L

$$P_L = V_L I \tag{6.7}$$

6.4.3 Efficiency

The device efficiency is the ratio of the load power to the thermal power

$$\eta = \frac{P_L}{P_{th}} \tag{6.8}$$

Individual forward and reverse current paths in this model are in detailed balance, so that one would expect that the efficiency would be constrained by the Carnot limit. We have found this to be so in our calculations. One can also derive this from the basic model, by working with the occupation probabilities that appear in the integral that defines the current [Equation (6.3)]. The term in brackets that contain the occupation probabilities can be written in the form

$$\left\{p_b(\epsilon_b)p_1(\epsilon_1)[1-p_a(\epsilon_a)][1-p_3(\epsilon_3)] - p_a(\epsilon_a)p_3(\epsilon_3)[1-p_b(\epsilon_b)][1-p_1(\epsilon_1)]\right\} =$$

$$\frac{\mathrm{e}^{\frac{\epsilon_a-\mu_a}{kT_h}}\mathrm{e}^{\frac{\epsilon_3-\mu_3}{kT_c}} - \mathrm{e}^{\frac{\epsilon_b-\mu_b}{kT_h}}\mathrm{e}^{\frac{\epsilon_1-\mu_1}{kT_c}}}{\left(1+\mathrm{e}^{\frac{\epsilon_b-\mu_b}{kT_h}}\right)\left(1+\mathrm{e}^{\frac{\epsilon_1-\mu_1}{kT_c}}\right)\left(1+\mathrm{e}^{\frac{\epsilon_a-\mu_a}{kT_h}}\right)\left(1+\mathrm{e}^{\frac{\epsilon_3-\mu_3}{kT_c}}\right)} \tag{6.9}$$

One sees that the electron flow is positive when the numerator is positive, which occurs when

$$\frac{\epsilon_a - \mu_a}{T_h} + \frac{\epsilon_3 - \mu_3}{T_c} \geq \frac{\epsilon_b - \mu_b}{T_h} + \frac{\epsilon_1 - \mu_1}{T_c}$$

which reduces to

$$\mu_3 - \mu_1 \; < \; (\epsilon_b - \epsilon_a)\left(\frac{T_h - T_c}{T_h}\right) \tag{6.10}$$

remembering that $\epsilon_b - \epsilon_a = \epsilon_3 - \epsilon_1$ from energy conservation. Since the incremental power delivered to the load is proportional to $\mu_3 - \mu_1$, and the incremental thermal power is proportional to $\epsilon_b - \epsilon_a$, the incremental efficiency for each contribution is $(\mu_3 - \mu_1)/(\epsilon_b - \epsilon_a)$. If the incremental thermal power is positive, then either (1) electron flow is positive and the energy quanta transferred $\epsilon_b - \epsilon_a$ is positive or (2) electron flow is negative and the energy quanta transferred $\epsilon_b - \epsilon_a$ is negative. In both cases we have that the incremental efficiency for each contribution satisfies the Carnot limit

$$\frac{\mu_3 - \mu_1}{\epsilon_b - \epsilon_a} < \frac{T_h - T_c}{T_h} \tag{6.11}$$

When this inequality is not satisfied, the incremental thermal power is either zero or negative, and the associated contribution does not improve device operation.

Chapter 7

Secular equations partitioning method calculation

In the previous chapter we have specified a model for our device and derived expressions for the various performance figures, assuming that the effective interaction U_{eff} is known. In this chapter we describe how to use the partitioning technique to eliminate intermediate states and arrive at an expression for the effective interaction. This type of calculation has been carried out for the effective couplings between the donor and acceptor states in aggregated molecular assemblies [13]. The calculation in [13] does not include loss terms while here we have incorporated loss appropriately.

Our model is a special case of a more basic problem. Suppose there are two reservoirs connected through arbitrary levels and we want to calculate the flux between the two reservoirs. Specifically, we want to compute the flux from an initial state Ψ_i to a final state Ψ_f. The intermediate levels are denoted as Ψ_j's. The initial state and the final states are resonant at energy E. The initial states constitute a continuum α and the final states constitute a continuum β.

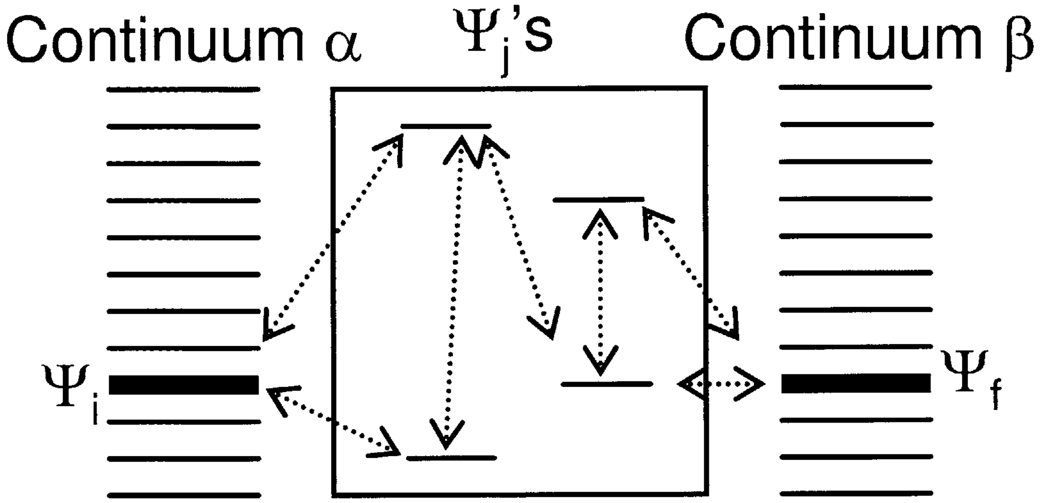

Figure 7-1: Energy level diagram of basic problem. Initial state Ψ_i resides in continuum α while the final state Ψ_f resides in continuum β. They are connected through a network of intermediate states Ψ_j's.

7.1 Basic sector equations

See Figure 7-1 for an illustration of the basic problem. We use the secular equations partitioning method to solve this problem. First we write down algebraic sector equations, assuming the coupling matrix elements V's are all real for the sake of simplicity:

$$E\,\Psi_i = H_i\,\Psi_i + \sum_{j\neq i,f} V_{ij}\,\Psi_j \tag{7.1}$$

$$E\,\Psi_j = H_j\,\Psi_j + \sum_{j'\neq i,j,f} V_{jj'}\,\Psi_{j'} + V_{ji}\,\Psi_i + V_{jf}\,\Psi_f \tag{7.2}$$

$$E\,\Psi_f = H_f\,\Psi_f + \sum_{j\neq i,f} V_{fj}\,\Psi_j \tag{7.3}$$

Each level might be coupled to a reservoir with a decay rate Γ into the reservoir.

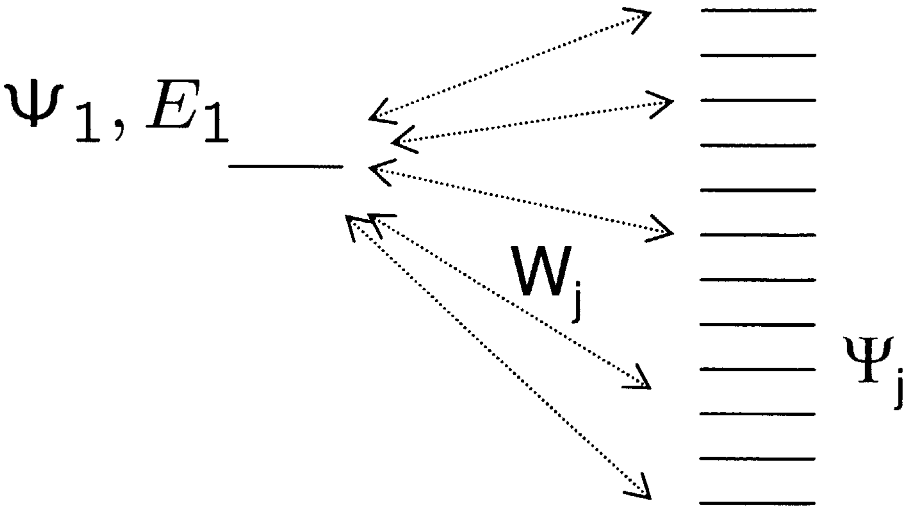

Figure 7-2: Lossy level Ψ_1 coupled to a continuum of states Ψ_j's with matrix elements W_j's

Taking this into account, the H's are defined as:

$$\forall p, H_p = E_p - i\hbar\frac{\Gamma_p}{2}. \tag{7.4}$$

where E_p is the energy of level p and the imaginary part is the loss term.

7.2 Loss term

Here we explain the derivation of the loss term. Suppose we have a lossy level Ψ_1 coupled to a continuum of states Ψ_j's with matrix elements W_j's. (See Figure 7-2). We write down the secular equations:

$$E\,\Psi_1 = E_1\,\Psi_1 + \sum_{j\neq 1} W_j\,\Psi_j \tag{7.5}$$

$$E\,\Psi_j = E_j\,\Psi_j + W_j\,\Psi_1 \tag{7.6}$$

Substituting Eq. (7.6) into Eq. (7.5) gives

$$E\,\Psi_1 \;=\; E_1\,\Psi_1 \;+\; \sum_{j\neq 1} \frac{|W_j|^2\,\Psi_1}{E-E_j}$$

We evaluate the second term in the above equation:

$$\sum_{j\neq 1} \frac{W_j}{E-E_j} \;\approx\; -\int \frac{|W_j|^2\,\rho(E_j)}{E_j-E} dE_j \;=\; -\oint_{C_1} \frac{|W_j|^2\,\rho(E_j)}{E_j-E} dE_j - \oint_{C_2} \frac{|W_j|^2\,\rho(E_j)}{E_j-E} dE_j$$

where contour C_1 consists of two line paths $E_j = -\infty \sim E-\epsilon$ and $E_j = E+\epsilon \sim \infty$, and contour C_2 is a hemisphere $E_j = E + \epsilon \cdot \mathrm{e}^{i\theta}, \theta = -\pi \sim 0$. In the limit $\epsilon \to 0^+$, the two contour integrals become:

$$-\oint_{C_1} \frac{|W_j|^2\,\rho(E_j)}{E_j-E} dE_j \;\longrightarrow\; \sum_{E_j\neq E} \frac{|W_j|^2}{E_j-E}$$

which is the self-energy term, and

$$-\oint_{C_2} \frac{|W_j|^2\,\rho(E_j)}{E_j-E} dE_j \longrightarrow -i\pi|W_j|^2\rho(E_j) \;=\; -i\hbar\frac{\Gamma}{2}$$

which is the loss term, and Γ here is the Golden Rule decay rate of level Ψ_1.

7.3 Vector and matrix notation

We introduce some matrix notations to facilitate our discussion.

1. $\overline{\Psi}_j$ is the column vector of all Ψ_j's.

2. $\overline{\overline{K}}$ is the coupling matrix among the Ψ_j's:

$$\forall p, q \neq i, f \quad \left(\overline{\overline{K}}\right)_{pq} \;=\; H_p\,\delta_{pq} \;+\; V_{pq} \tag{7.7}$$

   Because V_{pq} is assumed real,

$$V_{pq} = V_{qp}$$

Therefore $\overline{\overline{K}}$ is symmetric.

3. $\overline{V}^i$ is the coupling column vector between Ψ_i and Ψ_j's:

$$\left(\overline{V}^i\right)_j = V_{ij} \tag{7.8}$$

4. $\overline{V}^f$ is the coupling column vector between Ψ_f and Ψ_j's:

$$\left(\overline{V}^f\right)_j = V_{fj} \tag{7.9}$$

7.4 Vector and matrix equations

With the above definitions, we rewrite the algebraic sector equations into matrix equations:

$$E\,\Psi_i = H_i\,\Psi_i + \left(\overline{V}^i\right)^T \overline{\Psi}_j \tag{7.10}$$

$$E\,\overline{\Psi}_j = \overline{\overline{K}}\,\overline{\Psi}_j + \overline{V}^i\,\Psi_i + \overline{V}^f\,\Psi_f \tag{7.11}$$

$$E\,\Psi_f = H_f\,\Psi_f + \left(\overline{V}^f\right)^T \overline{\Psi}_j \tag{7.12}$$

From eq. (7.11),

$$\overline{\Psi}_j = \left[E - \overline{\overline{K}}\right]^{-1} \cdot \left[\overline{V}^i\,\Psi_i + \overline{V}^f\,\Psi_f\right] \tag{7.13}$$

Substituting eq. (7.13) into eq. (7.10), we obtain

$$E\,\Psi_i = H_i\,\Psi_i + U_{ii}\,\Psi_i + U_{if}\,\Psi_f \tag{7.14}$$

where

$$U_{ii} \equiv \left(\overline{V^i}\right)^T \cdot \left[E - \overline{\overline{K}}\right]^{-1} \overline{V^i} \tag{7.15}$$

$$U_{if} \equiv \left(\overline{V^i}\right)^T \cdot \left[E - \overline{\overline{K}}\right]^{-1} \overline{V^f} \tag{7.16}$$

Substituting eq. (7.13) into eq. (7.12), we obtain

$$E\,\Psi_f = H_f\,\Psi_f + U_{ff}\,\Psi_f + U_{fi}\,\Psi_i \tag{7.17}$$

where

$$U_{ff} \equiv \left(\overline{V^f}\right)^T \cdot \left[E - \overline{\overline{K}}\right]^{-1} \cdot \overline{V^f} \tag{7.18}$$

$$U_{fi} \equiv \left(\overline{V^f}\right)^T \cdot \left[E - \overline{\overline{K}}\right]^{-1} \cdot \overline{V^i} \tag{7.19}$$

U_{fi} is equal to U_{if}:

$$U_{if} = U_{if}^T = \left[\left(\overline{V^i}\right)^T \cdot \left[E - \overline{\overline{K}}\right]^{-1} \cdot \overline{V^f}\right]^T$$

$$= \left[\left[E - \overline{\overline{K}}\right]^{-1} \cdot \overline{V^f}\right]^T \cdot \overline{V^i} = \left(\overline{V^f}\right)^T \cdot \left[E - \overline{\overline{K}}\right]^{-1} \cdot \overline{V^i} = U_{fi}$$

Note that U_{if} is equal to its transpose because U_{if} is a scalar.

7.5 Effective matrix element

In the previous chapter we have described how to compute the device performance given the matrix element $U_{eff}(E)$. Here we give the detailed calculation of $U_{eff}(E)$. We apply the theory in the last section to our device. Please refer back to Figure 6-2. Let us define the real and imaginary parts of $\overline{\overline{K}}$:

$$\overline{\overline{K}} \equiv \overline{\overline{A}} - i\,\hbar\,\frac{\overline{\overline{\Gamma}}}{2}. \tag{7.20}$$

where $\overline{\overline{A}}$ contains the real components of $\overline{\overline{\overline{K}}}$, namely the energy terms, and $\overline{\overline{\Gamma}}$ contains the imaginary components of $\overline{\overline{\overline{K}}}$, namely the loss terms. The columns and rows of the matrices are listed with the following order of intermediate states: $|b, r_1\rangle$, $|r_b, 1\rangle$, $|b, 1\rangle$, $|a, r_2\rangle$, $|a, 2\rangle$, $|a, 3\rangle$, $|r_a, 2\rangle$, $|a, r_3\rangle$, and $|r_a, 3\rangle$.

$$\overline{\overline{A}} \equiv \begin{bmatrix} E_b + \epsilon_1 & 0 & W_1 & 0 & 0 & 0 & 0 & 0 & 0 \\ 0 & \epsilon_b + E_1 & W_b & 0 & 0 & 0 & 0 & 0 & 0 \\ W_1 & W_b & E_b + E_1 & 0 & U & 0 & 0 & 0 & 0 \\ 0 & 0 & 0 & E_a + \epsilon_2 & W_2 & 0 & 0 & 0 & 0 \\ 0 & 0 & U & W_2 & E_a + E_2 & V & W_a & 0 & 0 \\ 0 & 0 & 0 & 0 & V & E_a + E_3 & 0 & W_3 & W_a \\ 0 & 0 & 0 & 0 & W_a & 0 & \epsilon_a + E_2 & 0 & V \\ 0 & 0 & 0 & 0 & 0 & W_3 & 0 & E_a + \epsilon_3 & 0 \\ 0 & 0 & 0 & 0 & 0 & W_a & V & 0 & \epsilon_a + E_3 \end{bmatrix} \tag{7.21}$$

$$\overline{\overline{\Gamma}} \equiv \begin{bmatrix} \Gamma_{b,r_1} & 0 & 0 & 0 & 0 & 0 & 0 & 0 & 0 \\ 0 & \Gamma_{r_b,1} & 0 & 0 & 0 & 0 & 0 & 0 & 0 \\ 0 & 0 & \Gamma_{b,1} & 0 & 0 & 0 & 0 & 0 & 0 \\ 0 & 0 & 0 & \Gamma_{a,r_2} & 0 & 0 & 0 & 0 & 0 \\ 0 & 0 & 0 & 0 & \Gamma_{a,2} & 0 & 0 & 0 & 0 \\ 0 & 0 & 0 & 0 & 0 & \Gamma_{a,3} & 0 & 0 & 0 \\ 0 & 0 & 0 & 0 & 0 & 0 & \Gamma_{r_a,2} & 0 & 0 \\ 0 & 0 & 0 & 0 & 0 & 0 & 0 & \Gamma_{a,r_3} & 0 \\ 0 & 0 & 0 & 0 & 0 & 0 & 0 & 0 & \Gamma_{r_a,3} \end{bmatrix} \tag{7.22}$$

The energy of the system is

$$E = \epsilon_b + \epsilon_1 = \epsilon_a + \epsilon_3.$$

The Γ's are obtained from the Golden Rule:

$$\Gamma_{b,r_1} = \frac{2\,\pi}{\hbar}\, W_b^2\, \rho_b\,(\epsilon_b) \tag{7.23}$$

$$\Gamma_{r_b,1} = \frac{2\,\pi}{\hbar}\, W_1^2\, \rho_1\,(\epsilon_1) \tag{7.24}$$

$$\Gamma_{b,1} = \frac{2\,\pi}{\hbar}\, W_b^2\, \rho_b\,(E - E_1) + \frac{2\,\pi}{\hbar}\, W_1^2\, \rho_1\,(E - E_b) \tag{7.25}$$

$$\Gamma_{a,r_2} = \frac{2\,\pi}{\hbar}\, W_a^2\, \rho_a\,(\epsilon_a) \tag{7.26}$$

$$\Gamma_{a,2} = \frac{2\,\pi}{\hbar}\, W_a^2\, \rho_a\,(E - E_2) + \frac{2\,\pi}{\hbar}\, W_2^2\, \rho_2\,(E - E_a) \tag{7.27}$$

$$\Gamma_{a,3} = \frac{2\,\pi}{\hbar}\, W_a^2\, \rho_a\,(E - E_3)\,. + \frac{2\,\pi}{\hbar}\, W_3^2\, \rho_3\,(E - E_a) \tag{7.28}$$

$$\Gamma_{r_a,2} = \frac{2\,\pi}{\hbar}\, W_2^2\, \rho_2\,(\epsilon_2) \tag{7.29}$$

$$\Gamma_{a,r_3} = \frac{2\,\pi}{\hbar}\, W_a^2\, \rho_a\,(\epsilon_a) \tag{7.30}$$

$$\Gamma_{r_a,3} = \frac{2\,\pi}{\hbar}\, W_3^2\, \rho_3\,(\epsilon_3) \tag{7.31}$$

The coupling column vectors for the initial and final states are

$$\overline{V}^i = \begin{bmatrix} W_b & W_1 & 0 & 0 & 0 & 0 & 0 & 0 & 0 \end{bmatrix}^T$$

and

$$\overline{V}^f = \begin{bmatrix} 0 & 0 & 0 & 0 & 0 & 0 & 0 & W_a & W_3 \end{bmatrix}^T$$

Therefore the effective matrix element between the initial state and the final state is

$$U_{eff} = U_{fi} = \left(\overline{V}^f\right)^T \cdot \left[E - \overline{\overline{K}}\right]^{-1} \cdot \overline{V}^i.$$

7.6 Discussion

We have specified the expression for the effective coupling matrix element U_{eff}, which along with the model presented in the previous chapter gives a way to calculate all the device characteristics of interest to us. In the next chapter we embark on numerical evaluations of our model.

Chapter 8

Results from secular equations partitioning method

We previously calculated numerical figures such as current and load power with the Bloch equations model. It was recognized that the Bloch equations were inconsistent with thermodynamics and could not give sensible results for the off-resonance case. The brute-force numerical approach presents an alternative to the Bloch equations but using it to analyze complex problems is costly both in terms of development time and simulation time. However, the validity of the brute-force numerical approach seems good as the method gives results matching those from the secular equations partitioning method. In the previous two chapters we have been developing formulations for the device characteristics using the secular equations partitioning method, and in this chapter we apply numerical parameters to the formulations. The on-resonant current and power figures are comparable to those from the Bloch equations model, and we have also successfully analyzed the off-resonant case.

8.1 Numerical values

In the calculations described in this section, we take the hot-side temperature T_h to be 600 K, and the cold-side temperature T_c to be 300 K. The quantum well on the hot-side has energy levels separated by 100 meV. This energy separation, denoted by ΔE, was selected because it maximizes the load power given the temperatures. We have assumed that the quantum well on the cold-side has energy levels matched to those on the hot-side. The Fermi levels μ_a, μ_b, and μ_1 are set to ground, and assumed to be matched to the energy of levels a and 1 (also as a result of load power optimization). The tunneling matrix element V is defined in terms of the associated Rabi oscillation frequency

$$\Omega = \frac{V}{\hbar} = 2\pi \times 10^{12} \frac{\text{rad}}{\text{sec}} \tag{8.1}$$

We have assumed that the coupling between the levels of the hot-side quantum well and the first cold-side quantum well is twice the tunneling matrix element

$$U = 2V$$

This choice maximizes load power. For simplicity, we have taken all of the relaxation times for transitions from the one-electron states a, b, 1 and 3 to be matched to the coherent transitions

$$\Gamma_a = \Gamma_b = \Gamma_1 = \Gamma_3 = \Omega$$

Simulations indicate that the highest load power values are obtained when the decay rate of these important discrete levels to their respective reservoirs are matched to the coherent transition rates.

We model each reservoir as a continuum of levels with a uniform density of states independent of energy. A quantum well level is coupled to each level in a reservoir with a constant matrix element W. These coupling matrix elements are assumed to be a thousand times smaller than the tunneling coupling (couplings to a continuum involve small individual matrix elements; for given relaxation times our results are independent of the choice of these couplings as long as they are sufficiently small):

$$W_1 = W_2 = W_a = W_b = 10^{-3}\, \hbar\Omega$$

The density of states ρ for the reservoir is defined such that the Golden Rule is satisfied for the chosen decay rate Γ and matrix element W:

$$\rho = \frac{\hbar\Gamma}{2\pi|W|^2}$$

The density of states for reservoir R_2 is assumed to be the same as that of reservoir R_1: $\rho_2 = \rho_1$. The matrix element W_2 is such that the Golden Rule is satisfied:

$$W_2 = \sqrt{\Gamma_2 \cdot \frac{\hbar}{2\pi\rho_2}}$$

An individual device occupies a quantum dot, or a pixel, and the number of pixels that can be packed into a unit area determines the power and current density of an array of the device. In this calculation we have assumed that a single device occupies an area of 120 nm × 120 nm, or 6.9×10^9 devices/cm^2. Examples of quantum dot arrays with small dot sizes and small inter-dot spacings include a ZnS quantum dot array with dot diameter 2.66±0.22 nm and spacing 12 nm [14], and close packed quantum dots with tunable diameter 3-10 nm of various materials [15]. A dense array ($\sim 10^{11}$ dots/cm^2) of InAs quantum dots of size 12±1 nm in GaAs substrate have been fabricated and characterized [16]. InSb quantum dots in a GaSb matrix with lateral size ~10 nm and density $\sim 6 \times 10^{10}$ cm^{-2} have also been reported [17].

8.2 Level 2 loss

Loss from level 2 (the excited state of the cold-side quantum well near the gap) has a different effect on the system than the loss associated with the other levels. For example, transitions from reservoir R_1 to level 1 sustain the population of level 1, allowing the device to function hence such transitions are critical to the device operation. Similarly, the thermalization of level 3 to reservoir R_3 is required for current to be provided to the load. Loss in the case of level 2 simply drains electrons that otherwise might have delivered power to the load. In this case, loss from level 2 directly reduces efficiency and degrades device performance.

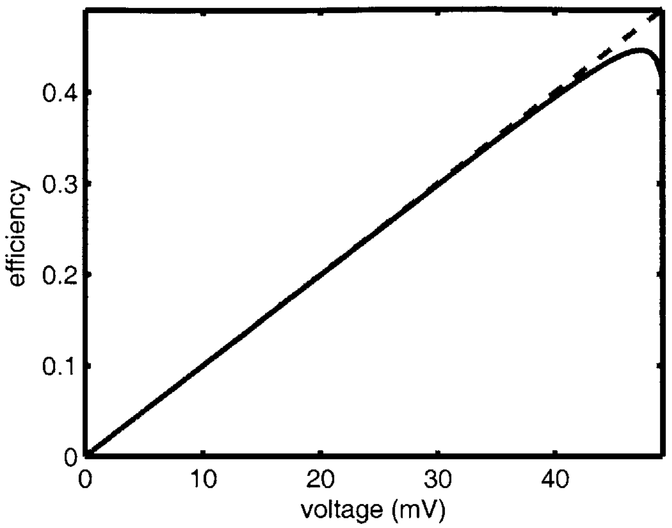

Figure 8-1: Efficiency as a function of voltage for case with zero level 2 loss. Each point on the curve corresponds to a different device with level 3 matched to level 2 at that particular operating voltage. The efficiency approaches the Carnot limit 0.5 as the voltage approaches 50 mV. The dashed line is the linear efficiency from the Bloch equation analysis

It is useful to consider device performance in the idealized limit when the loss from level 2 is set to zero. Although there are a variety of issues involved in the physics and modeling that are probably worthy of comment, we elect to dispense with them for the purposes of this discussion, and simply present the results for efficiency as a function of voltage in Figure 8-1. In this plot, we show results from calculations that correspond to a collection of different devices, each one designed so that level 3 is matched to level 2 at the operating voltage, and each run with an optimum electrical load. One can see that the efficiency is essentially

$$\eta = \frac{\mu_3 - \mu_1}{\Delta E} \tag{8.2}$$

most of the way to the Carnot limit, which is what we have obtained in the Bloch equations analysis. In essence, the promotion of the cold-side electron due to excitation transfer from the hot-side leads to an energy of $\epsilon_b - \epsilon_a$ that can be used to drive a load at voltages up to

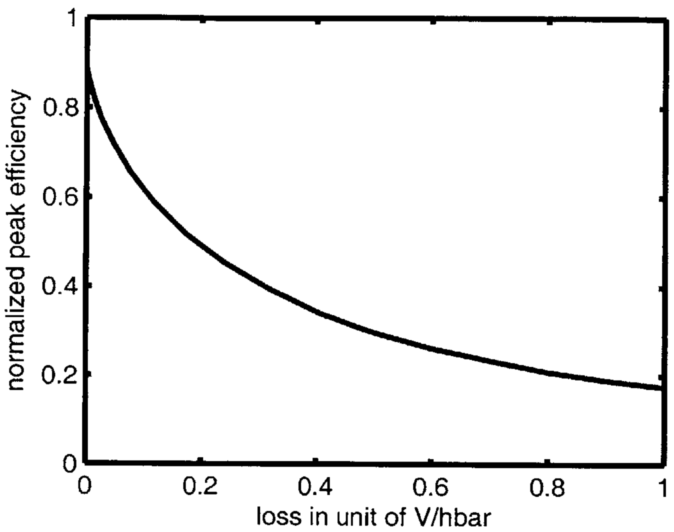

Figure 8-2: The maximum efficiency obtainable for each given level 2 loss. The efficiency shown is normalized to the Carnot limit. As the loss increases from 0 to $0.2\mathrm{V}/\hbar$, the peak efficiency drops from 0.9 of the Carnot limit to half of the Carnot limit.

$$V_L \leq \frac{\Delta E}{e}\left(\frac{T_h - T_c}{T_h}\right) \tag{8.3}$$

At voltages less than this maximum, we are not using the transferred energy efficiently, and hence the device efficiency is reduced proportionally. We are not able to maintain efficiency up to the Carnot limit since there is a spread in the distribution of electron energies transferred.

In Figure 8-2 we show the peak efficiency obtainable as a function of level 2 loss. One sees a rapid reduction in efficiency with increasing level 2 loss, such that the maximum device performance reaches half the Carnot limit approximately when

$$\Gamma_2 \ = \ 0.2\frac{V}{\hbar} \ = \ 0.2\,\Omega \qquad \text{(half Carnot limit)} \tag{8.4}$$

This places a premium in this type of scheme in working to preserve level 2 population as much as possible. In the calculations that follow, we have adopted a value of

$$\Gamma_2 = 0.1\frac{V}{\hbar} = 0.1\ \Omega \qquad \text{(simulations)} \tag{8.5}$$

which leads to a maximum efficiency of about 60% of the Carnot limit.

8.3 Results with moderate level 2 loss

In Figure 8-3, we show current as a function of voltage. Two plots, one for the on-resonance case (solid curve) and the other for the off-resonance case (dashed curve), are superimposed on the same graph. The on-resonance case again refers to the results for a set of devices, each one designed so that level 3 is matched to level 2 at the operating voltage. The off-resonance case is the characteristics for a particular device of which level 3 energy is equal to 70 meV when the voltage across the load is zero. When the voltage changes, level 3 energy changes along because level 3 is coupled to reservoir R_3 of which Fermi level μ_3 changes with the voltage, assuming reservoir R_1 is at ground. Therefore for the off-resonance case level 3 is only matched to level 2 at the voltage of 30 mV when the level 3 energy is raised from 70 meV to 100 meV. We see from Figure 8-3 that the on-resonance case short-circuit current is about 18 nA/pixel. With an assumed pixel area 120 nm×120 nm=1.44×10^{-10}cm^2, the short-circuit current density is estimated to be around 125 A/cm^2. The open-circuit voltage is approximately $\Delta E \times \text{(Carnot efficiency)}/e = 50$ mV as indicated by Eq. (8.3).

For the off-resonance case, levels 2 and 3 are matched when the voltage is equal to 30 mV, and the off-resonance curve coincides with the on-resonance curve at this voltage. Away from this voltage, the current becomes suppressed as the mismatch between levels 2 and 3 increases. The range of voltage where the off-resonance current is within a half of the on-resonance current is about ±10 mV, which indicates the flexibility in the operating voltage for a single device. Thinking of the levels 2 and 3 mismatch from another perspective, if we fix $\mu_3 - \mu_1 = 30$ meV and all other parameters while varying E_3, we obtain a line-shape (shown in Figure 8-4). It has

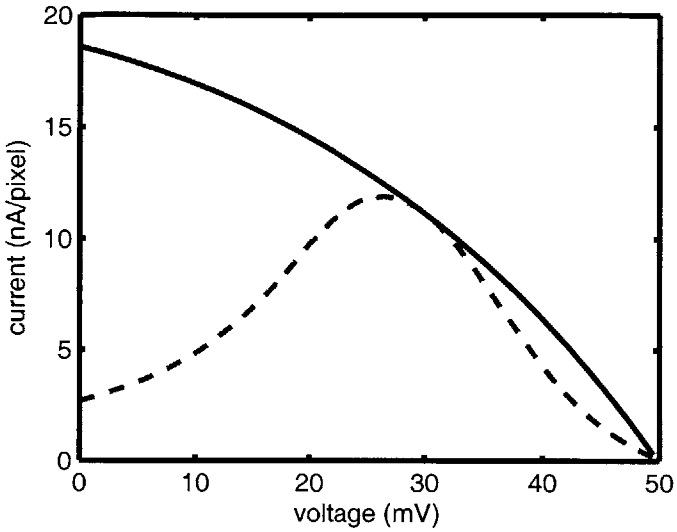

Figure 8-3: Current versus voltage characteristic for the on-resonance (solid curve) and off-resonance (dashed curve) cases. The on-resonance case refers to a set of devices, each of which has level 3 matched to level 2 at the particular voltage. The off-resonance case is the results for a device of which level 3 energy is equal to 70 meV when the voltage is zero.

a Lorentzian dependence with a FWHM of 13 meV, which is a consequence of the choice of τ in the design. This is relevant to the device tolerance on the level energies. If we instead vary E_2, we again find a Lorentzian line-shape (see Figure 8-5) but the width 11.6 meV is slightly smaller. This is due to the fact that changing level 2 makes not only the tunneling transition off-resonant, but it also changes the degree of resonance for the excitation transfer from the hot-side.

Figure 8-6 shows the power delivered from the hot-side as a function of voltage with the solid curve being the on-resonance case and the dashed curve being the off-resonance case. The maximum thermal power occurs at short-circuit and is equal to 2.12 nW/pixel or 14.7 W/cm^2 for an assumed pixel area of 120 nm×120 nm. This level of thermal power is comparable to the value 12.50 W/cm^2 of a micron-gap thermo-photovoltaic cell that has been reported in the literature [4].

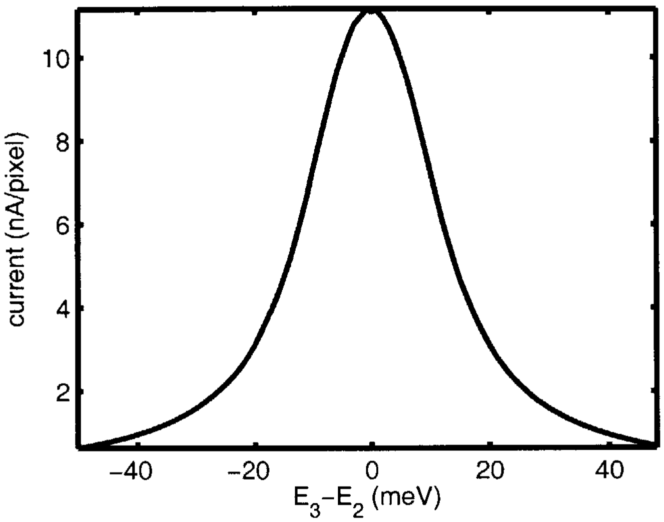

Figure 8-4: Line-shape for the current when level 3 energy is varied while fixing all other parameters. A Lorentzian dependence is observed and the FWHM is 13 meV.

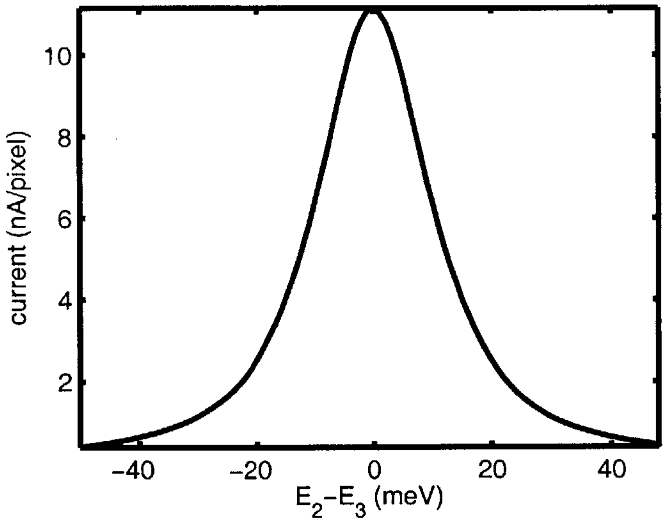

Figure 8-5: Line-shape for the current when level 2 energy is varied while fixing all other parameters. A Lorentzian dependence is observed and the FWHM is 11.6 meV.

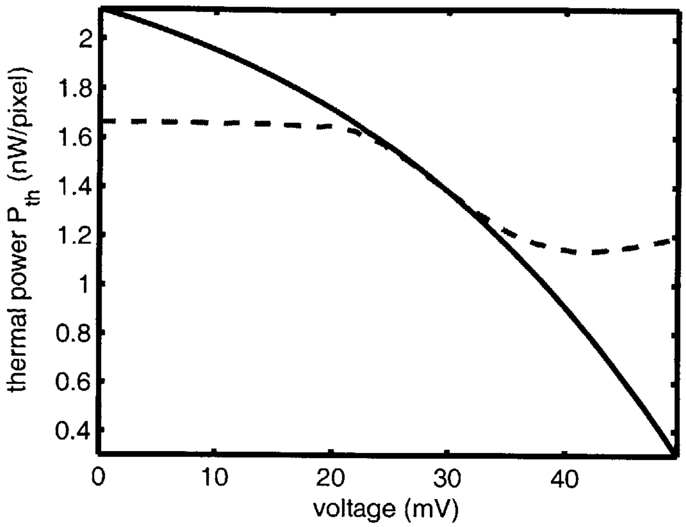

Figure 8-6: thermal power delivered from the hot-side as a function of voltage for the on-resonance (solid curve) and off-resonance (dashed curve) cases. The on-resonance case refers to a set of devices, each of which has level 3 matched to level 2 at the particular voltage. The off-resonance case is the results for a device of which level 3 energy is equal to 70 meV when the voltage is zero.

Figure 8-7 shows the power delivered to the load as a function of voltage. The solid curve is again the on-resonance case and the dashed curve is the off-resonance case. The load power reaches maximum 0.335 nW/pixel, or 2.33W/cm^2, at the voltage of 30 mV. From Figure 8-6 we see that the power delivered from the hot-side at this voltage is 1.38 nW/pixel or 9.58 W/cm^2 for the assumed pixel area, and hence the efficiency at this voltage is 2.33/9.58, or 24.3%, which is slightly lower than the maximum efficiency 28% achievable at the voltage of 40 mV. Recall that these power values are obtained under the assumption of 1.44×10^{-10} cm^2 pixel area, but in principle this number can be made smaller. For example, the active area of the design in Chapter 11 is only 6.53×10^{-13} cm^2. A smaller pixel area would lead to a larger power value.

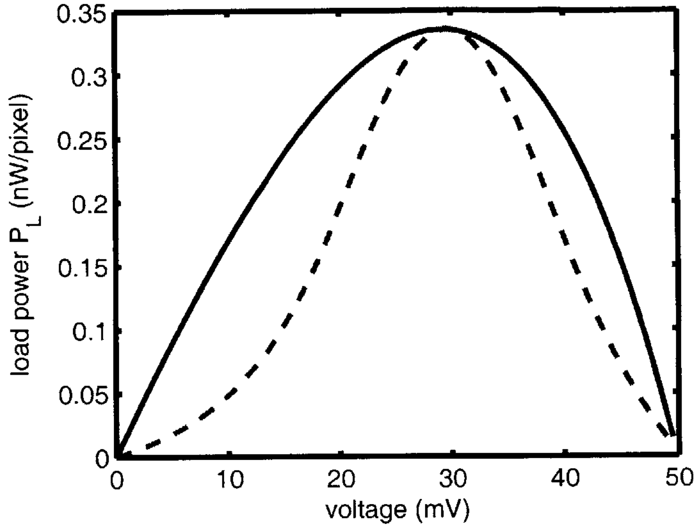

Figure 8-7: Load power as a function of voltage for the on-resonance (solid curve) and off-resonance (dashed curve) cases. The on-resonance case refers to a set of devices, each of which has level 3 matched to level 2 at the particular voltage. The off-resonance case is the results for a device of which level 3 energy is equal to 70 meV when the voltage is zero.

8.4 Optimization

We can optimize the load power by changing ΔE. The rest of the device parameters are assumed to be the same as in the last subsection (T_h = 600 K, T_c = 300 K, $V = \hbar\Omega = \Gamma$'s, $U = 2\hbar\Omega$, W's= $10^{-3}\hbar\Omega$). Figure 8-8 shows contours of equal load power as ΔE and the efficiency are varied (the efficiency is varied by changing the voltage). Next to each contour is a number indicating the value of load power in units of 0.1 nW/pixel. We see that the choice of $\Delta E = 100$ meV maximizes the load power when the matrix elements and relaxation times are fixed.

Our choice of U also maximizes the load power for fixed matrix element $V = \hbar\Omega$ and other device parameters (T_h = 600 K, T_c = 300 K, Γ's= $\hbar\Omega$, ΔE = 100 meV). The value of ΔE is 100 meV in accordance with the previous optimization. Figure 8-9 shows the contours of load power when matrix element U is varied and when the efficiency is changed by varying the voltage. Next to each contour is a number

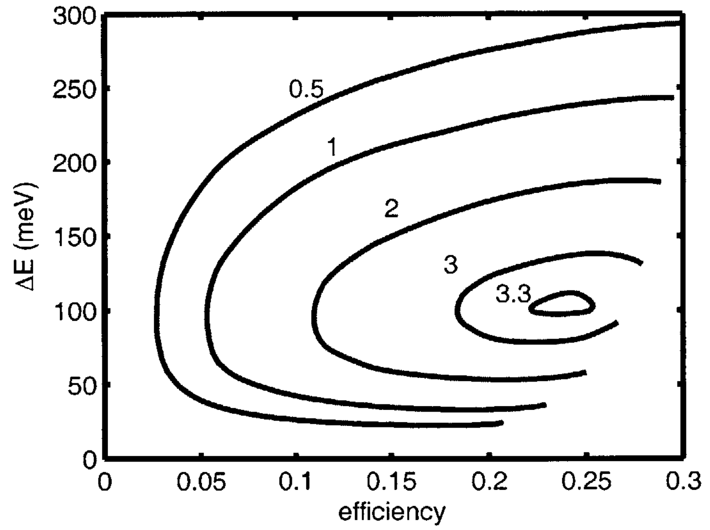

Figure 8-8: Optimization of load power by varying ΔE and the efficiency while fixing all other parameters. For a particular ΔE value, variation of the efficiency is achieved by increasing the voltage from 0V up until the maximum efficiency is reached. Contours of equal load power are shown in the graph. Next to each contour is a number indicating the value of load power in unit of 0.1 nW/pixel. It can be seen that load power is maximized at $\Delta E = 100$ meV and efficiency 24%.

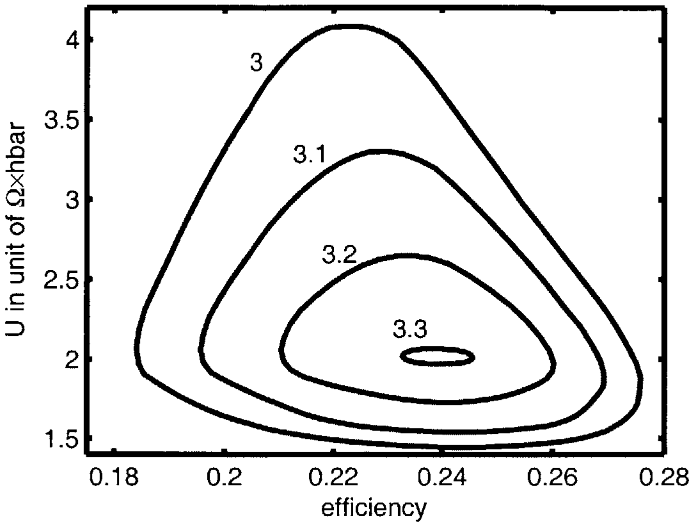

Figure 8-9: Optimization of load power by varying U and the efficiency while fixing all other parameters. For a particular U value, variation of the efficiency is achieved by changing the voltage. Contours of equal load power are shown in the graph. Next to each contour is a number indicating the value of load power in unit of 0.1 nW/pixel. It can be seen that load power is maximized at $U = 2\Omega \times \hbar$ and efficiency 24%.

indicating the value of load power in unit of 0.1 nW/pixel. The maximum power 3.35 W/cm^2 is obtained at $U = 2\Omega \cdot \hbar$ and the corresponding efficiency is 24.3%. It is observed that further increase in U decreases the power. An explanation is that when the Coulomb coupling is large, an electron promoted to level 2 is quickly de-excited to level 1 to transfer energy back to the hot-side, and there is not enough time for the electron to tunnel to level 3. On the other hand, when U is small, energy transfer across the vacuum gap becomes the bottleneck of the conversion process and the power drops with decreasing U.

8.5 Discussion

We have presented a model for analyzing the characteristics of the new thermal to electric conversion scheme. Example calculations have been done which indicated the potential competitiveness of the scheme. We would like to move towards calculations for more specific material and dimension designs of the device, which are developed in the following chapters.

Chapter 9

Electrostatic potentials near a gap

This chapter is reproduced from Prof. Peter Hagelstein's notes with the same title. The electronic file for the original notes has been lost. Also, there are some typos and missing definitions in the document. Therefore, the corrected version is included here as a chapter for completeness and easier reference.

Up until this point we have been applying assumed parameters into our model to obtain numerical results. A key parameter is the Coulomb coupling matrix element U. We would like to calculate this matrix element given the gap thickness and the materials on both sides of the gap. Therefore, we need to compute the Coulomb interaction energy between electrons residing in the hot-side and the cold-side materials.

We first consider solving the electric potential for a two-media problem using the method of image charge (see for example [18]). The image charge method has an advantage of easy generalizability into the three-media problem via the use of reflection and transmission coefficients.

9.1 The two-region problem

We begin with a consideration of the simple two region problem, for which a simple exact analytic solution is available. The situation is illustrated in Figure 9-1.

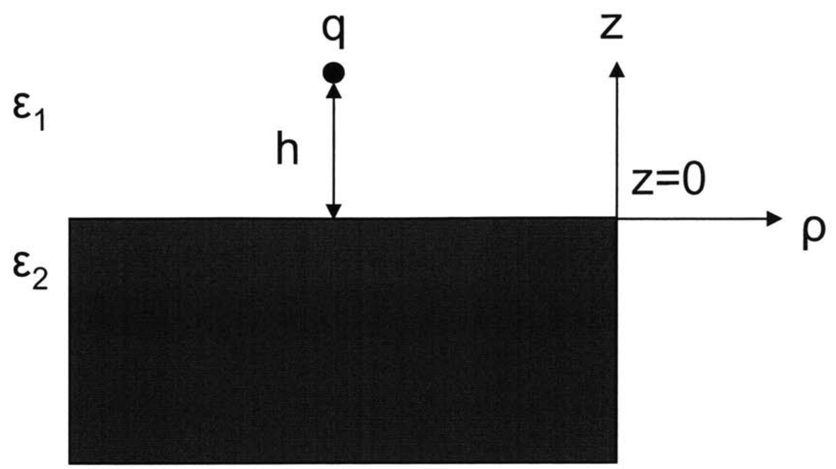

Figure 9-1: Charge q above a boundary between two dielectric regions.

We are interested in developing solutions to the Poisson equation

$$-\nabla \cdot (\epsilon \nabla \Phi) \;=\; \rho$$

for this arrangement of charge and dielectric constants.

It is known that a solution can be constructed in the form

$$\Phi(\mathbf{r}) \;=\; \begin{cases} \frac{q}{4\pi\epsilon_1 \sqrt{(z-h)^2+\rho^2}} + \frac{A}{\sqrt{(z+h)^2+\rho^2}} & z \geq 0 \\ \frac{B}{\sqrt{(z-h)^2+\rho^2}} & z < 0 \end{cases}$$

where A and B are constants to be determined by matching the boundary conditions.

The boundary conditions at the boundary between the dielectrics are given in terms of the electric fields in the two regions

$$\hat{\mathbf{n}} \cdot (\epsilon_1 \mathbf{E_1} \;-\; \epsilon_2 \mathbf{E_2}) \;=\; 0$$

$$\hat{\mathbf{n}} \times (\mathbf{E_1} \;-\; \mathbf{E_2}) \;=\; 0$$

where the field is determined from the potential from

$$\mathbf{E} = -\nabla\Phi$$

in the two regions.

The second of these conditions can be met by making the potential continuous across the boundary

$$\Phi_1(\rho, 0) = \Phi_2(\rho, 0)$$

The first of these requires that the derivatives in z satisfy

$$\epsilon_1 \left[\frac{\partial\Phi_1(\rho, z)}{\partial}\right]_{z=0} = \epsilon_2 \left[\frac{\partial\Phi_2(\rho, z)}{\partial z}\right]_{z=0}$$

Matching the boundary conditions on our solutions in the two regions leads to the two constraints

$$\frac{q}{4\pi\epsilon_1} + A = B \tag{9.1}$$

$$\epsilon_1 \left[\frac{q}{4\pi\epsilon_1} - A\right] = \epsilon_2 B \tag{9.2}$$

This leads to explicit expressions for A and B

$$A = \frac{q}{4\pi\epsilon_1}\left(\frac{\epsilon_1 - \epsilon_2}{\epsilon_1 + \epsilon_2}\right)$$

$$B = \frac{q}{2\pi(\epsilon_1 + \epsilon_2)}$$

The solution that results is

$$\Phi(\mathbf{r}) = \begin{cases} \frac{q}{4\pi\epsilon_1\sqrt{(z-h)^2+\rho^2}} + \frac{q}{4\pi\epsilon_1\sqrt{(z+h)^2+\rho^2}}\left(\frac{\epsilon_1 - \epsilon_2}{\epsilon_1 + \epsilon_2}\right) & z \geq 0 \\ \frac{q}{2\pi(\epsilon_1 + \epsilon_2)\sqrt{(z-h)^2+\rho^2}} & \end{cases}$$

9.2 Thinking about the problem in terms of reflection and transmission

We would like to extend the two-region problem to a more complicated three-region problem. To facilitate this generalization, it is useful to re-examine our solutions to the two-region problem. Note that the form of the solution for the two-region problem is similar in form to solutions to wave equations. In such problems, an incident wave encounters a discontinuity, and one finds reflected and transmitted waves. The electrostatic problem under discussion of course has no waves; however, we can see a similar form in the solution that we constructed. The electrostatic field of the charge encounters a discontinuity in the dielectric, which gives rise to an image charge field in the upper sector (which is a reflection of sorts), and a field that penetrates into the region with a different dielectric region. We might write the solution in terms of a reflection and transmission coefficient

$$\Phi(\mathbf{r}) = \begin{cases} \frac{q}{4\pi\epsilon_1\sqrt{(z-h)^2+\rho^2}} + r\frac{q}{4\pi\epsilon_1\sqrt{(z+h)^2+\rho^2}} & z \geq 0 \\ t\frac{q}{4\pi\epsilon_2\sqrt{(z-h)^2+\rho^2}} & z < 0 \end{cases}$$

where

$$r = \frac{\epsilon_1 - \epsilon_2}{\epsilon_1 + \epsilon_2}$$

$$t = \frac{2\epsilon_2}{\epsilon_1 + \epsilon_2}$$

We note the similarity between these coefficients, and coefficients that one finds for wave-interface problems.

If we think of the potential solution in this way, then it provides some intuition as to how to go about constructing a potential solution for the three-dielectric problem considered in the next section.

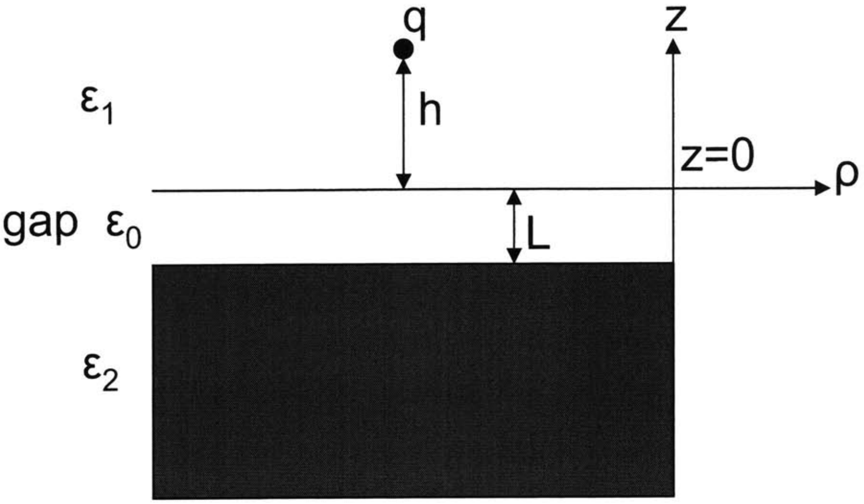

Figure 9-2: Three-region electrostatic problem with a charge above a gap between two dielectric regions

9.3 The three region problem

We now consider the development of solutions to the Poisson equation in the case of a charge situated over a gap between two dielectric regions as illustrated in Figure 9-2.

Based on the discussion given above for the two-region problem, we can extend the basic approach to develop solutions for the three-region problem. The idea is to imagine an image charge calculation in which the amplitudes of the image charges are determined from combinations of reflection and transmission coefficients. For example, we develop a solution from an image charge expansion that can be written formally as

$$\Phi = \Phi_0 + \Phi_1 + \Phi_2 + \cdots$$

In which Φ_0 is the solution in the case that no boundary interactions are included.

$$\Phi_0 = \begin{cases} \frac{q}{4\pi\epsilon_1\sqrt{(z-h)^2+\rho^2}} & z \geq 0 \\ 0 & -L \leq z < 0 \\ 0 & z < -L \end{cases}$$

The next term in the expansion includes terms that involve a reflection or transmission at a single boundary

$$\Phi_1 = \begin{cases} r_{101}\frac{q}{4\pi\epsilon_1\sqrt{(z+h)^2+\rho^2}} & z > 0 \\ t_{01}\frac{q}{4\pi\epsilon_0\sqrt{(z-h)^2+\rho^2}} & -L \leq z < 0 \\ 0 & z < -L \end{cases}$$

Based on the discussion above, we may write

$$r_{101} = \frac{\epsilon_1 - \epsilon_0}{\epsilon_1 + \epsilon_0}$$

$$t_{01} = \frac{2\epsilon_0}{\epsilon_1 + \epsilon_0}$$

The notation for transmission t_{01} is that the solution begins in region 1 and ends up in region 0. The notation for the reflection r_{101} is that the solution begins in region 1, encounters a boundary with region 0, and then reflects back into region 1.

The next term in the expansion involves terms with two boundary interactions. We have

$$\Phi_2 = \begin{cases} 0 & z \geq 0 \\ r_{020}t_{01}\frac{q}{4\pi\epsilon_0\sqrt{(z+h+2L)^2+\rho^2}} & -L \leq z < 0 \\ t_{20}t_{01}\frac{q}{4\pi\epsilon_2\sqrt{(z-h)^2+\rho^2}} & z < -L \end{cases}$$

The associated reflection and transmission coefficients are

$$r_{020} = \frac{\epsilon_0 - \epsilon_2}{\epsilon_0 + \epsilon_2}$$

$$t_{20} = \frac{2\epsilon_2}{\epsilon_0 + \epsilon_2}$$

In general, we will have

$$r_{iji} = \frac{\epsilon_i - \epsilon_j}{\epsilon_i + \epsilon_j}$$

The next term in the expansion involving three boundary interactions is

$$\Phi_3 = \begin{cases} t_{10} r_{020} t_{01} \frac{q}{4\pi\epsilon_1 \sqrt{(z+h+2L)^2+\rho^2}} & z \geq 0 \\ r_{010} r_{020} t_{01} \frac{q}{4\pi\epsilon_0 \sqrt{(z-h-2L)^2+\rho^2}} & -L \leq z < 0 \\ 0 & z < -L \end{cases}$$

We can continue to develop such solutions at will. The next one can be written as

$$\Phi_4 = \begin{cases} 0 & z \geq 0 \\ r_{020} r_{010} r_{020} t_{01} \frac{q}{4\pi\epsilon_0 \sqrt{(z+h+4L)^2+\rho^2}} & -L \leq z < 0 \\ t_{20} r_{010} r_{020} t_{01} \frac{q}{4\pi\epsilon_2 \sqrt{(z-h-2L)^2+\rho^2}} & z < -L \end{cases}$$

9.3.1 The solution below the gap

From the discussion given above, we may develop a solution for the region below the gap with dielectric constant ϵ_2. We may write

$$\Phi^{(2)}(\mathbf{r}) = t_{20} t_{01} \frac{q}{4\pi\epsilon_2 \sqrt{(z-h)^2+\rho^2}} + t_{20} r_{010} r_{020} t_{01} \frac{q}{4\pi\epsilon_2 \sqrt{(z-h-2L)^2+\rho^2}} + \cdots$$

This can be developed somewhat more compactly in series notation. We have

$$\Phi^{(2)}(\mathbf{r}) = t_{20} t_{01} \sum_n \left[r_{010} r_{020}\right]^n \frac{q}{4\pi\epsilon_2 \sqrt{(z-h-2nL)^2+\rho^2}}$$

We recall that

$$r_{010}r_{020} = \left(\frac{\epsilon_0 - \epsilon_1}{\epsilon_0 + \epsilon_1}\right)\left(\frac{\epsilon_0 - \epsilon_2}{\epsilon_0 + \epsilon_2}\right)$$

$$t_{20}t_{01} = \frac{4\epsilon_0\epsilon_2}{(\epsilon_0 + \epsilon_1)(\epsilon_0 + \epsilon_2)}$$

The solution for $z < -L$ is then

$$\Phi^{(2)}(\mathbf{r}) = \frac{4\epsilon_0\epsilon_2}{(\epsilon_0 + \epsilon_1)(\epsilon_0 + \epsilon_2)}\sum_{n=0}^{\infty}\left(\frac{\epsilon_0 - \epsilon_1}{\epsilon_0 + \epsilon_1}\right)^n\left(\frac{\epsilon_0 - \epsilon_2}{\epsilon_0 + \epsilon_2}\right)^n\frac{q}{4\pi\epsilon_2\sqrt{(z-h-2nL)^2+\rho^2}}$$

If we have another charge q situated at $z < -L$, then the Coulombic interaction energy between the charge in medium 1 and the charge in medium 2 is

$$U(\mathbf{r}) = \frac{4\epsilon_0\epsilon_2}{(\epsilon_0 + \epsilon_1)(\epsilon_0 + \epsilon_2)}\sum_{n=0}^{\infty}\left(\frac{\epsilon_0 - \epsilon_1}{\epsilon_0 + \epsilon_1}\right)^n\left(\frac{\epsilon_0 - \epsilon_2}{\epsilon_0 + \epsilon_2}\right)^n\frac{q^2}{4\pi\epsilon_2\sqrt{(z-h-2nL)^2+\rho^2}} \tag{9.3}$$

9.3.2 The solution above the gap

We can similarly develop a solution in the region above the gap for $z \geq 0$. The solution in this region is

$$\Phi^{(1)}(\mathbf{r}) = \frac{q}{4\pi\epsilon_1\sqrt{(z-h)^2+\rho^2}} + r_{101}\frac{q}{\sqrt{(z+h)^2+\rho^2}}$$

$$+ t_{10}r_{020}t_{01}\frac{q}{4\pi\epsilon_1\sqrt{(z+h+2L)^2+\rho^2}} + t_{10}r_{020}r_{010}r_{020}t_{01}\frac{q}{4\pi\epsilon_1\sqrt{(z+h+4L)^2+\rho^2}} + \cdots$$

This can be written more compactly as

$$\Phi^{(1)}(\mathbf{r}) = \frac{q}{4\pi\epsilon_1\sqrt{(z-h)^2+\rho^2}} + r_{101}\frac{q}{4\pi\epsilon_1\sqrt{(z+h)^2+\rho^2}}$$

$$+ \sum t_{01} \left[r_{020} r_{010}\right]^{n-1} r_{020} t_{01} \frac{q}{4\pi\epsilon_1 \sqrt{(z+h+2nL)^2+\rho^2}} + \cdots$$

Substituting in for the various reflection and transmission coefficients leads to

$$\Phi^{(1)}(\mathbf{r}) = \frac{q}{4\pi\epsilon_1 \sqrt{(z-h)^2+\rho^2}} + \left(\frac{\epsilon_1 - \epsilon_0}{\epsilon_1 + \epsilon_0}\right) \frac{q}{4\pi\epsilon_1 \sqrt{(z+h)^2+\rho^2}}$$

$$+ \frac{4\epsilon_0\epsilon_1}{(\epsilon_0 + \epsilon_1)(\epsilon_0+\epsilon_1)} \sum_{n=1}^{\infty} \left(\frac{\epsilon_0 - \epsilon_1}{\epsilon_0 + \epsilon_1}\right)^{n-1} \left(\frac{\epsilon_0 - \epsilon_2}{\epsilon_0 + \epsilon_2}\right)^{n} \frac{q}{4\pi\epsilon_1 \sqrt{(z+h+2nL)^2+\rho^2}} + \cdots$$

9.3.3 The solution within the gap

Finally, we may use the results above to develop solutions within the gap region. We may write

$$\Phi^{(0)} = t_{01} \frac{q}{4\pi\epsilon_0 \sqrt{(z-h)^2+\rho^2}} + r_{020} t_{01} \frac{q}{4\pi\epsilon_0 \sqrt{(z+h+2L)^2+\rho^2}}$$

$$+ r_{010} r_{020} t_{01} \frac{q}{4\pi\epsilon_0 \sqrt{(z-h-2L)^2+\rho^2}} + r_{020} r_{010} r_{020} t_{01} \frac{q}{4\pi\epsilon_0 \sqrt{(z+h+4L)^2+\rho^2}} + \cdots$$

we may write this more compactly as

$$\Phi^{(0)} = \sum_{n=0}^{\infty} \left[r_{010} r_{020}\right]^n t_{01} \frac{q}{4\pi\epsilon_0 \sqrt{\left[z-h-2nL\right]^2+\rho^2}}$$

$$+ \sum_{n=0}^{\infty} \left[r_{010} r_{020}\right]^n r_{020} t_{01} \frac{q}{4\pi\epsilon_0 \sqrt{\left[z+h+2(n+1)L\right]^2+\rho^2}}$$

If we substitute in for the various reflection and transmission coefficients, we obtain

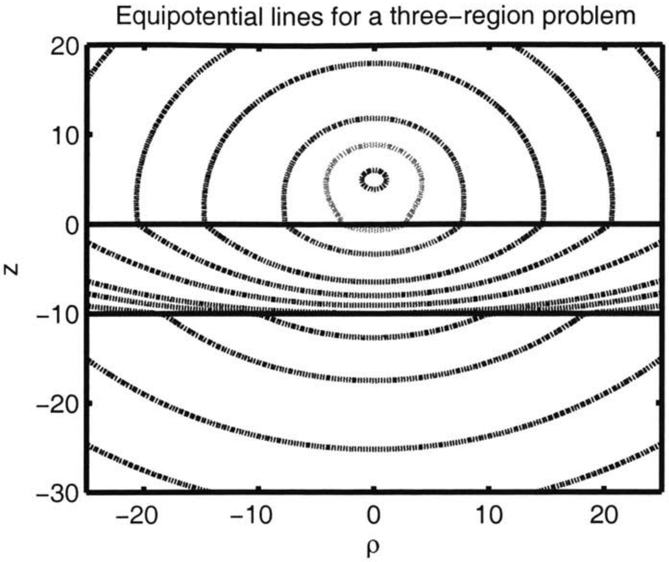

Figure 9-3: The dotted lines are the equipotential lines for an example three-region problem with $q/4\pi$ taken to be 1 and $\epsilon_0 = 1$, $\epsilon_1 = \epsilon_2 = 10$, $h = 5$, and $L = 10$.

$$\Phi^{(0)} = \left(\frac{2\epsilon_0}{\epsilon_1 + \epsilon_0}\right) \sum_{n=0}^{\infty} \left(\frac{\epsilon_0 - \epsilon_1}{\epsilon_0 + \epsilon_1}\right)^n \left(\frac{\epsilon_0 - \epsilon_2}{\epsilon_0 + \epsilon_2}\right)^n \frac{q}{4\pi\epsilon_0\sqrt{(z-h-2nL)^2+\rho^2}}$$

$$+ \left(\frac{2\epsilon_0}{\epsilon_1 + \epsilon_0}\right) \sum_{n=0}^{\infty} \left(\frac{\epsilon_0 - \epsilon_1}{\epsilon_0 + \epsilon_1}\right)^n \left(\frac{\epsilon_0 - \epsilon_2}{\epsilon_0 + \epsilon_2}\right)^{(n+1)} \frac{q}{4\pi\epsilon_0\sqrt{\left[z+h+2(n+1)L\right]^2+\rho^2}}$$

As a demonstration, in Figure 9-3 we compute the field solutions and plot the equipotential lines for a three-region problem.

9.4 Hamiltonian for dipole-dipole interaction across a gap

We are interested in the development of a Hamiltonian for two dipoles that are separated by a gap. To develop an appropriate expression, we begin with the interaction energy between two charges on either side of the gap

$$U_{ij} = \frac{4\epsilon_0\epsilon_2}{(\epsilon_0+\epsilon_1)(\epsilon_0+\epsilon_2)} \sum_{n=0}^{\infty} \left(\frac{\epsilon_0-\epsilon_1}{\epsilon_0+\epsilon_1}\right)^n \left(\frac{\epsilon_0-\epsilon_2}{\epsilon_0+\epsilon_2}\right)^n \tag{9.4}$$

$$\times \frac{q_i q_j}{4\pi\epsilon_2\sqrt{(z_i-z_j+2nL)^2+(x_i-x_j)^2+(y_i-y_j)^2}}$$

where we assume that the charges are located such that $z_i > z_j$.

The dipole-dipole Hamiltonian is obtained through a process of linearization. For example, supposed that the charge associated with each radiator is localized in the vicinity of some center position, so that

$$x_i = X_i + \delta x_i$$

$$y_i = Y_i + \delta y_i$$

$$z_i = Z_i + \delta z_i$$

$$x_j = X_j + \delta x_j$$

$$y_j = Y_j + \delta y_j$$

$$z_j = Z_j + \delta z_j$$

We consider the X, Y, and Z variables to define center of mass positions of the radiators, and the δx, δy, and δz coordinates to keep track of the location of the charge relative to the center of mass coordinates. In this case the static interaction becomes

$$U_{ij} \;=\; \frac{4\epsilon_0\epsilon_2}{(\epsilon_0+\epsilon_2)}\sum_{n=0}^{\infty}\left(\frac{\epsilon_0-\epsilon_1}{\epsilon_0+\epsilon_1}\right)^n\left(\frac{\epsilon_0-\epsilon_2}{\epsilon_0+\epsilon_2}\right)^n$$

$$\times\frac{q_iq_j}{4\pi\epsilon_2\sqrt{(Z_i-Z_j+\delta z_i-\delta z_j+2nL)^2+(X_i-X_j+\delta x_i-\delta x_j)^2+(Y_i-Y_j+\delta y_i-\delta y_j)^2}}$$

The next step is to linearize this expression. For this purpose, it is convenient to introdue new quantities in order to simplify the notations somewhat. We define the difference vector

$$\Delta\mathbf{R}_{ijn} \;=\; \hat{\mathbf{i}}_x(X_i-X_j)+\hat{\mathbf{i}}_y(Y_i-Y_j)+\hat{\mathbf{i}}_z(Z_i-Z_j+2nL)$$

We also define the deviation vectors

$$\mathbf{r}_i \;=\; \hat{\mathbf{i}}_x\delta x_i \;+\; \hat{\mathbf{i}}_y\delta y_i \;+\; \hat{\mathbf{i}}_z\delta z_i$$

$$\mathbf{r}_j \;=\; \hat{\mathbf{i}}_x\delta x_j \;+\; \hat{\mathbf{i}}_y\delta y_j \;+\; \hat{\mathbf{i}}_z\delta z_j$$

With these definitions, we may rewrite the interaction energy as

$$U_{ij} \;=\; \frac{4\epsilon_0\epsilon_2}{(\epsilon_0+\epsilon_1)(\epsilon_0+\epsilon_2)}\sum_{n=0}^{\infty}\left(\frac{\epsilon_0-\epsilon_1}{\epsilon_0+\epsilon_1}\right)^n\frac{q_iq_j}{4\pi\epsilon_2|\Delta\mathbf{R}_{ijn}\;+\;(\mathbf{r}_i-\mathbf{r}_j)|}$$

We note that

$$\frac{1}{|\Delta\mathbf{R}_{ijn}\;+\;(\mathbf{r}_i-\mathbf{r}_j)|} \;=\; \frac{1}{\sqrt{|\Delta\mathbf{R}_{ijn}|^2\;+\;2\Delta\mathbf{R}_{ijn}\cdot(\mathbf{r}_i-\mathbf{r}_j)+|\mathbf{r}_i-\mathbf{r}_j|^2}}$$

This can also be written as

$$\frac{1}{|\Delta\mathbf{R}_{ijn}\;+\;(\mathbf{r}_i-\mathbf{r}_j)|} \;=\; \frac{1}{|\Delta\mathbf{R}_{ijn}|}\frac{1}{\sqrt{1+\frac{2\Delta\mathbf{R}_{ijn}\cdot(\mathbf{r}_i-\mathbf{r}_j)}{|\Delta\mathbf{R}_{ijn}|^2}\;+\;\frac{|\mathbf{r}_i\;-\;\mathbf{r}_j|}{|\Delta\mathbf{R}_{ijn}|^2}}}$$

We recall that the Taylor expansion of $\sqrt{1+x}$ is

$$\frac{1}{\sqrt{1+x}} = 1 - \frac{1}{2}x + \frac{3}{8}x^2 - \frac{5}{16}x^3 + \cdots$$

Consequently, we may expand to obtain

$$\frac{1}{|\Delta\mathbf{R}_{ijn} + (\mathbf{r}_i - \mathbf{r}_j)|} =$$

$$\frac{1}{|\Delta\mathbf{R}_{ijn}|}\left[1 - \frac{\Delta\mathbf{R}_{ijn}\cdot(\mathbf{r}_i - \mathbf{r}_j)}{|\Delta\mathbf{R}_{ijn}|^2} - \frac{1}{2}\frac{|\mathbf{r}_i - \mathbf{r}_j}{|\Delta\mathbf{R}_{ijn}|^2} + \frac{3}{2}\frac{[\Delta\mathbf{R}_{ijn}\cdot(\mathbf{r}_i - \mathbf{r}_j)]^2}{|\Delta\mathbf{R}_{ijn}|^4} + \cdots\right]$$

Here we have kept terms up to second order in $\mathbf{r}_i - \mathbf{r}_j$. This can be recast as

$$\frac{1}{|\mathbf{R}_{ijn} + (\mathbf{r}_i - \mathbf{r}_j)|} =$$

$$\frac{1}{|\Delta\mathbf{R}_{ijn}|} - \frac{\Delta\mathbf{R}_{ijn}\cdot(\mathbf{r}_i - \mathbf{r}_j)}{|\Delta\mathbf{R}_{ijn}|^3} - \frac{1}{2}\frac{|\mathbf{r}_i - \mathbf{r}_j|^2}{|\Delta\mathbf{R}_{ijn}|^3} + \frac{3}{2}\frac{[\Delta\mathbf{R}_{ijn}\cdot(\mathbf{r} - \mathbf{r}_j)]^2}{|\Delta\mathbf{R}_{ijn}|^5} + \cdots$$

From this we are able to extract the dipole-dipole interaction. The terms in this series that are responsible are the ones involving a single occurrence of $\mathbf{r}_i$ and a single occurrence of $\mathbf{r}_j$. These terms are

$$\cdots + \frac{\mathbf{r}_i\cdot\mathbf{r}_j}{|\Delta\mathbf{R}_{ijn}|^3} - \frac{3(\mathbf{r}_i\cdot\Delta\mathbf{R}_{ijn})(\Delta\mathbf{R}_{ijn}\cdot\mathbf{r}_j)}{|\Delta\mathbf{R}_{ijn}|^5} + \cdots$$

Using this result, we may obtain the dipole-dipole Hamiltonian $\hat{H}_{int}$

$$\hat{H}_{int} = \frac{4\epsilon_0\epsilon_2}{(\epsilon_0 + \epsilon_1)(\epsilon_0 + \epsilon_2)}$$

$$\times \sum_{n=0}^{\infty} \left(\frac{\epsilon_0 - \epsilon_1}{\epsilon_0 + \epsilon_1}\right)^n \left(\frac{\epsilon_0 - \epsilon_2}{\epsilon_0 + \epsilon_2}\right)^n \frac{1}{4\pi\epsilon_2} \left[\frac{\mathbf{d}_i \cdot \mathbf{d}_j}{|\Delta\mathbf{R}_{ijn}|^3} - \frac{3(\mathbf{d}_i \cdot \Delta\mathbf{R}_{ijn})(\Delta\mathbf{R}_{ijn} \cdot \mathbf{d}_j)}{|\Delta\mathbf{R}_{ijn}|^5}\right]$$

where $\mathbf{d}_k$ is the dipole operator

$$\mathbf{d}_k = q_k \mathbf{r}_k$$

This can also be written as

$$\hat{H}_{int} = \frac{4\epsilon_0\epsilon_2}{(\epsilon_0 + \epsilon_1)(\epsilon_0 + \epsilon_2)}$$

$$\times \sum_{n=0}^{\infty} \left(\frac{\epsilon_0 - \epsilon_1}{\epsilon_0 + \epsilon_1}\right)^n \left(\frac{\epsilon_0 - \epsilon_2}{\epsilon_0 + \epsilon_2}\right)^n \frac{1}{4\pi\epsilon_2|\Delta\mathbf{R}_{ijn}|^3} \left[\mathbf{d}_i \cdot \mathbf{d}_j - 3(\mathbf{d}_i \cdot \hat{\mathbf{i}}_{ijn})(\hat{\mathbf{i}}_{ijn} \cdot \mathbf{d}_j)\right]$$

where

$$\hat{\mathbf{i}}_{ijn} = \frac{\Delta\mathbf{R}_{ijn}}{|\Delta\mathbf{R}_{ijn}|}$$

9.5 Discussion

We have derived the classical expression for the interaction energy between a pair of electrons located in two media separated by a gap. We can apply this result to obtain the Coulomb coupling matrix element U by taking the expectation of the interaction energy over the product electron states of the hot-side and the cold-side. Namely, $U = \langle b, 1|U_{ij}|a, 2\rangle$ where states a, b, 1, and 2 are as defined in Chapter 7 and U_{ij} is as in Eq. 9.4. In the next chapter we then aim to calculate the wavefunctions of the electrons for a given design of the quantum wells. In this chapter we have also derived a formula for the dipole approximation of the interaction energy, which will be useful later on for analyzing the case where the hot-side material consists of a continuum of small absorbing dipoles.

Chapter 10

Numerical modeling of quantum dots

In our quantum-coupled conversion scheme we have assumed the existence of quantum wells containing one or two discrete levels. To implement such wells one can embed a semiconductor material with a lower conduction bandedge in a matrix of another semiconductor material with a higher conduction bandedge, forming a quantum dot. Given suitable conduction bandedge difference between the two materials, we can expect one or two discrete electron states to reside in the dot if the dot size is small enough. In this chapter we briefly explain the numerical method used to compute the energies and wavefunctions of the dot states.

10.1 Simple potential

Let us consider a quantum well sitting against a vacuum gap with conduction bandedge profile as depicted in Figure 10-1. Material 2 has an elevated conduction bandedge relative to that of material 1. The potential goes to infinity at the boundary with the gap as the electron should not escape into the vacuum gap. A bound-state of the quantum well satisfies the time-independent Schrodinger's equation:

$$-\frac{\hbar^2}{2}\frac{d}{dx}\left(\frac{1}{m(x)}\cdot\frac{d\psi(x)}{dx}\right)+V(x)\cdot\psi(x) \;=\; E\cdot\psi(x) \tag{10.1}$$

where $V(x)$ is the potential profile and $m(x)$ is the space-dependent effective mass of the electron. Region 1 consists of a homogeneous material with electron mass denoted m_1. Region 2 consists of another homogeneous material with electron mass denoted m_2. Within region 1 or region 2, the mass is constant and we can write the Schrödinger's equation as

$$-\frac{\hbar^2}{2m}\frac{d^2\psi(x)}{dx^2}+V(x)\cdot\psi(x) \;=\; E\cdot\psi(x)$$

From Eq. 10.1, the following boundary conditions need to hold at the boundary between the two materials ($x = d$) to avoid impulses in the wavefunction:

$$\psi(d^-) \;=\; \psi(d^+) \tag{10.2}$$

$$\left.\frac{1}{m_1}\frac{d\psi(x)}{dx}\right|_{x=d^-} = \left.\frac{1}{m_2}\frac{d\psi(x)}{dx}\right|_{x=d^+} \tag{10.3}$$

10.2 Numerical scheme

We can solve the Schrödinger's equation numerically via finite-difference schemes. Lets suppose we put $N_1 - 1$ grids in region 1 and $N_2 - 1$ grids in region 2. See Figure 10-2. We can use a simple three-point differencing scheme for the second derivative (with O(h^2) error where h is the spacing between adjacent grids on the x axis), resulting in the following equation:

$$-\frac{\hbar^2}{2m}\left[\frac{\psi_{j-1}-2\psi_j+\psi_{j+1}}{h^2}\right] \;+\; V(x_j)\cdot\psi_j \;=\; E\cdot\psi_j$$

where m is equal to m_1 in region 1 and equal to m_2 in region 2. The above equation applies to grids of which neighboring grids are well-defined without any problem, but for grids near the boundaries we need to take extra care. What are the values of the

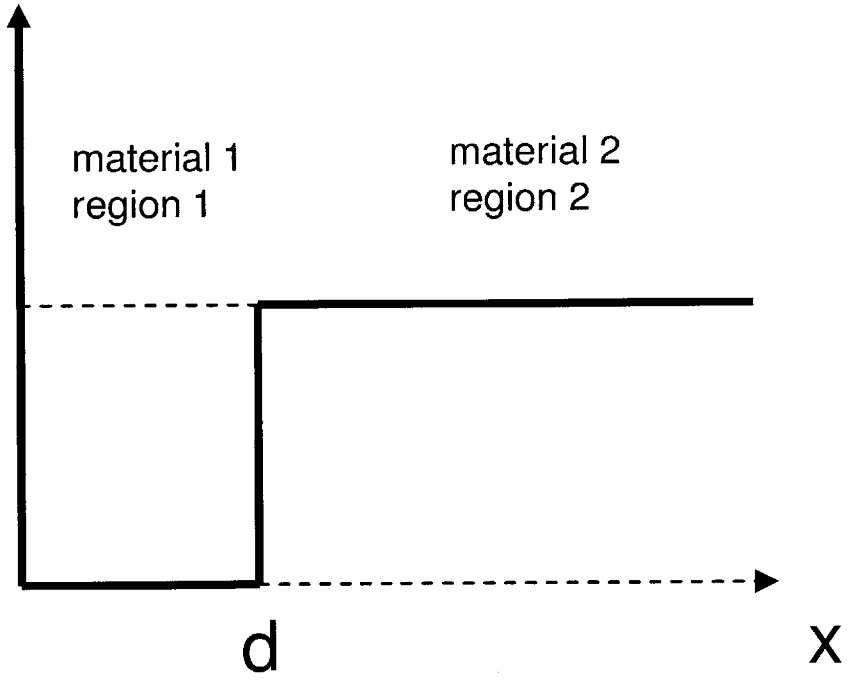

Figure 10-1: One-dimensional potential profile for a quantum well sitting against the gap. Material 2 has an elevated conduction bandedge relative to that of material 1. The potential goes to infinity at the boundary with the gap.

wavefunction at the boundary? The wavefunction should be zero at the gap boundary as the potential is infinity there: $\psi_0 = 0$. Since a bound-state wavefunction decays away exponentially in region 2, we take $\psi_{N_1+N_2-1} = 0$. At the boundary between region 1 and region 2, we are subject to the boundary conditions Eq. (10.2) and Eq. (10.3). Denoting the wavefunction at the boundary to be ϕ, we can use a simple two-point differencing scheme with O(h) error to express Eq. (10.3):

$$\frac{1}{m_1} \cdot \frac{\phi - \psi_{N_1-1}}{h} = \frac{1}{m_2} \cdot \frac{\psi_{N_1} - \phi}{h}$$

which solves to give

$$\phi = \frac{m_2 \cdot \psi_{N_1-1} + m_1 \cdot \psi_{N_2-1}}{m_1 + m_2} \tag{10.4}$$

The Schrödinger's equation at x_{N_1-1} is originally:

$$-\frac{\hbar^2}{2m_1}\left[\frac{\phi - 2\psi_{N_1-1} + \psi_{N_1-2}}{h^2}\right] + V(x_{N_1-1}) \cdot \psi_{N_1-1} = E \cdot \psi_{N_1-1} \tag{10.5}$$

We eliminate ϕ by applying Eq. (10.4) into the above equation to obtain:

$$-\frac{\hbar^2}{2m_1 \cdot h^2}\left[\left(\frac{-2m_1 - m_2}{m_1 + m_2}\right)\psi_{N_1-1} + \left(\frac{2m_1 + m_2}{m_1 + m_2}\right)\psi_{N_1-2}\right] + V(x_{N_1-1})\psi_{N_1-1} = E \cdot \psi_{N_1-1} \tag{10.6}$$

We can construct a similar equation for grid x_{N_1}. Altogether, we can obtain a matrix equation of the following form:

$$\overline{\overline{H}} \cdot \overline{\psi} = E \cdot \overline{\psi}$$

where $\overline{\psi}$ is a column vector containing ψ_1, $\psi_2, \cdots$, $\psi_{N_1+N_2-2}$. The above is a matrix eigen problem and we can use any of the available matrix packages to solve for the eigen-values and eigen-vectors to give us the energies and wavefunctions of the bound states.

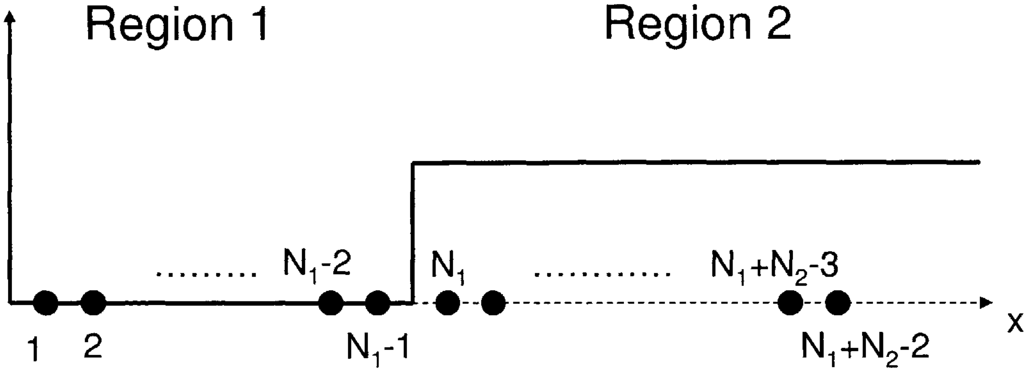

Figure 10-2: Finite-difference scheme with the grid discretizations shown.

10.3 Order of error

We have described the basic approach to solving bound-state energies and wavefunctions of one-dimensional quantum wells. This approach can be generalized to solve two-dimensional and three-dimensional potential well problems. One important point to note is the order of error. In the above example we have used a $O(h^2)$ three-point differencing scheme for the second derivative and a $O(h)$ two-point differencing scheme for the first derivative of the boundary condition. Altogether, the accuracy is limited by that of the boundary condition and the overall error is of order $O(h)$. Therefore, to achieve desired accuracy one would need to match the order of error for both the second derivative discretization of Schrödinger's equation and the first derivative discretization of the boundary condition. In this chapter we demonstrate the numerics with three-point differencing scheme for the second derivative and two-point differencing scheme for the first derivative for the sake of clarity. In the next chapter we describe a quantum dot implementation of our device, and in calculating the three-dimensional wavefunctions of the dot states we have used a six-point differencing scheme for the second derivative and a five-point differencing scheme for the first derivative, resulting in $O(h^4)$ order of error (see pp. 914 of [19] for the associated formulae). Using a higher point differencing scheme could increase the error order but would also require more grids, leading to a longer simulation time. To keep the run time manageable, we have used six grids in each of the regions in each of the dimension for the three-dimensional quantum dot problems. Even though the relatively low number of grids might lead to some error, the analysis suffices here as our focus is on the new thermal to electric conversion scheme and not on precise calculations of quantum dot wavefunctions.

10.4 Two-dimensional scheme

We describe how to generalize the numerical method to solve two-dimensional problems. Figure 10-3 shows a two-dimensional well sitting against an infinite potential wall. The potential is lower inside the square and higher outside, and it goes to infinity at the wall to the right of the square. We put grids on the x-y plane as shown in Figure 10-4. The numbering of the grids starts from the upper left and increases from right to left and top to bottom. There are n grid points in each row. The line on the right indicates the infinite wall while the square indicates the potential well. The Schrödinger's equation reads

$$-\frac{\hbar^2}{2}\nabla\left(\frac{1}{m(x,y)}\nabla\psi(x,y)\right) \;+\; V(x,y)\psi(x,y) \;=\; E\cdot\psi(x,y)$$

Inside a homogeneous region, the Schrödinger's equation can be expanded as

$$-\frac{\hbar^2}{2m}\left[\frac{\partial^2}{\partial x^2}+\frac{\partial^2}{\partial y^2}\right]\psi(x,y) \;+\; V(x,y)\psi(x,y) \;=\; E\cdot\psi(x,y)$$

Differencing gives

$$-\frac{\hbar^2}{2m}\left[\frac{\psi_{j-1}-2\psi_j+\psi_{j+1}}{h_x^2}+\frac{\psi_{j-n}-2\psi_j+\psi_{j+n}}{h_y^2}\right] \;+\; V(x_j,y_j)\psi_j \;=\; E\cdot\psi_j$$

where h_x is the spacing between adjacent grids on the x axis and h_y is the spacing between adjacent grids on the y axis. For the boundary condition we can use the one-dimensional result Eq. 10.4. For example, Figure 10-4 shows a boundary relation in the y direction among ψ_{k-n}, ϕ, and ψ_k:

$$\phi = \frac{m_1 \cdot \psi_{k-n} + m_2 \cdot \psi_k}{m_1 + m_2} \tag{10.7}$$

where m_1 is the electron mass inside the well and m_2 is the electron mass outside the well. Figure 10-4 also shows a boundary relation in the x direction among ψ_g, θ, and ψ_{g-1}:

$$\theta = \frac{m_1 \cdot \psi_g + m_2 \cdot \psi_{g-1}}{m_1 + m_2} \tag{10.8}$$

We use Eq. (10.7) and Eq. (10.8) to eliminate ϕ and θ from the differenced Schrödinger's equations, similar to the one-dimensional case of going from Eq.(10.5) to Eq. (10.6). Therefore we can construct and solve a matrix eigen problem for a column vector $\overline{\psi}$ containing all the ψ_j's. Figures 10-5, 10-6, and 10-7 show the three bound-state wavefunctions for an example two-dimensional potential well as described above. The well has a width of 45 $\AA$ in the x direction and a width of 145 $\AA$ in the y direction. The potentail inside the well is 697 meV lower than that outside the well. The effective electron mass outside the well is $0.067m_0$, where m_0 is the free electron mass. The effective electron mass inside the well is $0.024m_0$. The calculation is done with a six-point differencing scheme for the second derivative and a five-point differencing scheme for the first derivative, The number of grids used is 120 in the x direction and 90 in the y direction. We can see from the figures that in the x direction the well is only wide enough to hold one state while the well is wider in the y direction. The well holds three states and the excitations are in the y direction.

10.5 Three-dimensional problem

In this section we consider a three-dimensional potential well problem. Figure 10-8 shows a cubic shape quantum dot sitting against an infinite wall. The potential at the wall is infinite and the potential inside the well is lower than that outside the well. The Schrödinger's equation reads

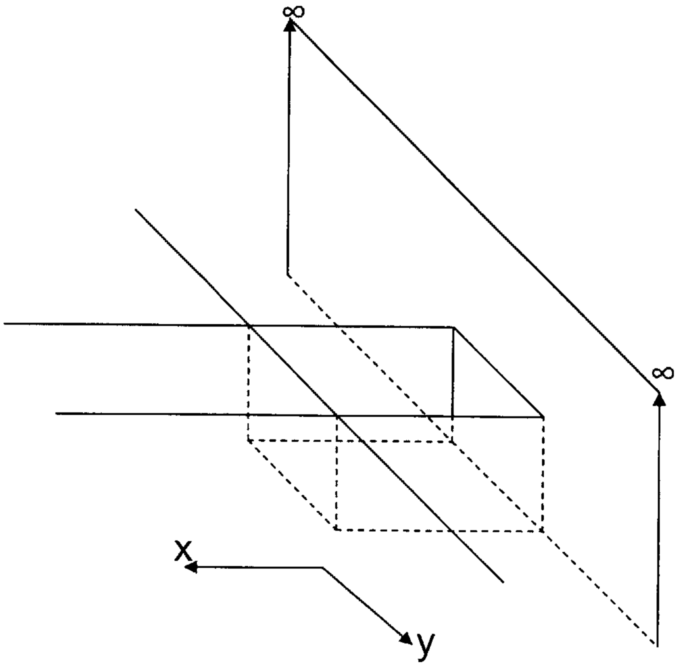

Figure 10-3: Two-dimensional potential well sitting against an infinite wall.

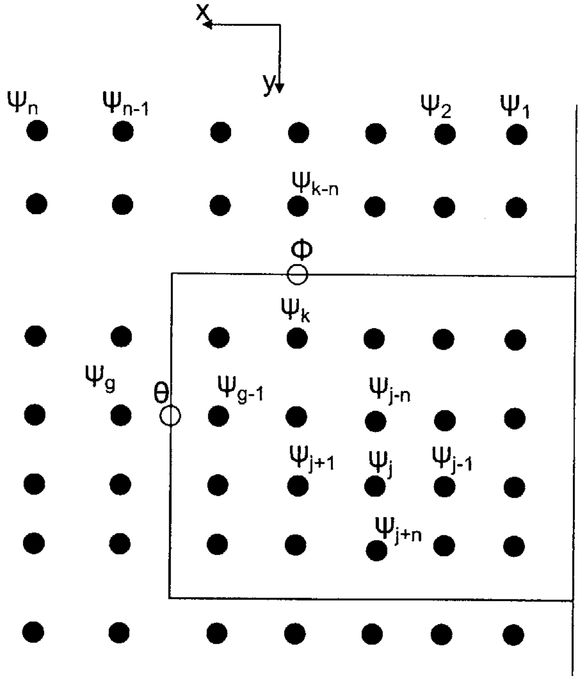

Figure 10-4: Grid discretizations for the two-dimensional potential well problem.

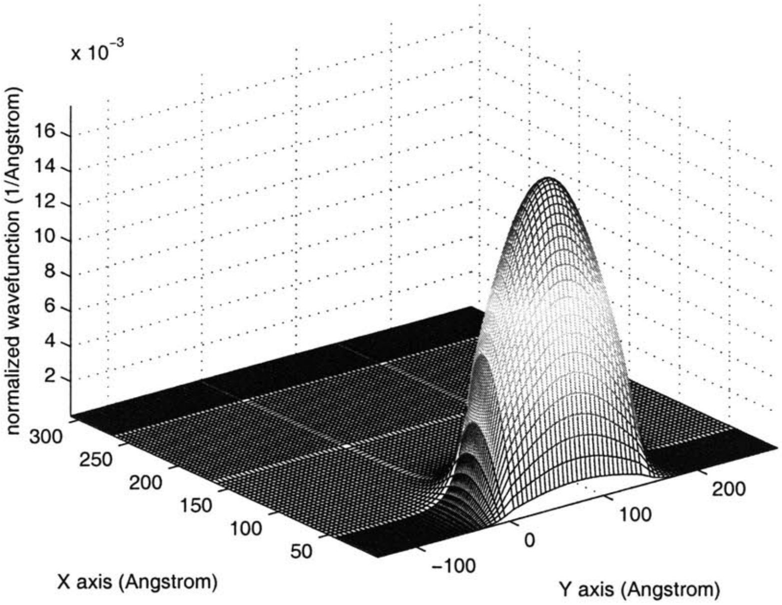

Figure 10-5: Normalized ground-state wavefunction of the two-dimensional potential well.

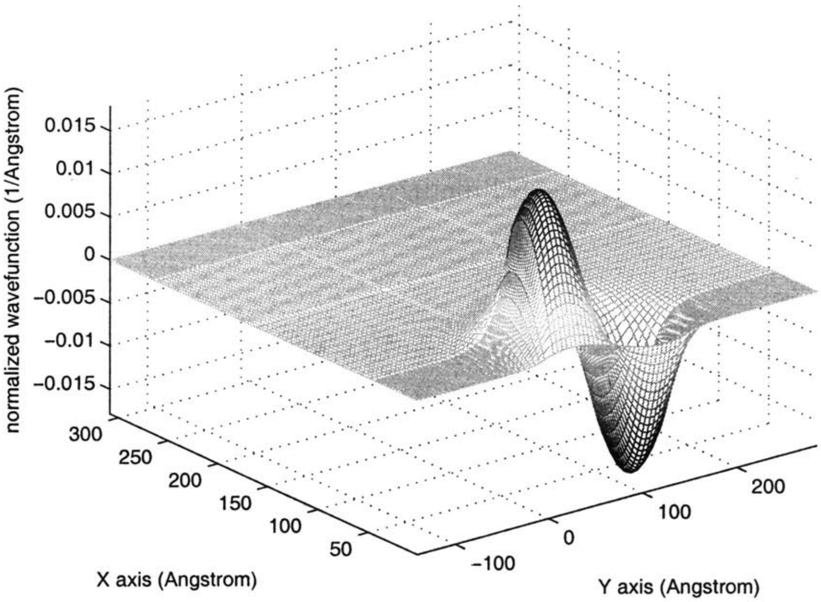

Figure 10-6: Normalized first-excited wavefunction of the two-dimensional potential well.

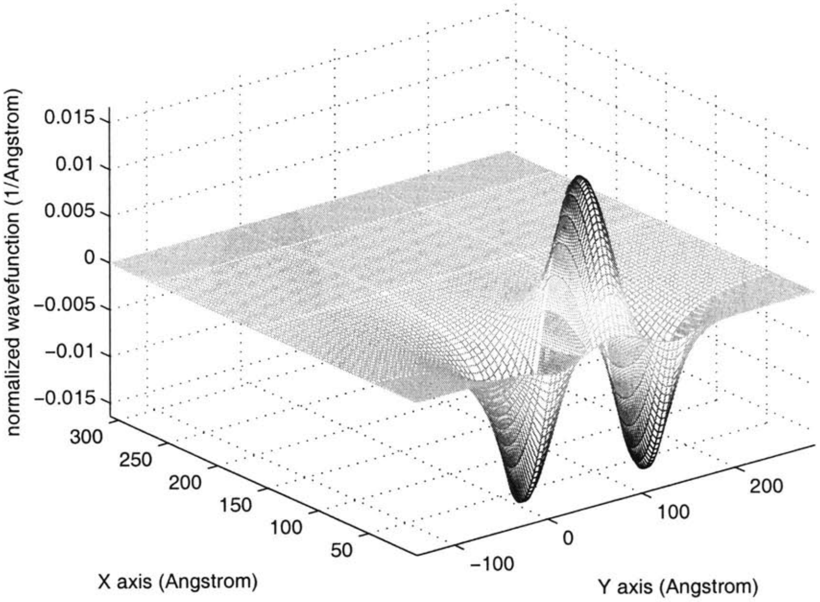

Figure 10-7: Normalized second-excited wavefunction of the two-dimensional potential well.

$$-\frac{\hbar^2}{2}\nabla\left(\frac{1}{m(x,y,z)}\nabla\psi(x,y,z)\right) \;+\; V(x,y,z)\psi(x,y,z) \;=\; E\cdot\psi(x,y,z)$$

Inside a homogeneous region, the Schröndiger's equation can be expanded as

$$-\frac{\hbar^2}{2m}\left[\frac{\partial^2}{\partial x^2}+\frac{\partial^2}{\partial y^2}+\frac{\partial^2}{\partial z^2}\right]\psi(x,y,z) \;+\; V(x,y,z)\psi(x,y,z) \;=\; E\cdot\psi(x,y,z)$$

We discretize the problem with grids shown in Figure 10-9. The numbering of the grid increases with increasing x coordinate, then increasing y coordinate, and finally increasing z coordinate. There are n grid points in the x direction and g grid points in the y direction. Differencing the Schrödinger's equation gives

$$-\frac{\hbar^2}{2m}\left[\frac{\psi_{j-1}-2\psi_j+\psi_{j+1}}{h_x^2}+\frac{\psi_{j-n}-2\psi_j+\psi_{j+n}}{h_y^2}+\frac{\psi_{j-n\cdot g}-2\psi_j+\psi_{j+n\cdot g}}{h_z^2}\right]$$

$$+V(x_j,y_j,z_j)\psi_j = E\cdot\psi_j$$

where h_x is the spacing between adjacent grids in the x direction, h_y is the spacing between adjacent grids in the y direction, h_z is the spacing between adjacent grids in the z direction. The boundary condition Eq. 10.4 still applies in the three-dimensional case. Again, a matrix eigen problem for the vector of ψ's can be developed and solved. We calculate the bound states for the problem of 45Å × 145Å × 45Å size quantum dot in the x, y, and z directions with the potential inside the dot being 697 meV lower than outside. The effective mass inside the dot is 0.024 m_0 and that outside the dot is 0.067 m_0. The calculation is done with a six-point differencing scheme for the second derivative and a five-point differencing scheme for the first derivative, The number of grids used is 24 in the x direction, 18 in the y direction, and 18 in the z direction. Figures 10-10, 10-11, and 10-12 show the cross-sectional view of the normalized ground-state wavefunction in the x-y, x-z, and y-z plane. Figures 10-13, 10-14, and 10-15 show the cross-sectional views for the first excited state. Due to the additional dimension leading to a lower level of confinement, this three-dimensional potential well only has two bound states as opposed to three as in the case of the two-dimensional potential well. It can be seen that in the x and z directions the well holds only one state while in the y direction the well is wider and holds one more excited state.

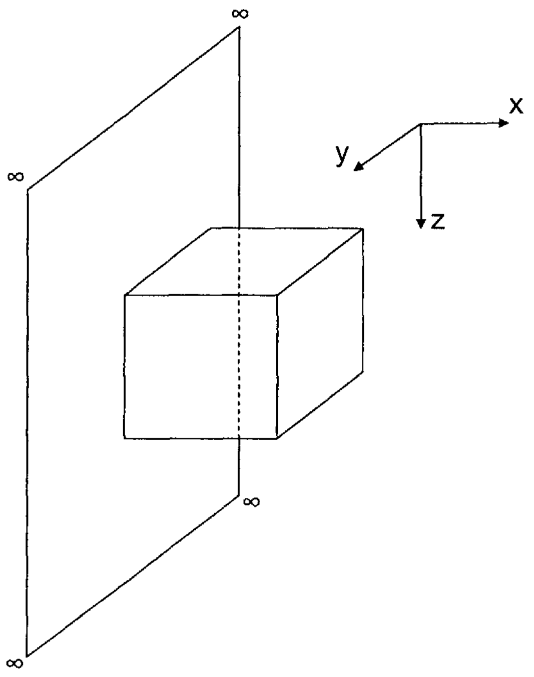

Figure 10-8: Three-dimensional potential well sitting against an infinite wall.

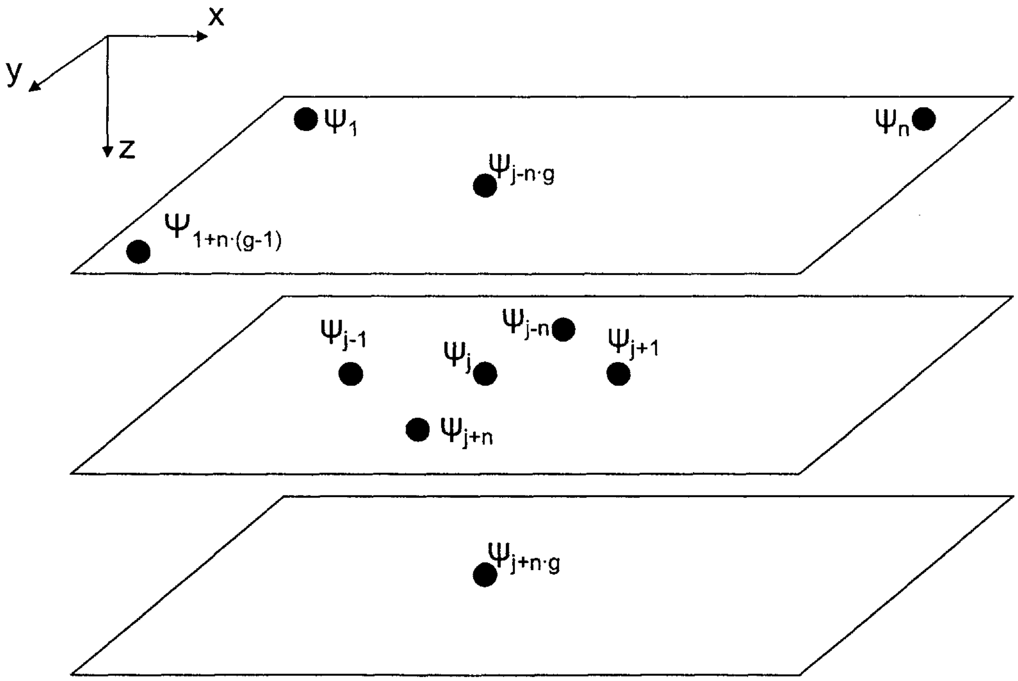

Figure 10-9: Grid discretizations for the three-dimensional potential well problem.

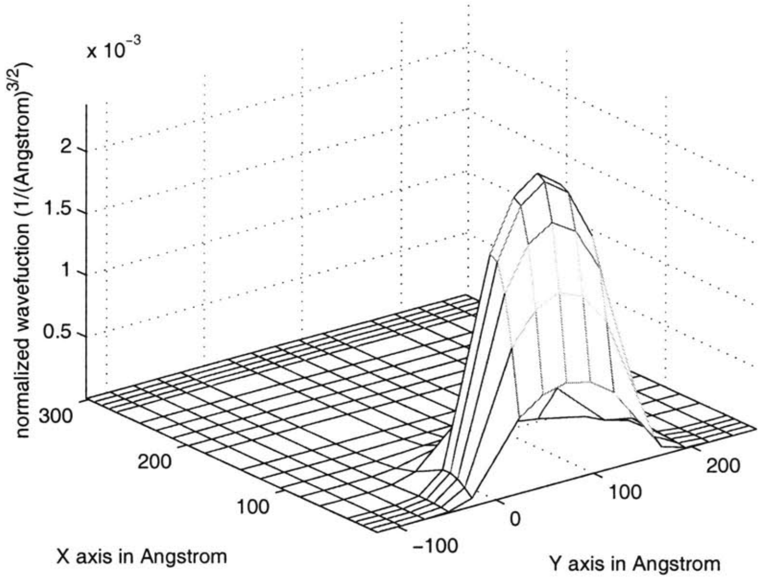

Figure 10-10: x-y cross-section view through the center of the quantum dot for the normalized ground-state wavefunction of the three-dimensional potential well problem.

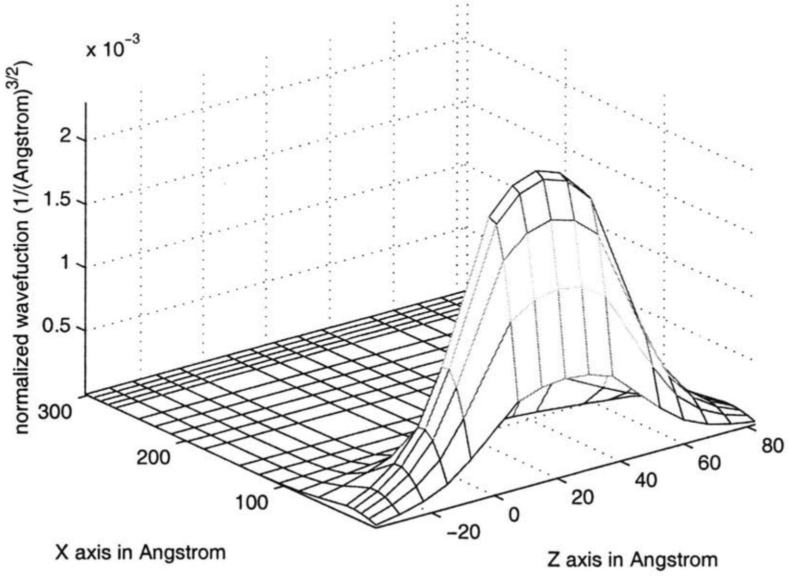

Figure 10-11: x-z cross-section view through the center of the quantum dot for the normalized ground-state wavefunction of the three-dimensional potential well problem.

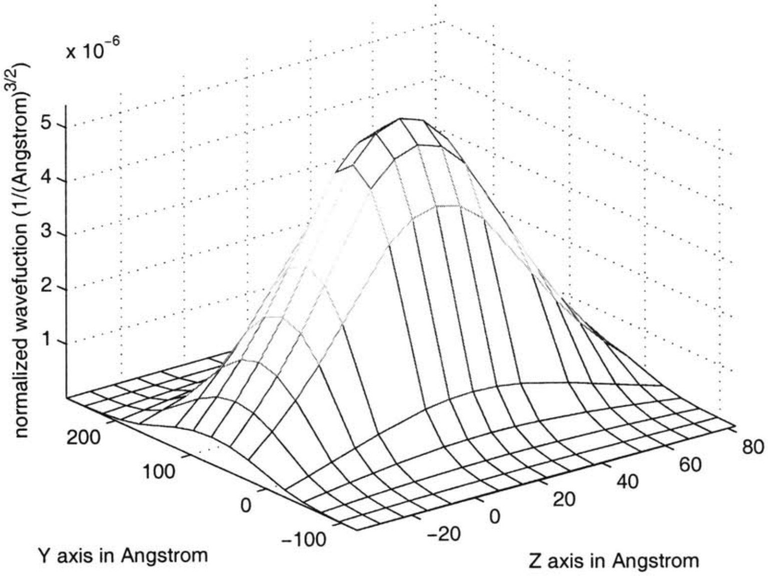

Figure 10-12: y-z cross-section view through the center of the quantum dot for the normalized ground-state wavefunction of the three-dimensional potential well problem.

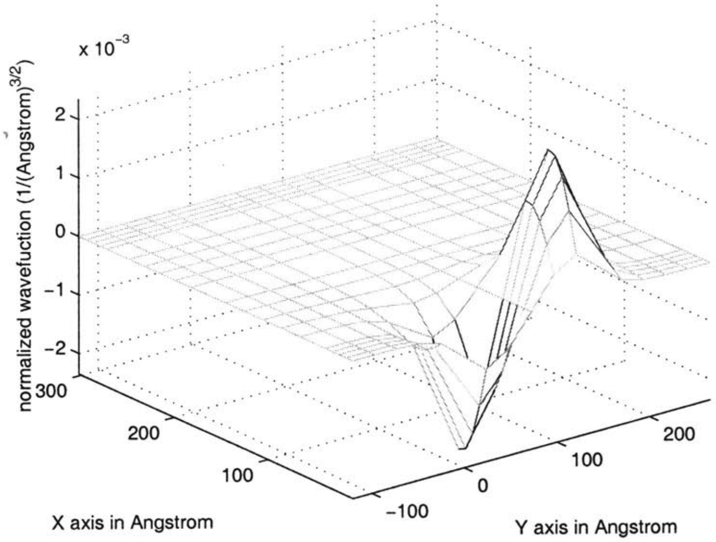

Figure 10-13: x-y cross-section view through the center of the quantum dot for the normalized first-excited state wavefunction of the three-dimensional potential well problem.

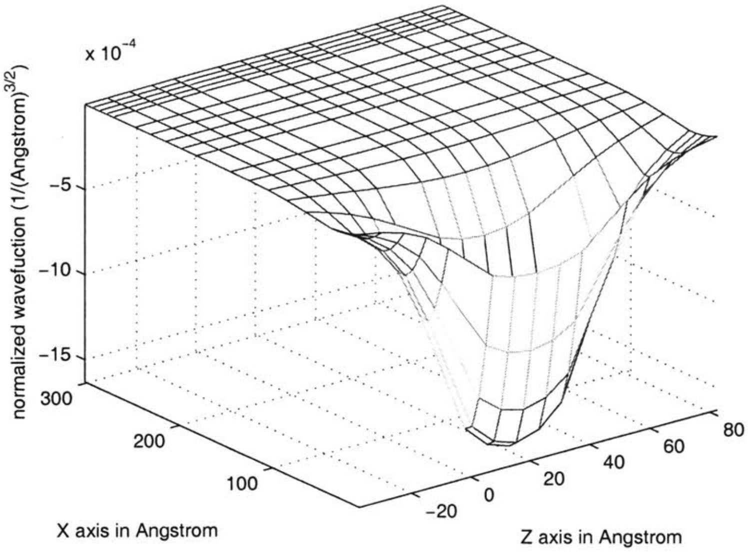

Figure 10-14: x-z cross-section view through the center of the quantum dot for the normalized first-excited state wavefunction of the three-dimensional potential well problem.

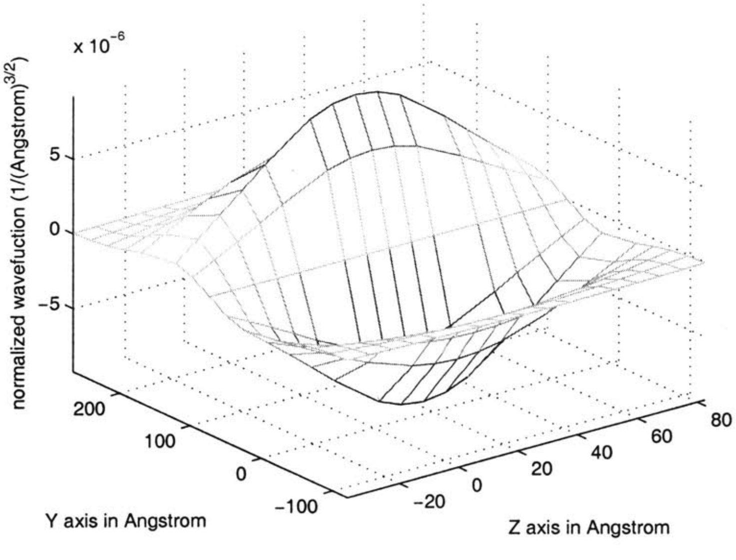

Figure 10-15: y-z cross-section view through the center of the quantum dot for the normalized first-excited state wavefunction of the three-dimensional potential well problem.

Chapter 11

Quantum dot design, issues, and parameters

We have done much analysis on the quantum-coupled thermal to electric conversion scheme. To further explore the feasibility of such a scheme, we present a particular design of the device where quantum dots are used to implement the potential wells of the scheme. Even though the precise fabrication of the device seems difficult, there has been evidence showing research progress towards the various components essential to the implementation of the design.

11.1 Design basics

Here we outline the basic quantum dot design of the thermal to electric converter. Please refer to Figure 11-1. The hot-side consists of a semiconductor substrate with a quantum dot on the surface having two levels matched to those of a cold-side dot. There is a doped layer of semiconductor underneath the hot-side dot which acts as a reservoir. Across the gap, the cold-side has two quantum dots on the surface. Dot 1 has two levels (levels 1 and 2) and they couple to the hot-side dipole via a Coulomb interaction. Dot 2 has one level (level 3) and it couples to the excited level (level 2) of dot 1 through tunneling. The lower level (level 1) of dot 1 relaxes to reservoir 1, which is at ground voltage. The dot 2 level relaxes to reservoir 2 which is at an

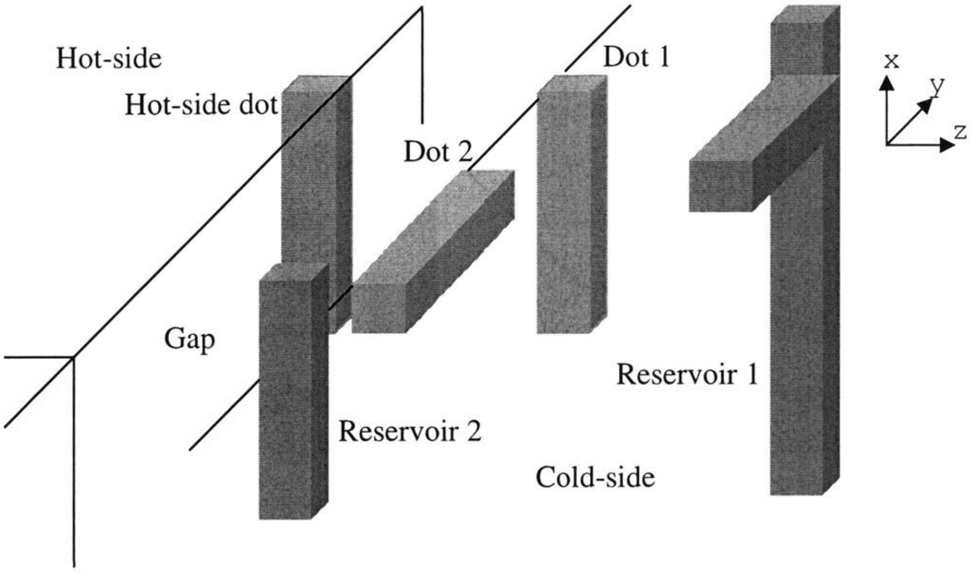

Figure 11-1: An example implementation of one unit of the device. The hot-side has a dot facing dot 1 across the gap. The hot-side dot has two levels matched to those of dot 1. Dot 1 holds two levels and dot 2 holds one level. The dots are presumed to be implemented in a substrate that is not shown. There is a layer of reservoir underneath the hot-side dot which is also not shown. Reservoir 1 is at ground while reservoir 2 is at an elevated voltage. The unit is repeated over a larger area with common reservoirs 1 and 2.

elevated voltage. Reservoir 1 has a branch off the bus in order to couple the lower level of dot 1. The branch is horizontal to dot 1 and it faces the center of dot 1 with a distance. Reservoir 2 is parallel to dot 1 and it runs on the surface next to dot 2 with a distance. The cold-side structure is repeated over the surface with the reservoir 1 buses linked together and the reservoir 2 buses linked together. Reservoir 1 and reservoir 2 are connected through the load. Figure 11-2 shows an array of the device units and their interconnections.

11.2 Materials and dimensions

The hot-side is at temperature 600 K and the cold-side is at 300 K. Dot 1 has a x × y × z dimension (145 Å) × (45 Å) × (45 Å) and is implemented using InAs. The energy separation of the dot 1 levels is 92 meV. Both reservoir 1 and reservoir 2 are

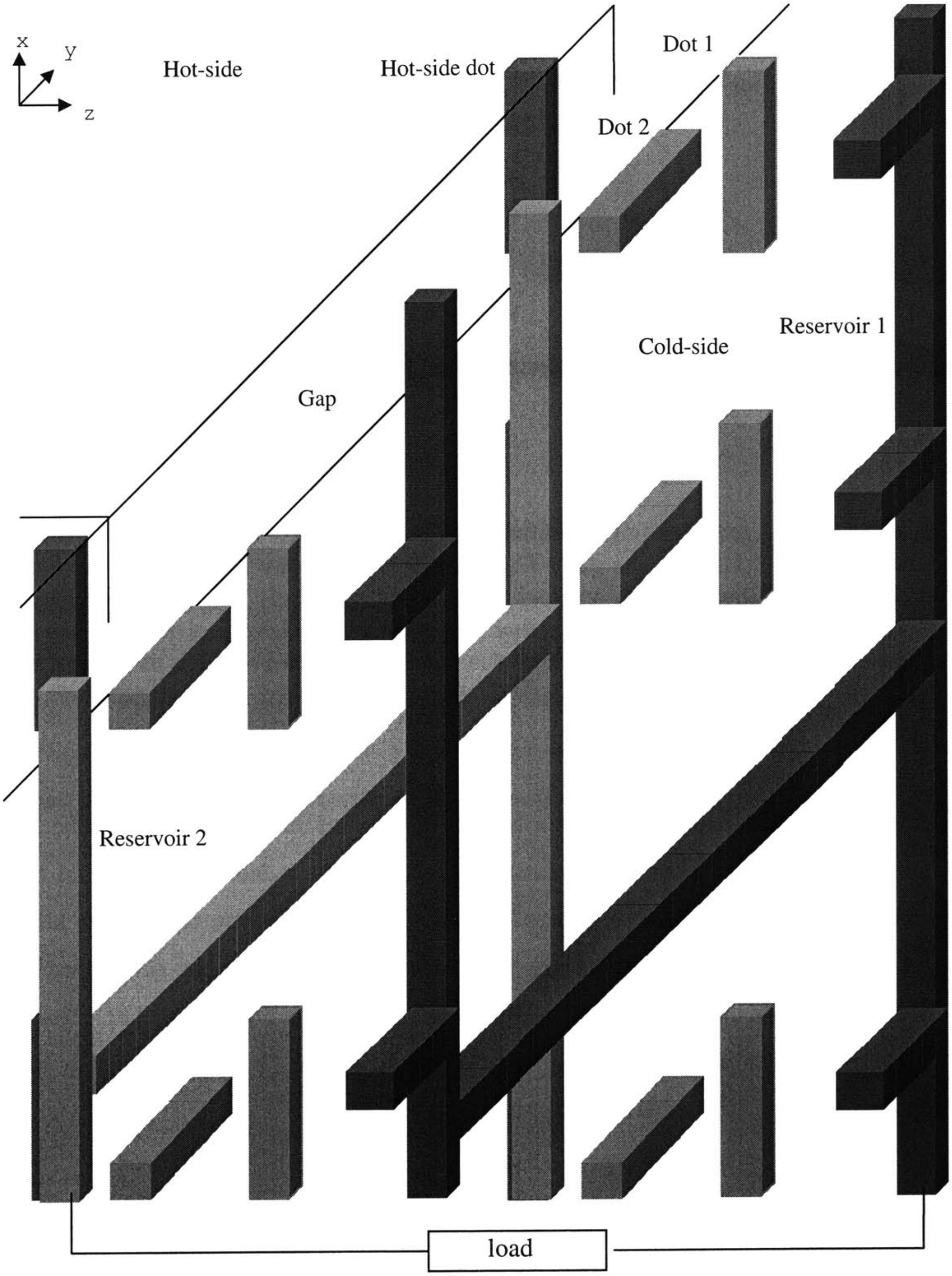

Figure 11-2: A schematic showing how the individual device units might be interconnected. The dots are presumed to be implemented on a substrate that is not shown.

made up of n-type InAs with 6×10^{18} cm^{-3} doping. The hot-side is made up of InAs quantum dots on GaAs matrix, with the dots having the same size as the cold-side dot 1. The hot-side dot and the cold-side dot 1 are aligned such that they face each other across the gap. There is a layer of n-type 2.1×10^{18} cm^{-3} doped InAs 65Å below the hot-side dots. On the cold-side, dot 2 is assumed to be InAs, with dimensions (45 Å) × (45 Å) × (70 Å), and is horizontally pointing to the top part of dot 1. The wavefunction of the excited level of dot 1 has a peak in the upper half of the dot in x direction. On the other hand, the ground state wavefunction of dot 1 has a peak in the middle of the dot and is of lower value than the excited level in the upper half of the dot. Therefore, having dot 2 horizontally pointing to the upper half of the dot makes the dot 2 level couple to the excited state of dot 1 preferentially due to the spatial configuration. In addition, the excited state of dot 1 is more extended and it couples to dot 2 more strongly due to its higher tunneling probability. Dot 2 holds a level that is lower than the excited level of dot 1 by 40 meV such that at a voltage of 40 mV they become resonant. Note that Figure 11-1 is not drawn to scale. The distance between dot 1 and dot 2 is 35 Å. The reservoir 1 branch with transverse size (10 Å) × (10 Å) is horizontally positioned 30 Å away from the center of dot 1. Due to this spatial orientation, reservoir 1 coupling to the excited level of dot 1 is much smaller than the coupling between reservoir 1 and the ground state of dot 1. Reservoir 2 is located 30 Å away from dot 2 and it has a transverse size of (45 Å) × (45 Å). The substrate on the cold-side is GaAs. The gap thickness is assumed to be nanometer-scaled. Gaps of 5-15 nm are well within the present state of the art [20] and a nanometer gap has been used to demonstrate cooling by room-temperature thermionic emission [21].

We have picked the material choice of InAs/GaAs because this is one of the most extensively studied quantum dot systems. The purpose of the substrate is to hold the dots and reservoir in place and also to provide finite barrier between the dots for tunneling to be possible.

11.3 Fabrication issues

The fabrication of quantum dots presents a challenge. The quantum dots need to meet two criteria. First of all, the dots need to be small enough to contain only one or two states. One common method of quantum dot fabrication is the Stranski-Krastanow (SK) growth mode, namely strain-induced self-organization growth of quantum dots [22]. Using the SK growth, InAs/GaAs quantum dots containing as few as three states have been reported [23] (flat elliptical lens-shaped dots with height 2.5 nm and base length 25 nm) and it is conceivable that fewer-state dots are achievable. Second, precise positioning of the dots is required. Using pre-patterned templates with the SK method, growth of InAs/GaAs dots on designated areas has been carried out [24, 25, 26, 27], but exact positioning of single quantum dots is still difficult.

There are other nanofabrication techniques aside from the SK method. Electron beam lithography has been shown to produce resist dots of approximately 5 to 6 nm[28]. Scanning tunneling microscope lithography has been used to fabricate 15 nm wide trenches in Si [29]. Dip-pen nanolithography has been used to write alkanethiols with 30-nanometer linewidth on a gold thin film [30] and to deposit $AuC_{12}H_{25}S$ (2.5 nm in diameter) gold nanocluster islands (lateral dimensions 67 nm × 72 nm) on a silica surface. It is possible that these methods could be adapted to construct nano-structures demonstrating the quantum properties we desire.

Another fabrication issue is the highly ordered nano-sized reservoir array as shown in Figure 11-2. The reservoir branch that couples to the cold-side dot requires smaller dimension and might be implemented as conductive carbon nanotubes. The size of single-well carbon nanotubes is typically 1 to 3 nm in diameter [31]. The reservoir interconnects could potentially be of larger sizes and might be implemented as doped regions or semiconductor nanowires. Doped regions can be shaped by resist of which resolution can be 5 to 6 nm with electron beam lithography [28]. Good control over the diameter and length of nanowires has been demonstrated in nearly monodisperse indium phosphide nanowires of diameters 10, 20, and 30 nm and lengths 2, 4, 6, and 9 μm [32]. Doping is required to make the nanowires into electron reservoirs and we have seen examples of B-doped silicon nanowires of diameter 150 nm and P-doped silicon nanowires of diameter 90 nm [33]. Connecting individual wires into the complex branched array structure of Figure 11-2 presents a great challenge, which would require further research.

11.4 Parameter estimations

Having specified a design of the device, we wish to evaluate its performance. Before we can do so, we need to estimate the various material parameters associated with the design.

11.4.1 Quantum dot parameters

A calculation of the energy levels in InAs/GaAs quantum dots is performed in [34] and we use their conduction band discontinuity of 697 mV in this work. Unlike [34] which assumes a unique effective mass 0.067 throughout the structure, we use the InAs effective mass 0.024 in the InAs region and the GaAs effective mass of 0.067 in the GaAs region. The two levels in dot 1 are computed to be 525 meV and 617 meV above the conduction bandedge of InAs. The level in dot 2 is computed to be 577 meV above the conduction bandedge of InAs. Following the numerical method described in the previous chapter we calculate the quantum dot wavefunctions. The Coulomb coupling matrix element is obtained by applying the wavefunctions to the three-region Coulomb interaction energy result using Eq. 9.3. As is done in [35], we use the square of the refractive index at the transition frequency as the dielectric response in Eq. 9.3 instead of the static dielectric constant. The tunneling matrix element is estimated to be $V = 3.3$ meV, which matches a relaxation time of $\hbar/V = 0.2$ ps.

11.4.2 Fermi levels

Solving the following equation gives the Fermi level of the reservoir:

$$N_D = N_c F_{1/2}(\eta_c)$$

where N_D is the doping level and N_c is the effective density of states of the conduction band of InAs 8.7×10^{16} cm^{-3}. $F_{1/2}$ is the Fermi-Dirac integral of order 1/2. η_c is the normalized energy spacing between the Fermi level and the conduction band edge $\eta_c = (E_F - E_c)/kT$. Both the hot-side and the cold-side reservoirs are solved to have the Fermi level above the conduction band edge by 525 meV, matching the ground-state energy of dot 1 and the hot-side dot.

11.4.3 Relaxation times

The relaxation times on the hot-side dot levels is estimated using the approach described in Chapter 13. For the hot-side dot, the ground state relaxation time is calculated to be 0.2 ps while that of the excited state is estimated to be 0.06 ps. On the cold-side, level 1 and level 3 also have a relaxation time of 0.2 ps. The relaxation of level 2 is considered below.

11.4.4 Loss

As noted before, the relaxation of level 2 in dot 1 constitutes loss. This relaxation consists of three components. The first component is the phonon-assisted relaxation. The second component is the relaxation into reservoir 1. The last component is the relaxation into surface states. The phonon-assisted [23] relaxation is characterized by a relaxation time of 37 ps from [23]. The level spacing between the two levels in dot 1 is 92 meV, which is 20 meV detuning from 72 meV, a multiple of the GaAs LO-phonon energy $\hbar\omega_0$=36 meV. This detuning is the same as that in [23] and therefore we use their measured lifetime of 37 ps as the phonon-assisted loss relaxation time of the excited level in dot 1. This lifetime of QD levels is considerably longer than that of bulk or two-dimensional heterostructures because there are no levels to relax to at $\hbar\omega_0$ harmonies; namely, the density of states is restricted. In addition, the polaronic nature of the confined electron coupled to the phonon [23] results in inefficient phonon-assited relaxation, and therefore implementing the cold-side with quantum dots has an advantage of lower loss compared to the two-dimensional heterostructure implementation.

The lifetimes for the relaxations into reservoir 1 and the surface are estimated using the approach described in Chapter 13. The lifetime of level 2 relaxation into reservoir 1 is estimated to be 20 ps. The relaxation time into the surface states is dependent on how far the dot is from the surface and in principle can be made long. A discussion on the relaxation into surface states is deferred to Chapter 13. Here we only consider the effects of the phonon-assisted relaxation of lifetime 37 ps and relaxation into reservoir 1 of lifetime 20 ps. The total equivalent relaxation time is

$$\left(\frac{1}{20\text{ ps}} + \frac{1}{37\text{ ps}}\right)^{-1} \approx 13\text{ ps}$$

11.5 Discussion

A specific quantum dot design of the proposed thermal to electric conversion has been decribed and the various parameters associated with the design have been estimated. We are now in a position to apply the parameters to our augmented secular equations model and to obtain numerical device characteristics, which will be the topic of next chapter.

Chapter 12

Numerical results

In the last chapter we have given a quantum dot design of the quantum-coupled single-electron conversion scheme. We have also given specific values to all the essential parameters of the design except the Coulomb coupling, which is dependent on the gap thickness. In this chapter we present numerical results of the device performance for the case of 5 nm gap, and also give the gap-dependence of the load power.

12.1 Load power and efficiency

For a gap of 5 nm, the Coulomb coupling matrix element U is 2.5×10^{-4} eV. We assume each device unit occupies an area of 1000 Å × 1000 Å. We assume that at this size dot 1 only couples to the hot-side dot directly across the gap and it does not couple to other hot-side dots 1000 Å or further away. The calculated device load power as a function of voltage is shown in Figure 12-1. The load power is similar to a parabolic curve of a typical thermoelectric device characteristic with the maximum value occurring somewhere in the middle of the voltage range. The maximum load power is 23 mW/cm^2 at a voltage 27.5 mV with a corresponding efficiency of 26%.

The calculated conversion efficiency along with the dashed line Bloch equations result $q \cdot V/\Delta E$ is plotted in Figure 12-2, where q is the electron charge, V is the voltage, and ΔE is the energy spacing of the dot 1 levels. Intuitively, after an excitation transfer occurs, one electron on the cold-side receives energy ΔE and then does work $q \cdot V$ on the load. Therefore, we expect the efficiency to be simply $q \cdot V/\Delta E$. However, there are complications to this simple argument. First of all, because the dot levels have finite relaxation times, their energies have spreadings due to the energy-time uncertainty relation. Therefore the excitation received from the hot-side is not exactly ΔE. Second, the excited level of dot 1 has a relaxation that constitutes loss and this degrades the efficiency.

Please refer to Figure 12-2. Initially the efficiency increases with voltage roughly following the $q \cdot V/\Delta E$ line until it reaches its maximum value 43% at 42 mV. The loss takes greater effects beyond this point and the efficiency drops rapidly with further voltage increase. The corresponding load power at the maximum efficiency is 8 mW/cm^2.

The efficiency is rather independent of the gap thickness for a given device, but the load power is strongly dependent on the Coulomb coupling matrix element and thus is dependent on the gap. Figure 12-3 shows the maximum load power for gap thickness 1 nm through 10 nm. The maximum load power drops from 257 mW/cm^2 at 1 nm to 3.4 mW/cm^2 at 10 nm. The thermal power follows a similar gap-dependence to go from 1.66 W/cm^2 at 1 nm to 152 mW/cm^2 at 5 nm to 23 mW/cm^2 at 10 nm. At larger gap thickness, the dipole-dipole interaction energy has a $1/R^3$ dependence, where R is the distance between the two dipoles. The Coulomb matrix element U thus has a $1/R^3$ dependence and is small at large gaps. The current and power then have a U^2 Golden rule dependence and the dependence on distance is $1/R^6$.

12.2 Comparison with TPV and MTPV

We compare the performance of the quantum dot design with that of TPV and MTPV. The figures for TPV are taken from the experimental results of [8]. The numbers for MTPV are experimental results from [4] done at a 0.12 μm gap. Figure 12-4 shows the total thermal power transferred from the emitter to the TPV diode

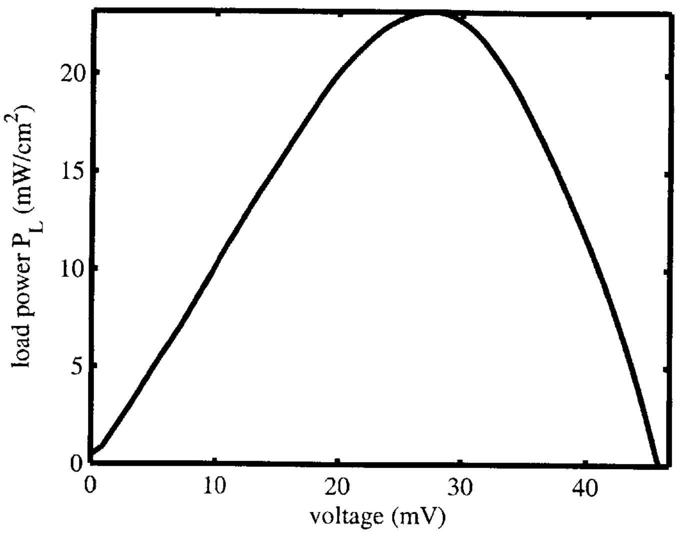

Figure 12-1: Load power versus voltage for a 5 nm gap implementation of the design. The maximum load power is 23 mW/cm^2 at voltage 27.5 mV with a corresponding efficiency of 26%.

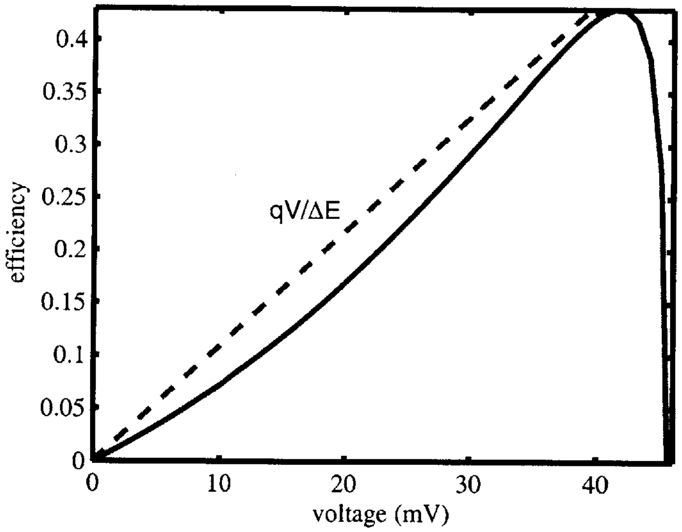

Figure 12-2: Efficiency versus voltage for a 5 nm gap implementation of the design. The maximum efficiency is 43% occurring at voltage 42 mV with load power 8 mW/cm^2.

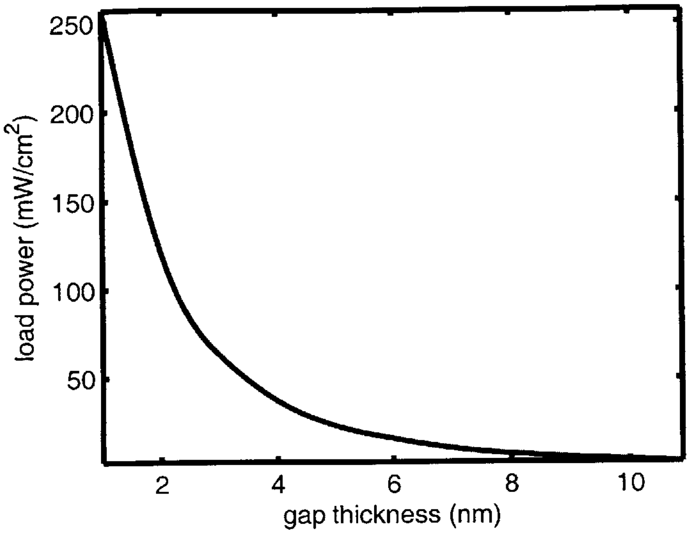

Figure 12-3: Maximum load power for gap thickness from 1 nm to 10 nm. The maximum load power drops from 257 mW/cm^2 at 1 nm to 3.4 mW/cm^2 at 10 nm

or quantum converter. Also shown are the blackbody limit σT^4 for TPV and the evanescent coupling limit $n^2\sigma T^4$ for MTPV, where n^2 is the averaged refractive index of silicon for the case of [4]. The calculations for the quantum dot design assume a lower temperature of 600 Kelvin and we have presented two results, where the higher power case corresponds to a design with 1 nm gap and the lower one corresponds to a design with 5 nm gap. Both power per unit area and power per unit active area are presented. Note that the load power for our device is dependent on the density of device units, and we have assumed a 100 nm × 100 nm device unit area. Recall that the active area fill factor assumed is 0.0065 and the power per unit active area represents the potential power the device can achieve. It is clear from Figure 12-4 that the TPV power is an order of magnitude or lower than the blackbody radiation limit and the MTPV power is also an order of magnitude lower than the evanescent coupling limit, while the quantumd dot design of the single-electron conversion scheme can potentially exceed these limites by orders of magnitude.

Figure 12-5 shows the conversion efficiency for TPV [8] and the quantum-coupled scheme, along with the Carnot limit, the fundamental upper bound for thermal to

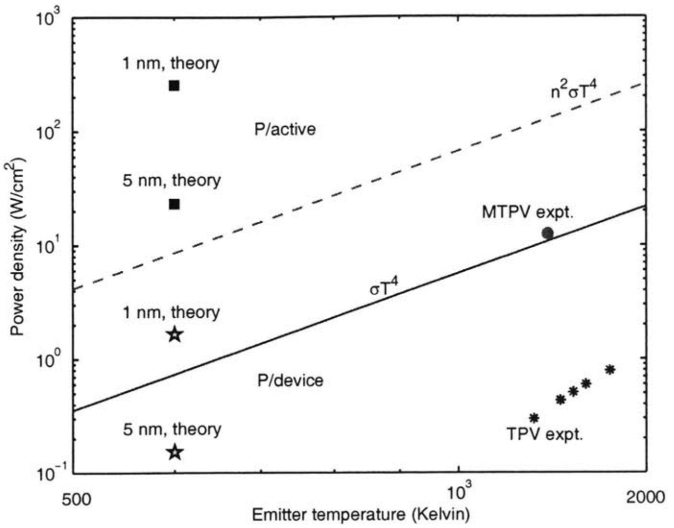

Figure 12-4: Thermal power for TPV, MTPV, and quantum dot design with 1 nm and 5 nm gaps. The values for TPV and MTPV are experimental results from [8] and [4]

electric conversion efficiency. The efficiency for the MTPV is not available. The 1 nm gap and 5 nm gap cases have the same efficiency and therefore only one data point is shown for the quantum dot design. We see that the potential conversion efficiency for the quantum dot design is high, approaching the Carnot limit, while the efficiencies for TPV are below 30% of the Carnot limit. Note that in our present calculation we have neglected Coulomb-coupled heat flow, which is expected to be the dominant loss mechanism. We have derived a formula for the evaluation of this loss in Appendix C and a calculation will be carried out in the future.

12.3 Constraints

The load power is constrained by how fast electrons can be transported between the quantum dots and the reservoirs, namely the relaxation times, and how fast the excitation can be transferred from the hot-side to the cold-side, namely the Coulomb coupling. It appears that with this design, the Coulomb coupling matrix element is the bottleneck to the load power. For the quantum dot design at 5 nm gap, the

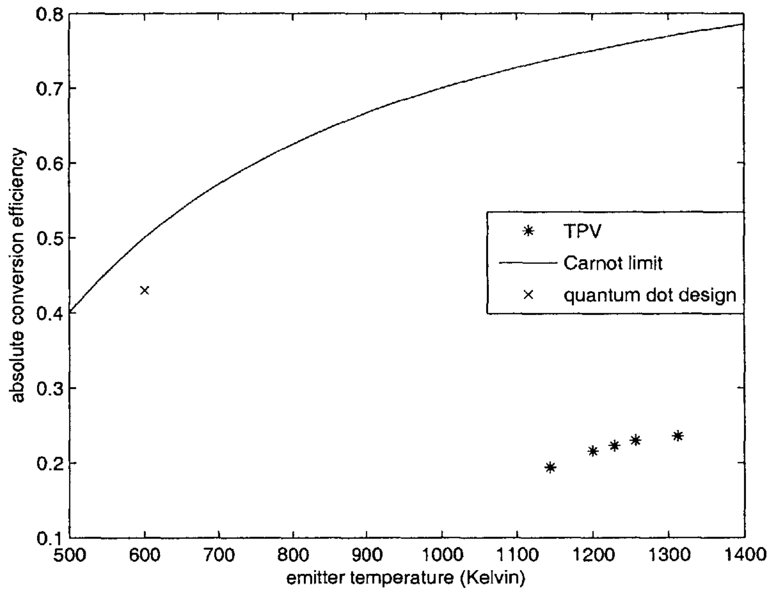

Figure 12-5: Efficiency for TPV and quantum dot design. The efficiency for the quantum dot design with 1 nm gap and that for 5 nm gap are the same and only one data point is shown for the qauntum dot design. The values for TPV are experimental results from [8]. There is no efficiency value reported in [4] for MTPV.

Coulomb coupling matrix element is $U = 2.5 \times 10^{-4}$ eV, corresponding to a time scale of $\hbar/U = 2.6$ ps, an order of magnitude slower than the relaxation time 0.2 ps.

The Coulomb coupling matrix element is constrained by two factors. First, the high dielectric constants of the hot-side and cold-side semiconductors decrease the interaction energy between a hot-side electron and a cold-side electron. Second, the transition dipole moment between the two levels in dot 1 is small, due to the small size of dot 1 and arising from the limitation that dot 1 has only two levels.

12.4 Discussion

We have shown that a quantum dot design of the quantum-coupled conversion scheme could lead to high efficiency and decent load power. There is no fundamental limit such as the blackbody limit or the evanescent coupling limit to the power of our device, and the calculations have shown that indeed the power of the quantum dot design of the single-electron conversion scheme could greatly exceed those limits. Also, the predicted efficiency of is very high.

It is natural to ask if there exists an alternative design of the quantum-coupled single-electron conversion scheme, and in the next chapter we consider such a design.

Chapter 13

Relaxation times

Relaxation times are important paramters critical to the function of our proposed device. In this chapter we consider how to estimate the loss relaxation time of level 2 in dot 1 and the lifetime of relaxations into reservoirs for other levels. As mentioned in Chapter 11, the loss relaxation time of level 2 consists of phonon-assisted relaxation and relaxations into reservoir 1 and surface states. In our design, the InAs dots are right on to the surface, and therefore we expect the interactions of the quantum dots (QD) levels with surface states to degrade the QDs' optical properties [36] and contribute to loss. In order to reduce loss, we could position the QDs underneath the surface to decrease these interactions at the expense of weaker Coulombic coupling between the hot-side and the cold-side dots. Here we investigate how the loss is affected by the distance between the QDs and the surface.

13.1 Measurement

The photoluminescence (PL) intensity and the corresponding lifetime are measured for InAs QDs in a GaAs matrix with varying distances to the surface [36]. Note that the lifetime measured in [36] is that of electron-hole pair creations and not intersubband transitions as in our thermal to electric conversion scheme. However, this lifetime still contains information about the effects of the surface states. The emission lifetime decreases from 550 ps for the distance to the surface of 51 nm to 65 ps for the distance of 9 nm [36]. This decrease in lifetime is caused by the competition between the capture of the photocarriers in the QDs and the surface states [37]. Therefore the capture of the carriers by the surface states is on the order of 65 ps for the distance of 9 nm to the surface. Note that as the distance to the surface decreases, the linewidth increases faster than the decrease in lifetime [36] due to the partial strain relaxation in the thin layer between the QDs and the surface [37] and this effect should not be mistaken as the surface states effects. As the distance to surface is decreased further from 9 nm, the surface states effects would be more pronouned and potentially could be detrimental to the efficiency of our device. To control the distance to the surfaceof the QDs, one first grows InAs QDs on GaAs surface and then caps the QDs with GaAs growth of desired thickness [37].

13.2 Simple one-dimensional analysis

In this section we describe a simple model for the relaxation caused by the surface states. Plotted in Figure 13-1 is the normalized wavefunction magnitude squared ($|\Psi|^2$) versus the distance to the surface for a ground state electron residing in a one-dimensional InAs quantum well of width 1.5 nm sandwiched by GaAs layers. There is not a numerical value for the QD height given in [36], and our choice of 1.5 nm width is a result of fitting our calculation to the measured lifetime for the distance of 9 nm in [36]. Note that the discontinuity in slope comes from the different effective masses, 0.067 for GaAs and 0.024 for InAs. The two vertical lines in the graph at 9 m and 10.5 nm indicate the two InAs/GaAs boundaries. The GaAs region to the right of the InAs region, denoted region II, is assumed to extend to infinity. The GaAs region to the left of the InAs region, denoted region I, has a width of 9 nm and its left boundary is the surface to the gap. In our calculation we have assumed that the wavefunction slope going into the surface is zero. Following the Gamow approximation approach in section 8.5 of [10], an estimation of the decay rate γ_s caused by the surface states is

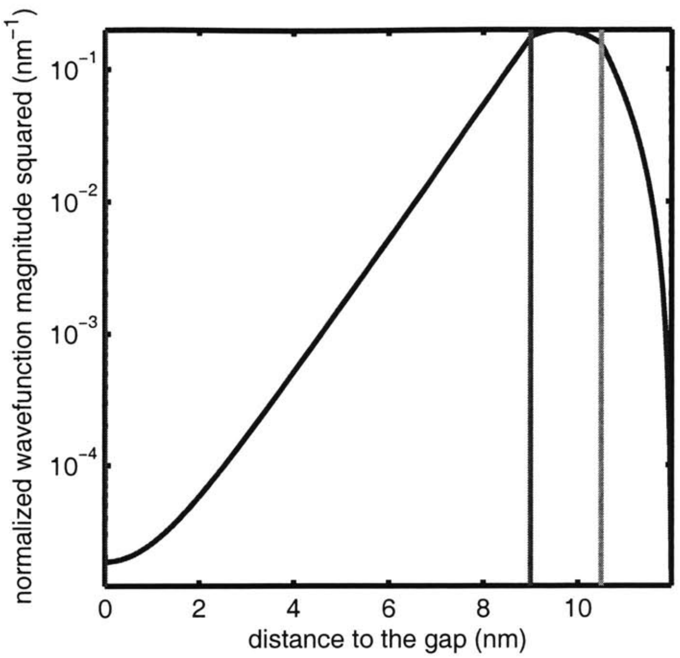

Figure 13-1: Normalized wavefunction magnitude squared versus distance to the surface

$$\gamma_s = \frac{\hbar k}{2m \times (\text{width of InAs well})} \cdot \mathrm{e}^{-2\alpha d} \cdot f \tag{13.1}$$

where k is the wavenumber and m is the electron effective mass, both in the InAs region. The variable α is the decay constant of the electron wavefunction in region I. Here d refers to the thickness of region I. The variable f denotes the chance of an electron approaching the surface getting captured by the surface states, and it is assumed to be 1 in this calulation. The reasoning behind this expression is as follows. An electron rattles inside the well with a velocity $\hbar k/m$. Therefore the rate at which the electron hits the left boundary of the well is $\frac{\hbar k}{2m\times(\text{width of InAs well})}$. The tunneling probability for the electron to tunnel to the surface is $\mathrm{e}^{-2\alpha d}$. Multiplying the above two quantity with the chance of surface state capture gives us the Gamow approximation [10].

When the QD's are away from the surface, the QD's have a PL lifetime of 550 ps. Therefore, the total PL decay rate is the sum of contributions from the surface and the bulk 550 ps decay:

$$\gamma = \gamma_s + \frac{1}{550 \text{ ps}}$$

and the expression for the lifetime is

$$T = \left(\frac{\hbar k}{2m \times (\text{width of region I})} \cdot \mathrm{e}^{-2\alpha d} + \frac{1}{550 \text{ ps}} \right)^{-1} \tag{13.2}$$

Shown in Figure 13-2 are the measured lifetimes from [36] and the calculated lifetimes for various distances to the surface. The lifetime is predicted to drop dramatically as the distance shortens. There are several ways of increasing the lifetime of the electron. First of all, we can increase the width of the InAs well, leading to a lower energy and less extended electron state, hence lowering the interactions between the electron state and the surface states. Figure 13-3 shows the improvement in lifetime if the InAs well is made 3 nm wide. We can also use a material with a higher conduction bandedge for region I, effectively increasing the barrier height of region I and protecting the electron in the well from interacting with the surface states. Figure 13-4 shows the effect on the calculated lifetime when region I has a band edge 500 meV higher than that of GaAs. Finally, we can use a material with a heavier electron mass for region I to make it more effective in separating the electron from the surface states. Plotted in Figure 13-5 is the longer estimated lifetime for the case of an 0.2 effective mass carrier in region I.

13.3 Surface modifications

Functionalization of the surface could supress surface state density and improve the carrier lifetime of QDs. This has been demonstrated in the case of self-assembed 1.6 nm octadecylthiol (ODT) monolayer on the GaAs surface [38]. Growth of ODT monolayer on the GaAs surface suppresses the surface state densities by arsenide-

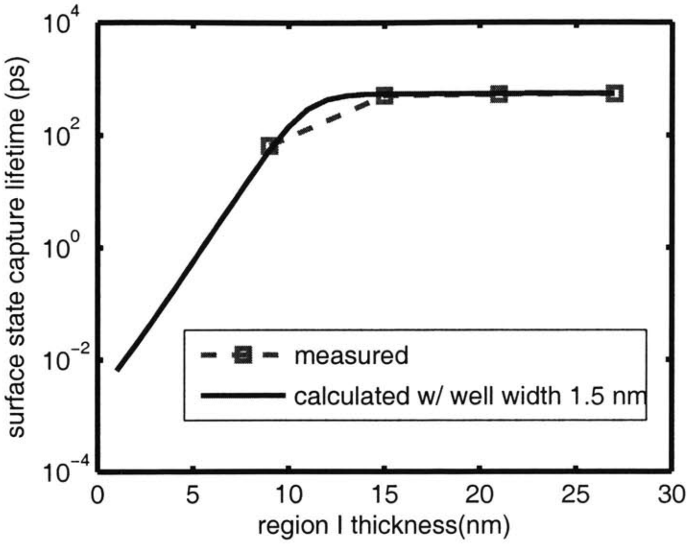

Figure 13-2: Mesaured and calculated lifetime for difference cases of region I thickness

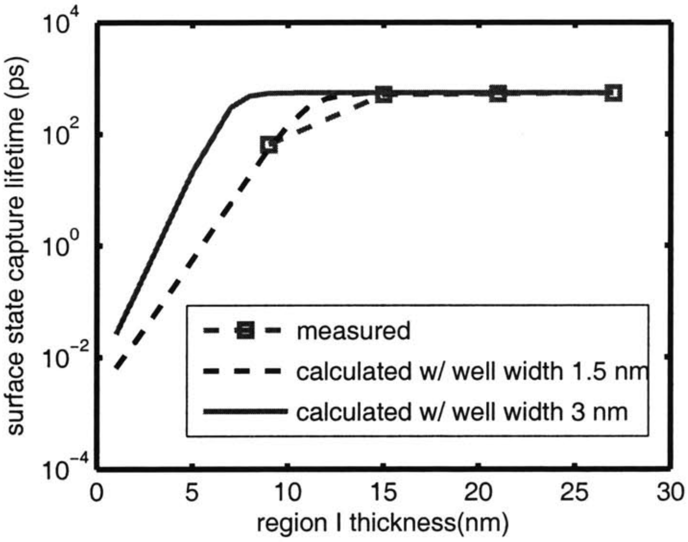

Figure 13-3: Calculated lifetime for the case of an increased InAs well width to 3 nm

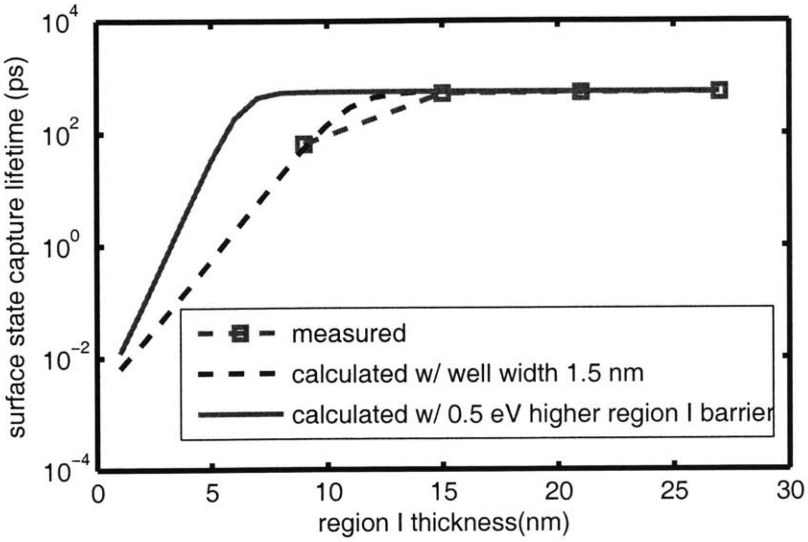

Figure 13-4: Calculated lifetime for the case of increased region I barrier height by 500 meV

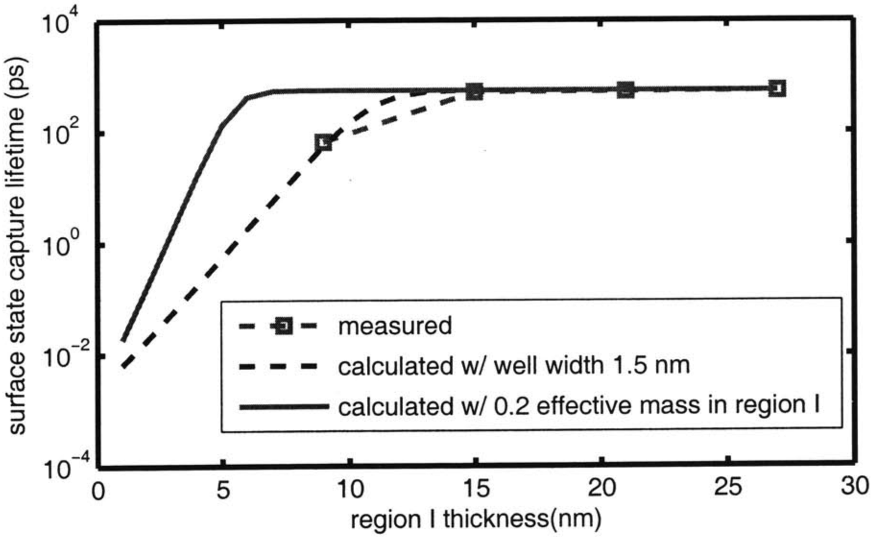

Figure 13-5: Calculated lifetime for the case of increased region I electron mass to $0.2m_0$

sulfide coupling [38]. The PL intensity is increased by up to a factor of 1.9 after the coating of the ODT monolayer for the cases of InAs QDs 10, 20, and 30 nm underneath the surface. We would also expect improvement in relaxation time after the functionalization of the GaAs surface. The chemical stability of the ODT coating is good as the PL intensity is measured to be pretty much the same after leaving the sample in air at room temperature for a month [38]. The thermal stability of the ODT coating is also good as demonstrated through the PL measurement after heating the sample at 573 K [38].

13.4 Bulk defects

There exist defects and impurities in GaAs and other III-V semiconductors [39]. Hydrogen can be used to neutralize or passivate these defects and an increase by a factor of up to 50 has been observed in the room-temperature emission of bulk InAs/GaAs self-assembled QDs subjected to a hydrogen-passivation treatment [39]. The 37 ps lifetime measurement of [23] was done on a sample without any passivation step [40], and hence it is possible to reduce the loss of level 2 via suitable bulk (and surface) passivations.

13.5 Discussion

It has been shown experimentally that bringing quantum dots closer to the surface decreases their lifetime due to carrier capture by the surface states. The measured capture time 65 ps at a distance of 9 nm to the surface is longer than the level 2 lifetime estimate of 13 ps mentioned in Chapter 11. Quantum dots closer than 9 nm to the surface could potentially have much shorter lifetimes, but using a better barrier material for region I or increasing the width of the InAs region could lead to an improved capture time. Furthermore, organic materials can be grown to functionalize the surface, reducing the surface state density and increasing the capture time. Loss can also come from bulk defects in addition to surface states, and hydrogenation has

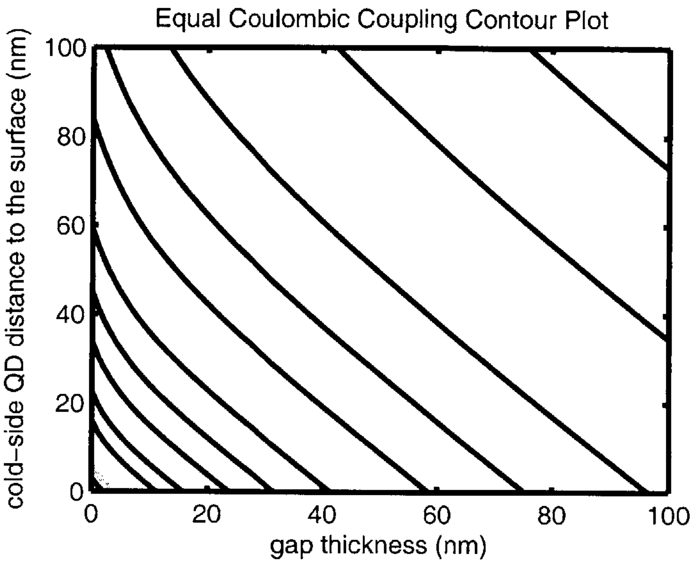

Figure 13-6: Contour plot of the Coulombic coupling matrix element with respect to the distance to the surface and the gap thickness.

been shown to be effective in passivating the bulk defects to reduce loss.

From our analyses so far it is clear that there is a tradeoff between the level 2 loss to surface states and the distance between the QD and the surface. The larger this disance is the smaller the Coulombic coupling matrix element would be. However, does this distance have the same impact on the Coulombic coupling matrix element as the gap thickness? From Eq. 9.4 it seems that increasing the distance to the surface would have less effect on the Coulombic coupling matrix element than increasing the gap thickness, as the gap thickness is amplified by the number the reflections. This is indeed the case. Shown in Figure 13-6 is a contour plot of the Coulombic coupling matrix element with respect to the distance to the surface and the gap thickness calculated from Eq. (9.4) for two electrons each residing 22.5 Å underneath the surface of a GaAs cold-side and a GaAs hot-side. It is seen that the Coulombic coupling matrix element decreases slower for increasing distance to the surface than increasing gap thickness.

13.6 Hot-side relaxation time

The above Gamow approach can also be used to estimate the hot-side relaxation time. On the hot-side, there is a heavily doped layer 65 Å underneath the dot. We can think of the electron in the dot as rattling back and forth. Every time the electron hits the boundary of the dot it has a chance of tunneling out of the dot. If the electron tunnels out of the dot and travels towards the doped layer, it gets captured when it reaches the doped layer. The doped layer thus acts like a surface in the above surface capture problem. We follow the above one-dimensional estimation using the dot height 45 Å as the width of the InAs region and 65 Å as the distance to the surface. Using Eq. 13.1, the relaxation time for the ground state is calculated to be 0.2 ps and that of the excited state is estimated to be 0.06 ps.

13.7 Cold-side dot 1 relaxation times into reservoir 1

We can apply the Gamow approximation to obtain the relaxation times into reservoir 1. Please refer to Figure 11-1. An electron in dot 1 is rattling back and forth in the z direction and it has a chance of tunneling out of the dot. Once it leaves dot 1, it has a chance of reaching the reservoir 1 branch provided that the electron's x position matches that of the reservoir 1 branch. The expression for the relaxation rate into the reservoir is thus:

$$\gamma = \frac{\hbar k}{2m \cdot w} \cdot \mathrm{e}^{-2\alpha d} \cdot p$$

where k is the wavenumber in dot 1 and m is the electron effective mass in dot 1. The variable α is the decay constant of the electron wavefunction in the GaAs region. w is the width of the InAs dot in the z direction. The variable d refers to the distance between dot 1 and the reservoir 1 branch. THe variable p is the probability that the electron in dot 1 has an x position matching that of the reservoir 1 branch. The probability that an electron reaching the reservoir will be captured is taken to be one. The excited state wavefunction of dot 1 has a zero at the center of the dot which the reservoir 1 branch faces. On the other hand, the ground state wavefunction has a maximum at the center of the dot. Therefore, we would expect the ground state relaxation time to be much shorter than that of the excited state. Using the above expression we calculate the relaxation rates and hence the relaxation times for the two levels in dot 1. The ground state has a relaxation time into reservoir 1 of 0.2 ps while that of the excited state is computed to be 20 ps. We similarly obtain the relaxation time into reservoir 2 for the dot 2 level to be 0.2 ps.

13.8 Summary

We have used the Gamow approximation to estimate the loss caused by the surface states, and we have shown that the loss can be reduced by changing the distance to the surface and the material choice of the design. The literature also suggests the use of hydrogen passivation to reduce loss. The Gamow approximation has also been applied to the calculations of the hot-side and cold-side relaxation times into the reservoirs to obtain the parameters in Chapter 11.

Chapter 14

Thermal radiation loss

We have previously focused on level 2 loss as the main source of loss. However, the thermal radiation from the hot-side would be absorbed by the cold-side. In this chapter we estimate this source of energy loss. Note that dipole-dipole Coulomb coupling dominates the heat loss, but estimates were not available at the time the thesis was written.

14.1 Thermal radiation

The thermal radiation inside an infinite homogeneous material can be obtained from combining Eq. (7.84) and Eq. (7.96) in [41]

$$R = \int_0^\infty P(E)dE$$

$P(E)$ is the spectrum of the radiation

$$P = \frac{2\pi c E^3 n^2(E)}{(hc)^3(e^{E/k_BT} - 1)},$$

where E is the energy of the photon, c is the speed of light in vacuum, h is Planck's constant, k_B is Boltzmann's constant, T is the absolute temperature, and $n(E)$ is the frequency-dependent refractive index. The factor of $n^2(E)$ is included because of the small gap used in our design [5]. When the gap is large, the expression for the radiation power spectral density does not have the factor $n^2(E)$ as in the above equation. However, it has been observed that the heat transfer increases as the gap decreases [42, 43, 44], and at our small gap it is suitable to include the factor $n^2(E)$ as explained in [5].

14.2 Thermal radiation in a finite material

Since our device relies on surface structures for the thermal to electric conversion, in principle the hot-side and the cold-side can be thin. (See Figure 14-1). The hot-side has two boundaries H_1 and H_2. The cold-side has two boundaries C_1 and C_2. The hot-side has a finite thickness of d_H and the cold-side has a finite thickness of d_C. The question is how much radiation the hot-side emits. Let us first consider the case as depicted in Figure 14-2 where the hot-side is semi-infinite, extending beyond H_1 to the left infinitely. The radiation going through boundary H_1 is P. Going through a distance of d_H, this radiation would be reduced to $P \cdot \mathrm{e}^{-\alpha_H d_H}$, where α_H is the absorption coefficient of the hot-side material and it could be temperature-dependent. The total radiation at boundary H_2 is P, which consists of the contribution from the material to the left of H_1 and the contribution from the material between H_1 and H_2. Since we know the contribution from the material to the left of H_1 is $P \cdot \mathrm{e}^{-\alpha_H d_H}$, the thermal radiation at H_2 for a hot-side with thickness d_H is $P \cdot \left[1 - \mathrm{e}^{-\alpha_H d_H}\right]$, as shown in Figure 14-3. The radiation spectrum for a GaAs hot-side of thickness 1 μm is shown in Figure 14-4.

14.3 Transmissions

The thermal radiation needs to be transmitted through boundaries H_2 and C_1 to enter the cold-side. (See Figure 14-5). At each boundary the radiation is reduced due to reflection. The reflection coefficient can be obtained from Eq. (8-140) in [45]:

$$\Gamma = \frac{1 - 1/\sqrt{\epsilon}}{1 + 1/\sqrt{\epsilon}}$$

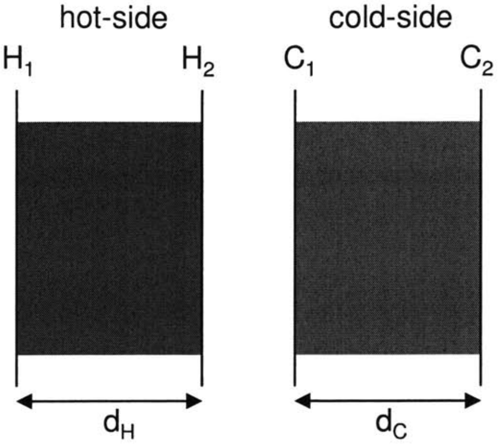

Figure 14-1: Finite-thickness of hot-side and cold-side

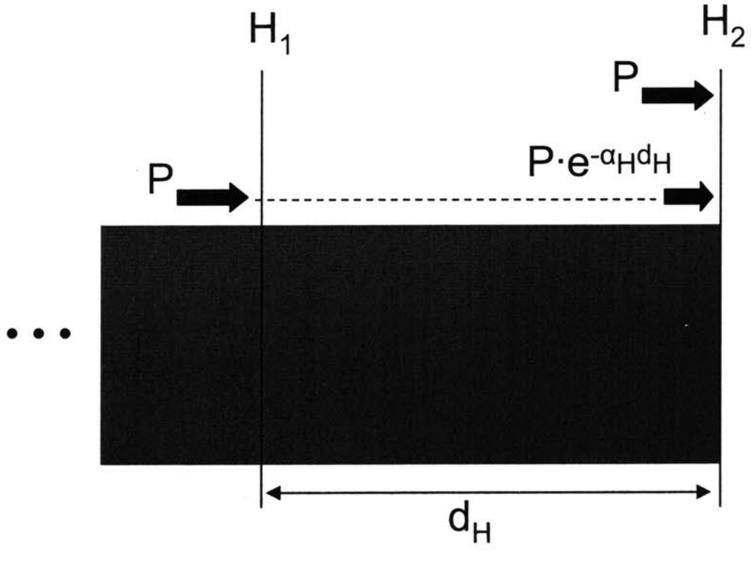

Figure 14-2: Thermal radiation for the case of a semi-infinite hot-side.

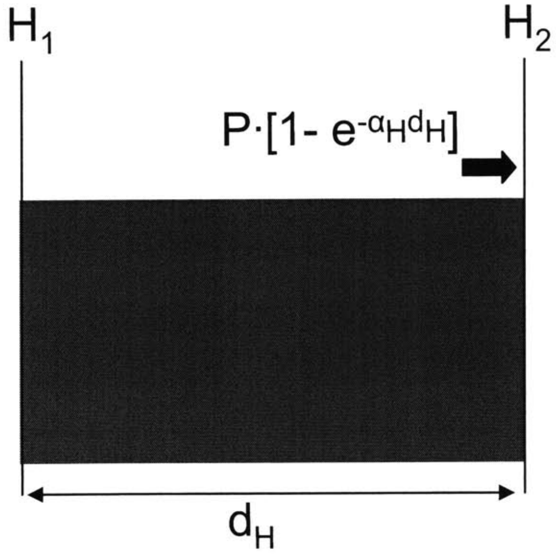

Figure 14-3: Thermal radiation for the case of a hot-side with finite thickness

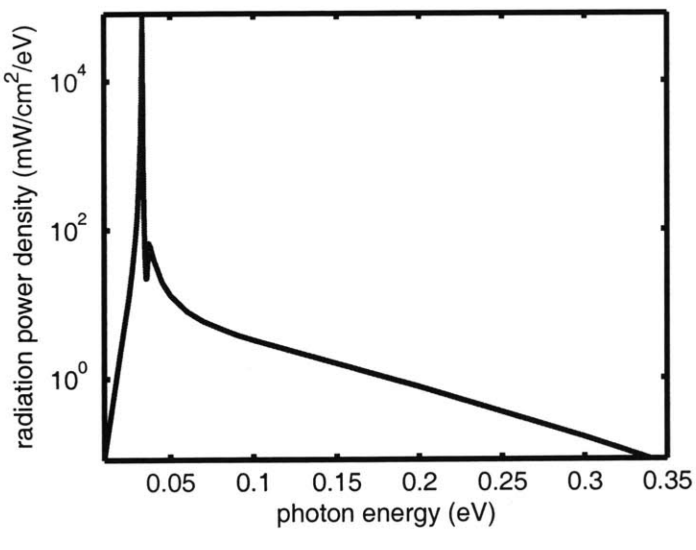

Figure 14-4: Radiation spectrum for GaAs of finite thickness 1 μm.

where ϵ is the dielectric constant of the hot-side or the cold-side. The amount of radiation impinging on H_2 is

$$P \cdot \left[1 - \mathrm{e}^{-\alpha_H d_H}\right].$$

The amount of radiation transmitted through H_2 is

$$P_1 = P \cdot \left[1 - \mathrm{e}^{-\alpha_H d_H}\right] \cdot \left[1 - |\Gamma_H|^2\right],$$

where Γ_H is the reflection coefficient for H_2. The amount of radiatioin entering into the cold-side is then

$$P_1 \left[1 - |\Gamma_C|^2\right],$$

where Γ_C is the reflection coefficient for C_1. The amount of radiation finally reaching C_2 is

$$P_1 \left[1 - |\Gamma_C|^2\right] \cdot \mathrm{e}^{-\alpha_C d_C},$$

where α_C is the absorption coefficient of the cold-side. Therefore the amount of radiation absorbed on the cold-side is

$$P_1 \left[1 - |\Gamma_C|^2\right] \cdot \left[1 - \mathrm{e}^{-\alpha_C d_C}\right]$$

The radiation that is not absorbed by the cold-side can be recycled by putting a reflector in back of the cold-side or using a TPV cell to convert the radiation.

14.4 Estimated loss

We use the above expression to evaluate the thermal radiation loss on the cold-side. Figure 14-6 shows the loss as a function of the hot-side thickness and the cold-side thickness. The achievable load power is greater than 50 mW/cm^2 for gaps smaller than 3 nm (Figure 12-3). When the hot-side and the cold-side thickness are less than

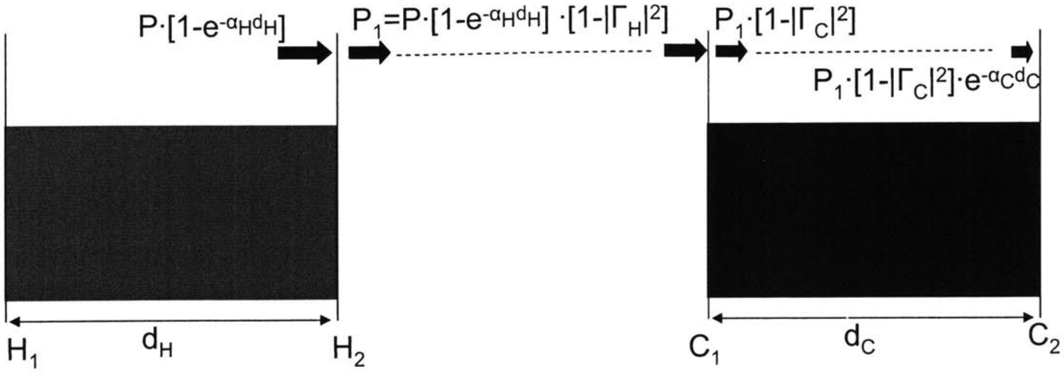

Figure 14-5: Amounts of radiation at various boundaries of the hot-side and the cold-side

1 μm the thermal radiation loss is less than 1.3 mW/cm^2, which is small compared to the achievable load power of 50 mW/cm^2 .

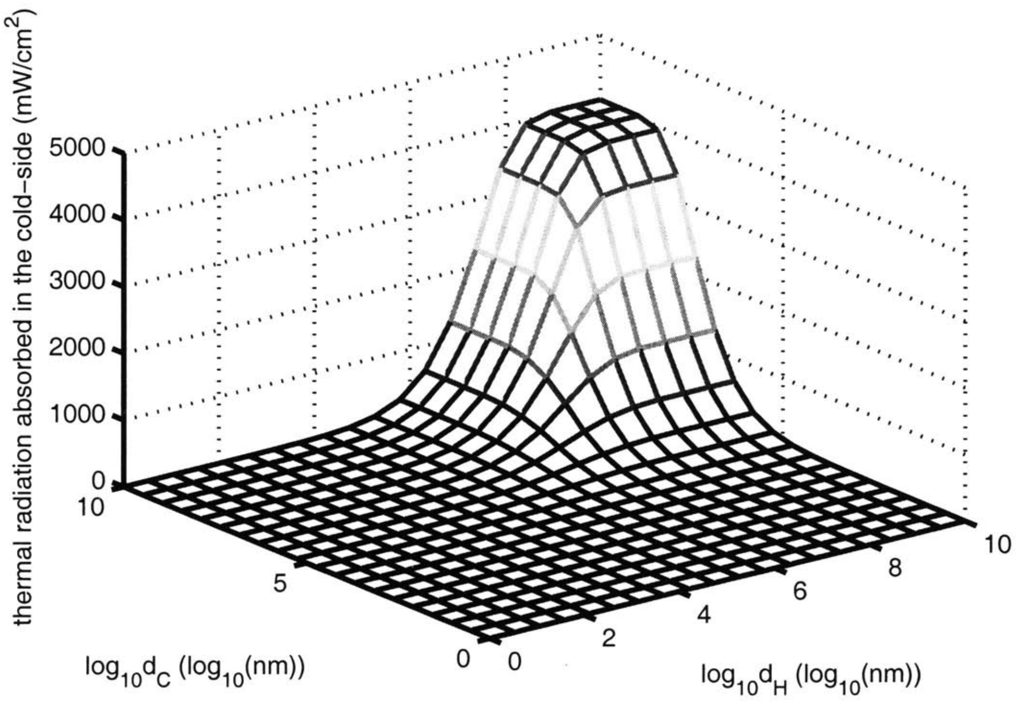

Figure 14-6: Thermal radiation loss as a function of the hot-side and the cold-side thicknesses

Chapter 15

Hot-side dielectrics design

In the previous chapter we have presented a quantum dot implementation of the quantum-coupled thermal to electric conversion device. One of the difficulties associated with that design is the spatial alignment of quantum dots on the hot-side with quantum dots on the cold-side. In addition, the hot-side temperature is limited as quantum dots diffuse at high temperatures and the device ceases to function as modeled at high temperatures. An alternative approach is to replace the hot side simply with a dielectric material that absorbs at the transition energy 92 meV of the cold-side dot 1. The transition energy is the energy difference between the two levels in dot 1. In this chapter we describe modeling and simulation results for such an implementation.

15.1 Basic model

Please see Figure 15-1 for an illustration of the device. The hot-side is now a dielectric material absorbing at the energy of 92 meV. The loss of an absorbing dielectric can be modelled as a reservoir comprising a continuum of harmonic oscillators [46]. Here we take the simple view of treating the loss as a reservoir of two-level dipoles. The circled two-level dipoles in Figure 15-1 represent the reservoir of dipoles responsible for the absorption of light. When the dielectric is heated, the excited electron in each dipole can transfer its excitation to the cold-side through Coulomb interaction and the transferred excitation can be turned into electrical work through the same cold-side converter as described previously. Shown in Figure 15-2 is the two-electron level diagram constructed for a reservoir of dipoles of level a and level b coupled to the cold-side quantum dot levels through a Coulomb interaction matrix element U. Transitions from state $|b, r_1\rangle$ to state $|a, r_3\rangle$ represent pumping electrons from state r_1 in reservoir R_1 to state r_3 in reservoir R_3 to do electrical work. Transitions from state $|b, r_1\rangle$ to state $|a, r_2\rangle$ represents energy transfer from the hot-side to the cold-side to excite an electron to level 2, but the electron loses its energy and relaxes into reservoir R_2, contributing to loss.

Following a similar approach to that of Chapter 6, we obtain the effective coupling matrix element U_{eff} between state $|b, r_1\rangle$ and state $|a, r_3\rangle$:

$$U_{\text{eff}} = \frac{UVW_1W_3}{d_{b,1}(d_{a,2}d_{a,3} - V^2) - U^2 d_{a,3}}$$

where

$$d_{b,1} = \epsilon_1 - E_1 + i\hbar\Gamma_{b,1}/2$$

$$d_{a,2} = \hbar\omega + \epsilon_1 - E_2 + i\hbar\Gamma_{a,2}/2$$

$$d_{a,3} = \hbar\omega + \epsilon_1 - E_3 + i\hbar\Gamma_{a,3}/2$$

$$\Gamma_{b,1} = \frac{2\pi}{\hbar} W_1^2 \rho_1(\epsilon_1)$$

$$\Gamma_{a,2} = \frac{2\pi}{\hbar} W_2^2 \rho_2(\hbar\omega + \epsilon_1)$$

$$\Gamma_{a,3} = \frac{2\pi}{\hbar} W_3^2 \rho_3(\hbar\omega + \epsilon_1)$$

The notations are as follows. ϵ_1 is the reservoir state r_1 energy. E_1, E_2, and E_3 are the energies of the cold-side levels 1, 2, and 3. W_1, W_2, and W_3 are the coupling matrix elements between levels 1, 2, 3 and their associated reservoir levels. ρ_1, ρ_2, and ρ_3 are the reservoir density of states. The energy spacing between the two levels a and b of the hot-side dipole is $\hbar\omega$.

In the last chapter, at a gap of 5 nm the Coulomb matrix element U between the hot-side and the cold-side quantum dot dipoles is calculated to be 2.5×10^{-4} eV, or $\hbar/U = 2.6$ ps, which is ten times longer than the cold-side relaxation rate. Even for a gap of 1 nm, the $\hbar/U = 0.76$ ps is still long. The hot-side dielectric dipoles are expected to be smaller than the transition dipole moment of an artificial quantum dot. In addition, most of the dipoles are distributed further away in the bulk of the hot-side. Hence the matrix element U between the hot-side dielectric dipoles and the cold-side quantum dot dipole is much smaller than the cold-side relaxation rates. In this case, we approximate the effective matrix element U_{eff} by omitting the U term in the denominator and we obtain

$$\frac{U_{\text{eff}}}{U} \approx \frac{V W_1 W_3}{d_{b,1}(d_{a,2}d_{a,3} - V^2)}.$$

The contribution from a hot-side dipole of level a and level b with energy spacing $\hbar\omega$ to the device current is then

$$I_{\text{dipole}} = q|U|^2 \int d\epsilon_1 \rho_1(\epsilon_1)\rho_3(\epsilon_1 + \hbar\omega)\frac{2\pi}{\hbar}|\langle r_a, r_3|\frac{U_{\text{eff}}}{U}|r_b, r_1\rangle|^2$$

$$\times\{p_{\text{low}}(\omega)p_1(\epsilon_1)\left[1 - p_3(\epsilon_1 + \hbar\omega)\right] - p_{\text{high}}(\omega)p_3(\epsilon_1 + \hbar\omega)\left[1 - p_1(\epsilon_1)\right]\}$$

where $p_{\text{low}}(\omega)$ is the thermal equilibrium probability that the dipole is in its lower energy state (level a) and $p_{\text{high}}(\omega)$ is the probability that the dipole is in the higher energy state (level b). The values of these two probabilities are

$$p_{\text{low}}(\omega) = \frac{1}{1 + \mathrm{e}^{-\hbar\omega/kT_h}}$$

$$p_{\mathrm{high}}(\omega) = \frac{\mathrm{e}^{-\hbar\omega/kT_h}}{1+\mathrm{e}^{-\hbar\omega/kT_h}}$$

To calculate the total device current, we integrate through all the dipoles with different frequencies and spatial positions. Because the dipoles in principle can have arbitrary orientation, we use the averaged Coulomb matrix element squared in the following expression.

From Chapter 9 we see that the dipole interaction energy between a hot-side dipole $\mathbf{d}_j$ and a cold-side dipole $\mathbf{d}_i$ is

$$U = \frac{4\epsilon_0\epsilon_2|\mathbf{d}_j|}{(\epsilon_0+\epsilon_1)(\epsilon_0+\epsilon_2)}$$

$$\times\sum_{n=0}^{\infty}\left(\frac{\epsilon_0-\epsilon_1}{\epsilon_0+\epsilon_1}\right)^n\left(\frac{\epsilon_0-\epsilon_2}{\epsilon_0+\epsilon_2}\right)^n\frac{1}{4\pi\epsilon_2|\Delta\mathbf{R}_{ijn}|^3}\left[\mathbf{d}_i\cdot\hat{\mathbf{n}}_j-3(\mathbf{d}_i\cdot\hat{\mathbf{i}}_{ijn})(\hat{\mathbf{i}}_{ijn}\cdot\hat{\mathbf{n}}_j)\right]$$

where $\hat{\mathbf{n}}_j$ is the unit vector in the direction of $\mathbf{d}_j$, and $\hat{\mathbf{i}}_{ijn}$ is a unit vector in the direction of $\mathbf{d}_i-\mathbf{d}_j$. The hot-side dipole in principle can have a random orientation, and we do an averaging to relate the expectation of the Coulombic matrix element squared to the dipole moment:

$$\langle|U|^2\rangle = \frac{\epsilon_0^2|\mathbf{d}_j|^2}{\pi(\epsilon_0+\epsilon_1)^2(\epsilon_0+\epsilon_2)^2}\left\langle\left|\sum_{n=0}^{\infty}\left(\frac{\epsilon_0-\epsilon_1}{\epsilon_0+\epsilon_1}\right)^n\left(\frac{\epsilon_0-\epsilon_2}{\epsilon_0+\epsilon_2}\right)^n\frac{1}{|\Delta\mathbf{R}_{ijn}|^3}\right.\right.$$

$$\left.\left.\times\left[\mathbf{d}_i-3(\mathbf{d}_i\cdot\hat{\mathbf{i}}_{ijn})\hat{\mathbf{i}}_{ijn}\right]\cdot\hat{\mathbf{n}}_j\right|^2\right\rangle$$

$$= \frac{\epsilon_0^2|\mathbf{d}_j|^2}{3\pi(\epsilon_0+\epsilon_1)^2(\epsilon_0+\epsilon_2)^2}\left|\sum_{n=0}^{\infty}\left(\frac{\epsilon_0-\epsilon_1}{\epsilon_0+\epsilon_2}\right)^n\left(\frac{\epsilon_0-\epsilon_2}{\epsilon_0+\epsilon_2}\right)^n\right.$$

$$\times \frac{1}{|\Delta \mathbf{R}_{ijn}|^3} \left[\mathbf{d}_i - 3(\mathbf{d}_i \cdot \hat{\mathbf{i}}_{ijn})\hat{\mathbf{i}}_{ijn} \right] \Bigg|^2 .$$

We define $f(\mathbf{r},\omega)$ as

$$f(\mathbf{r},\omega) = \frac{\epsilon_0^2}{3\pi(\epsilon_0+\epsilon_1)^2(\epsilon_0+\epsilon_2)^2} \left| \sum_{n=0}^{\infty} \left(\frac{\epsilon_0-\epsilon_1}{\epsilon_0+\epsilon_2} \right)^n \left(\frac{\epsilon_0-\epsilon_2}{\epsilon_0+\epsilon_2} \right)^n \frac{1}{|\Delta \mathbf{R}_{ijn}|^3} \left[\mathbf{d}_i - 3(\mathbf{d}_i \cdot \hat{\mathbf{i}}_{ijn})\hat{\mathbf{i}}_{ijn} \right] \right|^2$$

The total current with contributions from all the dipoles is expressed in the following integral:

$$\begin{aligned} I_{\text{total}} &= \frac{2\pi q}{\hbar} \int d^3\mathbf{r}\rho_r \int d\omega \rho_\omega(\omega) |\mathbf{d}_j|^2 f(\mathbf{r},\omega) \int d\epsilon_1 \rho_1(\epsilon_1) \rho_3(\epsilon_1 + \hbar\omega) \\ &\times |\langle r_a, r_3 | \frac{U_{\text{eff}}}{U} | r_b, r_1 \rangle|^2 \{ p_{\text{high}}(\omega) p_1(\epsilon_1) \left[1 - p_3(\epsilon_1 + \hbar\omega) \right] \\ &- p_{\text{low}}(\omega) p_3(\epsilon_1 + \hbar\omega) \left[1 - p_1(\epsilon_1) \right] \} \qquad (15.1) \end{aligned}$$

where ρ_r (assumed uniform) and ρ_ω are the spatial and spectral density of dipoles in the dielectric.

15.2 Absorption and dipoles

The equation relating the photoabsorption rate per unit volume and the dipole moments and the density of dipoles is from the Golden Rule [47]

$$\gamma = \frac{2\pi}{\hbar} |\mathbf{d}|^2 |\mathbf{E}_0|^2 \rho(E) \qquad (15.2)$$

where γ is the absorption rate, $\mathbf{d}$ is the dipole moment, $\mathbf{E}_0$ is the electric field of the light, and $\rho(E)$ is the density of dipoles per unit energy. Expressing γ in terms of the absorption coeffcient [47], we get

$$\gamma = \frac{\alpha S}{\hbar\omega} \qquad (15.3)$$

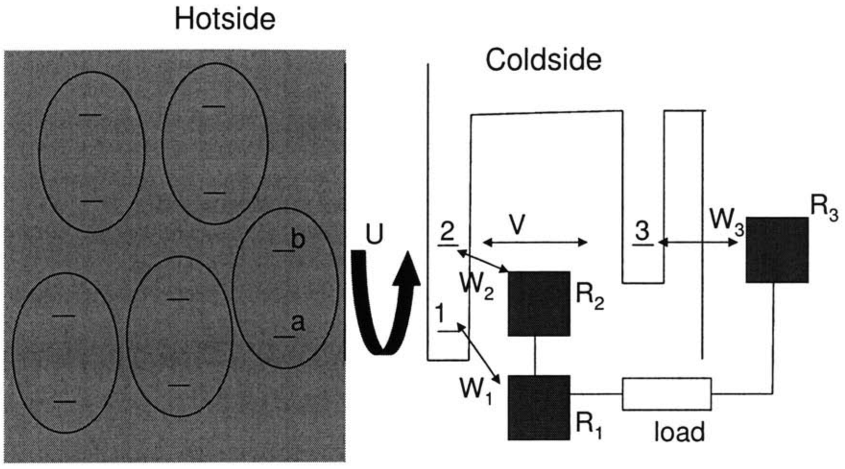

Figure 15-1: A schematic for the device structure with the hot-side being a dielectric material absorbing at the energy of 92 meV. The absorption of the dielectric is modeled as due to a reservoir of two-level dipoles each of which is circled in the diagram

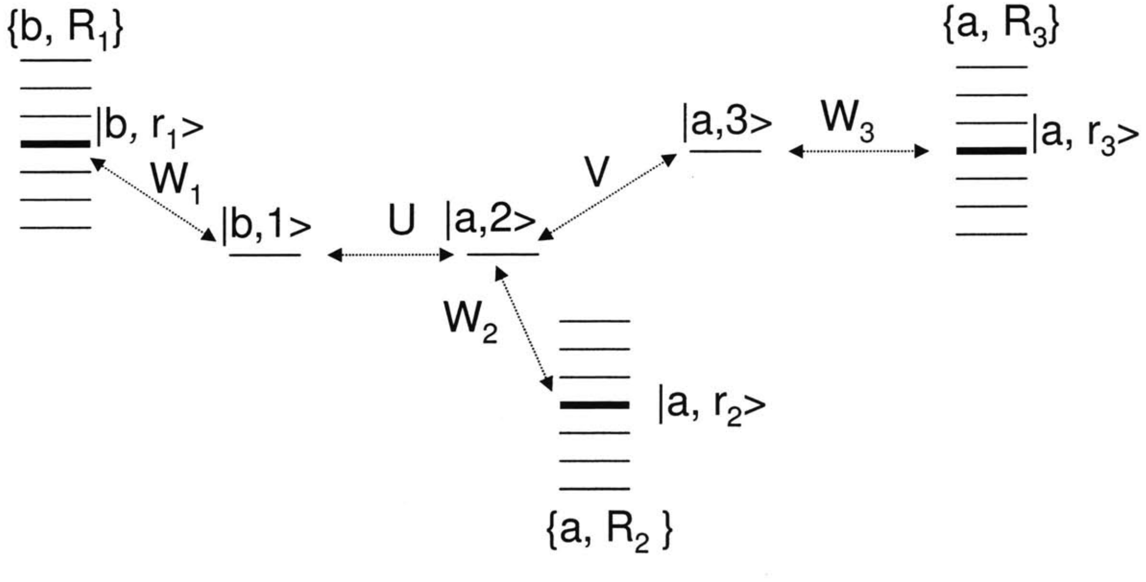

Figure 15-2: Two-electron level diagram constructed for a reservoir containing dipoles of level a and level b coupled to the cold-side quantum dot levels.

The intensity can be computed from the expectation value of the Poynting vector operator [47]

$$S = |\langle \hat{E} \times \hat{H} \rangle|$$

Applying the field operators quantized in a lossy medium [48]:

$$S = \sqrt{\frac{\epsilon_0}{\mu_0}} \langle (\mathbf{E}_0 + \mathbf{E}_0^*) \left(\mathbf{E}_0 \cdot (n+ik) + \mathbf{E}_0^*(n-ik)\right) \rangle = 4n\sqrt{\frac{\epsilon_0}{\mu_0}} \langle \mathrm{Re}\{\mathbf{E}_0\}^2 \rangle = 2n\sqrt{\frac{\epsilon_0}{\mu_0}} |\mathbf{E}_0|^2 \tag{15.4}$$

where n is the real part of the refractive index. Combining equations (15.2), (15.3), and (15.4) gives the absorption coefficient

$$\alpha = n\sqrt{\frac{\mu_0}{\epsilon_0}} \pi\omega |\mathbf{d}|^2 \rho(E)$$

The quantity $\rho(E)$ actually encompasses three components. The first component is the spatial density of dipoles: ρ_r. The second component is the density of two-level dipoles with energy spacing $\hbar\omega$: ρ_ω. The third component is the equilibrium probability that the dipole is in its lower enegy state, namely p_{low}. Altogether we have the following equation

$$\begin{aligned} \alpha(\omega) &= n(\omega)\sqrt{\frac{\mu_0}{\epsilon_0}} \pi\omega |\mathbf{d}|^2 p_{\mathrm{low}} \rho_r \rho_\omega(\omega) \\ &= \frac{n(\omega)}{1 + \mathrm{e}^{-\hbar\omega/kT}} \sqrt{\frac{\mu_0}{\epsilon_0}} \pi\omega |\mathbf{d}|^2 \rho_r \rho_\omega(\omega) \end{aligned}$$

Therefore we can express the integral involving the hot-side dipole moments, occupation probability, and density of states, as a function of the absorption coefficient:

$$|\mathbf{d}|^2 \rho_r p_{\mathrm{low}}(\omega) \rho_\omega(\omega) = \sqrt{\frac{\epsilon_0}{\mu_0}} \frac{\alpha(\omega)}{n\pi\omega} \tag{15.5}$$

Similaraly

$$|\mathbf{d}|^2 \rho_r p_{\mathrm{high}}(\omega) \rho_\omega(\omega) = \mathrm{e}^{-\hbar\omega/kT_h} \sqrt{\frac{\epsilon_0}{\mu_0}} \frac{\alpha(\omega)}{n\pi\omega} \tag{15.6}$$

From Eq. (15.1), Eq. (15.5), and Eq. (15.6), we formulate an expression for the current that can be evaluated given the refractive index and absorption coefficient data of the materials and the cold-side dipole moment $|\mathbf{d}_i|$:

$$I_{\text{total}} = \int d^3\mathbf{r} \int d\omega f(\mathbf{r},\omega)\alpha(\omega)\frac{2q}{n(\omega)\hbar\omega}\sqrt{\frac{\epsilon_0}{\mu_0}} \int d\epsilon_1 |\langle r_a, r_3|\frac{U_{\text{eff}}}{U}|r_b, r_1\rangle|^2 \rho_1(\epsilon_1)\rho_3(\epsilon_1+\hbar\omega)$$

$$\times\{\mathrm{e}^{-\hbar\omega/kT_h} p_1(\epsilon_1)\left[1 - p_3(\epsilon_1 + \hbar\omega)\right] - p_3(\epsilon_3 + \hbar\omega)\left[1 - p_1(\epsilon_1)\right]\}$$

We can evaluate the above expression to obtain the load current. A similar formula can be derived for the loss current. Dividing the load current by the sum of the load and the loss currents gives us the efficiency.

15.3 Aluminum oxide Al_2O_3 results

We apply the model described above to the case where the hot-side is aluminum oxide Al_2O_3 as this material has absorptions around the energy of 92 meV. The room temperature optical constants of aluminum oxide are obtained from [49]. The absorption coefficient for the temperature of 600 K is inferred from the room temperature values through Eq. 15.5. There appears to be two sets of inconsistent data from [50] and [51], and we have chosen to use the data from [50]. We have used the data for the ordinary polarization because it has one plane of polarization as opposed to the extraordinary polarization which is only in one direction. Therefore, we expect the data for the ordinary polarization to play a dominant role.

Figure 15-3 shows the load power as a function of voltage for the case of an aluminum oxide hot-side with a 5 nm gap. The maximum power is 76 mW/cm^2 at the voltage of 29 mV with a corresponding efficiency of 28%. Figure 15-4 shows the efficiency as a function of voltage. The maximum efficiency is 42% at 41 mV. The load power corresponding to a maximum efficiency is 34 mW/cm^2.

The power has a dependence of $1/R^6$ for the hot-side quantum dot design, but the dependence for the hot-side dielectric case is slower. The maximum load power drops from 620 mW/cm^2 at a 1 nm gap to 0.03 mW/cm^2 at a 100 nm gap. The load power is higher than that of the quantum dot design. The maximum thermal power drops from around 4 W/cm^2 at 1 nm gap to 478 mW/cm^2 at 5 nm gap to 0.2 mW/cm^2 at 100 nm gap. At larger gaps, the dipole-dipole interaction decreases as $1/R^3$ and the Coulomb coupling matrix element squared decreases as $1/R^6$. The volume of dipoles the cold-side dipole couples to increases as R^3. Therefore the overall dependence is $1/R^3$. We can show this more formally. If we integrate the Coulomb matrix element squared over the hot-side dipole located at z below the surface with a lateral displacement ρ from the cold-side dipole we obtain:

$$\int_0^\infty dz \int_0^\infty \frac{2\pi\rho d\rho}{((z+R)^2+\rho^2)^{3/2}} = \frac{1}{R^3}\int_0^\infty d(z/R) \int_0^\infty \frac{2\pi\rho/Rd(\rho/R)}{((z/R+1)^2+\rho^2/R^2)^{3/2}}$$

$$= \frac{1}{R^3}\int_0^\infty dt \int_0^\infty \frac{2\pi x dx}{((t+1)^2+x^2)^{3/2}}$$

The efficiency is rather independent of the gap thickness from this model. There are parasitic losses that we have not considered. Thermal radiation from the hot-side can be absorbed on the cold-side and this loss is discussed in the next section. In addition, heat transfer via Coulomb coupling between the dipoles on the two sides leads to loss as well. This loss has not been evaluated.

15.4 Thermal radiation loss

The thermal radiation emitted from the hot-side can also be absorbed on the cold-side to give loss. Therefore, we would like to minimize this radiation. As discussed in

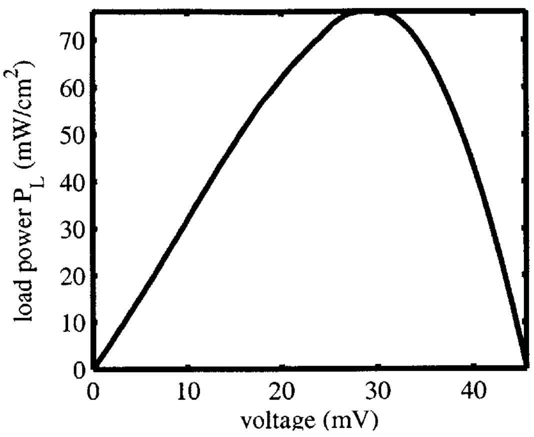

Figure 15-3: Load power as a function of voltage for the hot-side aluminum oxide design. The maximum power is 76 mW/cm^2 at the voltage 29 mV with a corresponding efficiencyof 28%

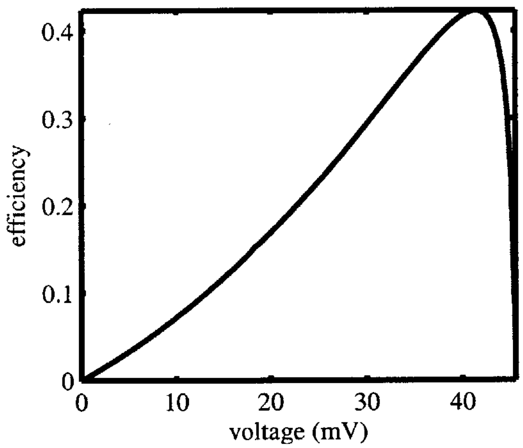

Figure 15-4: Efficiency as a function of voltage for the hot-side aluminum oxide design. The maximum efficiency is 42% at the voltage 41 mV with a corresponding load power of 34 mW/cm^2

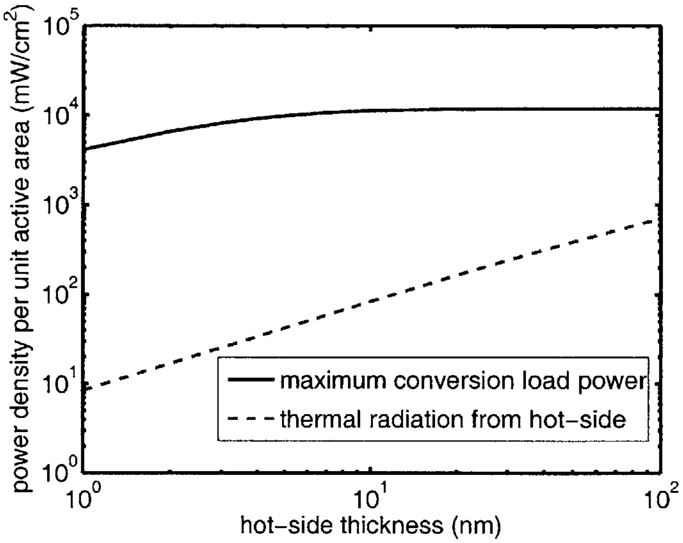

Figure 15-5: The maximum device load power (with 5 nm gap) and the thermal radiation as a function of the hot-side thickness.

Chapter 14, decreasing the hot-side thickness reduces the thermal radiation. However, in the hot-side dielectrics design decreasing the hot-side thickness reduces the amount of emitter dipoles on the hot-side and hence decreases the power throughput. Figure 15-5 shows the maximum device load power per unit active area (with a 5 nm gap) as well as the thermal radiation versus the hot-side thickness for the hot-side aluminum oxide design. We can see clearly the trade-off between increasing the load power and decreasing the thermal radiation. Figure 15-6 shows the spectrum of the thermal radiation for the hot-side thickness of 10 nm.

Alternatively we can decrease the cold-side thickness while keeping the infinite hot-side thickness. Following the approach described in Chapter 14 we calculate this loss as a function of the cold-side thickness (Figure 15-7). For a cold-side thickness of less than 300 nm, the thermal radiation loss would be less than 1 mW/cm^2 and small compared to the load power of 620 mW/cm^2 which is achievable at a gap of 1 nm and 76 mW/cm^2 achievable at a gap of 5 nm.

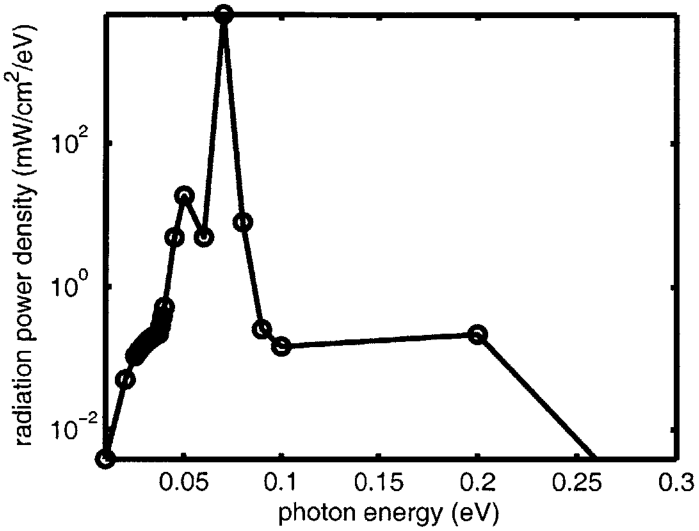

Figure 15-6: the spectrum of the thermal radiation for the hot-side thickness of 10 nm

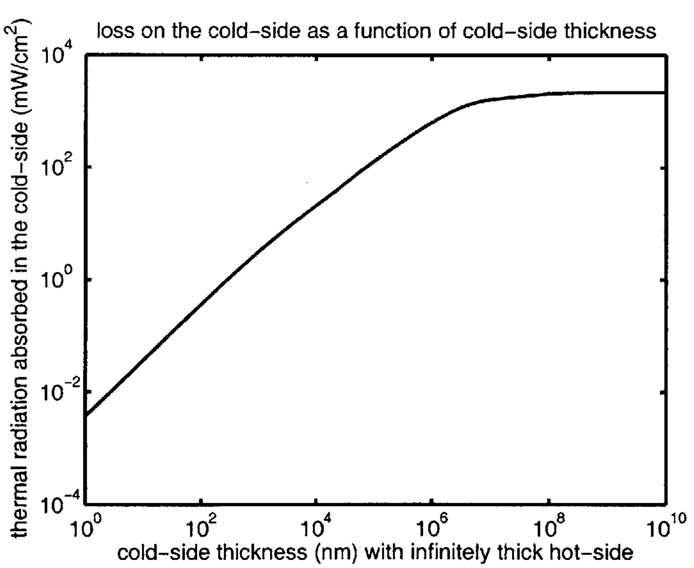

Figure 15-7: Thermal radiation loss on the cold-side as a function of cold-side thickness while the hot-side aluminum is assumed a thickness of infinity.

15.5 Summary

We have described a design where the hot-side is free of the restriction of quantum dot alignment with the cold-side. Instead, a dielectric which absorbs at the cold-side transition energy 92 meV is used as the hot-side. The load power is increased and has a slower dependence on gap thickness due to the presence of a reservoir of dipoles in the dielectric. In addition, the hot-side dielectric can operate at a higher temperature, which is detrimental to the hot-side quantum dot design as at high temperatures the quantum dots suffer from diffusion. Another advantage of this design is the potential for higher throughput. A hot-side dielectric material with a stronger absorption at 92 meV would increase the load power of such a device.

Chapter 16

Quantum model of the image charge

We have examined the case where the hot-side emitter is an aluminum oxide dielectric. Another possibility for the emitter is a material that supports surface carriers, for example a conductor or a highly-doped semiconductor. An electron q in the cold-side dot 1 induces an image charge on the hot-side if the hot-side is a good conductor. The Coulomb interaction between chagre q and the induced image charge could lead to excitation transfer. Our model described in previous chapters can be adapted to analyze this situation, but we need to figure out a way to calculate the coupling matrix element U. The strategy here is to first construct a classical model and a quantum model for the same problem and then extract matrix element U from the classical result. Below we detail the derivations.

16.1 Classical equation of motion

Let us first consider a problem similar to the three-region problem in Chapter 9 but with the charge q oscillating back and forth as $d\cos(\omega t)$. The gap thickness is L and charge q is located distance h from the boundary between medium 1 and the gap. Medium 2 is assumed to be a metal, a semi-metal, or a highly-doped semiconductor. Refer to Figure 16-1. Charge q moving above a metal surface with distance R

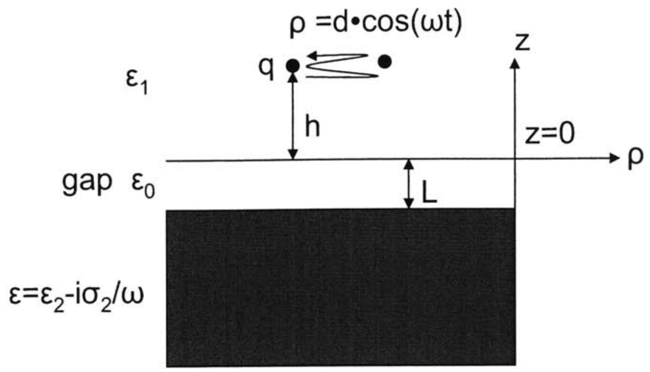

Figure 16-1: Charge q oscillating above a three-region configuration.

experiences a friction force due to its effect on the image charges in the metal [52]. Depending on whether charge q is moving parallel or vertical to the metal surface, the friction coefficients in Gaussian c.g.s units are [53, 54]

$$\Gamma_{\parallel} = \frac{q^2}{16\pi\sigma R^3}$$

$$\Gamma_{\perp} = \frac{q^2}{8\pi\sigma R^3}$$

where σ is the conductivity of the metal. Note that the above results assume the condition of a good conductor (Eq. (24) of [54]):

$$\frac{cv}{\sigma h} \ll 1$$

where c is the speed of light in vacuum and v is the velocity of charge q. What the above criterion says is basically that the conductivity of the material needs to be sufficiently high for the friction coefficients to hold. In our three-region problem the electric field needs to transmit through the boundary between medium 1 and the gap. Thus we amend the above two equations by introducing the transmission coefficient t_{10} to obtain

$$\Gamma_{\parallel} = \frac{t_{10}q^2}{16\pi\sigma(h+L)^3}$$

$$\Gamma_{\perp} = \frac{t_{10}q^2}{8\pi\sigma(h+L)^3}$$

where

$$t_{10} = \frac{2\epsilon_0}{\epsilon_1 + \epsilon_0}.$$

If there is no friction force, charge q oscillates as $\rho = d \cdot \cos(\omega t)$ and it experiences an external force $md\omega^2 \cos(\omega t)$. With the existence of the friction force from the image charges and assuming medium 1 has a relaxation time τ_1, the motion of charge q is governed by the following classical equation of motion:

$$m\left[\frac{d^2\rho}{dt^2} + \left(\frac{1}{\tau_1} + \Gamma\right)\frac{d\rho}{dt}\right] = -\, m\omega^2 d\cos(\omega t)$$

where Γ is equal to the parallel friction coefficient $\Gamma_{\|}$ or vertical friction coefficient $\Gamma_{\perp}$ depending on the orientation of charge q motion. Solving the above equation gives

$$\rho(t) = \mathrm{Re}\left\{\frac{-md\omega^2 e^{i\omega t}}{-m\omega^2 + im(1/\tau_1 + \Gamma)}\right\}.$$

For the sake of clarity, we change the phase and rewrite $\rho(t)$ as

$$\rho(t) = \frac{md\omega^2 \sin(\omega t)}{\sqrt{m^2\omega^4 + m^2(1/\tau_1 + \Gamma)^2}}$$

and the friction force is

$$f(t) = \frac{\Gamma md\omega^3 \cos(\omega t)}{\sqrt{m^2\omega^4 + m^2(1/\tau_1 + \Gamma)^2}}$$

16.2 Two-level approximation

The simplest quantum model for the image charge is a two-level approximation. The two levels are degenerate because the image charge is a free carrier. Let's denote the image charge two levels as $|\phi_a\rangle$ and $|\phi_b\rangle$. The oscillating charge q is also modelled as two levels $|\phi_1\rangle$ and $|\phi_2\rangle$. The image charge and charge q have individual Hamiltonians

$$\hat{H}_i \;=\; |\phi_a\rangle E_a \langle\phi_a| \;+\; |\phi_b\rangle E_b \langle\phi_b|$$

$$\hat{H}_q \;=\; |\phi_1\rangle E_1 | \langle\phi_1| \;+\; |\phi_2\rangle E_2 \langle\phi_2|$$

where subscript i stands for image charge and q stands for charge q. Note that the energy spacing of charge q satisfies $(E_2 - E_1)/\hbar = \omega$ in correspondence to the classical problem.

The electrostatic coupling between the image charge and charge q is represented as

$$\hat{U} \;=\; U\left[|\phi_a\rangle|\phi_2\rangle\langle\phi_b|\langle\phi_1| + |\phi_b\rangle|\phi_1\rangle\langle\phi_a|\langle\phi_2|\right] + U\left[|\phi_a\rangle|\phi_1\rangle\langle\phi_b|\langle\phi_2| + |\phi_b\rangle|\phi_2\rangle\langle\phi_a|\langle\phi_1|\right]$$

Note that $|\phi_a\rangle$ and $|\phi_b\rangle$ are degenerate and hence there are twice as many terms in the above equation as the number of U coupling terms in Eq. (2.1).
The overall Hamiltonian is then

$$\hat{H} \;=\; \hat{H}_i \;+\; \hat{H}_q \;+\; \hat{U}.$$

For a product wavefunction of the image charge and charge q

$$\psi \;=\; \psi_i(t)\psi_q(t)$$

the Schrödinger's equation reads

$$i\hbar\frac{\partial|\psi\rangle}{\partial t} \;=\; i\hbar|\psi_i\rangle\frac{\partial|\psi_q\rangle}{\partial t} \;+\; i\hbar|\psi_q\rangle\frac{\partial|\psi_i\rangle}{\partial t} \;=\; \hat{H}|\psi\rangle$$

$$= \; |\psi_q\rangle\left(\hat{H}_i|\psi_i\rangle\right) \;+\; \left(\hat{U}|\psi_q\rangle\right)|\psi_i\rangle \;+\; |\psi_i\rangle\left(\hat{H}_q|\psi_q\rangle\right) \;+\; \left(\hat{U}|\psi_i\rangle\right)|\psi_q\rangle$$

We decompose the above equation into the following two equations

$$i\hbar|\psi_q\rangle\frac{\partial|\psi_i\rangle}{\partial t} = |\psi_q\rangle\left(\hat{H}_i|\psi_i\rangle\right) + \left(\hat{U}|\psi_q\rangle\right)|\psi_i\rangle \tag{16.1}$$

$$i\hbar|\psi_i\rangle\frac{\partial|\psi_q\rangle}{\partial t} = |\psi_i\rangle\left(\hat{H}_q|\psi_q\rangle\right) + \left(\hat{U}|\psi_i\rangle\right)|\psi_q\rangle$$

multiply Eq. (16.1) by $\langle\psi_q|$ gives the evolution equation for the image charge:

$$i\hbar\frac{\partial|\psi_i\rangle}{\partial t} = \hat{H}_i|\psi_i\rangle + \langle\psi_q|\hat{U}|\psi_q\rangle|\psi_i\rangle \tag{16.2}$$

In order to infer the matrix element U from the classical equations, we construct a charge q wavefunction that would match the classical results ($\omega_1 = E_1/\hbar$, $\omega_2 = E_2/\hbar$):

$$|\psi_q\rangle = c_1(t)|\phi_1\rangle + c_2(t)|\phi_2\rangle$$

where

$$c_1(t) \equiv r_1 \mathrm{e}^{-i\omega_1 t} \tag{16.3}$$

$$c_2(t) \equiv r_2 \mathrm{e}^{-i\omega_2 t} \tag{16.4}$$

and

$$r_1 \equiv \frac{1}{2}\left[\sqrt{1+\frac{md\omega^2}{\sqrt{m^2\omega^4+m^2(1/\tau_q+\Gamma)^2}}}+\sqrt{1-\frac{md\omega^2}{\sqrt{m^2\omega^4+m^2(1/\tau_q^2+\Gamma)^2}}}\right]$$

$$r_2 \equiv \frac{1}{2}\left[\sqrt{1+\frac{md\omega^2}{\sqrt{m^2\omega^4+m^2(1/\tau_q+\Gamma)^2}}}-\sqrt{1-\frac{md\omega^2}{\sqrt{m^2\omega^4+m^2(1/\tau_q+\Gamma)^2}}}\right].$$

Note that r_1 and r_2 satisfy

$$r_1^2 + r_2^2 \;=\; 1$$

$$r_1 \cdot r_2 \;=\; \frac{md\omega^2}{2\sqrt{m^2\omega^4 + m^2(1/\tau_q + \Gamma)^2}} \tag{16.5}$$

We assume the dipole length of $|\phi_1\rangle$ and $|\phi_2\rangle$ to be d and they are out of phase by $-i/2$:

$$\langle\phi_2|\rho|\phi_1\rangle = de^{i\pi/2}$$

The expectation of the position of the wavefunction matches the oscillation in the classical model

$$\langle\psi_q|\rho|\psi_q\rangle \;=\; r_1^2\langle\phi_1|\rho|\phi_1\rangle \;+\; r_2^2\langle\phi_2|\rho|\phi_2\rangle \;+\; 2\mathrm{Re}\{c_2^* c_1\langle\phi_2|\rho|\phi_1\rangle\}$$

From Eq. (16.3), Eq. (16.4), and Eq. (16.5) we see that the oscillation term in the above equation is

$$2\mathrm{Re}\{c_2^* c_1\langle\phi_2|\rho|\phi_1\rangle\} = \frac{md\omega\sin(\omega t)}{\sqrt{m^2\omega^4 + m(1/\tau_q + \Gamma)^2}}$$

which corresponds to the oscillation as described in Eq. (16.1). Given the wavefunction $|\phi_1\rangle$, we evaluate the coupling matrix element in Eq. (16.2):

$$\langle\psi_q|\hat{U}|\psi_q\rangle \;=\; U\left[|\phi_a\rangle\,(c_1^*c_2 + c_1c_2^*)\,\langle\phi_b| + |\phi_b\rangle\,(c_1^*c_2 + c_1c_2^*)\,\langle\phi_a|\right]$$

$$= \frac{Um\omega^2\cos(\omega t)}{\sqrt{m^2\omega^4 + m(1/\tau_q + \Gamma)^2}}\left[|\phi_a\rangle\langle\phi_b| + |\phi_b\rangle\langle\phi_a|\right]$$

Therefore, the equivalent coupling matrix element between the two image charge levels is

$$U(t) \;=\; \frac{Um\omega^2\cos(\omega t)}{\sqrt{m^2\omega^4 + m(1/\tau_q + \Gamma)^2}}. \tag{16.6}$$

From Eq. (18.6) in [10], a forced two-level system has a coupling matrix element

$$U(t) = -F(t)\langle\phi_a|\rho|\phi_b\rangle \tag{16.7}$$

where the force $F(t)$ is the force on the image charge, and is equal to the negation of the force on charge q:

$$F(t) = -f(t) = \frac{-\Gamma m d\omega^3 \cos(\omega t)}{\sqrt{m\omega^4 + m(1/\tau_1 + \Gamma)^2}}$$

The image charge dipole length is presumed to be the same as the charge q dipole length $\langle\phi_a|\rho|\phi_b\rangle = d$. Therefore Eq. (16.7) becomes

$$U(t) = \frac{-\Gamma m d^2\omega^3 \cos(\omega t)}{\sqrt{m\omega^4 + m(1/\tau_1 + \Gamma)^2}}$$

Compare the above equation with Eq. (16.6) gives

$$U = -\Gamma\omega d^2 \tag{16.8}$$

which is the Coulomb coupling matrix element between charge q and the induced image charge.

16.3 Example calculations

We compute the case where the hot-side is metallic barium and the cold-side is the same as in previous dot-dot and dielectric-dot designs. The choice of barium is because it has a relatively high resitivity. Barium has a resistivity of 6×10^{-7} ohm · m at 273 K [55], assuming a linear temperature dependence of resistivity [55], we expect the resistivity at 600 K to be 1.32×10^{-6} ohm · m or 1.47×10^{-16} s in c.g.s. unit. The electron charge is 4.8×10^{-10} esu. The dipole length in dot 1 of the cold-side is $d =$ 3.5 nm and the energy spacing between the two levels in dot 1 is 92 meV, which is equivalently $\omega = 1.4 \times 10^{14}$ s^{-1}. Given the dot size (145 Å) × (45 Å) × (45 Å), we take h to be the dot-center value 22.5 Å. Medium 1 is GaAs with a refractive index squared 10.69 at 92 meV, interpolated from [56]. Assuming we have a tiny gap of

$L = 5$ nm, the parallel friction coefficient is

$$\Gamma_{\parallel} = \frac{t_{10}q^2}{16\pi\sigma(h+L)^3} = 3.03 \times 10^{-19} \text{ gm} \cdot \text{sec}^{-1} = 3.03 \times 10^{-22} \text{ kg} \cdot \text{sec}^{-1}$$

From Eq. (16.8) the Coulombic coupling strength is 3.25×10^{-6} eV. The relaxation time of barium at 273 K is 1.9 fs [55]. Assuming an inverse linear temperature dependence, the relaxation time at 600 K is approximately 0.86 fs. Given the above parameters, we can compute the device performance. The efficiency (Figure 16-2) is slightly lower but is in general agreement with those obtained for the dot-dot and dielectric-dot designs. The load power (Figure 16-3) has similar shape but is almost six orders of magnitude smaller than that of the dielectric-dot design due to the small Coulombic coupling matrix element. Note that the plasma frequency of barium (with free electron density 3.15×10^{28} m^{-3}[55]) is

$$\omega_P = \sqrt{\frac{3.15 \times 10^{28} \cdot (1.6 \times 01^{-19})^2}{9.1 \times 10^{-31} \cdot 8.85 \times 10^{-12}}} = 10^{16} \text{ rad/s}$$

Therefore the cold-side dot 1 transition with frequency 1.4×10^{14} rad/s couples very weakly to the plasmon which is far off resonance. It is possible to replace barium with a doped semiconductor with a plasma frequency matched to the cold-side transition energy to enhance the coupling.

16.4 Discussion

The above analyses are only valid when the emitter is a good conductor, as noted in the first section. However, when the conductivity is high, the friction coefficient would be low, leading to a small Coulomb coupling matrix element U and low load power. It is possible to use less-conducting materials (with lower plasma frequencies) for the emitter in the hope of increasing the Coulombic coupling. However, it would require further modeling efforts to anaylze such cases.

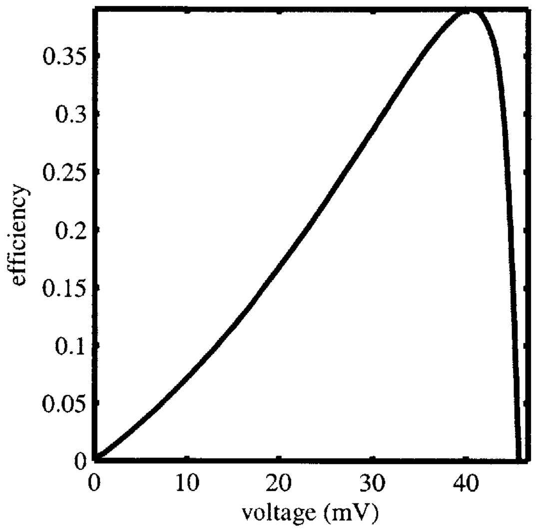

Figure 16-2: Efficiency as a function of voltage for the hot-side barium design. The maximum efficiency is 39% at the voltage 40.4 mV with corresponding load power 5.784×10^{-6} mW/cm^2

.

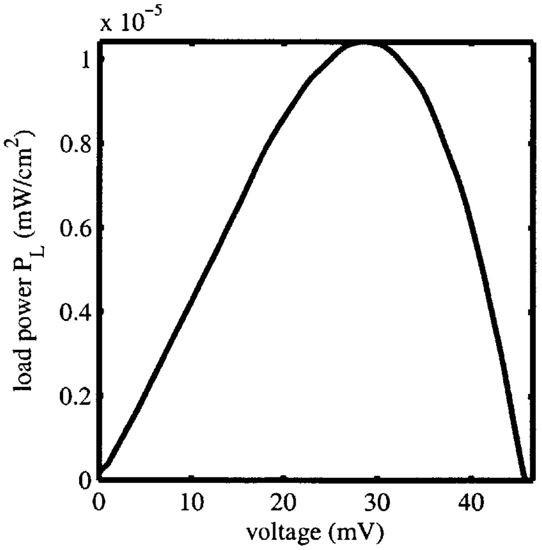

Figure 16-3: Load power as a function of voltage for the hot-side barium design. The maximum load power is 10^{-5} mW/cm^2 at the voltage 28.4 mV with corresponding efficiency 26.6%

Chapter 17

Conclusions

The thermal to electric conversion scheme analyzed in this thesis work is based on two concepts – (1) use of Coulomb coupling to increase throughput power/area, and (2) restriction of levels to try to improve efficiency. Coulomb coupling seems to work in our model, at least per unit active area. One can exceed the black body limit with Coulomb coupling, but the gap has to be very small. We found good power per unit active area at nano-scale gaps (see Figure 17-1 for a plot of the load power per unit active area for the case of alumina hot-side at 5 nm gap).

The designs also achieve very high efficiency, because efforts have been made to conserve entropy. The excitation transfer via Coulomb coupling is isentropic. The electron tunneling process is also isentropic. This model allows one in principle to keep the losses low and efficiency high.

Note that in our present calculation we have neglected Coulomb-coupled heat flow, which is expected to be the dominant loss mechanism. We have derived a formula for the evaluation of this loss in Appendix C and a calculation will be carried out in the future.

As mentioned in Chapter 4, the quantum-coupled single-electron conversion scheme can act as a refrigerator when the voltage is in a certain range. This application has

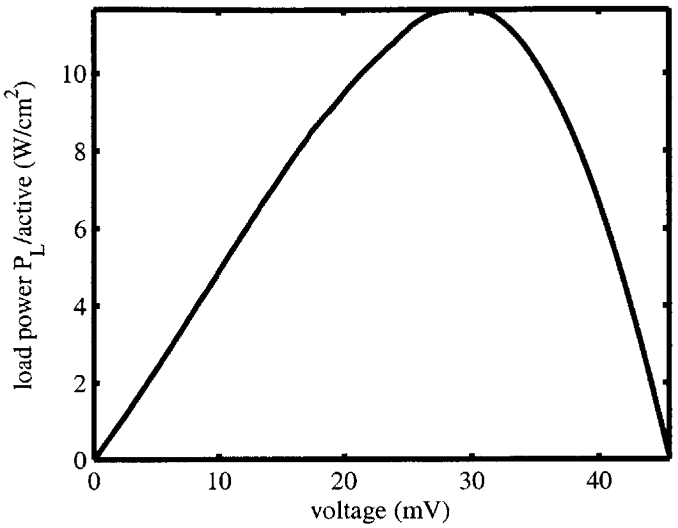

Figure 17-1: Load power per unit active area for the hot-side alumina design at 5 nm gap

not been properly analyzed and further explorations are needed.

17.1 Models

We have developed several models for analyzing our proposed thermal to electric conversion scheme. The first Bloch equations model gives good intuition on the device behavior and the different operation regimes. The Bloch equations model can also be easily evaluated to give numerical device characteristics. However, it is shown that the Bloch equations model is inconsistent with thermodynamics. The brute-force numerical approach is put forth as an alternative method for analyzing the scheme. Even though the brute-force numerical approach works well on simple problems, this approach is very computation-costly and it is not feasible to generalize the method to model complex problems such as our conversion scheme. The secular equations partitioning method augmented with loss is then developed as our working model. This model is consistent with thermodynamics and gives sensible numerical results.

To apply the secular equations model to specific designs, we considered detailed calculations of the Coulomb interaction energy and quantum dot electron wavefunctions, which give us the input parameters to the secular equations model. A design that can be readily analyzed by the secular equations model is a basic quantum dot design of the conversion scheme, where both the hot-side emitter and the cold-side converter consist of an array of quantum dots. It is also realized that the hot-side emitter can be replaced by a dielectric material or a conductor. Models for these two cases are developed and the device performance is analyzed.

17.2 Original contributions

Given a new quantum-coupled thermal to electric conversion scheme, this thesis work aims at understanding and analyzing the behavior and potential of devices implementing the new conversion scheme.

The full set of Bloch equations is developed based on an initial analysis by Prof. Hagelstein. Equilibrium values are incorporated into the equations. Expressions for the device figures such as current, power, and efficiency are derived. The Bloch equations are simplified to allow interpretations of the different regimes of device operation. Bloch equations are evaluated numerically to give device characteristics for the on-resonance case. Inconsistency between the Bloch equations and thermodynamics is identified when analyzing the off-resonance case.

In wrestling with the proper inclusion of loss in our models, A brute-force numerical method is implemented to solve simple problems. Secular equations partitioning method is extended to include loss and to verify the results from the brute-force numerical approach. The secular equations model is developed for the conversion scheme and expressions for the device characteristics are derived. Non-uniform grid Simpson integration in energy and matrix inversion with LU decomposition is used to implement the numerical simulations from the secular equations model.

Finite-difference equations for the one-dimensional, two-dimensional, and three-dimensional Schrodinger's equation are developed for the potential well problems. A quantum dot design of the thermal to electric converter is constructed. Quantum dot electron wavefunctions and energies are calculated from the finite-difference method. The device performance of the quantum dot design is numerically evaluated. An adapted model for the hot-side dielectric design is developed and implemented to give numerical results. Another model for the hot-side conductor design is constructed and numerical simulations are carried out.

17.3 Future prospects

The new thermal to electric conversion scheme seems to have an advantage of having a high efficiency exceeding 40% and load power per unit active area larger than 10 W/cm^2 (for a hot-side alumina design at 5 nm gap). To further improve the load power, one may explore the possibility of increasing the load power by packing the device units more densely. One may also try to use materials with lower dielectric constants in the hope of increasing the Coulomb coupling. Also, it is possible to obtain a larger transition dipole on the cold-side by using different materials. For the hot-side dielectric design, one possibility is to find highly absorbing (emitting) dielectric materials at the conversion frequency to increase the load power. Using doped semiconductors as the emitter is one case that has not yet been properly analyzed and further modeling is required.

The cold-side converter presents great fabrication challenges. As described in Chapter 11, research in the fields of quantum dot and nanowire fabrication has shown promising results. Other nano-structures which we have not considered might also exhibit similar quantum effects to be used to implement the conversion scheme. It is our hope that this work would stimulate further research efforts in both nano-fabrication methods and energy conversion concepts.

Appendix A

P_A computation

In this and subsequent subsections, we may denote $E_2^h - E_0^h = E_2^c - E_1^c = \Delta E$, and $\frac{\mu_b^c - \mu_a^c}{q} = \Delta V$, where q is the electron charge. We assume that N_{0b}, N_{0a}, N_{1b}, N_{1a}, N_{2b}, and N_{2a} are all constants equal to their equilibrium values and act as sources to our system of equations. In order to make this assumption consistent with our Bloch equations, we need to make $T_a^c = T_b^c = 0$ so that changes on the rest of the N's do not result in changes on N_{0b}, N_{0a}, N_{1b}, N_{1a}, N_{2b}, and N_{2a}.

From equations (3.35), (3.34), (3.37), (3.36), and (3.33), we can eliminate Q_C and P_C to obtain the following two equations:

$$P_A \, i_A + P_B \, i_B = 2\frac{U}{\hbar}\left[N_{21} - N_{12}\right] \tag{A.1}$$

$$P_A \, j_A + P_B \, j_B = 2\frac{V}{\hbar}\left[N_{13} - N_{12}\right] \tag{A.2}$$

$$i_A = \frac{1}{T_A} + \left(\frac{V}{\hbar}\right)^2 T_C + \frac{\Delta\Omega \, T_C \, \frac{V}{\hbar}}{\frac{1}{T_C} + \Delta\Omega^2 \, T_C + \left(\frac{V}{\hbar}\right)^2 T_A + \left(\frac{U}{\hbar}\right)^2 T_B} \tag{A.3}$$

$$i_B = \frac{V}{\hbar}\frac{U}{\hbar} T_C - \frac{\frac{U}{\hbar}\,\omega_{32}\,T_B}{\frac{1}{T_C} + \Delta\Omega^2\,T_C + \left(\frac{V}{\hbar}\right)^2 T_A + \left(\frac{U}{\hbar}\right)^2 T_B} \tag{A.4}$$

$$j_A = \frac{U}{\hbar}\frac{V}{\hbar} T_C + \frac{\omega_{32}\,\Delta\Omega\,\frac{U}{\hbar}\,\frac{V}{\hbar}\,[T_B + T_C]\,\Delta\Omega}{\frac{1}{T_C} + (\Delta\Omega)^2\,T_C + \left(\frac{V}{\hbar}\right)^2 T_A + \left(\frac{U}{\hbar}\right)^2 T_B} \tag{A.5}$$

$$j_B = \frac{1}{T_B} + \omega_{32}^2\,T_B + \left(\frac{U}{\hbar}\right)^2 T_C - \frac{\omega_{32}^2\,\left(\frac{U}{\hbar}\right)^2 [T_B + T_C]\,T_B}{\frac{1}{T_C} + (\Delta\Omega)^2\,T_C + \left(\frac{V}{\hbar}\right)^2 T_A + \left(\frac{U}{\hbar}\right)^2 T_B} \tag{A.6}$$

The strategy for solving P_A is then to first express N_{21}, N_{13}, and N_{12} in terms of P_A and P_B, and then along with the above two equations we can compute P_A.

A.0.1 Solving N_{21}

We repeat below equations 3.8, 3.2, and 3.5 in the steady-state limit:

$$\frac{N_{21}}{T_{21}} = \frac{N_{2a}}{T_1^c} + \frac{N_{01}e^{-\frac{\Delta E}{k\,T_h}}}{T_2^h} - \frac{U}{\hbar}P_A \tag{A.7}$$

$$\frac{N_{01}}{T_{01}} = \frac{N_{0a}}{T_1^c} + \frac{N_{11}}{T_1^h} + \frac{N_{21}}{T_2^h} \tag{A.8}$$

$$\frac{N_{11}}{T_{01}} = \frac{N_{1a}}{T_1^c} + \frac{N_{01}}{T_1^h} \tag{A.9}$$

Eliminating N_{11} from equations A.8 and A.9 gives

$$N_{01}\left[\frac{T_1^h}{T_{01}} - \frac{T_{11}}{T_1^h}\right] = N_{21}\frac{T_1^h}{T_2^h} + N_{0a}\frac{T_1^h}{T_1^c} + N_{1a}\frac{T_{11}}{T_1^c} \tag{A.10}$$

From the above equation and equation (A.7) we eliminate N_{01} to obtain the following equations, where

$$w \equiv \frac{T_1^h}{T_{01}} - \frac{T_{11}}{T_1^h} \tag{A.11}$$

$$N_{21}\left[\frac{e^{\frac{\Delta E}{k\,T_h}}}{T_{21}} T_2^h\, w - \frac{T_1^h}{T_2^h}\right] = -\frac{U}{\hbar} P_A\, e^{\frac{\Delta E}{k\,T_h}} T_2^h\, w + N_{0a}\frac{T_1^h}{T_1^c} + N_{1a}\frac{T_{11}}{T_1^c} + \frac{w}{T_1^c} e^{\frac{\Delta E}{k\,T_h}} T_2^h\, N_{2a} \tag{A.12}$$

If we let $P_A = 0$, then the starting three equations in this subsection are the same as those that would have been satisfied by the equilibrium values. Hence we can replace all the source terms in the above equation with the equilibrium value of N_{21}:

$$N_{21} = d_A\, P_A + n_2^{h,0} n_1^{c,0} \tag{A.13}$$

where $n_2^{h,0}$ and $n_1^{c,0}$ represent the hot side occupation probability on $u_2(z_1)$ and the cold side occupation probability on $\phi_1(z_2)$, and d_A is defined through

$$d_A \equiv \frac{-\frac{U}{\hbar} T_2^h\, w}{\frac{e^{\frac{\Delta E}{k\,T_h}}}{T_{21}} T_2^h\, w - \frac{T_1^h}{T_2^h}} \tag{A.14}$$

We can show that the denominator in equation (A.14) is positive. From equation (3.23),

$$\frac{T_2^h}{T_{21}} = \frac{T_2^h + T_1^c}{T_1^c} > 1 \tag{A.15}$$

Substitue the definitions of T_{01} equation (3.17) and the definition of T_{11} equation(3.20) into the definition of w equation (A.11),

$$w \equiv \frac{T_1^h}{T_{01}} - \frac{T_{11}}{T_1^h} = \frac{T_1^h}{T_1^c} + \frac{T_1^h}{T_1^h + T_1^c} + \frac{T_1^h}{T_2^h} e^{\frac{-(E_2^h - E_1^h)}{k\ T_h}} > \frac{T_1^h}{T_2^h} e^{\frac{-(E_2^h - E_1^h)}{k\ T_h}} \tag{A.16}$$

Substituting inequalities (A.15) and (A.16) into the denominator of equation (A.14) shows that the denominator is positive.

A.0.2 Solving N_{13}

We repeat equations (3.7), (3.4), (3.3), (3.41), (3.10), (3.10), (3.39), and (3.6) in the steady-state, double-resonance limit.

$$\frac{N_{13}}{T_{13}} = \frac{N_{03}}{T_1^h} + \frac{N_{1b}}{T_3^c} - \frac{V}{\hbar} P_B \tag{A.17}$$

$$\frac{N_{03}}{T_{03}} = \frac{N_{13}}{T_1^h} + \frac{N_{23}}{T_2^h} + \frac{N_{0b}}{T_3^c} - \frac{V}{\hbar} P_E \tag{A.18}$$

$$\frac{N_{02}}{T_{02}} = \frac{N_{12}}{T_1^h} + \frac{N_{22}}{T_2^h} + \frac{V}{\hbar} P_E \tag{A.19}$$

$$P_E = -\frac{2V}{\hbar} T_E \left[N_{02} - N_{03} \right] \tag{A.20}$$

$$\frac{N_{23}}{T_{23}} = \frac{N_{2b}}{T_3^c} + \frac{N_{03} e^{-\frac{\Delta E}{k\ T_h}}}{T_2^h} - \frac{V}{\hbar} P_D \tag{A.21}$$

$$\frac{N_{22}}{T_{22}} = \frac{N_{02} e^{-\frac{\Delta E}{k\ T_h}}}{T_2^h} + \frac{V}{\hbar} P_D \tag{A.22}$$

$$P_D = \frac{2V}{\hbar} T_D \left[N_{23} - N_{22} \right] \tag{A.23}$$

$$\frac{N_{12}}{T_1^h} = \frac{N_{02}}{T_1^h} + \frac{U}{\hbar} P_A + \frac{V}{\hbar} P_B \tag{A.24}$$

Substituting equation (A.23) into equations A.22 and A.21 gives

$$N_{22}\left[\frac{1}{T_{22}} + 2\left(\frac{V}{\hbar}T_D\right)^2\right] = N_{02}\frac{e^{-\frac{\Delta E}{k\,T_h}}}{T_2^h} + 2\left(\frac{V}{\hbar}\right)^2 T_D\, N_{23} \tag{A.25}$$

$$N_{23}\left[\frac{1}{T_{23}} + 2\left(\frac{V}{\hbar}T_D\right)^2\right] = \frac{N_{2b}}{T_3^c} + N_{03}\frac{e^{-\frac{\Delta E}{k\,T_h}}}{T_2^h} + 2\left(\frac{V}{\hbar}\right)^2 T_D\, N_{22} \tag{A.26}$$

Eliminating N_{22} from the above two equations gives

$$N_{23}\, w_{23} = N_{02}\frac{e^{-\frac{\Delta E}{k\,T_h}}}{T_2^h}2\left(\frac{V}{\hbar}\right)^2 T_D + \left[\frac{1}{T_{22}} + 2\left(\frac{V}{\hbar}\right)^2 T_D\right]\left(N_{03}\frac{e^{-\frac{\Delta E}{k\,T_h}}}{T_2^h} + \frac{N_{2b}}{T_3^c}\right) \tag{A.27}$$

, where w_{23} is defined as

$$w_{23} \equiv \frac{1}{T_{23}}\frac{1}{T_{22}} + 2\left(\frac{V}{\hbar}\right)^2\left(\frac{1}{T_{22}} + \frac{1}{T_{23}}\right)T_D \tag{A.28}$$

Substituting equation A.20 into equations A.19 and A.18 gives

$$N_{02}\left[\frac{1}{T_{02}} + 2\left(\frac{V}{\hbar}T_E\right)^2\right] = \frac{N_{12}}{T_1^h} + \frac{N_{22}}{T_2^h} + 2\left(\frac{V}{\hbar}\right)^2 T_E\, N_{03} \tag{A.29}$$

$$N_{03}\left[\frac{1}{T_{03}} + 2\left(\frac{V}{\hbar}\right)^2 T_E\right] = \frac{N_{13}}{T_1^h} + \frac{N_{23}}{T_2^h} + \frac{N_{0b}}{T_3^c} + 2\left(\frac{V}{\hbar}\right)^2 T_E\, N_{02} \tag{A.30}$$

Eliminating N_{02} from the above two equations gives

$$N_{03}\, w_{03} \;=\; \frac{{N_{12}}^2}{T_1^h} \left(\frac{V}{\hbar}\right)^2 T_E \;+\; \left[\frac{1}{T_{02}} \;+\; 2\left(\frac{V}{\hbar}\right)^2 T_E\right] \left(\frac{N_{13}}{T_1^h} \;+\; \frac{N_{23}}{T_2^h} \;+\; \frac{N_{0b}}{T_3^c}\right) \tag{A.31}$$

, where w_{03} is defined as

$$w_{03} \;\equiv\; \frac{1}{T_{03}} \frac{1}{T_{02}} \;+\; 2\left(\frac{V}{\hbar}\right)^2 \left(\frac{1}{T_{02}} \;+\; \frac{1}{T_{03}}\right) T_E \tag{A.32}$$

Eliminating N_{22} from equations A.25 and A.29 gives

$$\begin{aligned} N_{02} \left(w_{02} \;+\; \frac{1}{T_1^h}\left[\frac{1}{T_{22}} \;+\; 2\left(\frac{V}{\hbar}\right)^2 T_D\right]\right) \;&=\; 2\left(\frac{V}{\hbar}\right)^2 \frac{T_D}{T_2^h} N_{23} \\ &+\; \left[\frac{1}{T_{22}} \;+\; 2\left(\frac{V}{\hbar}\right)^2 T_D\right] \left[\frac{N_{12}}{T_1^h} \;+\; 2\left(\frac{V}{\hbar}\right)^2 \; T_E\; N_{03}\right] \end{aligned} \tag{A.33}$$

Eliminating N_{12} from the above equation and equation (A.24) gives

$$N_{02}\, w_{02} \;=\; 2\left(\frac{V}{\hbar}\right)^2 \frac{T_D}{T_2^h}\, N_{23} + \left[\frac{1}{T_{22}} \;+\; 2\left(\frac{V}{\hbar}\right)^2 \; T_D\right] \left(N_{03}\; 2\; \left(\frac{V}{\hbar}\right)^2 \; T_E \;+\; \frac{U}{\hbar} P_A \;+\; \frac{V}{\hbar} P_B\right) \tag{A.34}$$

where w_{02} is defined as

$$w_{02} \;\equiv\; \left[\frac{1}{T_{02}} \;+\; 2\left(\frac{V}{\hbar}\right)^2 \; T_E\right] \; \left[\frac{1}{T_{22}} \;+\; 2\left(\frac{V}{\hbar}\right)^2 \; T_D\right] - \frac{e^{-\frac{\Delta E}{k\, T_h}}}{(T_2^h)^2} - \frac{1}{T_1^h} \left[\frac{1}{T_{22}} \;+\; 2\left(\frac{V}{\hbar}\right)^2 \; T_D\right] \tag{A.35}$$

Eliminating N_{23} from equations (A.26) and (A.34) gives

$$N_{02}\, e_{02} \;=\; N_{03}\, e_{03} + \left(N_{2b}\, 2 \left(\frac{V}{\hbar}\right)^2 \frac{T_D}{T_2^h T_3^c} \;+\; w_{23}\, \frac{U}{\hbar} P_A \;+\; w_{23} \frac{V}{\hbar} P_B \right) \left[\frac{1}{T_{22}} \;+\; 2 \left(\frac{V}{\hbar}\right)^2 T_D \right] \tag{A.36}$$

where d_{03}, d_{02}, e_{02}, e_{03} are defined as follows:

$$d_{03} \;\equiv\; w_{23} \left[\frac{1}{T_{03}} \;+\; 2 \left(\frac{V}{\hbar}\right)^2 T_E \right] \;-\; \frac{e^{-\frac{\Delta E}{k\, T_h}}}{T_2^h} \left[\frac{1}{T_{22}} \;+\; 2 \left(\frac{V}{\hbar}\right)^2 T_D \right] \tag{A.37}$$

$$d_{02} \;\equiv\; e^{-\frac{\Delta E}{k\, T_h}}\; 2 \left(\frac{V}{\hbar}\right)^2 \frac{T_D}{(T_2^h)^2} \;+\; 2\, w_{23} \left(\frac{V}{\hbar}\right)^2 T_E \tag{A.38}$$

$$e_{02} \;\equiv\; w_{02}\, w_{03} \;-\; 4 \left(\frac{V}{\hbar}\right)^4 \left(\frac{T_D}{T_2^h}\right)^2 e^{-\frac{\Delta E}{k\, T_h}} \tag{A.39}$$

$$e_{03} \;\equiv\; 2 \left(\frac{V}{\hbar}\right)^2 \left[\frac{1}{T_{22}} \;+\; 2 \left(\frac{V}{\hbar}\right)^2 T_D \right] \left[\frac{T_D}{(T_2^h)^2} e^{-\frac{\Delta E}{k\, T_h}} \;+\; T_E\, w_{23} \right] \tag{A.40}$$

Eliminating N_{23} from equations (A.26) and (A.30) gives

$$\begin{aligned} N_{03}\, d_{03} \;=\; & N_{13} \frac{w_{23}}{T_1^h} \;+\; \frac{N_{2b}}{T_3^c} \left[\frac{1}{T_{22}} \;+\; 2 \left(\frac{V}{\hbar}\right)^2 T_D \right] \;+\; N_{0b} \frac{w_{23}}{T_3^c} \\ & + N_{02} \left[e^{-\frac{\Delta E}{k\, T_h}} 2 \left(\frac{V}{\hbar}\right)^2 \frac{T_D}{(T_2^h)^2} \;+\; 2\, w_{23} \left(\frac{V}{\hbar}\right)^2 T_E \right] \end{aligned} \tag{A.41}$$

Eliminating N_{02} from the above equation and equation (A.36) gives

$$N_{03} \left[d_{03} \;-\; \frac{d_{02}}{e_{02}} e_{03} \right] \;=\; N_{13} \frac{w_{23}}{T_1^h} \;+$$

$$\left[\frac{1}{T_{22}} + 2\left(\frac{V}{\hbar}\right)^2 T_D\right]\left[N_{2b}\left(\frac{1}{T_3^c} + 2\left(\frac{V}{\hbar}\right)^2 \frac{T_D}{T_2^h\, T_3^c}\frac{d_{02}}{e_{02}}\right) + w_{23}\left(\frac{d_{02}}{e_{02}}\frac{U}{\hbar}P_A + \frac{d_{02}}{e_{02}}\frac{V}{\hbar}P_B + \frac{N_{0b}}{T_3^c}\right)\right] \tag{A.42}$$

Eliminating N_{13} from the above equation and equation (A.17) gives

$$N_{13}\, h_{13} = \frac{f_A\, U}{f_{03}\, \hbar\, T_1^h}P_A + \frac{V}{\hbar}\left[\frac{f_A}{f_{03}\, T_1^h} - 1\right] P_B + \frac{f_{2b}\, N_{2b}}{f_{03}T_1^h} + \frac{N_{1b}}{T_3^c} + \frac{N_{0b}w_{23}}{T_3^c f_{03}T_1^h} \tag{A.43}$$

,where f_{03}, f_{2b}, f_A, and h_{13} are defined as follows

$$f_{03} \equiv d_{03} - \frac{d_{02}}{e_{02}}e_{03} \tag{A.44}$$

$$f_A \equiv w_{23}\frac{d_{02}}{e_{02}}\left[\frac{1}{T_{22}} + 2\left(\frac{V}{\hbar}\right)^2 T_D\right] \tag{A.45}$$

$$h_{13} \equiv \frac{1}{T13} - \frac{w_{23}}{(T_1^h)^2\, f_{03}} \tag{A.46}$$

Following a similar argument as in last subsection, if we let $P_A = P_B = P_D = P_E = 0$, then the starting equations should be satisfied by the equilibrium values. If we further demand $N_{02} = N_{03}$ and $N_{23} = N_{22}$, then the two quantum coupling equations (A.20) and (A.23) would be satisfied. We can make this demand because $\phi_2(z_2)$ does not relax to a reservoir and hence without quantum coupling the values of N_{02}, N_{12}, and N_{22} are undetermined. We denote $n_1^{h,0}$ as the equilibrium hot side occupation probability on $u_1(z_1)$ and $n_3^{c,0}$ as the equilibrium cold side occupation probability on $\phi_3(z_2)$. Grouping all the source terms into a single equilibrium term, N_{13} can then be re-expressed as

$$N_{13} \; = \; n_1^{h,0} n_3^{c,0} \; + \; C_A \, P_A \; + \; C_B \, P_B \tag{A.47}$$

where

$$C_A \; = \; \frac{f_A \, U}{f_{03} \, T_1^h \, h_{13} \, \hbar} \tag{A.48}$$

$$C_B \; = \; \frac{V}{\hbar} \left[\frac{f_A}{f_{03} \, T_1^h} \; - \; 1 \right] \frac{1}{h_{13}} \tag{A.49}$$

A.0.3 Solving N_{12}

Our goal is to express N_{12} in terms of P_A, P_B, and a source term. We can do this by successively expressing N_{12} in terms of N_{02}, N_{03}, ,N_{13}, and finally only P_A, P_B, and source terms. We invoke in sequence equations (A.24), (A.36), (A.17), and (A.47). The result is:

$$N_{12} \; = \; n_1^{h,0} \, n_2^{c,0} \; + \; y_A \, P_A \; + \; y_B \, P_B \tag{A.50}$$

where

$$y_A \; = \; \frac{e_{03}}{e_{02}} \frac{T_1^h}{T_{13}} C_A \; + \; \frac{U}{\hbar} \left[\frac{w_{23}}{e_{02}} \left[\frac{1}{T_{22}} \; + \; 2 \left(\frac{V}{\hbar} \right)^2 T_D \right] \; + \; T_1^h \right] \tag{A.51}$$

$$y_B \; = \; \frac{e_{03}}{e_{02}} \frac{T_1^h}{T_{13}} C_B \; + \; \frac{V}{\hbar} \left[\frac{w_{23}}{e_{02}} \left[\frac{1}{T_{22}} \; + \; 2 \left(\frac{V}{\hbar} \right)^2 T_D \right] \; + \; T_1^h \frac{e_{02} \; + \; e_{03}}{e_{02}} \right] \tag{A.52}$$

We can solve for P_A from equations (A.2), (A.1), (A.13), (A.47), and (A.50).

$$P_A \; = \; \frac{d}{a \, d \; - \; b \, c} 2 \frac{U}{\hbar} \left(n_2^{h,0} n_1^{c,0} \; - \; n_1^{h,0} n_3^{c,0} \right) \tag{A.53}$$

where

$$a = i_A + 2\frac{U}{\hbar}(y_A - d_A) \tag{A.54}$$

$$b = i_B \tag{A.55}$$

$$c = j_A + 2\frac{V}{\hbar}[y_A - C_A] \tag{A.56}$$

$$d = j_B + 2\frac{V}{\hbar}[y_B - C_B] \tag{A.57}$$

Appendix B

Probability transfer in a three-Level system

A kind of three-level system is encountered in Chapter 7 as well as in quantum computation application [57]. In such a system, we have three levels where level 1 and level 2 are coupled with matrix element U, while level 2 and level 3 are coupled with matrix element V. See Fig. B-1 for an energy diagram of the system. The energies of the three levels are E_1, E_2, and E_3, respectively, and we also denote $E = E_3$. Levels 1 and 2 are resonant and we assume $E_1 = E_2 = 0$ without loss of generality. U and V are assumed to be positive real numbers for ease of analysis. The system starts off at level 1 and then it oscillates among these three levels. We ask the question of what the maximum probability transfer to level 3 can be. A closed-form solution for the general case is difficult to obtain, but it exists in certain limiting cases.

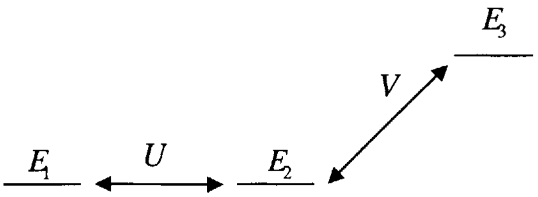

Figure B-1: Energy level diagram for the three-level system.

B.1 The case of $U >> V$

In this case, we treat V as a perturbation. The total Hamiltonian and the unperturbed Hamiltonian are

$$H = \begin{bmatrix} 0 & U & 0 \\ U & 0 & V \\ 0 & V & E \end{bmatrix}, H_0 = \begin{bmatrix} 0 & U & 0 \\ U & 0 & 0 \\ 0 & 0 & E \end{bmatrix}.$$

The perturbation matrix is:

$$H' = \begin{bmatrix} 0 & 0 & 0 \\ 0 & 0 & 1 \\ 0 & 1 & 0 \end{bmatrix}.$$

Therefore we have: $H = H_0 + V\ H'$ The unperturbed wavefunctions are:

$$u_x = \begin{bmatrix} 1/\sqrt{2} \\ 1/\sqrt{2} \\ 0 \end{bmatrix}, u_y = \begin{bmatrix} -1/\sqrt{2} \\ 1/\sqrt{2} \\ 0 \end{bmatrix}, u_z = \begin{bmatrix} 0 \\ 0 \\ 1 \end{bmatrix}.$$

The unperturbed energies are U, $-U$, and E, respectively. We carry out stationary perturbation theory [58] to first order and obtain the following three perturbed wavefunctions:

$$\begin{bmatrix} \frac{1}{\sqrt{2}} \\ \frac{1}{\sqrt{2}} \\ \frac{V}{\sqrt{2}(U-E)} \end{bmatrix}, \begin{bmatrix} \frac{-1}{\sqrt{2}} \\ \frac{1}{\sqrt{2}} \\ \frac{-V}{\sqrt{2}(U+E)} \end{bmatrix}, \begin{bmatrix} \frac{V\ U}{(E^2-U^2)} \\ \frac{V\ E}{(E^2-U^2)} \\ 1 \end{bmatrix}. \tag{B.1}$$

We start off at level 1, which is represented by the vector $\begin{bmatrix} 1 & 0 & 0 \end{bmatrix}^T$. After dot products with the perturbed wavefunctions to obtain superposition coefficients, we obtain the time evolution of the wavefunction:

$$\Psi(t) = \frac{1}{\sqrt{2}} \begin{bmatrix} \frac{1}{\sqrt{2}} \\ \frac{1}{\sqrt{2}} \\ \frac{V}{\sqrt{2}(U-E)} \end{bmatrix} e^{-it\frac{U}{\hbar}} - \frac{1}{\sqrt{2}} \begin{bmatrix} \frac{-1}{\sqrt{2}} \\ \frac{1}{\sqrt{2}} \\ \frac{-V}{\sqrt{2}(U+E)} \end{bmatrix} e^{it\frac{U}{\hbar}} + \frac{U\ V}{(E^2-U^2)} \begin{bmatrix} \frac{V\ U}{(E^2-U^2)} \\ \frac{V\ E}{(E^2-U^2)} \\ 1 \end{bmatrix} e^{-it\frac{E}{\hbar}}.$$

The maximum probability at level 3 is then

$$P_{max} = \left(|\frac{V}{2\,(U-E)}| + |\frac{V}{2\,(U+E)}| + |\frac{U\,V}{(E^2-U^2)}| \right)^2 . \tag{B.2}$$

The first two terms on the right hand side is determined by which of the following two has greater absolute value:

$$\frac{V}{2\,(U+E)} + \frac{V}{2\,(U-E)} = \frac{V\,U}{(U^2-E^2)} \tag{B.3}$$

$$\frac{V}{2\,(U+E)} - \frac{V}{2\,(U-E)} = \frac{-V\,E}{(U^2-E^2)}. \tag{B.4}$$

B.1.1 The case of $E \approx U$ or $E < U$

If $E \approx U$ or $E < U$, the absolute value of equation(B.3) is about equal to or greater than that of equation(B.4), and therefore

$$P_{max} \approx \left(\frac{U\,V}{(E^2-U^2)} + \frac{U\,V}{(E^2-U^2)} \right)^2 = \frac{4\,U^2\,V^2}{(E+U)^2\,(E-U)^2} \tag{B.5}$$

Equation(B.5) obviously breaks down when $E = U >> V$. What should P_{max} be in this case? In this case, we have the Hamiltonian

$$H = \begin{bmatrix} 0 & U & 0 \\ U & 0 & V \\ 0 & V & U \end{bmatrix} .$$

It is easy to see that the eigenvalues are approximately U , U and $-U$ (remember V is small). The eigenvector corresponding to $-U$ is approximately $\begin{bmatrix} 1/\sqrt{2} & -1/\sqrt{2} & 0 \end{bmatrix}^T$ from the splitting of the first two levels. The approximate eigenvectors corresponding to the approximate eigenvalue U has the form: $\begin{bmatrix} a & a & b \end{bmatrix}^T$,where $2a^2 + b^2 = 1$ for normalization. In order to know the ratio between a and b, we need a better approximation on the eigenvalues. Let $Q(x)$ be the characteristic polynomial of H.

We have

$$Q(x) = det(H - xI_3) = x^2(U - x) + V^2 \cdot x + U^2(x - U).$$

Suppose $x_0 \approx U$ is a root of $Q(x)$. Let $y = x_0 - U$. y is small and

$$0 = Q(y + U) = -(y + U)^2 y + V^2(y + U) + U^2 y \approx V^2 U - 2Uy^2.$$

As a result,

$$y \approx \pm\frac{V}{\sqrt{2}}.$$

It is easy to see that the approximate eigenvector corresponding to the approximate eigenvalue $U \pm \frac{V}{\sqrt{2}}$ is $\begin{bmatrix} \frac{1}{2} & \frac{1}{2} & \frac{\pm 1}{\sqrt{2}} \end{bmatrix}^T$ and from the three approximate eigenvectors we obtain

$$P_{max}(E = U) = (2 \cdot \frac{1}{2} \cdot \frac{1}{\sqrt{2}})^2 = \frac{1}{2}.$$

Since probability transfer in a two-level system has a Lorentzian behavior [9], we expect a similar form for P_{max}. Assuming a Lorentzian width parameter b:

$$P_{max} = \frac{4\ U^2\ V^2}{(E + U)^2\left[(E - U)^2 + b\right]}$$

$$P_{max}(E = U) = \frac{1}{2} \Longrightarrow b = 2\ V^2.$$

Due to symmetry, we need a width parameter for the $(E + U)^2$ term as well

$$P_{max} = \frac{4\ U^2\ V^2}{\left[(E + U)^2 + 2\ V^2\right]\left[(E - U)^2 + 2\ V^2\right]}.$$

Renormalize to get $P_{max}(E = U) = 0.5$

$$P_{max} = \frac{V^2\,(4\ U^2 + 2\ V^2)}{\left[(E + U) + 2\ V^2\right]\left[(E - U)^2 + 2\ V^2\right]}. \tag{B.6}$$

B.1.2 The case of $E >> U >> V$

If $E >> U >> V$, equation (B.4) is the dominating term in equation (B.2),

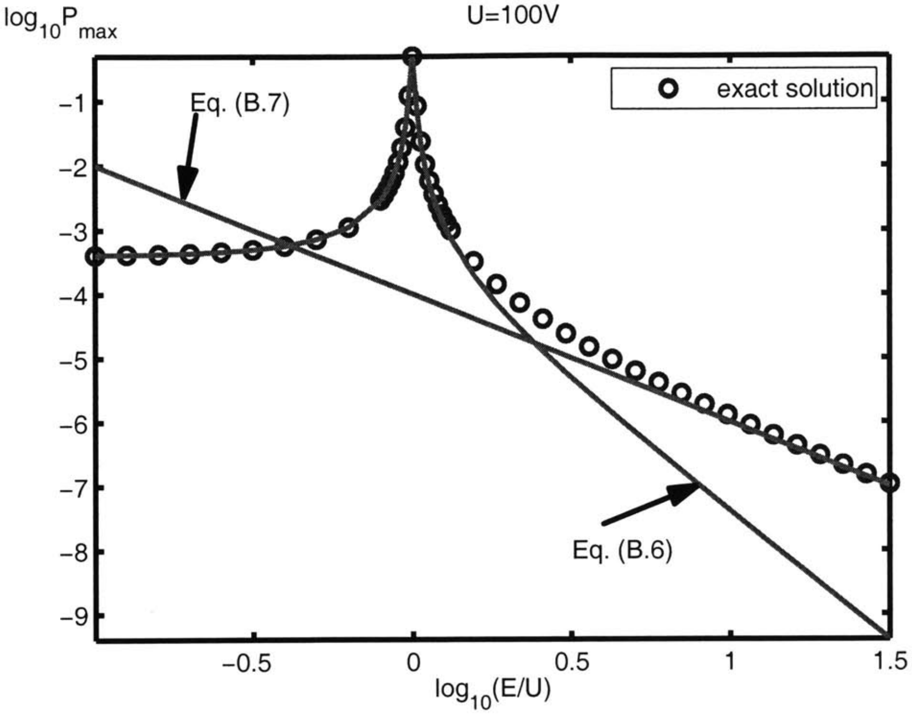

Figure B-2: Comparison of the exact solution with approximate analytical solutions (B.6) and (B.7) for $U = 100\ V$.

$$P_{max} \approx \left(\frac{V}{2\,(U-E)} - \frac{V}{2\,(U+E)}\right)^2 = \left[\frac{-V\ E}{(U^2-E^2)}\right]^2 \approx \frac{V^2}{E^2}. \tag{B.7}$$

In Fig B-2, we compare the exact solution [57] of P_{max} and the approximate analytical functions, equations (B.6) and (B.7), for the case of $U = 100\ V$. We only plot the positive E range as P_{max} is symmetric in E. We see that the functions are good approximations in respective limits ($E \leq U$ or $E \approx U$, and $E >> U$) and they are not so accurate in the transition region of E.

We denote $\hat{P}_{max}$ to be an approximate solution of P_{max} and the relative error to be $\epsilon = |\hat{P}_{max} - P_{max}|/P_{max}$. In Fig. B-3 we show a log plot of the relative error for equation (B.6). As expected, the estimate is only good when U is much bigger than V and E is not too much greater than U. In Fig. B-4, the log relative error plot for equation (B.7) is shown. It is accurate in the large E limit, regardless of whether

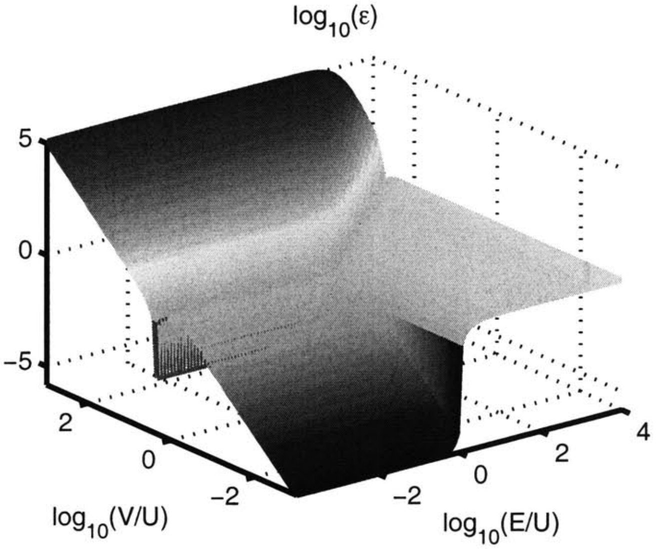

Figure B-3: Error plot for the approximate solution Eq. (B.6).

$V << U$ or not, because when E is sufficiently large, level 3 is far away and the first two levels is like a two-level system, and the perturbed wavefunctions equation (B.1) is a good estimate.

B.2 The case of $V >> U$

We consider the case when $E = 0$ first. In this case the Hamiltonian is diagnosable [57], and the eigenvectors are

$$\begin{bmatrix} V/\sqrt{V^2+U^2} \\ 0 \\ -U/\sqrt{V^2+U^2} \end{bmatrix}, \begin{bmatrix} U/\sqrt{2\,(V^2+U^2)} \\ 1/\sqrt{2} \\ V/\sqrt{2\,(V^2+U^2)} \end{bmatrix}, \begin{bmatrix} U/\sqrt{2\,(V^2+U^2)} \\ 1/\sqrt{2} \\ V/\sqrt{2\,(V^2+U^2)} \end{bmatrix}$$

with eigenvalues 0 ,$\sqrt{U^2+V^2}$, and $-\sqrt{U^2+V^2}$, respectively. P_{max} is then calculated to be

$$P_{max} = \frac{4\;U^2\;V^2}{(U^2+V^2)^2} \approx \frac{4\;U^2}{V^2}. \tag{B.8}$$

As argued before, when $E >> V >> U$, approximate eigenvectors from equation (B.1) are good estimates and hence equation (B.7) applies. However, equation (B.7)

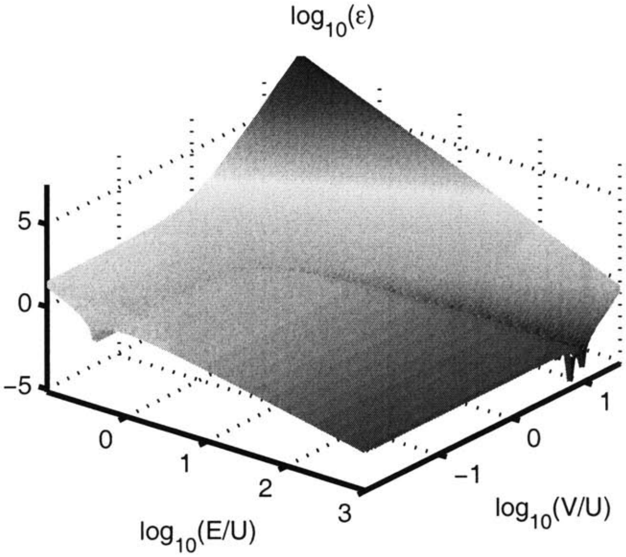

Figure B-4: Error plot for the approximate analytical solution Eq. (B.7).

blows up when E goes to 0, and yet we know the finite value of P_{max} at $E = 0$. Again, we need a Lorentzian width b:

$$P_{max} = \frac{V^2}{E^2 + b}$$

$$P_{max}\,(E = 0) = \frac{4\;U^2}{V^2} \Longrightarrow b \approx \frac{V^4}{4\;U^2}$$

Therefore,

$$P_{max} \;=\; \frac{V^2}{E^2 + \frac{V^4}{4\;U^2}}. \tag{B.9}$$

In Fig. B-5, we compare the exact solution [57] of P_{max} and the approximate analytical functions, equation (9) for the case of $V = 100\;U$. We see that the analytical solution is a good approximation overall. In Fig. B-6 we show a log plot of the relative error for equation (9). The estimate is accurate when U is much smaller than V.

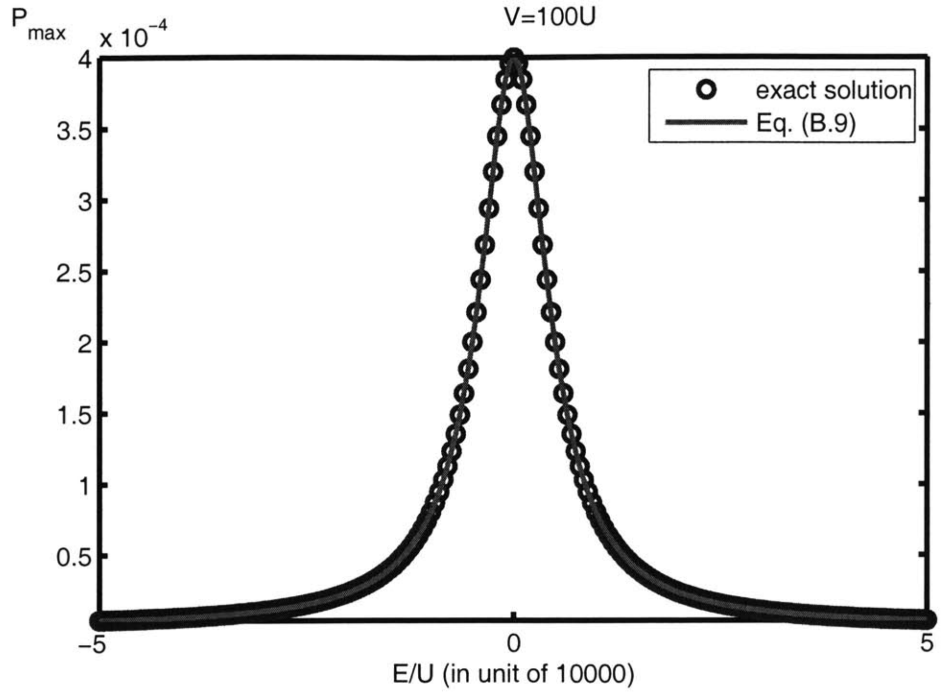

Figure B-5: Comparison of exact solution with the approximate analytical solution (B.9) for $V = 100\ U$.

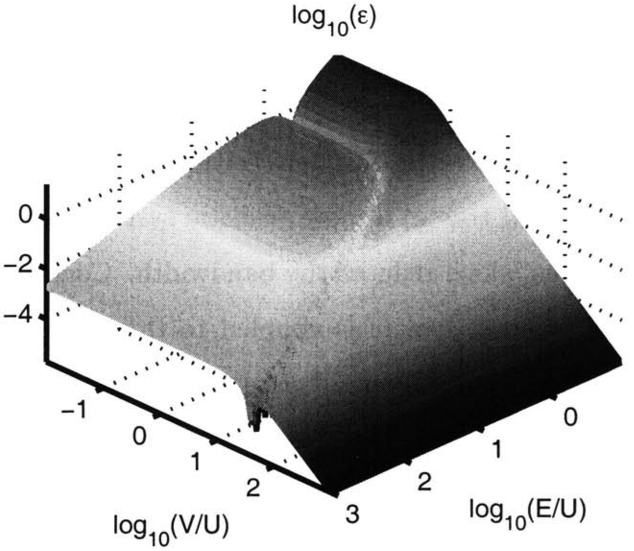

Figure B-6: Error plot for the approximate analytical solution Eq. (B.9).

B.3 Interpretation

In the $U >> V$ limit, the first two levels behave as a two-level system, and there is a level-splitting of magnitude U. Hence we have a peak of P_{max} at $E = \pm U$ as indicated by Eq. (B.6) and Fig. B-2. The width of this peak is proportional to V, which is reminiscent of a two level system [9] except with a $\sqrt{2}$ factor, possibly due to the fact that level 3 is only coupled to level 2 not coupled to level 1.

In the large E limit, level 3 is far away from levels 1 and 2. Level 3 practically only sees one level (levels 1 and 2 lumped together) and P_{max} goes down as V^2/E^2, same as the large E limit for a two-level system [9].

In the $V >> U$ limit, P_{max} is a Lorenzian peaked at $E = 0$. The width of the Lorenzian is proportional to V^2/U, and therefore when U is small compared to V we have large bandwidths. The reason for this is that when V is much stronger than U, level 2 and level 3 are strongly coupled and the coupling between level 1 and level 2 is the bottleneck of the probability transfer. Therefore, off-resonance effect between level 2 and level 3 does not become significant until these two levels are very far apart.

B.4 Lossy case

Equation (B.9) suggests that when $U << V$ broad bandwidths are generated given small U's. Would this hold true in a more realistic system? In such a system there would be presence of loss which reduces the bandwidth. Consider the following case where the original three-level system is coupled to three reservoirs. See Fig. B-7 for a schematic. Reservoir α is modeled as a whole spectrum of levels with each level coupled to level 1 with matrix element W_1. The Golden Rule rate for level 1 relaxation to reservoir α is Γ_1. Reservoir α has density of states $\rho_\alpha(E)$. Similarly, reservoir β is modeled as a spectrum of levels with each level coupled to level 3 with matrix element W_3. The Golden Rule rate for level 3 relaxation into reservoir β is Γ_3. W_3 and W_1 are assumed to be positive real. Reservoir β has density of states

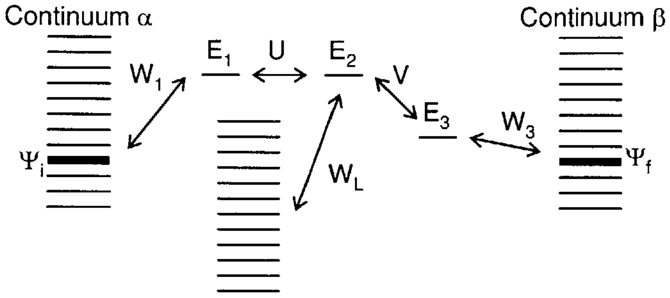

Figure B-7: Schematic for a lossy three-level system.

$\rho_\beta(E)$. Level 2 is coupled to each level in reservoir L with matrix element W_L and has loss characterized by the Golden Rule rate Γ_L. If an electron starts off at level Ψ_i in reservoir α, it goes through the three-level system and ends up at a resonant level Ψ_f in reservoir β. We consider the total flux from reservoir α to reservoir β, obtained by integrating the transition rate between each resonant states Ψ_i and Ψ_f over the whole energy spectrum. We are interested in finding out the bandwidth of such flux and how the bandwidth is affected by loss.

B.4.1 Secular Equations Partitioning Method

We use the augmented secular equations partitioning method to calculate the flux. Let E be an eigen-energy of the system. The H's are the energies of the corresponding levels adjusted with imaginary part to take into account losses,

$$H_1 = E_1 - i\hbar\frac{\Gamma_1}{2}$$

$$H_2 = E_2 - i\hbar\frac{\Gamma_L}{2}$$

$$H_3 = E_3 - i\hbar\frac{\Gamma_3}{2}$$

We write out scalar sector equations

$$E\,\Psi_i = H_i\,\Psi_i + W_1\,\Psi_1 \tag{B.10}$$

$$E\,\Psi_1 \;=\; H_1\,\Psi_1 \;+\; U\,\Psi_i + W_1\,\Psi_i \tag{B.11}$$

$$E\,\Psi_2 \;=\; H_2\,\Psi_2 \;+\; U\,\Psi_1 \;+\; V\,\Psi_3 \tag{B.12}$$

$$E\,\Psi_3 \;=\; H_3\,\Psi_3 \;+\; V\,\Psi_2 \;+\; W_3\,\Psi_f \tag{B.13}$$

$$E\,\Psi_f \;=\; H_f\,\Psi_f \;+\; W_3\,\Psi_3$$

rewrite equations (B.11), (B.12), and (B.13) into a matrix equation

$$E\begin{bmatrix}\Psi_1\\ \Psi_2\\ \Psi_3\end{bmatrix} = \begin{bmatrix}H_1 & U & 0\\ U & H_2 & V\\ 0 & V & H_3\end{bmatrix}\begin{bmatrix}\Psi_1\\ \Psi_2\\ \Psi_3\end{bmatrix} + \begin{bmatrix}W_1\\ 0\\ 0\end{bmatrix}\Psi_i + \begin{bmatrix}0\\ 0\\ W_3\end{bmatrix}\Psi_f$$

,which leads to

$$\begin{bmatrix}\Psi_1\\ \Psi_2\\ \Psi_3\end{bmatrix} = \begin{bmatrix}E-H_1 & -U & 0\\ -U & E-H_2 & -V\\ 0 & -V & E-H_3\end{bmatrix}^{-1}\left(\begin{bmatrix}W_1\\ 0\\ 0\end{bmatrix}\Psi_i + \begin{bmatrix}0\\ 0\\ W_3\end{bmatrix}\right). \tag{B.14}$$

Substituting eq. (B.14) into eq. (B.10) we obtain

$$E\,\Psi_i \;=\; H_i\,\Psi_i \;+\; U_{ii}\,\Psi_i \;+\; U_{if}\,\Psi_f$$

, where

$$U_{ii} = W_1^2 \begin{bmatrix} 1 & 0 & 0 \end{bmatrix} \begin{bmatrix} E-H_1 & -U & 0 \\ -U & E-H_2 & -V \\ 0 & -V & E-H_3 \end{bmatrix}^{-1} \begin{bmatrix} 0 \\ 0 \\ 1 \end{bmatrix}$$

$$U_{if} = W_1\, W_3 \begin{bmatrix} 1 & 0 & 0 \end{bmatrix} \begin{bmatrix} E-H_1 & -U & 0 \\ -U & E-H_2 & -V \\ 0 & -V & E-H_3 \end{bmatrix}^{-1} \begin{bmatrix} 0 \\ 0 \\ 1 \end{bmatrix}$$

U_{if} is the equivalent coupling matrix element between Ψ_i and Ψ_f. The transition rate from Ψ_i to Ψ_f is obtained from the Golden Rule to be $2\pi|U_{if}|^2\rho_3(E)/\hbar$. If we denote μ_1 and μ_3 to be the chemical potentials of reservoir 1 and reservoir 3, respectively, and we denote T_1 and T_3 to be the reservoir temperatures, the thermal equilibrium occupation probabilities for Ψ_i and Ψ_f are $p_i(E) = 1/(1 + exp\{-E/kT_1\})$ and $p_f = 1/(1 + exp\{-E/kT_3\})$. The forward flux from Ψ_i to Ψ_f is proportional to $p_i\ (1 - p_f)$. Similarly, the backward flux from Ψ_f to Ψ_i is $(1 - p_f)\ p_f$. Therefore, the total flux from reservoir 1 to reservoir 2 is

$$flux = \int [p_i(1-p_f) \ - \ (1-p_i)\ p_f]\, 2\pi|U_{if}|^2\rho_1(E)\,\rho_3(E)/\hbar \times dE. \qquad \text{(B.15)}$$

B.4.2 Numerical results

When E_3 varies, the system goes off-resonant and only the term $|U_{if}|^2$ changes in eq. (B.15). To investigate the effect of off-resonance on the flux, we hence only need to consider the following integral as a function of E_3: $\int |U_{fi}|^2 dE$, hereafter referred to as the core integral. An example lineshape of the core integral is shown in Fig. B-8 for the following choices of parameters: $\omega_R = 2\pi \cdot 10^{12}\ s^{-1}$, $V = \omega_R \cdot \hbar$, $E_1 = E_2 = 0\ eV$, $\Gamma_1 = \Gamma_3 = 1/\omega_R$, $U = 0.01V$, and $\Gamma_L = 100V/\hbar$. We can fit the lineshape with a Lorentzian and obtain the Full Width -Half Maximum (FWHM). Another example lineshape is shown in Fig.B-9 for the same set of parameters except $\Gamma_L = 0.01V/\hbar$.

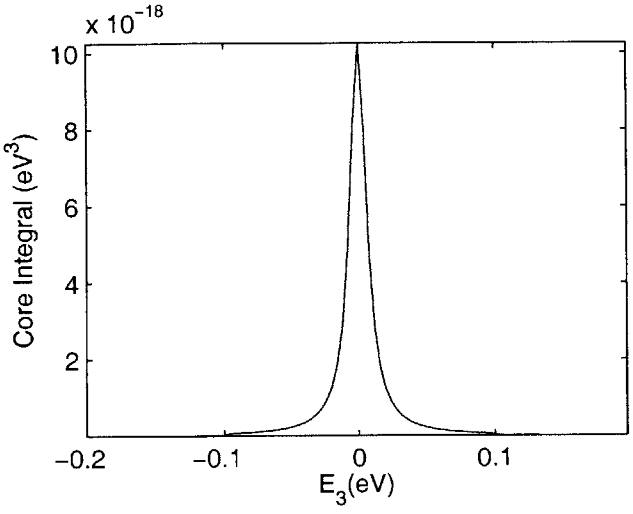

Figure B-8: Lineshape for $U = 0.01V$ and $\Gamma_L = 100V/\hbar$.

In this case of smaller Γ_L, there is a dip in the peak but the two sides still tail off as Lorentizan and we can again fit the lineshape with a Lorentzian to obtain the FWHM. In Fig. B-10 we show the width as a function of loss Γ_L and coupling U, all normalized to coupling V. Large widths are created with small U's, but the presence of loss reduces the widths. This is counter-intuitive as normally loss contributes to the uncertainty of the level 2 energy and hence should increase the bandwidth. In reality though the effect of flux lost into reservoir L dominates over the increase in level 2 energy uncerntainty and hence the bandwidth is reduced when the loss increases.

B.5 Conclusion

We have shown analytically how a large bandwidth can exist in probability transfer through a sequential three-level system given that the on-resonant coupling is much weaker than the off-resonant coupling. This phenomenon is counter-intuitive and may have potential applications. We have also demonstrated that the presence of loss reduces the bandwidth.

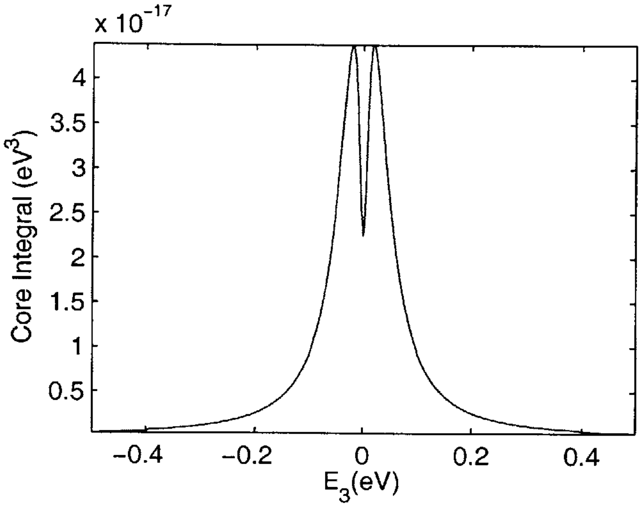

Figure B-9: Lineshape for $U = 0.01V$ and $\Gamma_L = V/\hbar$.

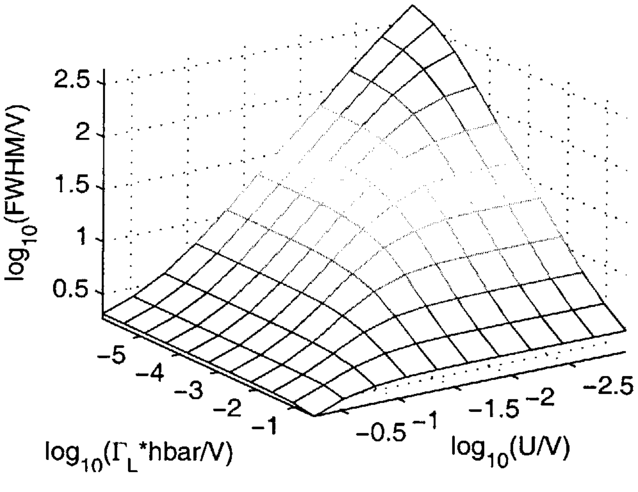

Figure B-10: FWHM as a function of Γ_L and U.

Appendix C

Coulomb coupling loss

From Chapter 9 we see that the dipole interaction energy between a hot-side dipole $\mathbf{d}_h$ and a cold-side dipole $\mathbf{d}_c$ is

$$U = \frac{4\epsilon_0\epsilon_2|\mathbf{d}_h||\mathbf{d}_c|}{(\epsilon_0+\epsilon_1)(\epsilon_0+\epsilon_2)}$$

$$\times \sum_{n=0}^{\infty}\left(\frac{\epsilon_0-\epsilon_1}{\epsilon_0+\epsilon_1}\right)^n\left(\frac{\epsilon_0-\epsilon_2}{\epsilon_0+\epsilon_2}\right)^n\frac{1}{4\pi\epsilon_2|\Delta\mathbf{R}_{chn}|^3}\left[\hat{\mathbf{n}}_c\cdot\hat{\mathbf{n}}_h-3(\hat{\mathbf{n}}_c\cdot\hat{\mathbf{i}}_{chn})(\hat{\mathbf{i}}_{chn}\cdot\hat{\mathbf{n}}_h)\right]$$

where $\hat{\mathbf{n}}_h$ is the unit vector in the direction of $\mathbf{d}_h$, $\hat{\mathbf{n}}_c$ is the unit vector in the direction of $\mathbf{d}_c$, and $\hat{\mathbf{i}}_{chn}$ is a unit vector in the direction of $\mathbf{d}_c-\mathbf{d}_h$. The hot-side and the cold-side dipoles in principle can have a random orientation, and we do an averaging to relate the expectation of the Coulombic matrix element squared to the dipole moments:

$$\langle|U|^2\rangle = \frac{\epsilon_0^2|\mathbf{d}_h|^2|\mathbf{d}_c|^2}{\pi(\epsilon_0+\epsilon_1)^2(\epsilon_0+\epsilon_2)^2}\left\langle\left|\sum_{n=0}^{\infty}\left(\frac{\epsilon_0-\epsilon_1}{\epsilon_0+\epsilon_1}\right)^n\left(\frac{\epsilon_0-\epsilon_2}{\epsilon_0+\epsilon_2}\right)^n\frac{1}{|\Delta\mathbf{R}_{chn}|^3}\right.\right.$$

$$\left.\left.\times\left[\hat{\mathbf{n}}_h\cdot\hat{\mathbf{n}}_c-3(\hat{\mathbf{n}}_c\cdot\hat{\mathbf{i}}_{chn})(\hat{\mathbf{i}}_{chn}\cdot\hat{\mathbf{n}}_h)\right]\right|^2\right\rangle = \frac{\epsilon_0^2|\mathbf{d}_h|^2|\mathbf{d}_c|^2}{3\pi(\epsilon_0+\epsilon_1)^2(\epsilon_0+\epsilon_2)^2}\left|\sum_{n=0}^{\infty}\left(\frac{\epsilon_0-\epsilon_1}{\epsilon_0+\epsilon_2}\right)^n\left(\frac{\epsilon_0-\epsilon_2}{\epsilon_0+\epsilon_2}\right)^n\right.$$

$$\times \frac{1}{|\Delta \mathbf{R}_{chn}|^3}\Bigg|^2 \left\langle \left| \hat{\mathbf{n}}_c \cdot \hat{\mathbf{n}}_h \; - \; 3 \; \left(\hat{\mathbf{n}}_c \cdot \hat{\mathbf{i}}_{chn}\right) \left(\hat{\mathbf{i}}_{chn} \cdot \hat{\mathbf{n}}_h\right) \right|^2 \right\rangle$$

where the last term is evaluted by Mathematica to be

$$\left\langle \left| \hat{\mathbf{n}}_c \cdot \hat{\mathbf{n}}_h - 3 \left(\hat{\mathbf{n}}_c \cdot \hat{\mathbf{i}}_{chn}\right) \left(\hat{\mathbf{i}}_{chn} \cdot \hat{\mathbf{n}}_h\right) \right|^2 \right\rangle = \int_0^{2\pi} \frac{d\theta}{2\pi} \int_0^{2\pi} \frac{d\phi}{2\pi} \left[\cos(\theta - \phi) - 3\cos\theta\cos\phi\right]^2 = \frac{5}{4}$$

We define $f(\mathbf{r}_h, \mathbf{r}_c, \omega)$

$$f(\mathbf{r}_h, \mathbf{r}_c, \omega) = \frac{5\epsilon_0^2}{12\pi(\epsilon_0 + \epsilon_1)^2(\epsilon_0 + \epsilon_2)^2} \left| \sum_{n=0}^{\infty} \left(\frac{\epsilon_0 - \epsilon_1}{\epsilon_0 + \epsilon_2}\right)^n \left(\frac{\epsilon_0 - \epsilon_2}{\epsilon_0 + \epsilon_2}\right)^n \frac{1}{|\Delta \mathbf{R}_{chn}|^3} \right|^2$$

From similar arguments to that of the previous chapter, we obtan the expression for the Coulomb coupling loss:

$$\text{loss} \; = \; \frac{2\pi}{\hbar} \int d^3\mathbf{r}_h \int d^3\mathbf{r}_c \rho_r^h \rho_r^c \int d\omega \hbar\omega \rho_\omega^h(\omega) \rho_\omega^c(\omega) |\mathbf{d}_h|^2 |\mathbf{d}_c|^2 f(\mathbf{r}_h, \mathbf{r}_c) \left[p_{\text{high}}^h p_{\text{low}}^c - p_{\text{high}}^c p_{\text{low}}^h\right]$$

Making use of equations 15.5 and 15.6 for both the hot-side and the cold-side, we arrive at the following expression for the loss:

$$\text{loss} \; = \; \frac{2\epsilon_0}{\pi\mu_0} \int d^3\mathbf{r}_h \int d^3\mathbf{r}_c \int d\omega f(\mathbf{r}_h, \mathbf{r}_c, \omega) \frac{\alpha_h(\omega)\alpha_c(\omega)}{\omega n_h(\omega) n_c(\omega)} \left[\mathrm{e}^{-\hbar\omega/kT_h} - \mathrm{e}^{-\hbar\omega/kT_c}\right]$$

Bibliography

[1] Wikipedia. *http://en.wikipedia.org/wiki/Oil_price_increases_of_2004_and_2005* .

[2] Robert C. Armstrong and Ernest J. Moniz. Report of the energy research council. *MIT Energy Research Council*, May 2006.

[3] M. Laroche, R. Carminati, and J.-J. Greffet. Near-field thermophotovoltaic energy conversion. *Journal of Applied Physics*, 100, September 2006.

[4] R. DiMatteo, P. Greiff, D. Seltzer, D. Meulenberg, E. Brown, E. Carlen, K. Kaiser, S. Finberg, H. Nguyen, J. Azarkevich, P. Baldasaro, J. Beausang, L. Danielson, M. Dashiell, D. DePoy, H. Ehsani, W. Topper, K. Rahner, and R. Siergiej. Micron-gap thermophotovoltaics (mtpv). In *AIP Conference Proceedings*, volume 738 of *THERMOPHOTOVOLTAIC GENERATION OF ELECTRICITY: Sixth Conference on Thermophotovoltaic Generation of Electricity: TPV6*, pages 42–51, November 2004.

[5] Janet L. Pan, Henry K. H. Choy, and Clifton G. Fonstad Jr. Very large radiative transfer over small distances from a black body for thermophotovoltaic applications. *IEEE TRANSACTIONS ON ELECTRON DEVICES*, 47:241–249, January 2000.

[6] Ivan Celanovi and Prof. John Kassakian. Photonic crystals for ir and near-ir applications: thermophotovoltaics, thermal radiation sources, ir sensors and beyond. *LEES Colloquium at MIT*, February 2005.

[7] Peter L. Hagelstein. Basic issues in electromagnetic coupling. *unpublished.*

[8] Bernard Wernsman, Richard R. Siergiej, Samuel D. Link, Robert G. Mahorter, Marc N. Palmisiano, Rebecca J. Wehrer, Robert W. Schultz, Gregory P. Schmuck, Rowan L. Messham, Susan Murray, Christopher S. Murray, Fred Newman, Daniel Taylor, David M. DePoy, and Thomas Rahmlow. Greater than 20% radiant heat conversion efficiency of a thermophotovoltaic radiator/module system using reflective spectral control. *IEEE Trans. Electron. Dev.*, 51:512–515, March 2004.

[9] C. Cohen-Tannoudji et al. *Quantum Mechanics.* Wiley-Interscience, 1977.

[10] Peter L. Hagelstein, Stephen D. Senturia, and Terry P. Orlando. *Introductory Applied Quantum and Statistical Mechanics.* Wiley-Interscience, 2004.

[11] Per-Olov Lowdin. A note on the quantum-mechanical perturbation theory. *The Journal of Chemical Physics*, 19:1396–1401, July 1951.

[12] Per-Olov Lowdin. Studies in perturbation theory part i. an elementary iteration-variation procedure for solving the schrodinger equation by partitioning technique. *Journal of Molecular Spectroscopy*, 10:12, 1963.

[13] Gregory D. Scholes, Xanthipe J. Jordanides, and Graham R. Fleming. Adapting the förster theory of energy transfer for modeling dynamics in aggregated molecular assemblies. *J. Phys. Chems. B*, 105:1640–1651, February 2001.

[14] S. Lee, C. Mao, C. E. Flynn, and A. M. Belcher. Ordering of quantum dots using genetically engineered viruses. *Science*, 296:892–895, May 2002.

[15] S. Coe-Sullivan, J. S. Steckel, W. K. Woo, M. G. Bawendi, and Bulovic V. Large-area ordered quantum-dot monolayers via phase separation during spin-casting. *Adv. Funct. Mater.*, 15:1117–1124, April 2005.

[16] M. Grundmann, J. Christen, N. N. Ledentsov, J. Bohrer, D. Bimberg, S. S. Ruvimov, P. Werner, U. Richter, U. Gosele, H. Heydenreich, V. M. Ustinov, A. Yu. Egorov, A. E. Zhukov, P. S. Kop'ev, and Zh. I. Alferov. Ultranarrow luminescence lines from single quantum dots. *Phys. Rev. Lett.*, 74:4043, 1995.

[17] A. F. Tsatsul'nikov, S. V. Ivanov, P. S. Kop'ev, A. K. Kryganovskii, N. N. Ledentsov, M. V. Maximov, B. YA. Mel'tser, P. V. Nekludov, A. A. Suvorova, A. N. Titkov, B. V. Volovik, M. Grundmann, D. Bimberg, and Zh. I. Alferov. Formation of indium antimonide qauntum dots in a gallium antimonide matrix. *Microelectronic Engineering*, 43:85–90, 1998.

[18] Markus Zahn. *Electromagnetic Field Theory: A Problem Solving Approach.* Krieger Publishing Company, 2003.

[19] Abramowitz and Stegun. *Handbook of Mathematical Functions.* Dover Publications.

[20] Y. Hishinuma, T. H. Genalle, B. Y. Moyzhes, and T. W. Kenny. Refrigeration by combined tunneling and thermionic emission in vacuum: Use of nanometer scale design. *Appl. Phys. Lett.*, 78:2572, April 2001.

[21] Yoshikazu Hishinuma, Theodore H. Geballe, Boris Y. Moyzhes, and T. W. Kenny. Measurements of cooling by room-temperature thermionic emission. *J. Appl. Phys.*, 94:4690, October 2003.

[22] I. N. Stranski and Von L. Krastanow. *Akad. Wiss. Lit. Mainz Math.-Natur. Kl. IIb*, 146:797, 1937.

[23] S. Sauvage, P. Boucaud, R.P.S.M. Lobo, F. Bras, G. Fishman, R. Prazeres, F. Glotin, J. M. Ortega, and J.-M. Gerard. Long polaron lifetime in indium arsenide/gallium arsenide self-assembled quantum dots. *Phys. Rev. Lett.*, 88:177402, April 2002.

[24] M. H. Baier, S. Watanabe, E. Pelucchi, and E. Kapon. High uniformity of site-controlled pyramidal quantum dots grwon on prepatterned substrates. *Appl. Phys. Lett.*, 84:1943–1945, March 2004.

[25] J H Lee, Zh M Wang, B L Liang, K A Sablon, and N W Strom. Size and density control of inas quantum dot ensembles on self-assembled nanostructured

templates. *Semiconductor Science and Technology*, 21:1547–1551, September 2006.

[26] Ritsuo Ohashi, Tomohiko Ohtsuka, Narihisa Ohta, Akira Yamada, and Makoto Konagai. Position control of inas quantum dots by afm oxidation. *Thin Solid Films*, 464-465:237–239, 2004.

[27] D. Schuh, J. Bauer, E. Uccelli, R. Schulz, A. Kress, F. Hofbauer, J.J. Finley, and G. Abstreiter. Controlled positioning of self-assembled inas quantum dots on (110) gaas. *Physica E*, 26:72–76, 2005.

[28] M. J. Lercel and H. G. Craighead. Sub-10 nm lithography with self-assmebled monolayers. *Appl. Phys. Lett.*, 68:1504–1506, March 1996.

[29] F. Keith Perkins, Elizabeth A. Dobisz, Susan L. Brandow, Jeffrey M. Calvert, John E. Kosakowski, and Christie R. K. Marrian. Fabrication of 15 nm wide trenches in si by vacuum scanning tunneling microscope lithography of an organosilane self-assmebled film and reactive etching. *Appl. Phys. Lett.*, 68:550–552, January 1996.

[30] Richard D. Piner, Jin Zhu, Feng Xu, Seunghun Hong, and Chad A. Mirkin. "dip-pen" nanolithography. *Science*, 283:661–663, January 1999.

[31] Riichiro Saito, Gene Dresselhaus, and Mildred S. Dresselhaus. *Physical Properties of Carbon Nanotubes.* Imperial College Press, 1998.

[32] Mark S. Gudiksen, Jianfang Wang, and Charles M. Lieber. Synthetic control of the diameter and length of single crystal semiconductor nanowires. *J. Phys. Chem. B*, 105:4062–4064, April 2001.

[33] Yi Cui, Xiangfeng Duan, Jiangtao Hu, and Charles M. Lieber. Doping and electrical transport in silicon nanowires. *J. Phys. Chem. B*, 104:5213–5216, June 2000.

[34] J.-Y. Marzin and G. Bastard. Calculation of the energy levels in indium arsenide/gallium arsenide quantum dots. *Solid State Commun*, 92:437–442, July 1994.

[35] Maria Francesca Iozzi, Benedetta Mennucci, and Jacopo Tomasi. Excitation energy tranfer (eet) between molecules in condensed matter: A novel application of the polarizable continuum model (pcm). *J. Chem. Phys.*, 120:7029, April 2004.

[36] C. F. Wang, A. Badolato, I. Wilson-Rae, P. M. Petroff, E. Hu, J. Urayama, and A. Imamoglu. Optical properties of single inas quantum dots in clsoe proximity to surfaces. *Applied Physics Letters*, 85:3423–3425, October 2004.

[37] S. Fafard. Near-surface inas/gaas quantum dots with sharp electronic shells. *Applied Physics Letters*, 76:2707–2709, May 2000.

[38] Klaus Adlkofer, Eric F. Duijs, Frank Findeis, Max Bichler, Artur Zrenner, Erich Sackmann, Gerhard Abstreiter, and Motomu Tanaka. Enhancement of photoluminescence from near-surface quantum dots by suppression of surface state density. *Phys. Chem. Chem. Phys.*, 4:785–790, January 2002.

[39] E. C. Le Ru, P. D. Siverns, and R. Murray. Luminescence enhancement from hydrogen-passivated self-assembled quantum dots. *Applied Physics Letters*, 77:2446–2448, August 2000.

[40] S. Sauvage, P. Boucaud, F. H. Julien, J.-M. Gerard, and V. Thierry-Mieg. Intraband absorption in n-doped inas/gaas quantum dots. *Applied Physics Letters*, 71:2785–2787, September 1997.

[41] Daniel V. Schroeder. *An Introduction to Thermal Physics.* Addison Wesley Longman, 1999.

[42] G. A. Domoto, R. F. Boehm, and C. L. Tien. Experimental investigation of radiative transfer between metallic surfaces at cryogenic temperatures. *ASME Journal of Heat Transfer*, 92:412–417, August 1970.

[43] C. M. Hargreaves. Anomalous radiative transfer between closely-spaced bodies. *Physics Letters A*, 30:491–492, December 1969.

[44] S. S. Kutateladze, N. A. Rubtsov, and Ya. A. Bal'tsevich. Effect of magnitude of gap between metal plates on their thermal interaction at cryogenic temperatures. *Sov. Phys. Dokl.*, 23:577–578, August 1978.

[45] David K. Cheng. *Field and Wave Electromagnetics.* Prentice Hall, 1989.

[46] Bruno Huttner and Stephen M. Barnett. Quantization of the electromagnetic field in dielectrics. *Phys. Rev. A*, 46:4306–4322, October 1992.

[47] Peter L. Hagelstein. On the intersubband scheme with coulomb coupling. *unpublished.*

[48] Reza Matloob and Rodney Loudon. Electromagnetic field quantization in absorbing dielectrics. *Phys. Rev. A*, 52:4823–4838, December 1995.

[49] Edward D. Palik. *Handbook of optical constants of solids III.* San Diego : Academic Press, 1998.

[50] T. Tomiki, Y. Ganaha, T. Futemma, T. Shikenbaru, Y. Aiura, M. Yuri, S. Sato, H. Fututani, H. Kato, T. Miyahara, J. Tamashiro, and A. Yonesu. Anisotropic optical spectra of α-al_2o_3 single crystals in the vacuum ultraviolet region. ii spectra of optical constants. *J. Phys. Soc. Jpn.*, 62:1372–1387, 1993.

[51] R. H. French, H. Mullejans, and D. J. Jones. Optical properties of aluminum oxide determined from vacuum ultraviolet and electron energy loss spectroscopies. *J. Am. Ceram. Soc.*, 81:2549–2557, 1998.

[52] Dominik Horinek and Josef Michl. Surface-mounted altitudinal molecular rotors in alternating electric field: Single-molecule parametric oscillator molecular dynamics. *Proceedings of the National Academy of Sciences*, 102:14175–14180, October 2005.

[53] M. S. Tomassone and A. Widom. Electronic friction forces on molecules moving near metals. *Phys. Rev. B*, 56:4938, August 1997.

[54] Timothy H. Boyer. Penertration of the electric and magnetic velocity fields of a nonrelativistic point charge into a conduting plane. *Phys. Rev. A*, 9:68, January 1974.

[55] Neil W. Ashcroft. *Solid State Physics.* Holt Rinehart and Winston, 1987.

[56] Sadao Adachi. *Optical constants of crystalline and amorphous semiconductors : numerical data and graphical information.* Boston : Kluwer Academic Publishers, 1999.

[57] M. H. S. Amin. Rabi oscillations in systems with small anharmonicity. *Low Temperature Physics*, 32:198–204, March 2006.

[58] L. I. Schiff. *Quantum Mechanics.* McGraw Hill, 1968.